THE UNIVERSITY OF GLASGOW

The Low Temperature Photoconductivity in Amorphous Silicon-Scaling and Time Dependence

by

Mohamed MOSTEFA B.Sc(Hon), M.Phil.

Submitted for the degree of Doctorate of Philosophy

in

The Department of Physics and Astronomy,

July 1992

To my family for taking so much of my time away from them.

CONTENTS

ABSTRACT

Recently, the low temperature photo-induced transport properties of amorphous semiconductors and the hydrogenated amorphous silicon (a-Si:H) in particular, have been the interest of many authors. These can be studied by various techniques, particularly by luminescence and photoconductivity measurements.

In the present work, the low temperature photoconductivity of a-Si:H is investigated. The samples were prepared in sandwich configuration by glow discharge and RF sputtering techniques.

The samples have been measured below 50K, at DC and audio frequencies, for constant temperature and varying the excitation intensity and vice-versa. The frequency dependent photoconductivity $\Delta\sigma_1(\omega, I)$ data of intrinsic and compensated materials for different intensities of illumination (I) when normalized to the appropriate DC photoconductivity $\sigma_1(0, I)$ follow a universal function of the reduced frequency $\omega/\sigma_1(0, I)$. Such scaling behaviour is well established for the temperature dependent dark conductivity of tunnelling samples, but has not been reported before for the photoinduced measurements. This scaling behaviour suggests strongly that the underlying recombination mechanism involves hopping in the band tails as suggested by several authors recently. Compensated samples showed a significant contribution to the dark conductivity at high temperatures due to the potential fluctuations. However, the scaling behaviour was almost identical for both intrinsic and compensated samples which implies that carriers trapped in these potential wells in the bands do not contribute significantly to the photoconductivity.

The d.c. photoconductivity was observed to vary as $\sigma_1(0, I) \propto I^{\gamma}$ with $\gamma \approx 1$. The change in the relative permittivity with the intensity of illumination $\Delta\epsilon_1 \propto I^{\beta}$ with $\beta \approx 0.16$.

The time dependence of the d.c. and a.c. photoconductivities of the samples was also studied at low temperatures. Both real (capacitance) and imaginary (conductance) parts of the dielectric constant rise linearly with time to a steady state value and then when the light is extinguished the signal decays towards the dark value. This is attributed to the trapped carriers that recombine through a tunnelling process leading to the long-lasting behaviour. The initial rate of rise is proportional to the intensity of illumination (i.e. $\frac{d\Delta\epsilon_1}{dt} \propto I^{\alpha}$ with $\alpha \approx 1$). The d.c response on the other hand was found to grow and decay instantaneously (within the experimental resolution) as the light is switched on or off. The behaviour was uniform throughout the range of intensities covered by the measurements, corresponding to carrier generation rates between approximately 10^{14} and $10^{18}\text{cm}^{-3}\text{s}^{-1}$. No sign of any transition from predominantly geminate to predominantly non-geminate recombination is seen. Comparing the data with the current theories, seems that there is no single model enable to explain it satisfactorily. A new analytical approach based on the Baranovskii et *al.*(1987) model is introduced to explain the data. A reasonable agreement with the experiment is obtained.

ACKNOWLEDGEMENTS

I would like to take this opportunity of thanking the following people for whose help I am most grateful. Foremost, my supervisor Dr. A. R. Long for his help, invaluable discussions, continuous encouragement and supply of ideas.

I am grateful to Professor W. E. Spear of the University of Dundee for supplying the glow discharge samples to me.

I am also grateful to the members of the Solid State Physics Group for many interesting discussions and to the technical staff particularily Mr. D. McDonald and Mr. A. Young for their help.

Mrs. M. Waterson for her excellent drawing assistance.

My family without whose love and moral support through the years, this thesis would never have been started.

The financial suport of the Algerian Ministere de L'enseignement Superieur et de la Recherche Scientifique is gratefully acknowledged.

DECLARATION

This thesis is a record of the work carried out by me in the department of Physics and Astronomy at the University of Glasgow between January 1989 and January 1992. The work described herein is my own, except where indicated otherwise. The glow discharge samples were provided by the Dundee group. Some of the work in this thesis can be found in the following papers:

- Frequency Scaling of the low-Temperature Photoconductivity of Amorphous Silicon, A.R. Long, M. Mostefa and R. Lemmon, *J. Phys.: Condens. Matter* **3**(1991)2589.
- Scaling of the Photo-induced Frequency Dependent Loss in Amorphous Silicon at Low Temperatures, A.R. Long, M. Mostefa and R. Lemmon, *J. Non-Cryst. Solids.* **137**&**138**(1991)419.
- Time dependence of the low-temperature hopping photoconductivity in amorphous silicon, A.R. Long and M. Mostefa, *Phil. Mag.*, **B 65**(1992)739.

This thesis has not previously been submitted for a higher degree.

M. MOSTEFA

July 1992

CHAPTER 1

INTRODUCTION

The purpose of this project was to study the photo-induced loss in amorphous silicon prepared by RF magnetron sputtering and glow discharge decomposition of silane (SiH_4) both intrinsic and compensated samples. The dark a.c. loss was measured so that information on the transport process can be obtained. Recent results (see Shimakawa et *al.* 1987) have shown that a contribution to the total loss in the intrinsic a-Si:H at high temperatures (T> 100K) follows an empirical formula $\omega^{1-\frac{T}{T_0}}$. This behaviour is attributed to inhomogeneous regions which exist in the material and act as carrier traps and increase the loss. The same investigation was carried out on three different sets of samples, one of which was an intrinsic and the other two were compensated with different compensated doping ratios. The results were then compared with Shimakawa et *al.* results.

The D.C. and A.C. photoinduced loss was measured at low temperatures below 50K and at higher intensities than previously reported measurements of Long et *al.*(1988b) in order to examine the relationship between the D.C. and A.C. photoconductivities. The time dependence of the loss was examined in order to obtain information on the dominating recombination mechanisms at low temperatures.

The thesis is organized as follows. The next chapter deals with a review on the theoretical models which are generally recognized to dominate the transport in amorphous semiconductors. Chapter 3 concentrates on the photoinduced phenomena: such as photoconductivity, photoluminescence, light-induced electron spin

resonance. A detail of a recent theoretical model proposed by Shklovskii, Fritzsche and Baranovskii (1989a,b) is presented. Chapter 4 gives a detail of the experimental procedures, sample preparation and techniques of cooling and illuminating the samples. The main body of results in this thesis is presented in chapter 5-7. In chapter 5, we present the results of dark D.C. and A.C. losses to aid comparison of our samples with those measured recently. Chapter 6 contains the photoinduced loss data together with the scaling of the low temperature photoconductivity and the discussion of the results in the light of the model presented in chapter 3. In chapter 7, we present the results of the time dependence of the D.C. and A.C. photoresponse, a comparison of the data with recent LESR data is made and new analytical approach is introduced to explain the data. A summary and conclusion drawn from the observations of the last three chapters are discussed in chapter 8.

CHAPTER 2

Electron Transport in Amorphous Semiconductors.

2.1 Introduction

In this chapter we review several theoretical models used to explain the general features of the d.c and the a.c losses in amorphous semiconductors, particularly of a-Si:H. The chapter is divided in two sections. The first one deals with the d.c and a.c transport in sputtered a-Si:H with high defect density. The second part deals with those of the glow discharge a-Si:H

2.2 Sputtered a-Si and a-Si:H

2.2.1 D.C. Conductivity.

In materials with high density of defect states of the order of 10^{18} cm^{-3} eV^{-1} such as sputtered a-Si and a-Si:H deposited on low temperature substrate, the electron transport is believed to take place between localized states by exchanging energy with the lattice Mott (1969). Mott considered two sites separated by a distance R and with an energy difference W. One site is filled and below the fermi level E_F, the other empty and above E_F. The amount W is either smaller or greater than the phonon energy $h\omega_0$, where ω_0 is the highest phonon frequency in the lattice. In the former case W $< h\omega_0$ the electron transfer from one site to the other involves only a single phonon. However if W $> h\omega_0$ several phonons assist the process (see Mott and Davis 1979).

Considering the first case, Mott calculated the transition rate and found the following expression:

$$\nu = \nu_0 e^{-2\alpha R_0} e^{-\frac{W}{k_B T}} \tag{2.1}$$

where α^{-1} is the localization length and $e^{-2\alpha R_0}$ is the probability of the electron transfer by tunnelling. The second term is the probability of the existence of a phonon with energy W. Using Einstein relation the conductivity can then be calculated.

$$\mu = \frac{eD}{k_B T} \tag{2.2}$$

where D = $\frac{\nu R^2}{6}$

Hence, the conductivity is:

$$\begin{aligned} \sigma &= ne\mu \\ &= \frac{ne^2R^2}{6k_BT} exp(-2\alpha R)\, exp\left(-\frac{W}{k_BT}\right) \end{aligned} \tag{2.3}$$

Mott (1969) suggested that at high temperatures the carriers are excited to the localized states at an energy E in the band edges and hence the conductivity is dominated mainly by hopping of carriers within kT of range E, to unoccupied levels of nearest neighbour centres.

At low temperatures, the number of phonons decreases and so does their energy. Therefore the carriers will preferentially hop to larger distances to find sites which lie energetically closer than the nearest neighbours.

To take this variable range into account, Mott applied an optimization procedure to the factor exp $\left(-2\alpha R - \frac{W}{k_B T}\right)$. This treatment leads to a temperature dependence of the conductivity of the form:

$$\sigma = \sigma_0 exp\left(\frac{T}{T_0}\right)^{-\frac{1}{4}} \tag{2.4}$$

where the pre-exponent factor σ_0 is of the form $\sigma_0 \sim [N(E_F)T]^p$ where

| p |$\leq$ 1 and T_0 is given as:

$$T_0 = \frac{18\alpha^3}{N(E_F)k_B} \tag{2.5}$$

The equation (2.4) is the Mott $T^{1/4}$ law, and the process is known as the variable-range hopping mechanism.

It must be mentioned here that Mott's derivation of variable range hopping involves a large number of simplifying assumptions, including: energy independence of the density of states at E_F, omission of subsidiary energy factors appropriate to multiphonon processes, and neglect of details of electron-phonon interaction. Many authors have demonstrated that the energy distribution of the density of states is of major importance in the theory of variable range hopping. Details of the multi-phonon process can be seen in Emin (1974).
A similar form to the Mott law has been obtained by other workers Ambegaokar et *al.*(1971), Pollak (1972) and Aspley and Hughes (1974, 1975).

Ambegaokar et *al.* considered a model in which charge is carried via phonon tunnelling of electrons between localised states which are randomly distributed in energy and position. In their calculation, the authors adopted the model of Miller and Abrahams (1960), by formulating the system as a resistance network. They considered the case of low electric field $\vec{E}$. In order to obtain an expresssion for the conductivity, they assumed that the temperature is sufficiently low which together with high tunnelling rate and high density of localised states implies that the hopping mechanism is predominant. The rate of transition for an electron from a site 1 to an empty site 2 separated in energy by $\Delta E_{12} = E_1 - E_2$ and in space by R_{12}, is given as:

$$\gamma_{12} = \gamma(R_{12}, \Delta E_{12}) \propto exp(-2\alpha R_{12}) \tag{2.6}$$

This is only correct in the case of $\Delta E_{12} > k_B$T. The average transition rate from site 1 to site 2 is denoted as Γ^0_{12}. Therefore the conductance G_{12} between the two sites is given as:

$$G_{12} = \frac{e^2}{k_B T}\Gamma^0_{12}(R_{12}, E_1, E_2) \tag{2.7}$$

To generalize this on the whole network, the latter is considered to consist of randomly distributed points linked to one another by conductances G_{ij}, with i and j two sites in the network. Consequently, any point will be connected by a large conductance to its close neighbours. In addition to that the strongest connections will occur for pairs of sites whose energies are near the Fermi level. The total conductivity of the resistance network is given by:

$$\sigma = \frac{\tilde{G}}{\tilde{R}} \tag{2.8}$$

where $\tilde{G}$ and $\tilde{R}$ are the characteristic conductance and length in the network respectively. The factor $\tilde{R}^{-1}$ varies very slowly with the parameters of the network and therefore the dominant variation in equation (2.8) will be contained in the conductance. This percolation treatment of the hopping conductivity is similar to Mott's variable range hopping theory. A full detail of the calculation of the conductivity is given in Ambegaokar et *al.*(1971).

2.2.2 A.C. Conductivity.

2.2.2.1 The Pair Approximation.

Unlike the d.c conduction where a continuous percolation path between the electrodes is necessary for the current to flow, the a.c. loss in amorphous semiconductors can be estimated by considering the polarizability of an isolated pair of states and to sum up the losses due to such pairs to obtain the response of the bulk sample. This model is known as the "Pair Approximation". The model was first proposed by Pollak and Geballe (1961) and updated by Pollak several times (1971, 1972) and by Mott and Davis (1979). In this section, we shall summarise the derivation as presented by Pollak and Geballe (1961).

They started by considering a pair of single electron states separated in energy by Δ_{12} and in space by a distance R_{12}. The polarizability of the pair in the presence

of small oscillation can be written as:

$$\frac{e^2 R_{12}^2}{4k_B T} \frac{1}{\cosh^2\left(\frac{\Delta_{12}}{2k_B T}\right)} \frac{1}{1+i\omega\tau} \tag{2.9}$$

where ω is the angular frequency of the applied a.c field.

τ is the effective relaxation time and has the form:

$$\tau = \frac{\tau_0}{2}\left[cosh\left(\frac{\Delta_{12}}{2k_B T}\right)\right]^{-1} \tag{2.10}$$

The polarizability has a Debye form $\frac{1}{1+i\omega\tau}$ and because of the factor $\cosh^2\left(\frac{\Delta_{12}}{2k_B T}\right)$, the loss will only occur for states separated by $\leq$ k_BT for they are closely enough spaced in energy to be linked in a relaxation process.

A similar expression was found by Austin and Mott (1969) with an extra $\cos^2(\theta)$ term, where θ is the angle between the electric field and the separation distance R_{12}. The pair approximation is likely to work best at high frequencies as in this regime the pairs which are closely spaced will have a shorter time of relaxation. However, at low frequencies the separation between the states involved in the a.c loss increases and the interactions with other neighbouring states will be important.

2.2.2.2 Model for Charge Transfer by Tunnelling.

This model is used for the states deep within the energy gap, which have a broad range of energies close to the Fermi level. D.c. conductivity below room temperature can be fitted to the Mott law $T^{-\frac{1}{4}}$ over many decades (Long 1982, Elliott 1987). The conduction is believed to occur by tunnelling of carriers between states close to the mid-gap. With the assumption that the tunnelling model is operative, the a.c conductivity can be evaluated. The relaxation time is similar to equation (2.10), but with τ_0 replaced by:

$$\tau_0 = 2\tau_{0t} exp(2\alpha R_{12}) \tag{2.11}$$

where τ_{0t}^{-1} is in the simpler models of the order of the phonon frequency. The above equation gives,

$$\tau = \frac{\tau_{0t} exp(2\alpha R)}{\cosh(\Delta_{12}/2k_BT)} \tag{2.12}$$

The tunnelling distance R_ω at a given frequency ω, with $\omega\tau = 1$, is given by:

$$R_\omega = -\frac{1}{2\alpha} \ln\left(\frac{1}{\omega\tau_0}\right) \tag{2.13}$$

It can be seen that R_ω is expected to be independent of temperature in this model.

The real part of the a.c. conductivity can be obtained using equation (2.9) and equation (2.12) together with the distribution of the pair separation in space. These give:

$$\sigma_1(\omega) = \frac{\pi^4}{12} \frac{e^2 g_0^2 k_B T}{2\alpha} \omega R_\omega^4 \tag{2.14}$$

where g_0 is the density of states. The equation (2.14) can be expressed empirically as:

$$\sigma_1(\omega) \sim \omega^s T^n \tag{2.15}$$

where s is given by;

$$s = 1 + \frac{4}{\ln(\omega\tau_{0t})} \tag{2.16}$$

For this model s is independent of temperature and is of the order of 0.8 for a frequency ($\omega \sim 10^4 s^{-1}$) and assuming τ_{0t} is of the order of the inverse optic phonon frequency or 10^{-13}s (see Long 1982).

2.2.2.3 Generalization of the PA Model (EPA).

Fig.(2.1) illustrates a typical behaviour of a variable range hopping system. The graph is divided into three regions. Region (1) is the D.C. conducitivity determined by Mott's law, region (3) is the high frequency regime where the PA is valid as we have seen in section (2.2.2.1) and region (2) at intermediate frequencies in between these two regions. As a first approximation, the total measured loss of the system over a range of frequency may be given by the sum of the d.c. and PA contribution.

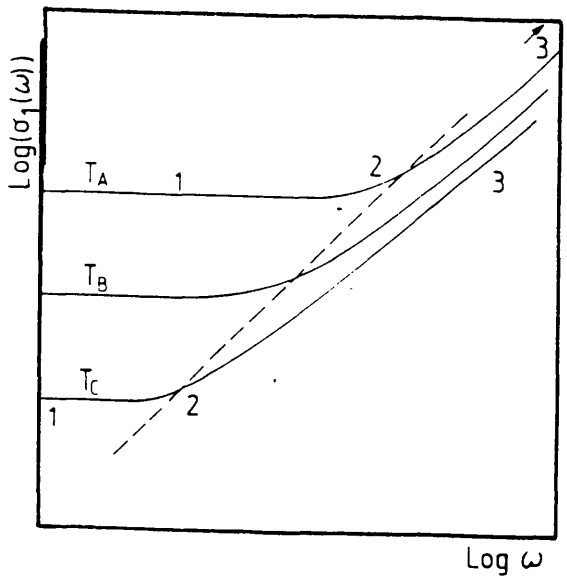

Figure 2.1: **Schematic diagram of the frequency dependence of the conductivity of a hopping system at three temperatures, $T_A > T_B > T_C$. The intermidiate frequency region 2 is shown between the DC limit and the high-frequency region 3 where the pair approximation is valid. The broken line, $\omega_c/\sigma_1(\omega_c)$= const., links equivalent points according to scaling ideas.**

This however ignores the contribution to the a.c. loss in region (2) from clusters of more than two states. As a result, an inadequacy arises when comparing the theory with the experimental data. A number of theoretical approaches have been put forward to investigate this intermediate frequency regime. These have been reviewed by Long (1991). One of them was first proposed by Summerfield and Butcher (1982). The authors were able to take into account the network of interacting localized states which contribute to both the d.c. percolation path through the material and the high frequency dispersive response. In their theory, they generalized the equivalent circuit proposed by Miller and Abrahams (1960), to take into account the effect of neighbouring states on the response of a pair of states. The response of the whole system can then be obtained by adding the elements in an average way. This model is well known as " The Extended Pair Approximation " (EPA).

Summerfield (1985) has shown that to a very good approximation when the conductivity is normalized to its d.c value at a particular temperature, it becomes a quasi-universal function of the reduced frequency $\tilde{\omega}$:

$$\tilde{\omega} = \frac{\omega e^2 \alpha}{\sigma_1(0) k_B T} \tag{2.17}$$

α is the decay parameter of the localized state wavefunction and $\sigma_1(0)$ the d.c. conductivity. Different loss curves taken at various temperatures see fig.(2.2a) can then be plotted as a function of $\tilde{\omega}$ on a single master curve (fig.2.2b). Here we show the scaling for the real part of the conductivity, but in fact this relationship applies to the imaginary part as well (see Long et *al.* 1988a). The EPA predicts a loss peak in the plots of the real and imaginary parts of the conductivity. These peaks have been reported by Long et *al.*(1983, 1985,1988a) for sputtered a-Ge, a-Si and a-Si:H. The EPA fits have also been applied to the frequency dependence of the photoconductivity of glow discharge a-Si:H, which will be discussed in more detailed later on (see chapter 6).

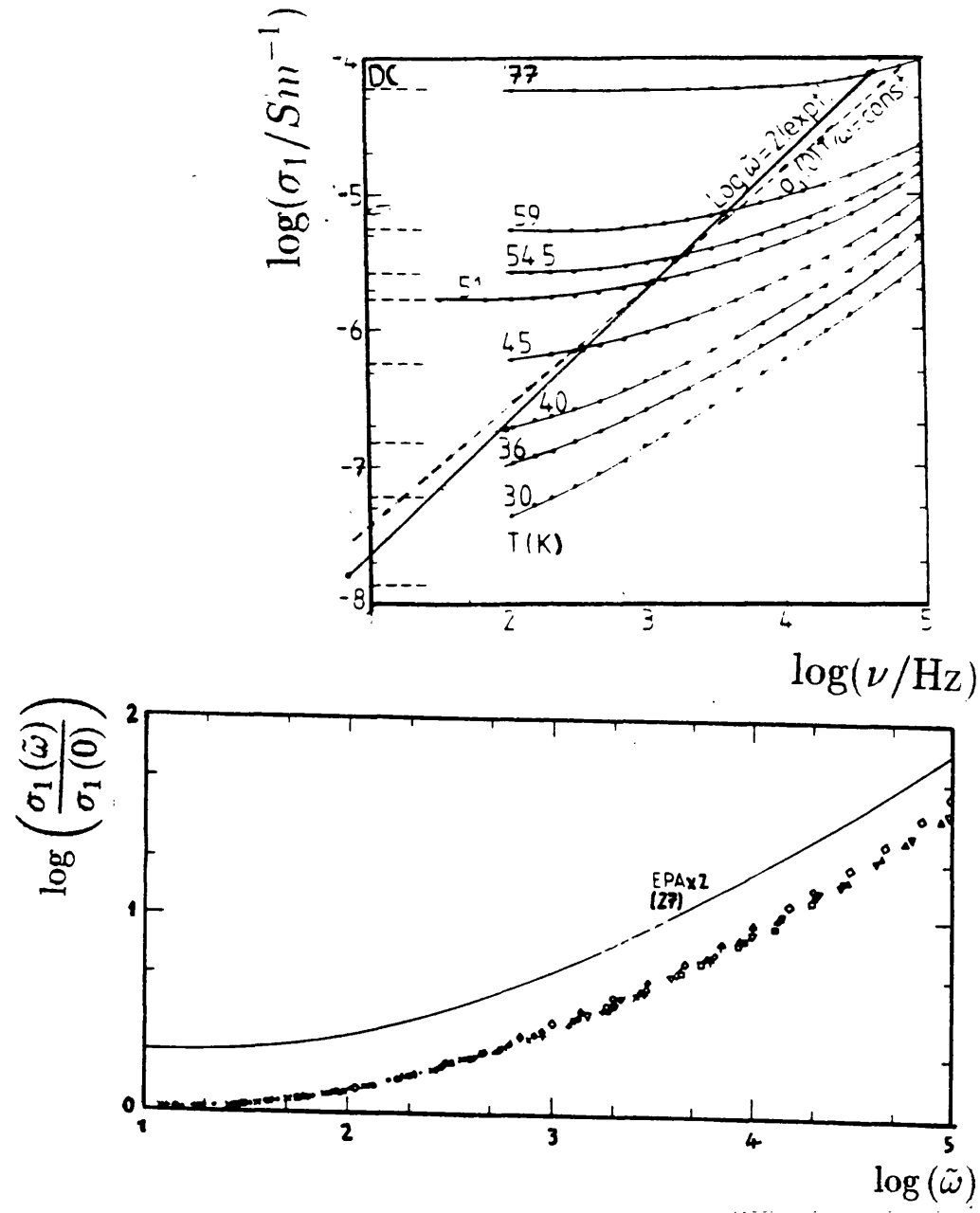

Figure 2.2: **(a) The real part of the conductivity of a sputtered a-Si:H plotted against frequency at various temperatures. The measured d.c. values are indicated by horizontal broken lines. The full circles are points where the fitted value of the scaled frequency $\tilde{\omega}$ is 100. The locus of these points is compared with a line obeying $\sigma_1(0)T/\omega=$ constant as suggested by the EPA scaling theory (b) The same data plotted in scaled form for all the temperatures in (a). The EPA prediction (for $(T_0/T)^{1/4} = 27$) is displaced vertically by a factor of two for clarity.** (after Long.et *al.* 1988a).

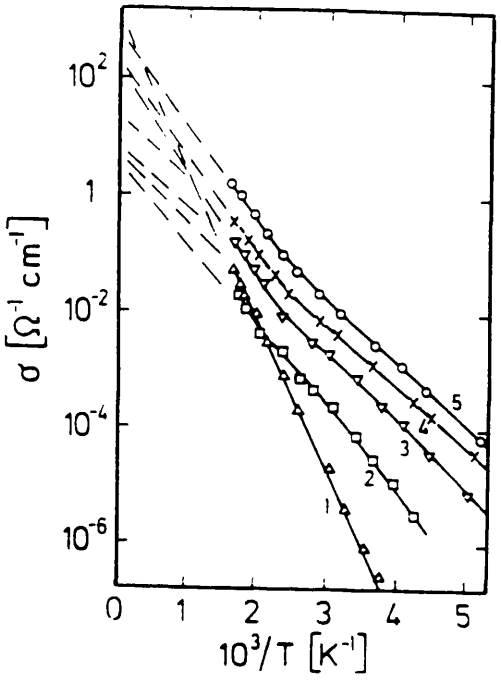

Figure 2.3a: **Conductivity for n-type a-Si:H films as a function of inverse temperature. $[PH_3]/[SiH_4] = 10^{-6}$ (1), $3\ 10^{-6}$ (2), $2.5\ 10^{-4}$ (3), 10^{-3} (4), and 10^{-2} (5).** (after Bayer et *al.* 1977).

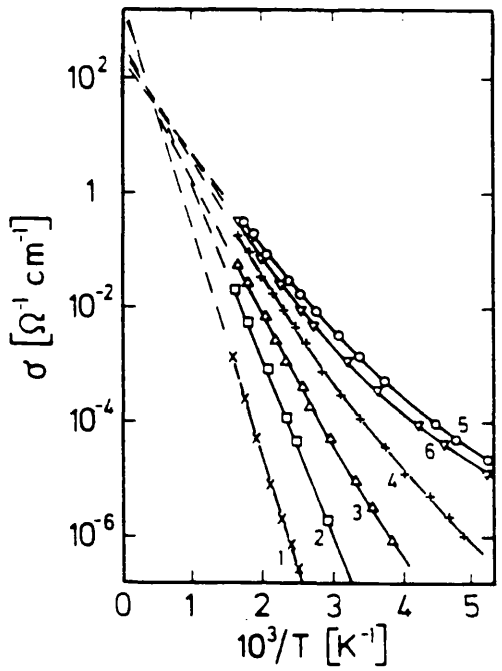

Figure 2.3b: **Conductivity for p-type a-Si:H films as a function of inverse temperature. $[B_2H_6]/[SiH_4] = 10^{-5}$ (1), 10^{-4} (2), 10^{-3} (3), 10^{-2} (4), $5\ 10^{-2}$ (5), $2\ 10^{-1}$ (6).** (after Bayer et *al.* 1977).

2.3 Glow Discharge Materials (a-Si:H)

2.3.1 D.C. Conductivity.

Materials prepared by the glow discharge technique are known to have lower densities of states in the centre of the gap than in sputtered materials, and therefore the mechanism dominating the electron transfer is expected to be different. Two different channels for conduction are discussed next.

2.3.1.1 Extended State Conduction.

According to Davis-Mott model the Fermi level is near the middle of the gap and hence far from the conduction band energy E_C (strictly the energy which separates the extended states from the localized states in the band tails). The conductivity may be evaluated from the Kubo-Greenwood formula as:

$$\sigma = -e \int N(E)\mu(E)k_B T \frac{\partial f(E)}{\partial E} dE \tag{2.18}$$

where f(E) is the Fermi-Dirac function and $\frac{\partial f(E)}{\partial E} = -f(E)\frac{[1-f(E)]}{kT}$.
μ is the mobility and N(E) the density of states.

With the assumption of a constant density of states and constant mobility, the conductivity to electrons excited beyond the mobility edge into the extended states is given by:

$$\sigma = \sigma_{min} \exp\left(-\frac{E_C - E_F}{k_B T}\right) \tag{2.19}$$

σ_{min} is of the order of Mott maximum metallic conductivity.
In contrast, the experimental data showed that the conductivity does not appear to be strictly activated: for example: for n-type materials there are marked kinks see fig.(2.3a),while for p-type samples there is a change in the slope see fig.(2.3b) (Beyer, Mell and Overhof 1977 and Beyer and Mell 1977). This suggests a shift in the Fermi level with respect to conduction band edge as function of temperature. In this case σ_0 and the activation energy E_0 cannot be determined using the standard

model. In reality the quantity ΔE_σ = E_C - E_F(T), from the plot of $\log\sigma$ vs $\frac{1}{T}$ is the real activation energy. In this case the energy at the Fermi level can be expressed by a linear temperature dependence as follows:

$$E_F(T) = E_F^*(0) - \gamma_F T \tag{2.20}$$

where a constant value of γ represents the first order approximation to the temperature dependence, and $E_F^*(0)$ is the value extrapolated to zero temperature. Hence the conductivity can be rewritten as:

$$\sigma = \sigma_{min} \exp\left(-\frac{E_C - E_F^*(0) - \gamma_F T}{k_B T}\right) = \sigma_0 \exp\left(-\frac{E_\sigma^*(0)}{k_B T}\right) \tag{2.21}$$

with $\sigma_0 = \sigma_{min}\exp(\frac{\gamma_F}{k_B})$ and $E_\sigma^* = E_C - E_F^*(0)$. The shift in the Fermi level gives rise to a difference between ΔE_C and E_σ^*. This value was deduced from above as $-\gamma_F T$. The shift in the Fermi level also leads to the Meyer-Neldel rule which states that the experimental pre-exponential factor σ_0^* is an exponential function of the experimental activation energy E_σ^* :

$$\ln(\sigma_0^*) = B + \frac{E_\sigma^*}{E_{MNR}} \tag{2.22}$$

where B is a constant and E_{MNR} is calculated from the linear part in the plot $\ln(\sigma_0^*)$ against E_σ^*. A value of around 0.043eV was obtained for a doped a-Si:H (see Overhof and Thomas 1989).

Beyer, Fischer and Overhof (1979) analysed the temperature dependence of the thermopower in the lithium-doped amorphous silicon and showed that it leads to the same result:

$$S = -\frac{k}{e}\left(\frac{E_C - E_F^*(0)}{k_B T} + A^*\right) \tag{2.23}$$

where S= the thermopower, e is the charge of carrier and $A^* = A + \frac{\gamma_F^*}{k}$ and A is a constant.

Comparison of equations. (2.21) and (2.23) shows that a plot of $\ln\sigma$ and S vs $\frac{1}{T}$ should have the same slope when conduction is in the extended states. Beyer et *al*

have considered a function combining the conductivity and the thermopower:

$$Q(T) = \ln \sigma(T) + \frac{e}{k_B} S(T) \tag{2.24}$$

where the shifts (kinks) mentioned above cancel. The quantity Q(T) showed a linear relationship when plotted against $\frac{1}{T}$ over the whole range of temperatures (see Overhof and Beyer 1981).

This type of mechanism is found to be dominant in glow discharge materials at high temperatures T > 250K (see Le Comber and Spear 1970).

2.3.1.2 Conduction in Band Tails.

The second channel is the transport by carriers excited into localized states at the band edges and hopping at energy at the bottom of the band tail (E_A) for the conduction band. Mott and Davis showed that the conductivity through this process has the form:

$$\sigma = \sigma_1 exp\left\{-\frac{E_A - E_F + w_1}{k_B T}\right\} \tag{2.25}$$

where w_1 is the activation energy for hopping in the band tail states. The pre-exponential σ_1 is expected to be smaller than σ_0 by several orders of magnitude, due to lower density of states near E_A compared with E_C and also because of a lower mobility in the band tails. This process is likely to be dominant at lower temperatures than the mechanism discussed in the previous section. Yet Beyer et *al.*(1979) have not noticed any change in the mechanism within their range of temperature (200-570K) and their doping range in lithium doped samples (up to Li/Si ratio of 10^{-2}). Although their data was not compatible with the model in which there is a transition from activated hopping in the band tails to extended state transport, they did not rule out its occurrence.

2.3.2 A.C. Conductivity.

The a.c. conductivity in hydrogenated amorphous silicon (a-Si:H) grown at high temperature using the glow discharge technique has been investigated extensively

recently. The general behaviour was well established, which is the a.c. conductivity $\sigma_{ac}(\omega) \propto \omega^s$ within the accessible range of frequencies. Where s is a function of temperature ($s \approx 1 - \frac{T}{T_0}$). T_0 is a characteristic temperature typically in the region of 500K. At temperature below 100K, s reaches a maximum value close to 1 then becomes independent of temperature at lower temperatures. The a.c. loss in the low temperature regime is believed to be due to a mechanism which involves the polarisation of carriers in deep states close to the Fermi level (see Shimakawa et *al.* 1987). However, the loss at high temperatures is assigned to processes occuring far from the Fermi level. But this was still not a satisfying interpretation. Recently, Overhof and Bayer (1983) pointed out that a-Si:H contains inhomogeneous regions, which were responsible for the inconsistencies of the d.c. conduction (see section 2.3.1.1) . Long (1989a,b) on the other hand introduced a new theoretical approach to take into account the effect of the long range potential fluctuations on the a.c. loss at high temperatures. A good fit to the data was obtained. A detail of the model is given in the next section.

2.3.2.1 The effect of potential fluctuations on the a.c. loss in inhomogeneous materials.

The study of the conduction behaviour of inhomogeneous media has a long history going back to Bruggeman (1935). The a.c. conductivity of an inhomogeneous material composed of a concentrations C of medium 1 and $1 - C$ of medium 2 in the form of spherical regions was investigated by Springett (1973), who obtained the complex dielectric constant of the equivalent effective medium $\hat{\epsilon}_m$ in terms of those of the constituents:

$$C\frac{\hat{\epsilon}_1 - \hat{\epsilon}_m}{\hat{\epsilon}_1 + 2\hat{\epsilon}_m} + (1 - C)\frac{\hat{\epsilon}_2 - \hat{\epsilon}_m}{\hat{\epsilon}_2 + \hat{\epsilon}_m} = 0 \tag{2.26}$$

where,

$$\hat{\epsilon}_j = \epsilon_j - \frac{i\sigma_j}{\epsilon_0\omega} \tag{2.27}$$

ϵ_j and σ_j being the real parts of the dielectric constant and the conductivity of the component j, respectively. Long (1989a) introduced a new theoretical approach to account for the contribution to the a.c. loss at high temperatures. In his calculation, Long studied the effect of a range of different conductivities by extending the above theory.

Long assumed that a-Si:H contains large spherical regions with high conductivity for each one. With respect to the Fermi level the energies in these regions are altered by long-range potential fluctuations of amplitude ΔE. The concentration of regions with a particular ΔE is given by a distribution function C(ΔE). To explain the features of the frequency dependent loss data in a-Si:H, Long considered three different distributions for the potential fluctuations: exponential, double-sided exponential and Gaussian. Here, we present the calculations in the case of an exponential distribution:

$$C(\Delta E) = \frac{C_0}{kT_0} exp\left(-\frac{\Delta E}{k_B T_0}\right) \tag{2.28}$$

with $\Delta E > 0$. The temperature T_0 gives the effective energy range of fluctuations. According to the Boltzmann distribution of carrier number, the conductivity can be written as:

$$\sigma = \sigma_b exp\left(\frac{\Delta E}{k_B T}\right) \tag{2.29}$$

where σ_b is the conductivity of the background material. In order to obtain the effect of different regions the equation (2.26) is applied many times and with the assumption that the real part of the dielectric constant is the same for all the regions, ϵ_b, hence:

$$\hat{\epsilon}_j = \epsilon_b - \frac{i\sigma_b}{\epsilon_0 \omega} \exp(\frac{\Delta E_j}{k_B T}) \tag{2.30}$$

Using the distribution in equation (2.28), the computational results of the conductivity of the effective medium σ_m as a function of the reduced angular frequency $\tilde{\omega}$ given by $\frac{\omega \epsilon_0 \epsilon_b}{\sigma_b}$ or $\omega \tau_b$ (where τ_b is the bulk conductivity relaxation time) is shown in fig.(2.4). It is in a reasonable agreement with the experimental findings. Particularly, the frequency exponent s was found to vary as 1- $\frac{T}{T_0}$ (see inset fig.2.4). Long

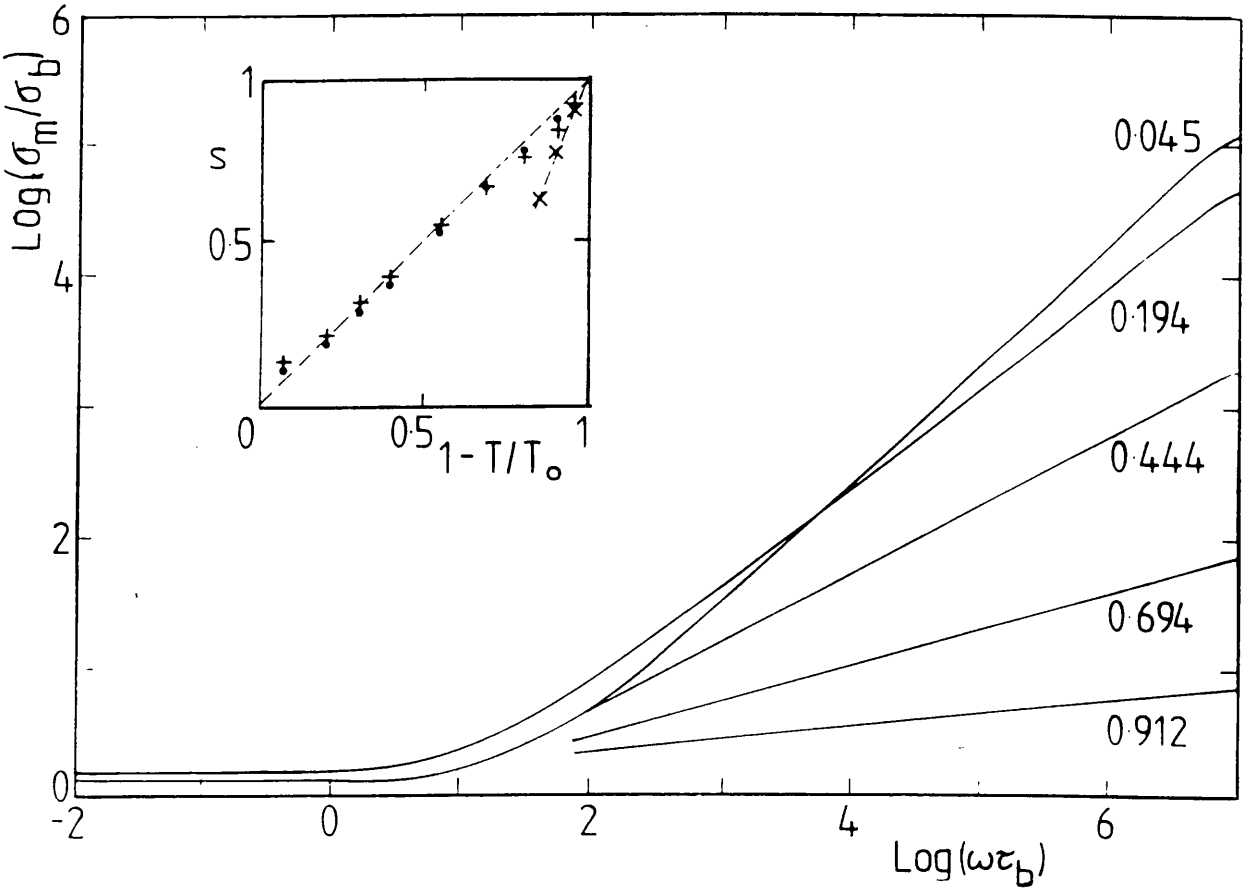

Figure 24: **Logarithmic plot of σ_m/σ_b versus $\omega\tau_b$ for 3-D exponential model with C_0= 0.174, parameter: T/T_0 value. Some curves suppressed below $\omega\tau_b$= 100 to improve clarity. Inset: frequency exponent s for computed curves versus 1-T/T_0 •: C_0= 0.174. +: C_0= 0.434. ×: Gaussian distribution with C_0= 0.174. The hatched line is of unit gradient.**

calculated the absolute a.c. conductivity by assuming that the d.c. conductivity is simply activated.

$$\sigma_b = \sigma_0 \exp(-\frac{E_0}{k_B T}) \tag{2.31}$$

and approximating the result from fig.(2.4) in the high-frequency region in the form :

$$\frac{\sigma_m}{\sigma_b} = C_0 (\omega \tau_b)^{1-\frac{T}{T_0}} \tag{2.32}$$

This gives;

$$\sigma_m = C_0 \sigma_0 exp\left(-\frac{E_0}{k_B T}\right)\left(\frac{\omega \epsilon_b \epsilon_0}{\tau_0}\right)^{1-\frac{T}{T_0}} \tag{2.33}$$

σ_m has a power-law behaviour with the exponent given by:

$$s = 1 - \frac{T}{T_0} \tag{2.34}$$

This empirical form for s has been found in glow discharge a-Si:H (see Shimakawa et *al.* 1987a). The calculation above was fitted to one of the sample measured by Shimakawa et *al.* From the results in fig.(2.5) the pre-exponential factor σ_0 and the activation energy E_0 can be estimated using equation (2.31) and T_0 can be deduced from the temperature dependence of s. This was found to be around 430K. The data is then fitted using equation (2.33), the results being the hatched lines in fig.(2.6). The solid lines are obtained by replacing $\frac{\sigma_0}{\epsilon_b \epsilon_0}$ in equation (2.33) by a frequency $\omega_{e0} = 1.2 \times 10^{11}$ rad/s which is two orders of magnitude smaller. In a recent refinement made by Long (1989b) to the model, he argued that an assumption implicit in the effective medium calculation is that the high conductivity regions are large enough to polarise in response to the applied field. This will occur only if they are larger than the appropriate screening length, otherwise they will not contribute to the response. For a high quality intrinsic a-Si:H, the shortest screening length due to localised states is of the order of 250 nm. This is the critical scale length for fluctuations. The deep states will not be able to take part in the screening process unless the escape frequency of carrier from the deep states is greater than or of the order of the measurement frequency. The critical response frequency in the problem

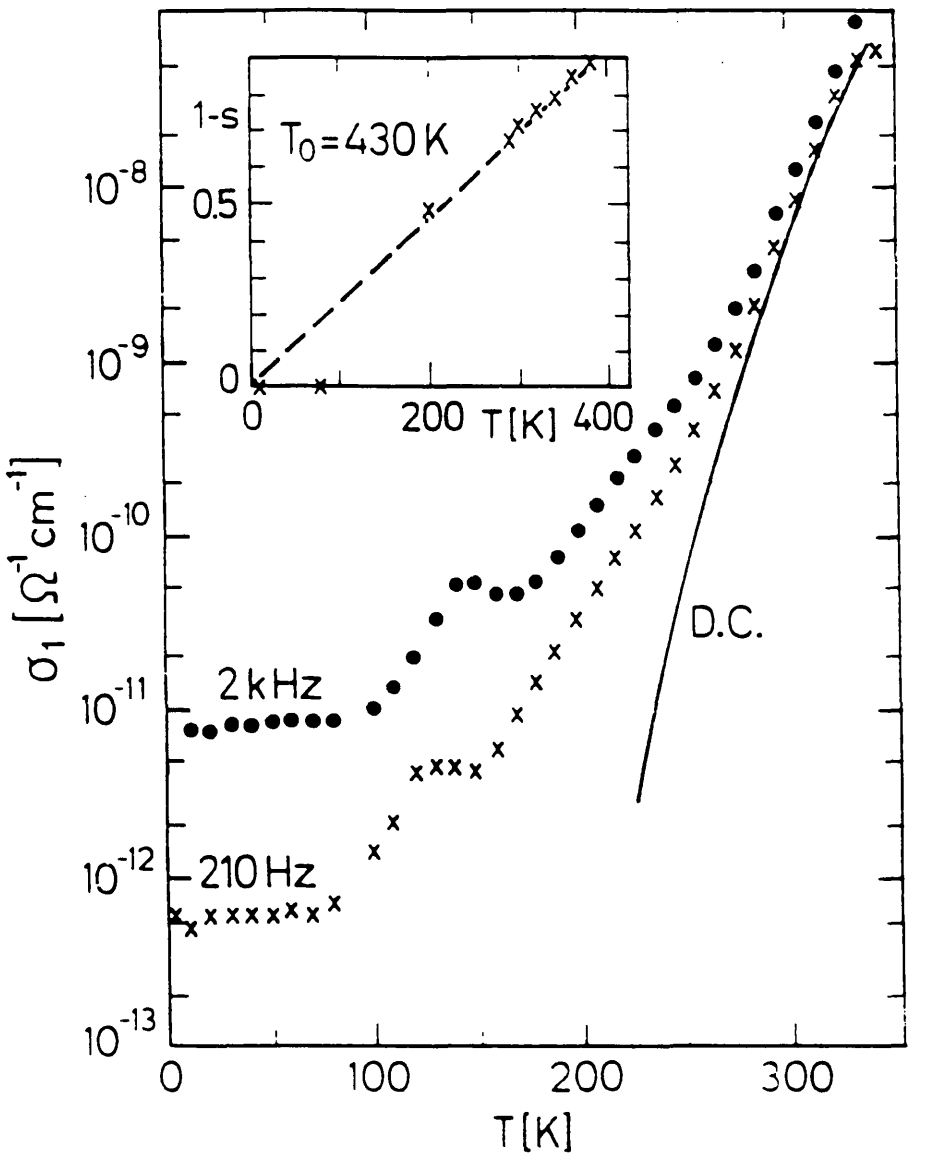

Figure 2.5: **A.C. conductivity for an intrinsic a-Si:H film as a function of the temperature. The inset shows the frequency exponent, 1-s.** After (Shimakawa et *al.* 1987a).

is therefore the slower of the conductivity relaxation frequency τ_b and the escape frequency. As the fitting of the data in fig.(2.6) requires a frequency ω_{e0} smaller than the relaxation frequency implies that the problem is dominated by the escape frequency and hence by deep state screening.

2.3.3 Experimental Review.

The a.c. loss in hydrogenated amorphous silicon (a-Si:H) grown by glow discharge decomposition of silane has been investigated by several workers over recent years including, Abkowitz et *al.*(1976), Nitta et *al.*(1977), Shimakawa et *al.*(1985, 1987a, 1987b). Abkowitz et *al* measured a sample in the audio-frequency range. The σ_{ac} was found to follow ω^s relationship, with s close to unity and the temperature dependence to $T^{0.8}$. They attributed the a.c. transport to the quantum mechanical tunnelling (QMT), with the electrons tunnelling between localised states near the Fermi level. However, this analysis has been criticised by Long (1982) in that both the magnitude of s and its temperature dependence are inconsistent with the QMT model.

Nitta et *al.*(1977) measured a sample at high temperatures (RT $< T <$ 520K) and high frequency (10^5 - 10^7 Hz).

Shimakawa et *al.*(1987a,b) studied the temperature dependence of the a.c conductivity in an intrinsic a-Si:H. They observed a peak at around 130K. This peak is not a feature of the bulk material but is associated with the n^+ contact layers. Aside from the peak, the characteristic see fig.(2.5) can be divided into two regimes, a low temperature regime where the conductivity is approximately temperature independent and a high temperature regime, where it increases rapidly with temperature until it merges with the d.c.conductivity. They ascribed the low temperature behaviour to a correlated hopping process occurring in deep states around the Fermi level. However, in the high temperature regime, the rapid increase suggested that the processes responsible are happening in the band tails away from the Fermi level. On the the-

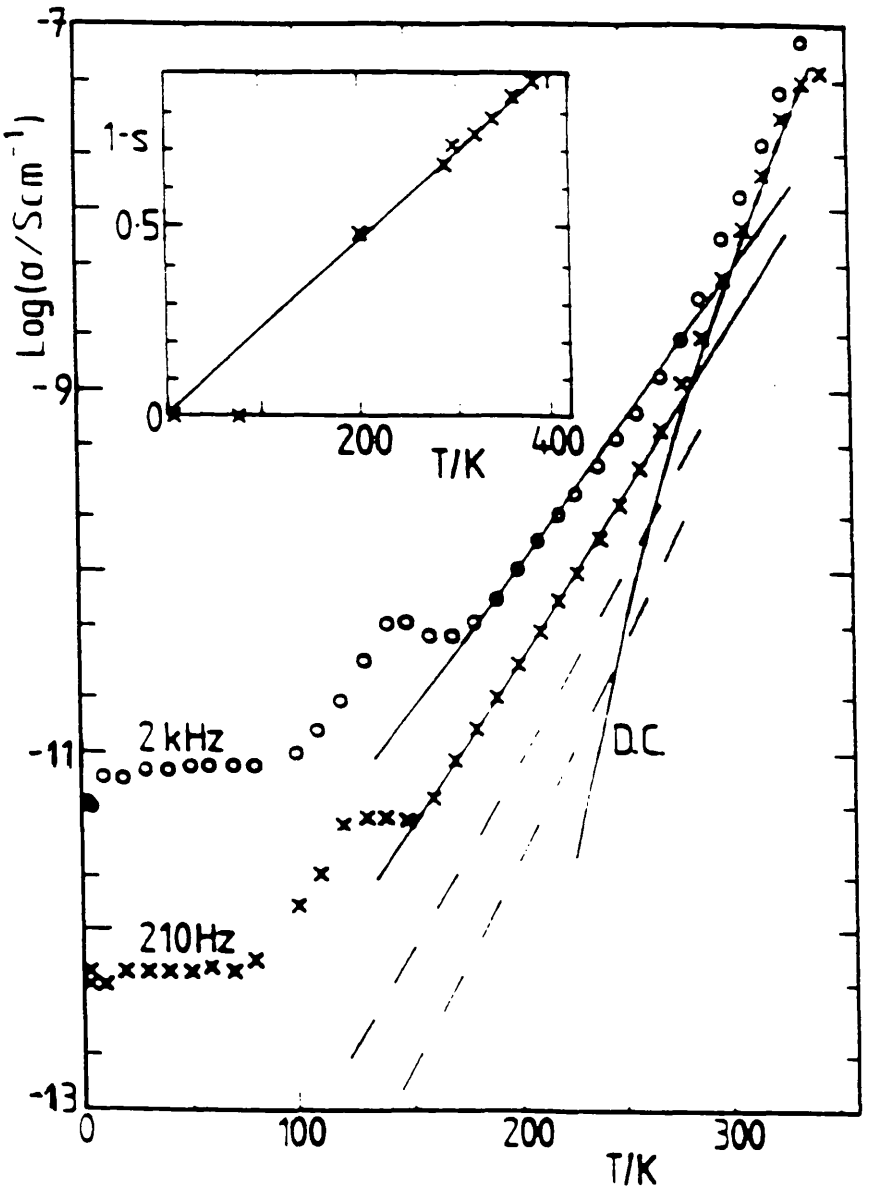

Figure 2.6: **A.C. conductivity at two frequencies and frequency exponent for an intrinsic a-Si:H sample. Parameters used: E_0=0.57 eV, $\sigma_0 = 1200 Sm^{-1}$, T_0= 430K, C_0= 0.25.** After (Long 1989b)

oretical side, recently Long (1989) proposed a model based on the idea of potential fluctuations. The model as discussed in the previous section, was very successful in explaining the high temperature regime observed in Shimakawa et *al.*(1987a) data see fig.(2.5).

CHAPTER 3

Photo-Induced Loss in Amorphous Semiconductors.

3.1 Introduction

Recombination mechanisms in a-Si:H have been studied using a number of experimental techninques, particularily photoconductivity, luminescence and light-induced electron spin resonance. It is well established from these experiments that the electron transport of photogenerated carriers at low temperature is different from that near and above room temperature. At low temperature, below 40K the photoconductivity is to a first approximation independent of temperature and of density of defect states. On the other hand the quantum efficiency of the photoluminescence reaches its maximum at temperatures below 50K (see section. (3.6.1)) and then becomes independent of temperature at lower temperatures. In the following, we concentrate on the discussion of these phenomena and give details of the theoretical model of the hopping photoconductivity at low temperature proposed by Shklovskii, Fritzsche and Baranovskii (1989a)

3.2 Recombination Processes in a-Si:H

In a material such as a-Si:H which luminesces, several mechanisms of recombination are involved. The nature of the process depends strongly on the structural properties of the sample (i.e defect density) and on the experimental conditions, for instance the range of temperature and level of excitation intensity.
Several mechanisms and their application have been discussed in a review article by

Street (1981a). Fig.(3.1) illustrates the possible recombination processes that can be identified.

The question of the radiative recombination mechanism is still debated. Street put forward the geminate model in which it is assumed that the photogenerated electron-hole pairs do not separate after thermalization and hence the recombination takes place between these geminate pairs. Dunstan however, in his distant pair model, suggests the carriers diffuse large distances, are trapped at random spatially and then recombine with their nearest neighbour non-geminately.

In this section we shall discuss only those processes which are related in one way or another to this work. Generally, recombination mechanisms can be divided into radiative and non-radiative processes. Two classes of radiative processes can occur in a-Si:H. The first geminate radiative recombination, is likely to be dominant in material with low concentration of defect states within the band gap, at low temperature and low excitation intensity because there is insufficient thermal energy to dissociate an electron-hole pair. The process is monomolecular, it involves an electron-hole pair that is created geminately. Recombination is geminate when the density of pairs is sufficiently low to make sure that there is no overlapping between neighbour pairs.

The second mechanism is non-geminate radiative recombination. This process occurs at high excitation levels. The process is bimolecular and occurs between non isolated pairs.

At high temperature the electron-hole pairs separate by a thermally activated diffusion process. The recombination is via one of two possible processes. If the excitation intensity is sufficiently low excitation, the carriers are trapped at defect states and recombine by tunnelling. At high excitation, the carriers are likely to recombine directly in non-geminate processes.

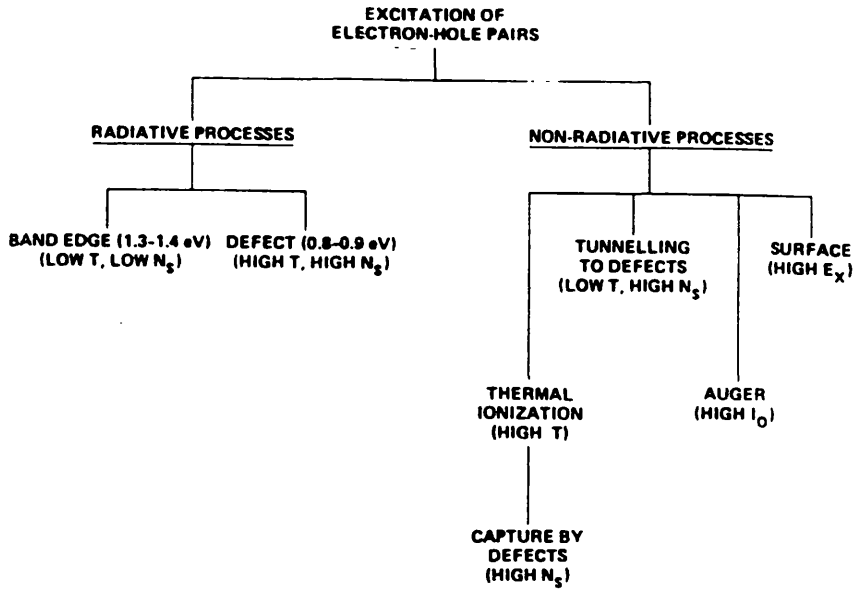

Figure 3.1: Schematic diagram showing the radiative and competing non-radiative processes, and the experimental conditions under which each dominates. N_S is the spin density, E_X the excitation energy and I_0 the excitation intensity. After (Street 1981a.)

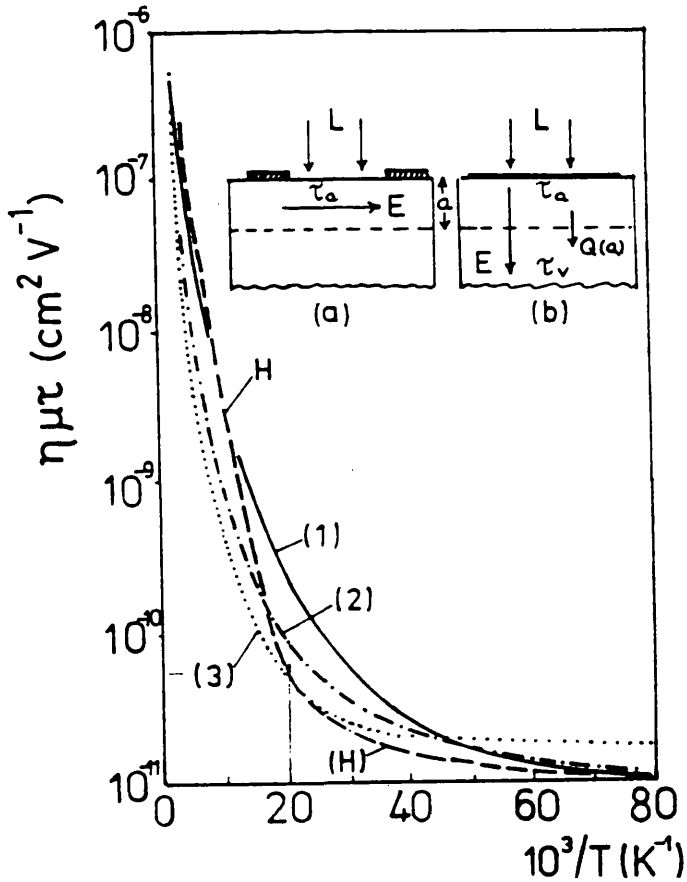

Figure 3.2: The $\eta\mu\tau$ product determined from steady-state photoconductivity measurements on undoped a-Si plotted as afunction of 10^3T^{-1}. Curve H: results of Hoheisel et *al.*(1984) using coplanar electrodes; curves (1)-(3): results on junction and Schottky barrier specimens. Inset: (a) coplanar electrodes: τ_a is the lifetime within the absorption depth a. (b) sandwich electrodes: τ_v is volume lifetime in i region. Curve (1)—p^+-i-n^+ (1.84μm): curve (2)-.-.-(r^+-i-n^+ (0.7μm) and cuve (3)...p^+-i-n^+ (1.3μm). After (Spear and Cloude 1987)

3.3 D.C. Photoconductivity.

In this work we are interested in the low temperature (i.e T$\leq$50K) steady state photoconductivity in a-Si:H. The experiment is basically done by illuminating the sample with a continuous (CW) light. Then, any optically induced change in the capacitance and the conductance of the sample as a function of temperature and intensity of illumination is measured.

The dark d.c. conductivity in a-Si:H samples is observed to increase under the effect of low intensity electromagnetic radiation at all temperatures. The phenomenon is different from the Staebler-Wronski effect, in that the latter is observed when the sample was illuminated with high intensity light at room temperature for as long as four hours (see Staebler and Wronski 1980). In this case the light induced a "light-soaked" state and then the sample saturates even under further illumination. To return to the dark state, the sample has to be annealed at around 150^0C. The rate of the reverse process is dependent on the annealing temperature. In the former phenomenon however, the d.c. conductivity changes under a much lower intensity of light. A steady state photoconductivity is reached after a short time. After the illumination is removed, the original dark value is regained without annealing the sample. In fact the photocurrent decays rapidly after the light is removed (see section 7.5). The d.c photoconductivity is determined by the generation rate of free carriers, their lifetimes τ_n and the absorbed flux F within the intensity range.

$$\sigma_{ph} = e\mu_n n = e\eta\mu_n\tau_n F \tag{3.1}$$

where η is the photogeneration effeciency, n the number of free carriers contributing to the photocurrent and μ_n their mobility, with the assumption that electrons dominate the holes. The dependence of the photoconductivity on the light intensity obeys a power law of the form.

$$\sigma_{ph} \propto I^{\gamma} \tag{3.2}$$

over the entire ranges of temperature and intensity (see Wronski and Carlson 1977,

Hoheisel et *al.* 1983 and 1984 and Huang et *al.* 1983). Wronski and Carlson measured the photoconductivity above 120K. Two regions were exhibited in the intensity dependence with γ equal to 0.7 and 0.5 depending on the intensity and temperature. Huang et *al.* reported a constant value for $\gamma \simeq 0.75$ at around room temperature over the range of intensities. As the temperature was decreased down to 200K, γ decreased to 0.6. The above results were in good agreement with a hypothetical recombination process in which an electron or a hole pass through the extended states in order to recombine. As the temperature is lowered below 50K the thermal energy is no longer available and carriers are trapped and therefore the photoconductivity will depend on the trap limited drift mobility. In this temperature regime the intensity exponent is close to unity (e.g $\gamma = 0.97 \pm .03$, see Hoheisel et *al*)

Some studies have been carried out recently by Hoheisel et *al.*(1983) and (1984), Vaněček et *al.*(1987) and Cloude, Spear, Le Comber and Hourd (1986) and Spear and Cloude (1987). They discussed the temperature dependence of the $\eta\mu\tau$ product. Hoheisel et *al* observed that between room temperature and at around 40K, $\eta\mu\tau$ decreased rapidly by four orders of magnitude and then reached approximately constant value of $\sim 10^{-11}\text{cm}^2\text{V}^{-1}$ see fig.(3.2). At low temperatures, $\gamma = 0.97$ and decreases with increasing temperature. They explained their results by suggesting that after the photogeneration, the carriers contribute to the conduction only during their thermalization in the extended states after which they are strongly localized in tail states below the mobility edge. Assuming an extended state mobility of 10 $\text{cm}^2\text{V}^{-1}\text{s}^{-1}$ and $\tau_{th} = 10^{-12}\text{s}$ for the thermalization time in the extended states, the observed $\eta\mu\tau$ value leads to the conclusion that the quantum efficiency for the generation of mobile carriers $\eta = 1$. This result indicates that even at the lowest temperature highly efficient generation of excess carriers takes place. Similar results have been reported by Vaněček et *al.*(1987).

However, Spear et *al.*(1987) criticized this value for η as unrealistic. They in-

vestigated the $\mu\tau$ product by transit experiments with the assumption that it is similar to the steady state. They obtained a value of around $3 \times 10^{-10} cm^2 V^{-1}$ and $\eta \sim 5 \times 10^{-2}$. They attributed the major contribution to the photocurrent at low temperature to the hopping of carriers in band tails and deduced any contribution during thermalization in the extended states is almost negligeble.

Recently, Johanson et *al.*(1989) have measured the photoconductivity between 4 and 300K for several amorphous semiconductors including hydrogenated and unhydrogenated a-Si. At low temperature, γ varies between 0.93 and 1 for all the samples measured and as the temperature increases γ decreases. At low temperatures the quantity $\frac{\sigma_{ph}}{eG}$ is constant and the value depends on the material (see fig.(3.3)).

The variation of $\frac{\sigma_p}{eG}$ with the dopant has been observed by Misra, Kumar and Agarwal (1984), Stachowitz, Fuhs and Jahn (1990) and Yoon and Fritzsche (1991). The last group have observed that $\frac{\sigma_p}{eG}$ decreases with increasing the boron doping and that T_2 increases to 70K. The temperature T_2 is defined to be the temperature at which the d.c. photoconductivity exceeds its value at T=0 value of equation (3.21) by a factor of two (see section (3.5.1) for more detail). Yoon and Fritzsche attributed this effect to a submicroscopic structural heterogeneity induced by boron doping and not to the concentration of dangling bonds defects. In contrast to this, Stackowitz et *al* made different observations. They found that $\frac{\sigma_p}{eG}$ decreases by a factor of three and T_2 increases to 82K. They attributed this to the increase in defect concentration which changes from 5×10^{15} to 5×10^{17} cm^{-3} under electron bombardment. Yoon and Fritzsche claimed that they observed this change only with their lower quality samples. On the other hand, Misra et *al* observed that after exposing their undoped sample to high intensity for 2 hours at room temperature, the photoconductivity is increased by 10 orders of magnitude and that γ decreased from 0.85 to 0.7 even at low temperature. In their interpretation they adopted the model of Hoheisel et *al.* 1983 discussed above.

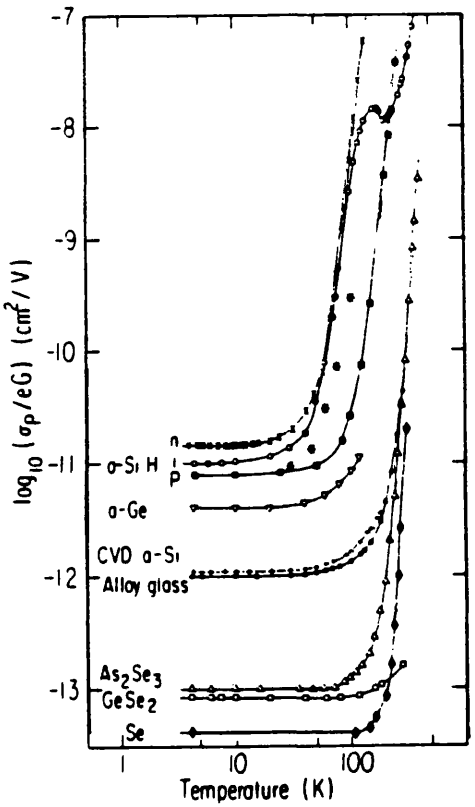

Figure 3.3: Normalized photoconductivity σ_p/eG of different samples as a function of temperature. The asterisks refer to calculated σ_p value by Fritzsche (1989). After (Johanson et *al.* 1989).

3.4 The effect of IR-radiation on the Photoconductivity.

Fuhs (1985) observed when a film of an undoped a-Si:H was excited by IR-radiation ($h\nu < 0.7$ eV), the transient photoconductivity exhibits a short enhancement which in the steady state is followed by a quenching at 130K and by an enhancement at 30K. Similar results have reported by Vanier and Griffith (1982). The results have been attributed to the enhancement of recombination by optical excitation of the trapped minority carriers. Fuhs explained the PC quenching in terms of the recombination approach originally proposed by Dersch et *al.*(1983) (see fig.(3.4)). These authors proposed that apart from the localized band tail states only one defect state is present. This defect is the dangling bonds which can exist in three charge states. The positively charged (D^+), neutral (D^0) and negatively charged (D^-). After creation (E) and thermalization (t_h,t_e) carriers are trapped in the localized tail states from where they can either be re-emitted (1a,1b) or recombine via the dangling bond defect states (2,3). The steps for the recombination are: The electrons tunnel to neutral dangling bonds D^0, thus form D^- states (2). Then they undergo a transition from D^- to the trapped holes in the valence band tail (3). The rate of recombination can be enhanced by diffusion of the trapped hole via D^- states.
The PC quenching has been observed in n-type materials at around 30K and above, whereas in p-type film is only seen at around 130K. The enhancement is observed at temperature below 50K in both types of films. The photoconductivity in this range, as we have seen in the previous section, is determined by the lifetime of the carriers near the mobility edge and the $\eta\mu\tau$ product showed a constant value $\sim 10^{-11}$ $cm^{-2}V^{-1}$ independent of the defect density and temperature.

The quenching in n-type and p-type films is observed up to 150K and 250K respectively. This is ascribed to a competition of thermal clearing of the trapped carriers with the optical effect. At these temperatures a trap depth of 0.11 eV for electrons in n-type material and 0.27 eV for holes in p-type can be obtained (see Fuhs 1985).

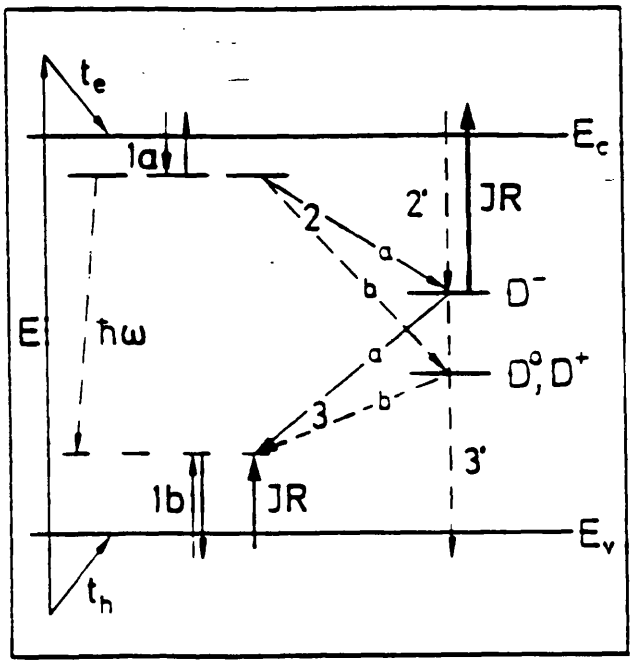

Figure 3.4: Recombination model - see text (Dersch et *al.*(1983).

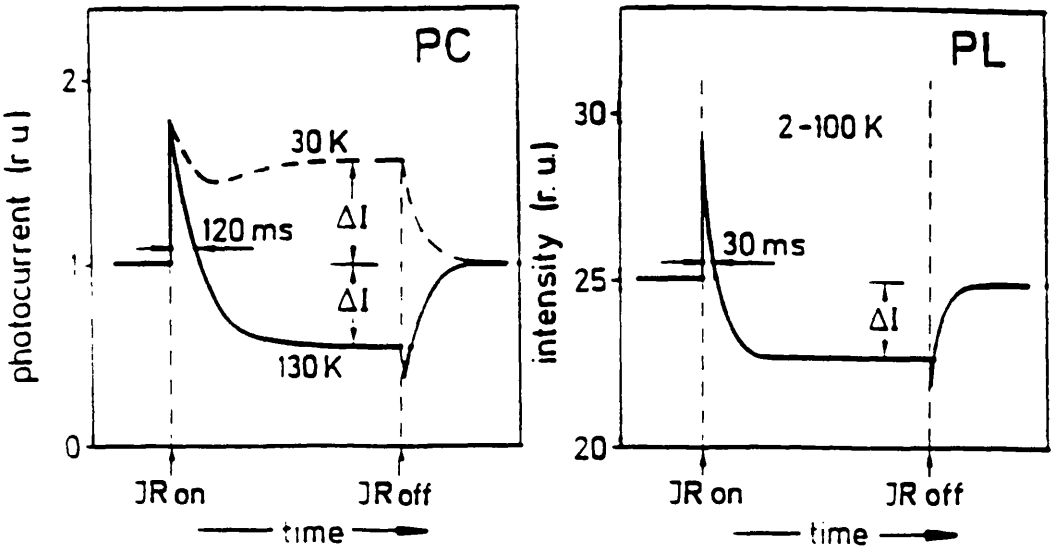

Figure 3.5: Transient behaviour of the photoconductivity and the photoluminescence in a dual beam experiment. After (Carius et *al.*1984).

The spectral dependence of the PC quenching begins at around 0.5-0.6 eV in all samples which is attributed to the transition being excited from D^- states by IR radiation. In n-types films the IR excitation of the majority carriers from D^- would result in the enhancement of the PC. However, as a result of the strong dependence of the tunnelling rate (process 2) on the concentration of D^0 states, a small incease in the number of D^0 will decrease the lifetime in the steady state. Hence, this will lead to a decrease in the photocurrent in a short time after the IR radiation is switched on. Such a transition can be seen in fig.(3.5). In p-type films however, a large number of D^0 states are produced and this means more electrons are encouraged to tunnel to these states and therefore the rate of recombination will increase. Dersch et *al.*(1983) pointed out that the tunnelling process is very important. These authors have suggested that as the temperature rises, the competition between a direct capture of electrons at D^0 (process 2') and the tunnelling process (process 2) becomes important. The effect is more significant in p-type than in n-type materials, as the number of free and trapped electrons in p-type films is significantly lower. Fuhs 1985 suggested that the disappearance of the IR-quenching occurs when direct capture of electrons at D^0 states becomes important. On the other hand the thermal quenching is assigned to the direct capture of the thermally activated holes at D^0 or D^- states.

3.5 Model for the Low Temperature Photoconductivity in Amorphous Semiconductors.

A model has recently been proposed by Shklovskii, Fritzsche and Baranovskii (1989a,b, 1990) and Baranovskii, Fritzsche, Levin, Ruzin and Shklovskii (1989) (hereafter called SFB model) to explain many of the observed low temperature photoconductivity phenomena in amorphous semiconductors, particularly a-Si:H. The dominating transport process in this model is hopping in band tails and the recombination is predominently radiative. To account for the d.c photoconductivity, they studied

the diffusion of carriers and for the a.c. photoconductivity they followed the pair approximation model proposed initially by Pollak and Geballe (1961) (see chapter 2).

Before discussing the model in detail, we should point out the main assumptions made by the authors. First, at very low temperature, carriers can only hop down in energy through the localised band tail states before recombination occurs by tunnelling. Secondly, for the sake of simplicity, the hole is assumed to be fixed and only the electron is involved in the process. Recent measurements of the drift mobilty (see Fritzsche 1989) using the travelling wave technique indicate that the low-T photoconductivity in a-Si:H is dominated by electrons. Thirdly, to calculate the photoconductivity, the density of states (DOS) g(E) in the tail is assumed to be exponentially distributed.

They considered an electron-hole pair generated in the band tails. From the second assumption the electron has two alternatives, it can either hop down in energy to a nearest neighbour state at a distance r with a rate.

$$\nu_d(r) = \nu_0 exp(-\frac{2r}{a}) \tag{3.3}$$

or it can recombine with the hole at a rate.

$$\nu_r(R) = \tau_0^{-1} exp(-\frac{2R}{a}) \tag{3.4}$$

where R is the electron hole separation and a is the localization radius of the electron. ν_0 is the phonon frequency i.e $\nu_0 = 10^{12} s^{-1}$ and $\tau_0^{-1} = 10^8 s^{-1}$.

Fig.(3.6) illustrates the possible diffusive steps that the electron can take before recombining. The motion is of special kind as the next hopping step occurs over a longer distance than the previous one. The electron-hole separation R_m after m steps is given by:

$$\langle R_m^2 \rangle = \sum_{k=1}^{m} \langle r_k^2 \rangle \tag{3.5}$$

and $\langle r_m^2 \rangle = 2^{2/3} \langle r_{m-1}^2 \rangle$. The factor $2^{2/3}$ arises in the following way. If we consider the m^{th} jump, we have N_m density of localised states accessible to the electron during

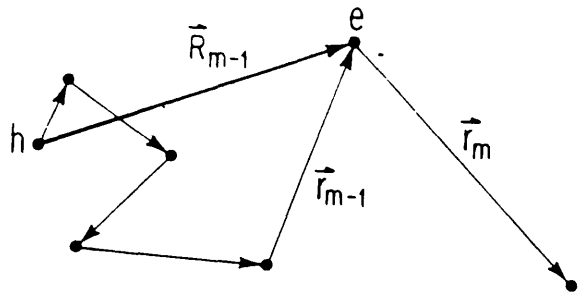

Figure 3.6: Diffusion path of an electron.

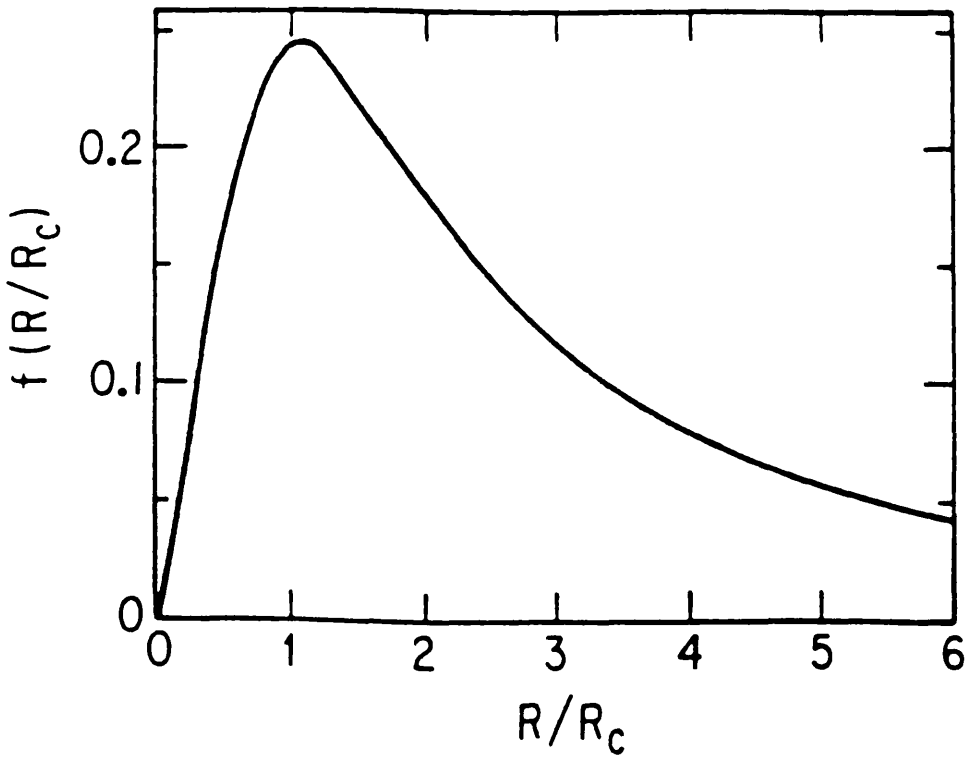

Figure 3.7: Geminate recombination $f(R/R_C)$ as a function of geminate pair separation R in units of the critical length scale R_C. After (Shklovskii et *al.* 1989a).

the $(m+1)^{th}$ jump. In the case when there is no recombination in the next step, hence N_{m+1} will be distributed from 0 to N_m. The electron in the $(m+1)^{th}$ jumps to the nearest neighbour with a number M_{m+1} distributed from 1 to M_m, where M_m are the accessible states in the $(m+1)^{th}$ jump. Consequently,

$$N_{m+1} = yN_m \tag{3.6}$$

where y is a random number between 0 and 1, with $\langle y \rangle = \frac{1}{2}$. Therefore after each jump, the density of accessible states decreases approximately by 2 and the average distance between the states decreases by a factor of $2^{2/3}$. Comparing equations. (3.3) and (3.4) for the distance R_m and r_{m+1}, hence

$$\frac{\nu_d(r_{m+1})}{\nu_r(R_m)} = exp\left(\frac{2A}{a}\right) \tag{3.7}$$

where

$$A = R_C - (r_{m+1} - R_m) \tag{3.8}$$

and $R_C = a/2\ln(\nu_0\tau_0)$ is a critical length at which the diffusive regime and geminate recombination regime start competing against each other. If A> 0, this means that $\nu_d > \nu_r$ i.e diffusion is favoured. If A< 0, $\nu_r > \nu_d$ i.e recombination is favoured.
A is positive if r_{m+1} and $R_m < R_C$. However, if r_{m+1} and $R_m > R_C$ then A fluctuates between positive and negative values depending on the values of R_m and r_{m+1}.

We study the second case, when both R_m and r_{m+1} are larger than R_c in order to determine the expressions for the probability of escaping the recombination and the probability of radiative recombination. The fate of the electron in the $(m+1)^{th}$ step depends on how R_m is compared to r_{m+1}. Firstly, if $R_m < r_{m+1}$, this implies that A < 0, in accordance with equation. (3.8). Therefore, the electron recombines. Secondly, if $R_m > r_{m+1}$, this means that A > 0, i.e. the electron continues to diffuse along the accessible states. Let $\eta(R)$ be the probability of making M steps without recombining and is given by:

$$\eta(R) \propto q^M = exp(-M \mid \ln q \mid) \tag{3.9}$$

where q is a constant between 0 and 1. A typical length after M steps is of the order of.

$$R \sim (2^{1/3})^M R_C \Longrightarrow M \propto \frac{3\ln\frac{R}{R_C}}{\ln 2} \tag{3.10}$$

Then, equation. (3.9) can be written as:

$$\eta(R) \propto exp\left(-\frac{3\ln\frac{R}{R_C}}{\ln 2} \mid \ln q \mid\right) = exp\left(\ln\left(\frac{R_C}{R}\right)^{\frac{3|\ln q|}{\ln 2}}\right)$$

$$\eta(R) \propto \left(\frac{R_C}{R}\right)^{\beta} \tag{3.11}$$

where $\beta = \frac{3|\ln q|}{\ln 2}$. The probability for radiative recombination is denoted as P(R) = - $\frac{d\eta(R)}{dR}$. From equation. (3.11), P(R) can be expressed as:

$$P(R) \propto -\frac{R_C}{R^2}\left(\frac{R_C}{R}\right)^{\beta-1}$$

$$P(R) \propto R_C^{-1}\left(\frac{R}{R_C}\right)^{\beta+1} \tag{3.12}$$

For R$\gg R_C$, P(R) follows a power law as in equation. (3.12). The function $R_C P(R) = f(\frac{R}{R_C})$ is shown in fig.(3.7). At R< R_C, the magnitude is small, because the diffusion of the electron is dominant in this regime. Then P(R) reaches a maximum at R $\approx R_C$, at which the recombination starts dominating the hopping process. These prediction have been verified using a numerical modelling. The maximum occurs at around $\frac{R}{R_C} \approx 0.8$ and $\beta = 1.0 \pm 0.1$ for R> R_C. The function f(R/R_C) is called the geminate recombination function and β the geminate recombination index.

To study the static and dynamic photoconductivities, we need to define the steady state density n_0 of the nonequilibrium electrons as a function of the rate of generation. We consider a finite pair generation rate G, because here the recombination is entirely geminate. Hence, the main contribution to n_0 comes from the carriers which travel to a maximum separation. The number of these pairs is $G\eta(R)$. According to equation (3.11), the number of these pairs decreases slowly with increasing R. Under the steady state conditions, the recombination must occur at the mean distance $(\frac{1}{2}n_0^{-1/3})$. Generally, carriers which reach this distance do not recombine geminately

but they recombine with other carriers created from other pairs. Therefore, the number of the steady state carriers (electrons in this case) n_0 is determined by equating the term of the rate of generation of the longest-lived pairs (i.e $G\eta(R)$) with rate of the inter pair recombination over the mean distance. Hence;

$$G\eta(\frac{1}{2}n_0^{-1/3}) = \frac{n_0}{\tau}exp(-\frac{n_0^{-1/3}}{a}) \tag{3.13}$$

using eqations. (3.11) with $\beta = 1$, we find;

$$n_0(G) = (L(G)a)^{-3} \tag{3.14}$$

where L is the solution for the equation

$$L = \ln\left[G\tau_0 a^3 L^2 \ln(\nu_0\tau_0)\right]^{-1} \tag{3.15}$$

3.5.1 Hopping D.C. Photoconductivity.

The d.c. photoconductivity is due to relaxation of carriers and recombination processes. Hoheisel et *al.*(1983) have shown that twin (geminate) recombination does not contribute to the photoconductivity. Therefore, we allow only for the inter-pair recombination of carriers to determine the photoconductivity. The current density j is of the form:

$$\jmath = pG\eta(\frac{1}{2}n_0^{-1/3}) \tag{3.16}$$

p is the dipole moment established as a result of spatial separation of an electron and a hole when the inter-pair recombination occurs. Assuming an exponential distribution for the density of states g(E) as

$$g(E) = g_0 exp(-\frac{E}{E_0}) \tag{3.17}$$

where g_0 is the density of states at energies near the mobility edge, then, the average dipole moment p is given as:

$$p(r) = \frac{1}{3}\frac{e^2Fr^2}{E_0} \tag{3.18}$$

where F is the electric field. The dipole is determined by the last hop before the non-geminate recombination i.e r $\sim \frac{1}{2}n_0^{-1/3}$

$$p = p(\frac{1}{2}n_0^{-1/3}) \tag{3.19}$$

With $\sigma = \frac{J}{F}$, we obtain the d.c. photoconductivity

$$\sigma_p = \frac{1}{3}\frac{e^2G}{E_0}\eta\left(\frac{1}{2}n_0^{-1/3}\right)\frac{n_0^{-2/3}}{4} = \frac{1}{12}\frac{e^2Gn_0^{-2/3}}{E_0}\eta\left(\frac{1}{2}n_0^{-1/3}\right) \tag{3.20}$$

Using equations. (3.11) and (3.14) with $\beta = 1$;

$$\sigma_p = \frac{1}{12}\frac{Ge^2}{E_0}(La)^2a\ln(\nu_0\tau_0)(La)^{-1} = \frac{1}{12}\frac{Ge^2a^2}{E_0}L\ln(\nu_0\tau_0) \tag{3.21}$$

From equation. (3.15), G depends exponentially on L, hence σ_p can be witten as

$$\sigma_p \propto G^{\gamma} \tag{3.22}$$

with $\gamma = 1 - L^{-1}$. Taking G = 10^{20} $cm^{-3}s^{-1}$, a =1nm, E_0 = 0.025 eV and $\nu_0\tau_0 = 10^4$, they obtained $\frac{\sigma_p}{eG} = 4 \times 10^{-12}cm^{-2}V^{-1}$ and $\gamma = 0.93$ and L=13. These value are in reasonable agreement with the experimental results (see Hoheisel et *al.* 1983, Long et *al.* 1988b and Johanson et *al.* 1989).

Using this model, the authors were able to estimate an expression for the temperature T_2 after which the low-temperature photoconductivity starts rising with temperature above the value in equation (3.21). To calculate T_2 they take into account the effect of the hops up in energy and the temperature dependence of Monroe transport energy E_t (see Monroe 1985). After it is injected, the electron makes a series of hops down in energy. At the energy E_t, the process changes. Then if the electron hops to a state lower than E_t, it is favourable to hop up towards E_t. This hopping around E_t is similar to a dispersive conduction and E_t acts like a mobility edge. At the energy E_t the chances for down and up hops are the same. This energy is defined as:

$$E_t = 3E_0\ln\left[\frac{3E_0a}{2k_BT}N^{1/3}\right] \tag{3.23}$$

The estimated value for T_2 was found to be:

$$T_2 = \frac{3E_0}{2k_B L} \tag{3.24}$$

Taking E_0 = 0.025 eV and L=13, yields to T_2 = 35K. Yoon and Fritzsche (1991) found a value of 42K which seems to be in good agreement with the theory.

3.5.2 A.C. Photoconductivity

We shall consider now the a.c. photoconductivity $\sigma_p(\omega)$ at a frequency ω. The typical hopping distance r_ω appropriate for the frequency ω is obtained from $\nu_d(r_\omega) = \omega$ and is given by:

$$r_\omega = \frac{a}{2}\ln(\nu_0/\omega) \tag{3.25}$$

We do not consider the case of low frequency where $r_\omega > n_0^{-1/3}$ or the intermediate regime where r$\sim n_0^{-1/3}$ since a.c. and d.c. photoconductivities will be approximately the same. Therefore, we study the case where $r_\omega < n_0^{-1/3}$.

As mentioned earlier, Shklovskii et *al* adopted the pair approximation model proposed by Pollak and Geballe (1961). They calculated the concentration $N_{pr}(\omega)$ of the resonant pairs of localised states, which comply with these conditions:

(i)- The pair separation distance r between two states should be in the range $r = r_\omega \pm \frac{a}{2}$.

(ii)- Each state must contain one electron.

(iii)- The excitation energy is less than or equal to kT.

Under the steady state the concentration $N_{pr}(\omega)$ is found to be:

$$N_{pr} = n_0 \left(\frac{kT}{E_0}\right) r_\omega^2 a \tag{3.26}$$

The polarizability of resonant pairs is of the form.

$$\frac{1}{3}\frac{e^2 r_\omega^2}{kT}\omega \tag{3.27}$$

The $\sigma_p(\omega)$ is then expressed as:

$$\sigma_p(\omega) = \frac{n_0^2 kT}{E_0} \times \frac{1}{3}\frac{e^2 r_\omega^2}{kT} \times 4\pi r_\omega^2 a \times \omega = \frac{4}{3}\pi e^2 E_0^{-1} n_0^2 r_\omega^4 \omega$$

$$= \frac{4\pi}{3}\frac{e^2\omega}{aE_0}\frac{\left[\ln\left(\frac{\nu_0}{\omega}\right)\right]^4}{L^6} \tag{3.28}$$

From equation (3.15), the a.c photoconductivity can be expressed in terms of ω and G as:

$$\sigma_P(\omega) \propto \omega^s G^\beta \tag{3.29}$$

with

$$s = \frac{d\ln\sigma_p(\omega)}{d\ln\omega} = 1 - \frac{4}{\ln\frac{\nu_0}{\omega}} \tag{3.30}$$

and

$$\beta = \frac{d\ln\sigma_p(\omega)}{d\ln G} = \frac{6}{L} \tag{3.31}$$

Taking L = 20 and $\ln(\frac{\nu_0}{\omega}) = 20$ in the audio frequency range, leads to s = 0.8 and $\beta = 0.3$

Although the model was able to determine the expressions for the static and dynamic photoconductivties and to explain the dominant recombination process, there are some points which need to be clarified. We will discuss them in this section.

The theory did not consider the effect of Coulomb attraction. This effect is very pronounced in chalcogenide glasses, because of the low value of their dielectric constants. The effect enhances the geminate recombination and therefore, decreases the photoconductivity σ_p. This observation has been confirmed by Johanson et *al.*(1989) where they found that the photoconductivity in these materials is less than in amorphous silicon by two orders of magnitude. This result suggests that the SFB model cannot be used as a universal theory for all the materials.

The model also ignores any effect of nonradiative or nongeminate recombination processes particularily on the lifetime distribution of the excited carriers, as we will see in the next section that such processes may account for the disagreement between the theory with the experiment.

Recently, Searle (1990) presented a model, in which he criticized the idea of predominently geminate recombination in the SFB theory. He noted that the experimental observations from the intensity dependence of the Photoluminescence (PL) and the light electron spin resonance (LESR) signals at typical excitation intensities can be understood in a model with only one channel of recombination, nongeminate radiative recombination. Searle assumed that geminate recombination is negligible, then, under equilibrium conditions,

$$G = \frac{n}{\tau} \tag{3.32}$$

$$\text{with } \tau = \tau_0 \exp(-\frac{n^{-1/3}}{a})$$

This is similar to equation (3.13) but with $\eta = 1$. The above equation can be used to calculate τ and n. A power law can be obtained between τ and G of the form:

$$\tau = AG^g \tag{3.33}$$

$$\text{and } n \propto G^{1+g} \tag{3.34}$$

$$\text{with } -\frac{1}{g} = 1 + \frac{3}{\ln(\frac{\tau}{\tau_0})}$$

For a value of G = $10^{26}\text{m}^{-3}\text{s}^{-1}$, a= 1nm and $\tau_0 = 10^{-8}$s, give $g \sim -0.79$ and $n \propto G^{0.2}$. This is close to observation. The model is discussed in more detail in chapter 7 when we analyse the time dependence loss data.

3.6 Comparison of the Photoconductivity with other measurements.

3.6.1 Photoluminescence.

The photoluminescence in amorphous materials has been studied in parallel with the photoconductivity by many workers in order to establish a model for the recombination mechanism. The experiment consists of exciting the sample with either a short pulse of light or a constant radiation. The sample as a result emits light. A number of amorphous materials have been observed to show this phenomenon

including a-Si:H and chalcogenides. The photoluminescence in a-Si:H has been investigated extensively over the years, but even so the nature of the low temperature photoluminescence and the mechanism of radiative and non-radiative recombination are still interesting questions in the physics of the a-Si:H.

Early results by Street (1981a) and Dunstan (1985) established a model in which it is believed that at low temperature the photoexcited carriers are trapped in band tails from where they either recombine radiatively with the carrier in the other band tail or non-radiatively by tunnelling to defect states. The radiative process gives rise to the photoluminenscence (PL) of high efficiency with a broad band near 1.4 eV. Fig.(3.8) illustrates a spectral distribution of the photoluminescence in single and dual beam. The spectral data is obtained by exciting the sample with photons of energy (1.92 eV) and an additional excitation ($h\nu < 0.7$ eV) turned on and off.

Street (1981b) measured the temperature dependence of the intensity of luminescence (I_L) near the peak of the spectrum. Street observed that at sufficiently low excitation, the intensity I_L is constant up to 40K, above which it decreases see fig.(3.9). As the excitation energy is increased, I_L increases by up to 30% and reaches a maximum at around 50K. There is a small shift of the peak with temperature.

At temperatures above 50K the spin density in the sample becomes important. Street (1978) observed that the efficiency decreases with increasing spin density. The low temperature intensity is attributed to radiative transition within the localised states and if the intensity is sufficiently low the recombination is expected to be geminate. Street put forward an expression for the photoluminescence efficiency η_L as:

$$\eta_L = \frac{P_R}{[P_R + P_{NR}(G) + P_{NR}(T)]} \tag{3.35}$$

where P_R and P_{NR}(G) are the radiative and non-radiative rates respectively and $P_{NR}(T)$ is the temperature dependent non-radiative rate due to thermal ionization. The increase of temperature, creates more radiative channels, therefore η_L is temperature dependent, even if $P_{NR}(T)$ is negligible. When $P_{NR}(G)$ is comparable with

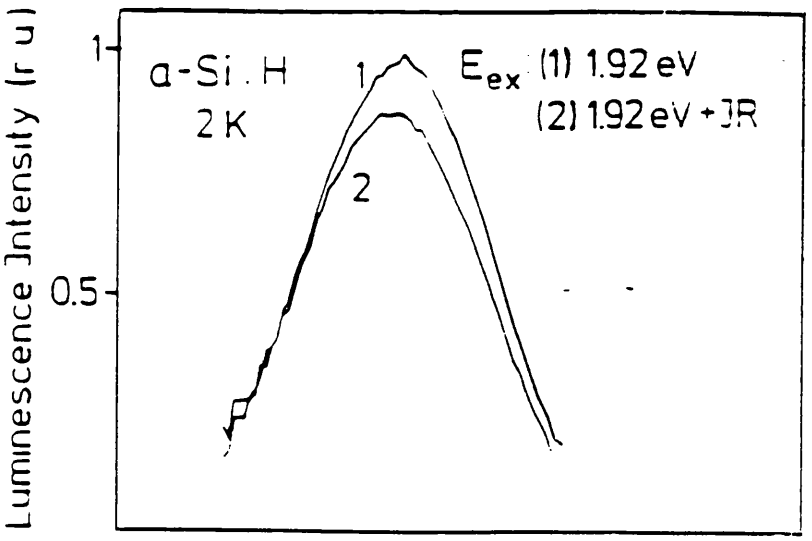

Figure 3.8: Luminescence spectra for single (1) and dual (2) beam measurements. After (Fuhs 1985).

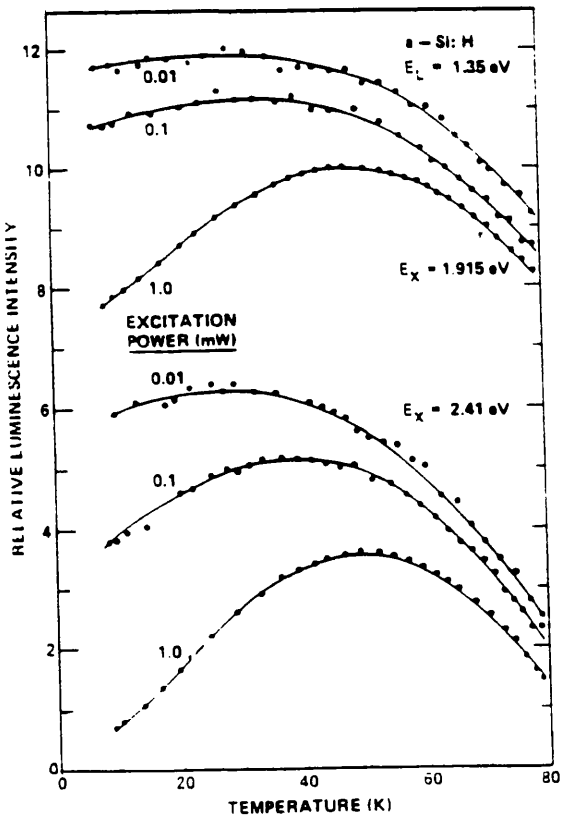

Figure 3.9: Temperature dependence of the luminescence intensity in the range 0-80K for various incident excitation powers and wavelength as shown. The data are normalized such that the maximum intensity is 10 units of the vertical scale, and the different curves have offset zeros. The illumination spot diameter is 2 mm. After (Street 1981).

P_R, the increase of P_R with temperature results in the increase of η_L as observed by Street (1981b). At low intensity, the low temperature quantum efficiency η_L decreases when the spin density N_S is larger than $\sim 10^{17}$ cm^{-3}. Therefore, samples with larger N_S have a weak temperature dependence until the temperature is sufficiently high, above which η_L is almost independent of N_S. This suggests a non-radiative process in which carriers tunnel to dangling bonds.

The IR-quenching of the photoluminescence has been observed in the range of 2-100K (Fuhs 1985). The effect is generally larger in p-type material than in n-type. The spectrum in fig.(3.8) becomes unsymmetric and shifts to lower energy. The effect can occur in the geminate model as well as in the distant pair model when the carriers are excited from the localized band tail states and diffuse to defects. A similar quenching has been observed due to high electric field (see next section). The thermal quenching is attributed to an electron being activated from band tail states as a result of the demarcation level being shifted to a lower energy as the electrons tunnel to D^0 states (process 2 fig.(3.4)).

As the wavelength is reduced the PL-quenching exhibits a cut-off near 0.5 eV similar to the cut-off in the PC-quenching (see section (3.4)). This may indicate the similarity of the process involved in PC and PL.

Varmis et *al.*(1984) pointed out that if the photoexcited carriers (holes) are trapped at 0.5 eV above the valence band edge then they are strongly localized and have low rates of recombination. The IR excitation causes the holes to move to shallow traps, where they become weakly localized and therefore able to recombine with electrons. This process enhances the luminescence and within a few milliseconds the tunnelling transitions produce more neutral dangling bonds (D^0). The non-radiative recombination is speeded up through the interactions of the delocalized electron-hole pairs with the dangling bonds. This increase in PL has been confirmed by Fuhs (1985) see fig.(3.5).

Bort et *al.*(1989, 1991) pointed out that by studying the distribution of lifetimes

P(τ) one should be able to decide between the geminate and the distant pair models. In the geminate model, P(τ) is independent of the density of the generated carriers, since the recombination occurs between the localized geminate pairs. In the distant pair model however, the P(τ) is likely to be a strong function of the steady state carrier concentration. Fig.(3.10) represents the lifetime distribution P(τ) derived from the frequency resolved spectroscopy (FRS) experiments at various generation rates G, at 10K. The spectra is dominated by a broad peak centered at $10^{-3} - 10^{-4}$s and a small shoulder which extends to shorter times around 10^{-6}s. In fig.(3.11) the peak position of P(τ) is plotted as a function of the generation rate G. The results have two different features .

At G $> 5 \times 10^{19}$ cm^{-3}s^{-1} the peak of P(τ) shifts to short time and hence τ_m decreases with increasing G in the form of $\tau_m \propto G^{\alpha}$ with $\alpha = -0.9$.

At G $< 5 \times 10^{18}$ cm^{-3}s^{-1} P(τ) does not shift and τ_m is independent of G. This suggests the existence of a transition from geminate to non-geminate recombination close to $10^{19} cm^{-3} s^{-1}$. A transition from a mechanism with a constant τ to a mechanism with a lifetime varying as a function of the steady state carrier concentration. At high G, the data fit quite well the distant pair model curve 1 (Dunstan 1985). The authors were able to obtain the function $\eta(R)$ and therefore P(R). P(τ) is related to P(R) in equation (3.12) using the relation in equation (3.4) gives:

$$P(\tau) = P(R(\tau)) \times a/2 \times 1/\tau$$

$$R(\tau) = a/2 \times \ln(\tau/\tau_0) \tag{3.36}$$

From fig.(3.7) P(R) increases slowly to the peak value R_C and then decreases slowly for R $> R_C$. P(τ) is proportional to $1/\tau$ over many orders of magnitude in τ. A comparison of the experimental data in fig.(3.10) with the P(R) in fig(3.7) revealed that the experimental lifetime distribution is much wider than the theory. This discrepancy was attributed to the fact that some recombination mechanisms which could influence the result of P(R) were not taken into account. Recently, Baranovskii, Saleh, Thomas and Vaupel (1991) reported that the influence of the nonradiative

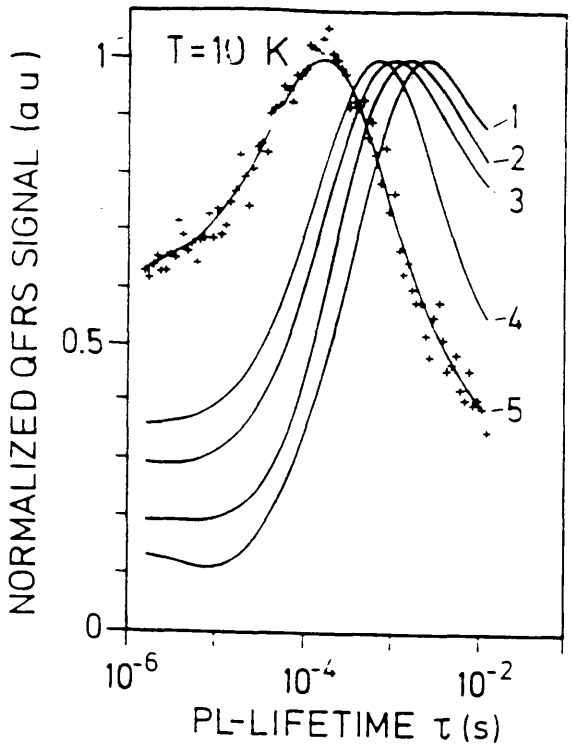

Figure 3.10: Lifetime distributions of a-Si:H (low defect density) at various excitation intensities: (1) $5.10^{15}cm^{-2}s^{-1}$; (2) $1.10^{16}cm^{-2}s^{-1}$; (3) $5.10^{16}cm^{-2}s^{-1}$; (4) $1.10^{17}cm^{-2}s^{-1}$; (5) $5.10^{17}cm^{-2}s^{-1}$. After (Bort et al.1991).

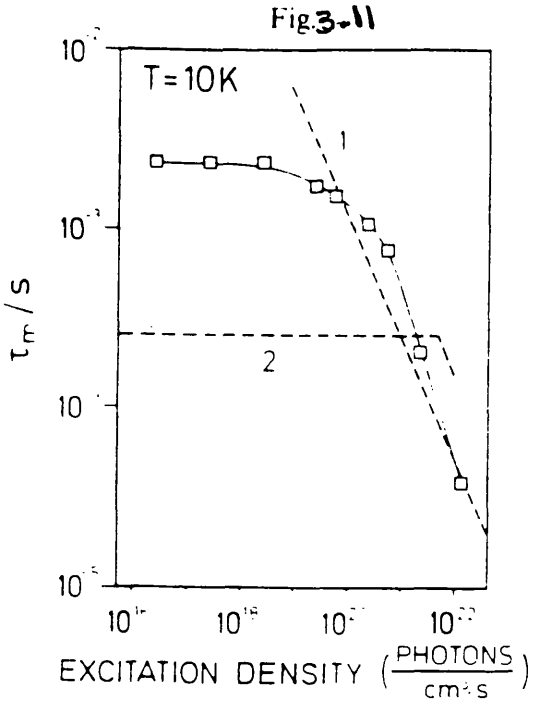

Figure 3.11: Peak position τ_m of $P(\tau)$ as a function of the excitation density. Curve 1: theoretical prediction for distant-pair recombination (Dunstan 1985). Curve 2: Data from decay experiments (Tsang and Street 1979). After (Bort et *al.* 1991).

processes on the narrow of the lifetime distribution is very minor and that the theoretical curve obtained is not too far from that observed by Bort et *al.*(1991) in the FRS experiment (see fig.3.10). However, non-geminate radiative may account for the experimental observations.

3.6.2 Field-Dependence of the Photoconductance and Photoluminescence

The effect of the electric field on the photoluminescence and the photoconductance in a-Si:H has been studied frequently by several workers, (see Jahn, Carius and Fuhs 1987, Jahn, Fuhs and Pierz 1989, Stachowitz et *al.* 1990). It has been observed that high electric fields (F> 6×10^4 V/cm) results in an enhancement of the photoconductance and a quenching of the photoluminescence intensity. The effects have been ascribed to a geminate-pair recombination. As we have seen already, only carriers which escape this type of recombination can contribute to the transport. This means that the photocurrent is determined by the generation process of free carriers. However, recent results have contradicted this model, but rather support a model where the e-h pairs are not linked, particularly in the high field regime. Fig.(3.12a) and (b) show the field dependences of G (photoconductance) and $\frac{\Delta I_{pl}}{I_{pl}}$ (relative change of the photoluminescence) respectively. Above F= 60 kV/cm there is a strong increase of G, whereas in (b) there is a quenching of the photoluminescence intensity I_{pl} by the high electric field. From the result above we may conclude that the effect of the high electric field on the photocurrent is much larger than that on the photoluminescence. In the low field region (F< 5×10^4 V/cm), there is a relationship between the two effects i.e :

$$\frac{\Delta\sigma}{\sigma_{pc}} = -A\frac{\Delta I_{pl}}{I_{pl}} \tag{3.37}$$

This anticorrelation between σ_{pc} and I_{pl} was attributed to the geminate-pair recombination model and A in equation (3.37) was related to the quantum efficiency. It was found (see Jahn et *al.* 1987 and 1989) that at low field both magnitudes in

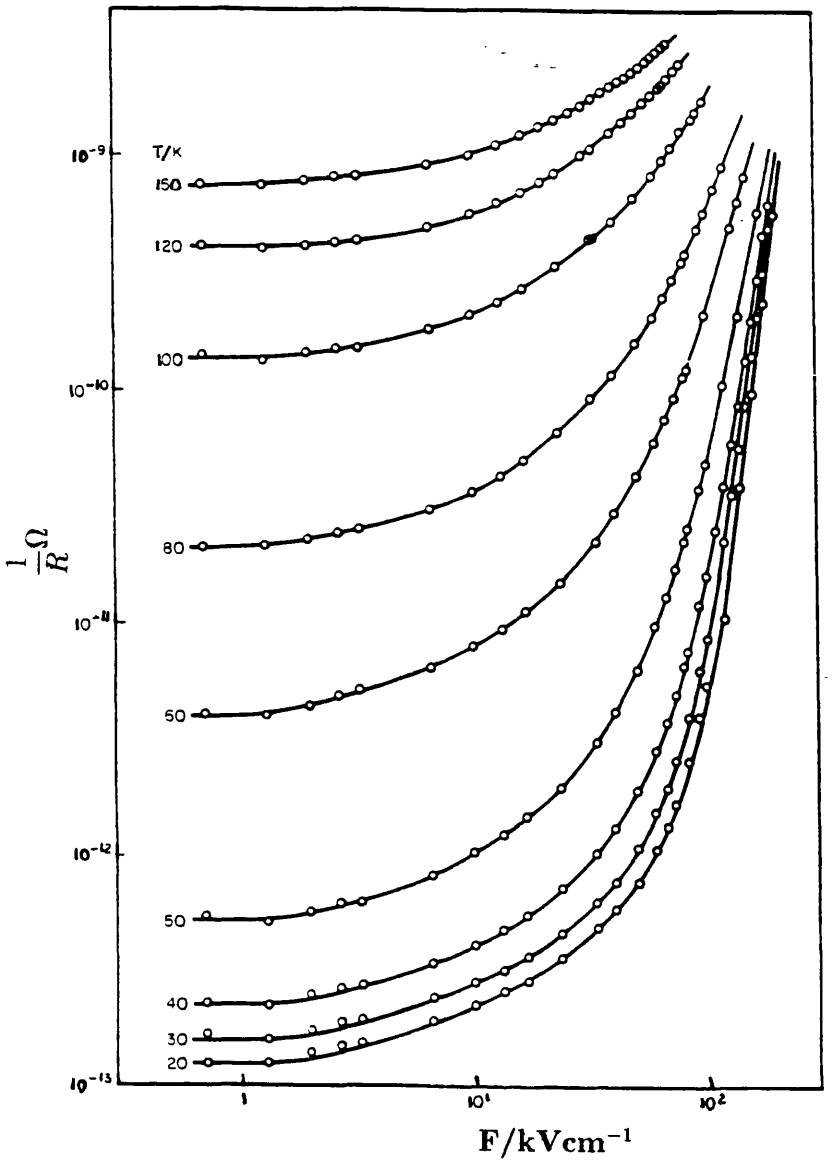

(*a*)

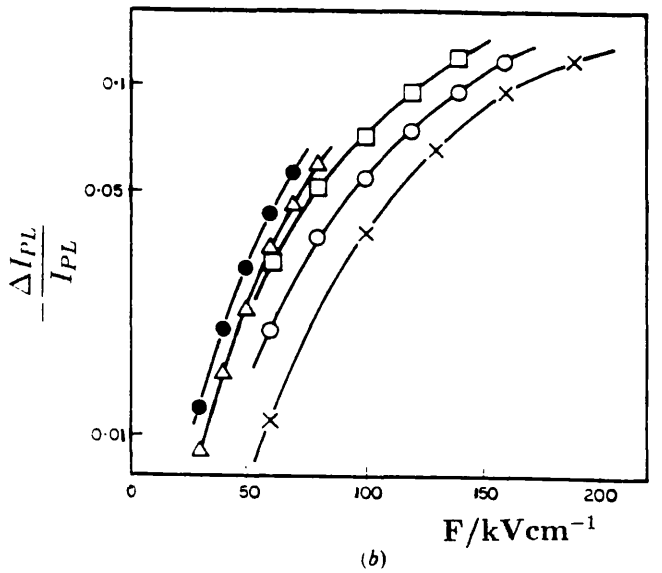

(*b*)

Figure 3.12: (a) Photoconducance G_p of a-Si:H as a function of electric field for different temperatures. (b) Field-induced quenching of the PL intensity at various temperatures: (×) 30K, (○) 50K, (□) 60K, (△) 120K . After (Stachowitz et *al.* 1990).

equation (3.37) decrease with increasing the defect density N_d in the undoped sample. This is a suprising result, as a field dependent separation process of a geminate pair is an intrinsic feature and does not depend on the defect density. It was also observed that both field induced effects are larger in n-type than in p-type films. This may suggest that the behaviour switches from a large to small field effects when the Fermi level crosses midgap. At high electric field the relationship becomes nonlinear. It was suggested (see Stachowitz et *al.* 1990) that the deviation from the linear relationship may arise from the field dependence of the photoconductance because as we have seen the effect on the photoluminescence is smaller. This lead to the conclusion that there is no correlation between the transport and the I_{pl} in the high field region.

3.6.3 Light Induced Electron Spin Resonance (LESR)

After the excitation of a sample with a band gap light (1.92 eV) a nonequilibrium distribution of trapped carriers persists with long lifetimes, which has been studied using their electron spin resonance (the so-called light induced electron spin resonance LESR) by several groups (Street and Biegelsen 1982, Boulitrop and Dunstan 1982 and Carius and Fuhs 1985). Fig.(3.13) shows that the removal of light causes the LESR signal to drop, initially at fast rate followed by a slow decay towards the equilibrium state. We describe here the experiment performed by Street and Biegelsen. The LESR decay measurements are recorded with the magnetic field set at the peak of the electron band tail absorption derivative showing that there is a strong element of charge due to trapped electrons. The data presented in fig.(3.14) represents the variation of the steady state concentration as a function the light excitation. The sublinear relation indicates that the recombination process is distant pair rather than geminate since if it was the latter a linear relationship would be expected. This is an indication that the LESR is a bimolecular process. Another indication, is that we can see in fig.(3.14) that the LESR lifetimes decrease with

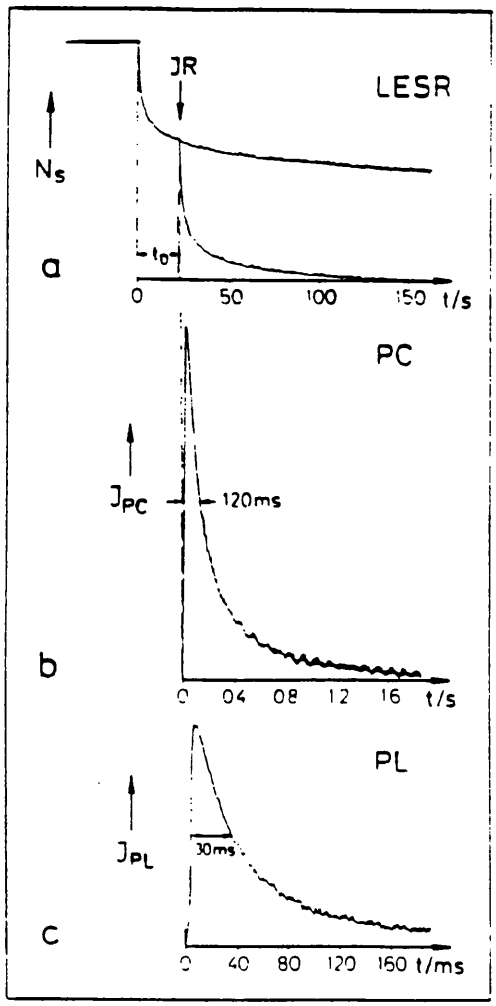

Figure 3.13: Transient of (a) LESR. (b) Photocurrent and (c) photoluminescence at 15K. The plots are exposed to an IR beam (of energy < 0.7eV). The same light intensities are used in (b) and (c), but that in (a) was much lower. After (Carius and Fuhs 1984).

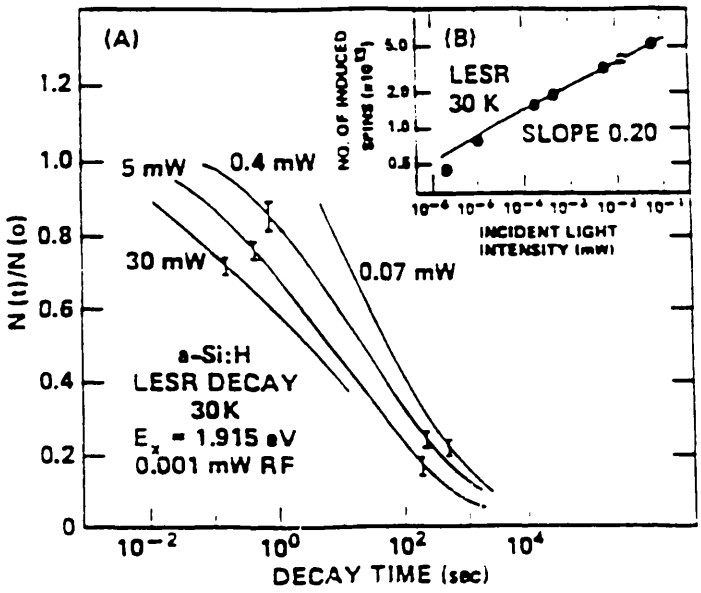

Figure 3.14: (A) LESR decay in a-Si:H at different illumination intensities. Steady state conditions were attained before removal of the pulse. (B) Dependence of the equilibrium valves reached, in an LESR experiment, plotted against the incident light intensity. After (Street and Biegelsen 1982).

increasing intensity, a characteristic of a bimolecular process. The long lifetimes at 30K suggests that diffusion is negligible at this low temperature.

In another experiment to differentiate between the monomolecular and bimolecular processes, Street and Biegelsen studied the response of the two processes to pulsed excitation. The system was excited by a sequences of pulses of 20ms duration applied every 12.5 s. In the geminate model, if the separations of the electron-hole pairs are such that they recombine before the next pulse arrives, each pulse creates the same distribution of pairs. This indicates that the low LESR and high luminescence expected should be independent of the number of pulses. In the distant pair case, the first pulse of light generates a small number of electrons and holes that are separated at random spatially. The luminescence is considered negligible for times shorter than the interval between two successive pulses (12.5 s), hence the LESR creation efficiency is 100%. More pulses increase the LESR density, this means that the separation of electron-hole decreases and therefore the rate of recombination and luminescence increase. Street and Biegelsen observed in the first pulse a high luminescence efficiency and a very low LESR efficiency. This behaviour is expected for a geminate process and cannot be accounted for the distant pair recombination, because the latter process predicts a low luminescence and high LESR efficiency.

Bort et *al.* 1991 measured both the transient PL and LESR in a-Si:H. The LESR measurements were made in the same way as the Street et *al* measurements with the magnetic field fixed to the peak of a resonance and measured the build up of the LESR signal with the illumination switched on. The results are shown in fig.(3.15). The risetime of the PL is less than one second and is limited by the phase sensitive detector, whereas the risetime of the LESR is larger by orders of magnitude than that of the PL. However, this time gets shorter when the rate of generation increases. This behaviour is similar to the risetime of the a.c. photoconductivity as we will see later on (see chapter 7). The spin density n_s in the LESR signal is known to be a sublinear function of the generation rate (Boulitrop and Dunstan 1982) in the form

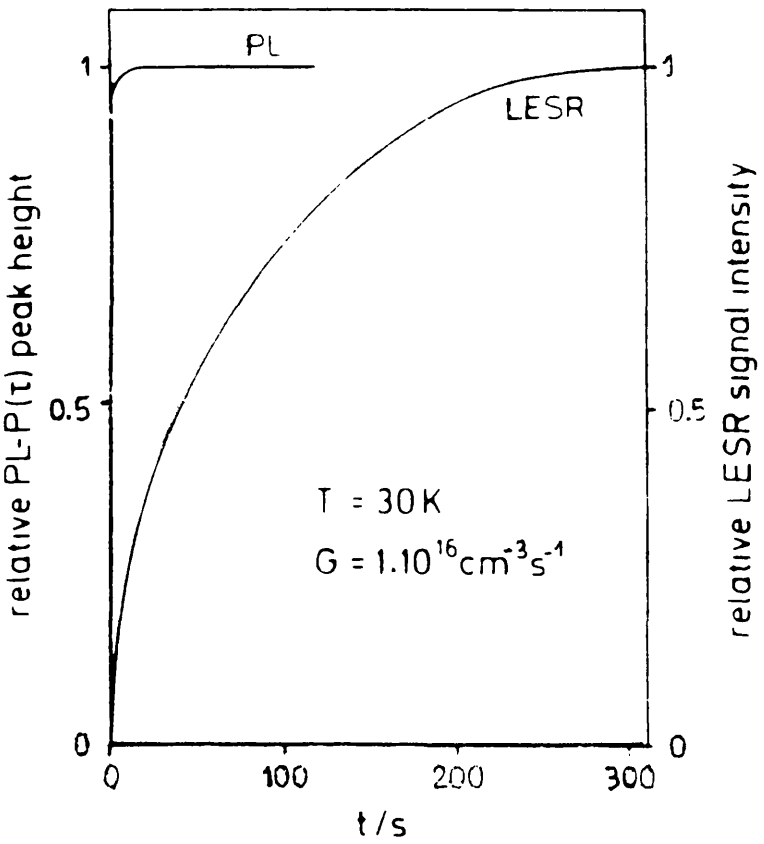

Figure 3.15: Rise curve of the photoluminescence intensity and of the LESR spin density n_s, when the light is turned on at a very low excitation rate of 10^{16} $cm^{-3}s^{-1}$. The steady state value of n_s amounted to 2 $\times 10^{16} cm^{-3}s^{-1}$. After (Bort et *al.* 1991).

of:

$$n_s \simeq G^{\zeta} \tag{3.38}$$

with $\zeta \approx$ 0.15-0.2. This relationship is very useful when it comes to determining the different parameters of our samples (see chapter 7). The magnitude of PL in fig.(3.15) corresponds to the peak of P(τ) at $\tau_m = 2\times10^{-3}$s see fig.(3.11). Therefore, the accumulated concentration n_s is around 3×10^{15} cm^{-3} and this is less than the steady state value $n_s \approx 2 \times 10^{16}$ cm^{-3}. This indicates that P(τ) is independent of n_S at low G. This behaviour is similar to that reported by Street and Biegelson (1982) and which we discussed above. The equation. (3.38) shows that the carrier lifetime is determined by n_s. This suggests that most of the generated carriers recombine geminately and only a small number of pairs diffuse to longer distances and result in the build up of a concentration of carriers in the localised states with long lifetimes. It is reasonable enough to assume that these carriers will recombine in a non-geminate process. The PL signal is not altered by the high steady state density n_s, because the rate of recombination associated with long lifetimes is low and does not contribute significantly to the signal.

CHAPTER 4

Sample Preparation and Experimental Methods

In this chapter the following items will be discussed: The methods used for the preparation of the samples, techniques of cooling the sample to low temperature, details of the optical measurements together with the calibration of the intensity and finally the electrical measurement procedures.

4.1 The Preparation Techniques.

The material investigated in this project was a-Si:H. The samples were grown either by R.F sputtering or glow discharge methode. A brief description of the two techniques is given below.

4.1.1 R.F. Sputtering.

The process of making sputtered a-Si or a-Si:H was carried out using a Nordiko sputtering unit. The chamber can be pumped down to low pressure ($\sim 10^{-7}$ Torr) using an Edwards diffusion pump and a liquid nitrogen trap for the removal of water vapour. The pressure raised to 5-10 mTorr of argon during sputtering. A plasma is created inside the chamber by applying a radio frequency (RF) voltage at 13.56 MHz between two electrodes see fig.(4.1). In the setting up of our system, the low electrode is made of the material to be deposited (target), the top electrode, to which the substrate (glass slide) is attached is earthed. The setting can be reversed. The application of the RF voltage causes the positive ions to be attracted to the

target during the negative half cycle. Since electrons are more mobile than positive ions, therefore more of them are attracted to the front surface of the target during the positive half cycle than positive ions in the negative half cycle. This results in the formation of a negative d.c. bias. This bias leads to the formation of plasma sheath across the surface of the target. The ions are then attracted from the plasma by the d.c. bias and bombard the target. The ejected material is carried to the substrate resulting in the build-up of an amorphous thin film.

The semiconductor and electrode materials diameters were 10cm. The separation between the target and the substrate was about 8cm and with an RF power of 100W, a typical $3\mathring{A}/s$ rate of deposition was obtained.

To obtain magnetron sputtered samples, a permanent magnet is placed behind the target, the current density increases dramatically from $1mA/cm^2$ in a conventional sputtering to 40 mA/cm^2. As a result faster deposition rate is expected.

All the targets are presputtered in pure argon for as long as an hour before the deposition to remove any contamination on the surface. The gas mixture of pure argon and hydrogen are prepared in 80 l tank at a corresponding ratio and let into the chamber at high pressure ($\sim$ 5mT).

A close control on different parameters discussed above such as: sputtering gas pressure, bias voltage of the target, substrate-target separation etc.., is necessary to ensure the reproducibility of the film characteristics. All the samples measured in this work were deposited with the substrate held at room temperature.

4.1.2 Glow Discharge Technique.

In 1975 Spear and Le Comber discovered that amorphous semiconductors grown with the glow discharge technique can be doped (n-type or p-type) and their electrical properties can be controlled.

As in the technique discussed previously, an RF voltage at typically 14MHz is applied between the electrodes to produce a plasma inside the chamber, which con-

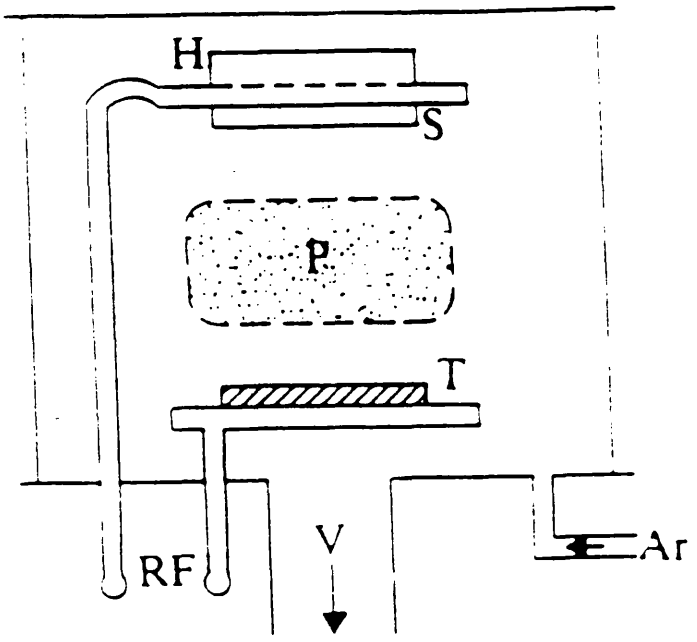

Figure 4.1: **Schematic illustration of an r.f. sputtering apparatus. The r.f field is applied between the target (T) electrode and the substrate (S) electrode. A sputtering gas (e.g. Ar) is introduced into the chamber and a plasma (P) is struck. The gas is pumped away by a vacuum system (V); the substrate may also be heated by an electrically insulated heater (H).**

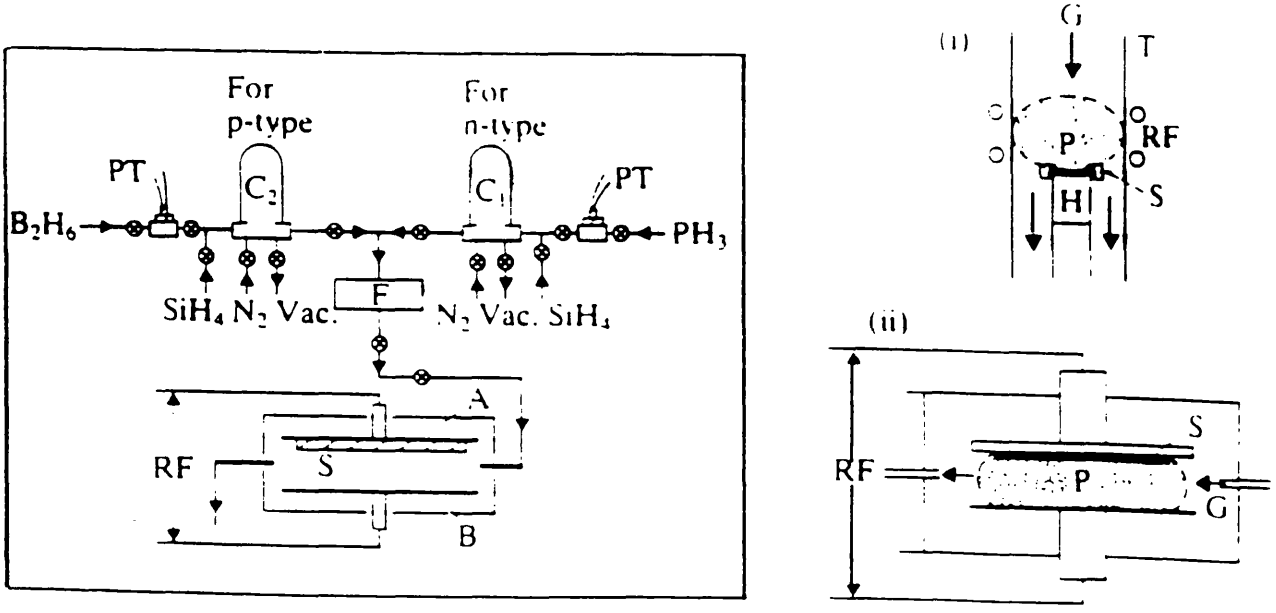

Figure 4.2: **Illustration of the glow-discharge decomposition preparative technique. (a) Schematic illustration of the preparative unit for the deposition of n-and p-type a-Si:H (C_1, C_2 glass cylinders; PT, pressure transducer; F, flow meter; S, substrate).**
(b) Methods of coupling the r.f. power to the plasma: (i) inductive, (ii) capacitive. (G, gas flow; P, plasma; S, substrate; H, heater; T, glass tube). After (Spear 1977).

tains a low pressure gas of silane (SiH_4). The electrodes can be either inductively or capacitively coupled see fig.(4.2). For producing larger surfaces, the latter configuration is preferred. Instead of ions ejecting material from the target, a chemical decomposition of the gas occurs, resulting in a deposition of a solid film onto the substrate. With a power of 1-10W, a rate of deposition of 1-10 $\AA$/s is usually attained.

Doping of a-Si:H can be achieved by introducing different gases such as B_2H_6 or PH_3 into the chamber along with SiH_4 . They can be introduced either separately to produce single doped material (p-type or n-type) or a mixture of both gases to make a compensated material. The level of doping or compensation depends strongly on the doping level or compensated doping ratio respectively. In the case of doped material, the dopants atoms are incorporated into the amorphous structure substitutionally, hence releasing excess electrons (for Phosphorus) or holes (for Boron). For the compensated material on the other hand, it is shown that two types of compensation can be present. The dopant sites B_4^- and P_4^+ can be randomly distributed, this is known as electronic compensation or a distribution of closely bonded B-P complexes, this is known as chemical compensation. We will see later in chapter 5 that the first compensation was achieved in our samples.

The glow discharge process is more complicated than sputtering since it depends strongly on plasma chemistry. Therefore, a number of factors can affect the properties of the deposited film. These factors include:

1. Gas pressure and temperature.

2. Gas flow rate and consequent dwell time in the chamber.

3. Chamber geometry and substrate position relative to the plasma.

4. R.F. power applied to plasma.

5. Method of coupling of r.f. power to plasma (i.e. inductive or capacitive.)

6. substrate bias.

7. substrate temperature.

The substrate temperature is a very crucial parameter, and results have shown that higher temperatures of around 520K or more are commonly used (see Spear 1977). High temperatures help to ensure that foreign species are not incorporated into the film.

4.2 Sample Specification.

4.2.1 Sample Geometry.

The samples measured during this work were of sandwich configuration with the amorphous semiconductor layer sandwiched between two electrodes. The reason for choosing this configuration is basically for their large conductance comparing to the coplanar geometry. Therefore, it makes it easy to perform the experiment using an a.c. bridge. Also the capacitance of the sample is dominated by the bulk of the semiconductor, and edge effects can be ignored. In a coplanar configuration however, these effects are significant (see Long 1982). One disadvantage with the sandwich geometry, is the contact effect due to the metal-semiconductor interface. However, due to the high density of states in the semiconductor, the electrical properties are not likely to be affected by any charge carriers at the metal-semiconductor interface. As reported recently by Holland (1987) and also observed in present work, the magnitude of the d.c. and a.c. conductances are independent of the thickness of the sample. Also the I-V characteristics are symmetric over the measuring voltage (no rectification occurs). This implies that the sample parameters are determined by the bulk of the amorphous semiconductor.

4.2.2 Glow Discharge Sample.

Two types of sample of a-Si:H were studied. These were intrinsic (n^+-i-n^+) and compensated (n^+-BP-n^+). They were deposited using a capacitively coupled r.f. reactor system delivering a power of 8 W to the plasma. All the samples were deposited on ITO coated glass substrates. These samples had n^+ layers on both the front and the back contacts acting as injecting contacts for electrons with thicknesses of the order of 200 $\AA$ see fig.(4.3). This highly doped n^+ surface layer was carried out by the addition of 3000 vppm in volume of PH_3 to the silane. Intrinsic a-Si:H was prepared by decomposition of pure silane (SiH_4) and compensated (BP) samples from silane pre-mixed with equal parts per million (vol.p.p.m) of phosphine (PH_3) and diborane (B_2H_6), these dopant mixtures then flowed together through the deposition unit. Compensated doping ratios are defined as $[PH_3]/[SiH_4] = [B_2H_6]/[SiH_4]$. In the present work two (2) compensated samples with compensated doping ratios of 2.5 and 5 vppm were investigated. The top electrode was of evaporated aluminum. The sample thickness was in the range of 1.7 to 2 μm. After the deposition of the top electrode the top n^+ layer was etched back around the aluminium to avoid any parallel conduction path or leakage current. Depositions were carried out at a substrate temperature of 290°C. The samples were prepared at the University of Dundee (Scotland) under the direction of Prof. W. E. Spear.

4.2.3 Sputtered Samples.

The samples were prepared by magnetron sputtering. The platinum target was used for both contacts. Prior to material deposition, the substrate was sputtered for one hour using a SiO_2 target, which was necessary, to enhance the adhesion of the other materials on the substrate and to remove the oxygen that may be left after the cleaning of the glass substrate. The bottom electrode was then deposited for 20 min. The silicon target was then presputtered for sufficient time, typically 1hour, with the material removed being deposited on a shutter. This is used to prevent

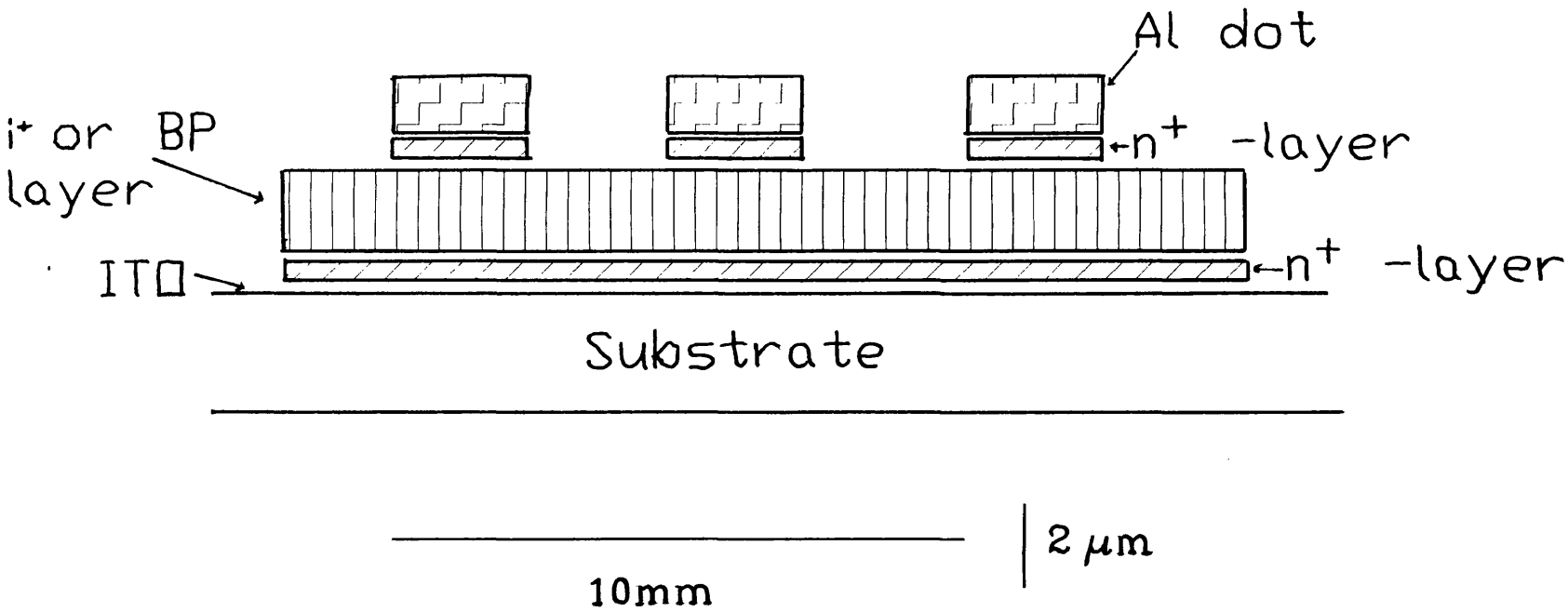

Figure 4.3: The Glow discharge sample configuration.

the deposition of foreign species on the substrate while sputtering the target. The procedure is achieved by placing a metal shutter between the two electrodes and letting only pure argon into the chamber. The silicon film was then deposited for 2 hrs plus 2 hrs (double thickness). A 100 W of RF power were used which generated a DC bias of 300 V for the magnetron sputtered a-Si and 1.2 kV for the orthodox Pt target.

It was only the a-Si films which were hydrogenated at a ratio of the Ar:H_2 mixture of 20:1. The substrate was kept at room temperature during the deposition. The deposition time of the top electrode was 9 min. This means that this electrode was thinner than the bottom one to facilitate the passage of light into the sample.

4.3 Temperature Measurements.

4.3.1 High Temperature Insert

For measurements in the temperature regime (from room temperature to 360K), a special sample holder was used. This is consisted of a flat copper plate connected by a thin stainless steel tube to a brass top-plate. The stainless steel was used for its low thermal conductivity. The sample was mounted on the copper tail-piece, and was glued to have a good thermal contact. The electrical connections were made by attaching thin wires to the electrodes by means of silver "dag" (highly conducting paint). The electrical connections to the ouside world were made with vinyl acetate coated copper wires to the top plate and then vacuum sealed by araldite. Coaxial cables were used to connect the insert to the measurement circuit.

The temperature was measured and stabilised using an Oxford Instrument DTC-2 Digital Temperature Controller. The temperature was measured with a copper coil thermometer on the rear of the copper plate in the insert and displayed by the DTC-2. The temperature can be checked with a thermocouple. A full description of the theory of operation of the instrument is given in sect. (4.3.4). In order to avoid any oxidation of the sample at high temperature and improve the thermal isolation, the

can surrounding the sample was evacuated before the measurements.

4.3.2 Low Temperature Measurements (RT < T < 12K)

For this temperature range a CTI Cryogenics Cryocooler unit (model 21SC) was used. It consists of a cold head model 21 and a compressor unit model 21SC. This cooler uses helium gas in four(4) stages to cool to low temperatures. In the first stage, the helium gas flows through the intake valve (see fig.4.4) to the warm end when the piston is at the cold end. In the second stage, when the piston moves to the warm end and the size of the cold end is increased, it causes the gas to displace towards the cold end through the regenerator. More gas is let through the supply valve, which remains open in order to keep the pressure constant. The expansion occurs when the supply valve is closed and the return valve is opened slowly. This causes the cold volume to be cooled down and the fourth stage occurs when the piston moves downwards to displace the remaining cold gas. After this, the return valve is closed and the cycle is repeated (see White 1979). Cooling the sample down to 12K can be achieved in about 2 hours.

During the photo-induced measurements carried out in the cryocooler, the sample was raised by two copper blocks and with the bottom electrode (ITO) facing the optical fibre see fig.(4.5). To avoid any short circuit, a very thin layer of mica was introduced between the sample and the copper blocks.

4.3.3 Measurements made using pumped helium

The temperature range between 10K and 1.2K was covered using cooling with liquid He_4. The Cryostat consists of a glass He_4 dewar within a stainless steel dewar see fig.(4.6). The insert was then placed into the glass dewar with the outer dewar filled with liquid nitrogen and the glass dewar filled with liquid helium. The liquid nitrogen minimizes the heat input through the walls and therefore extends the lifetime of the helium.

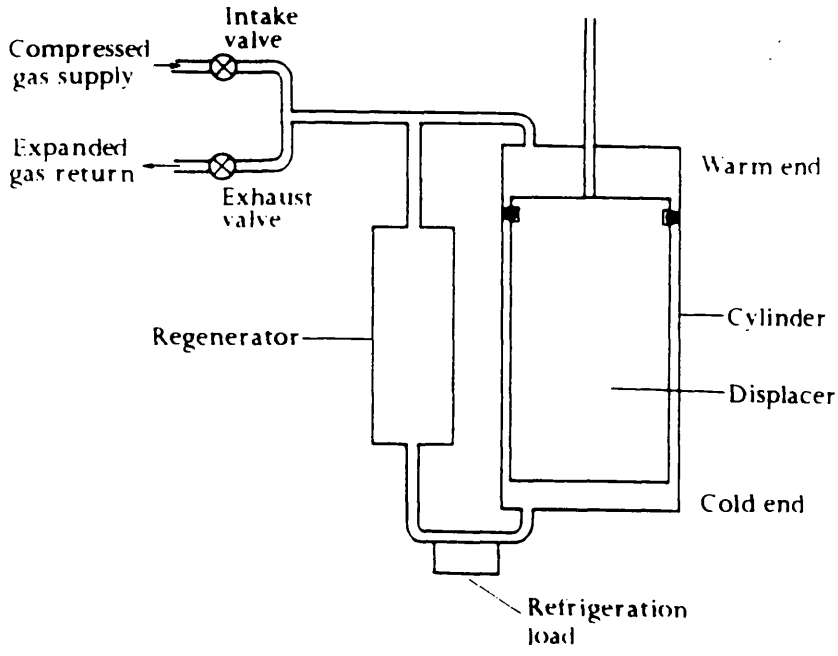

Figure 4.4: A single-stage version of the Gifford-McMahon refrigerator (White 1979).

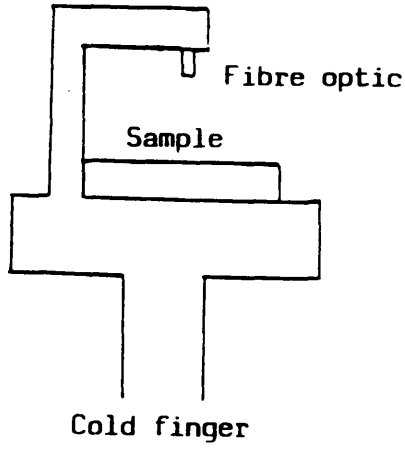

Figure 4.5: Illumination technique used in the cryocooler.

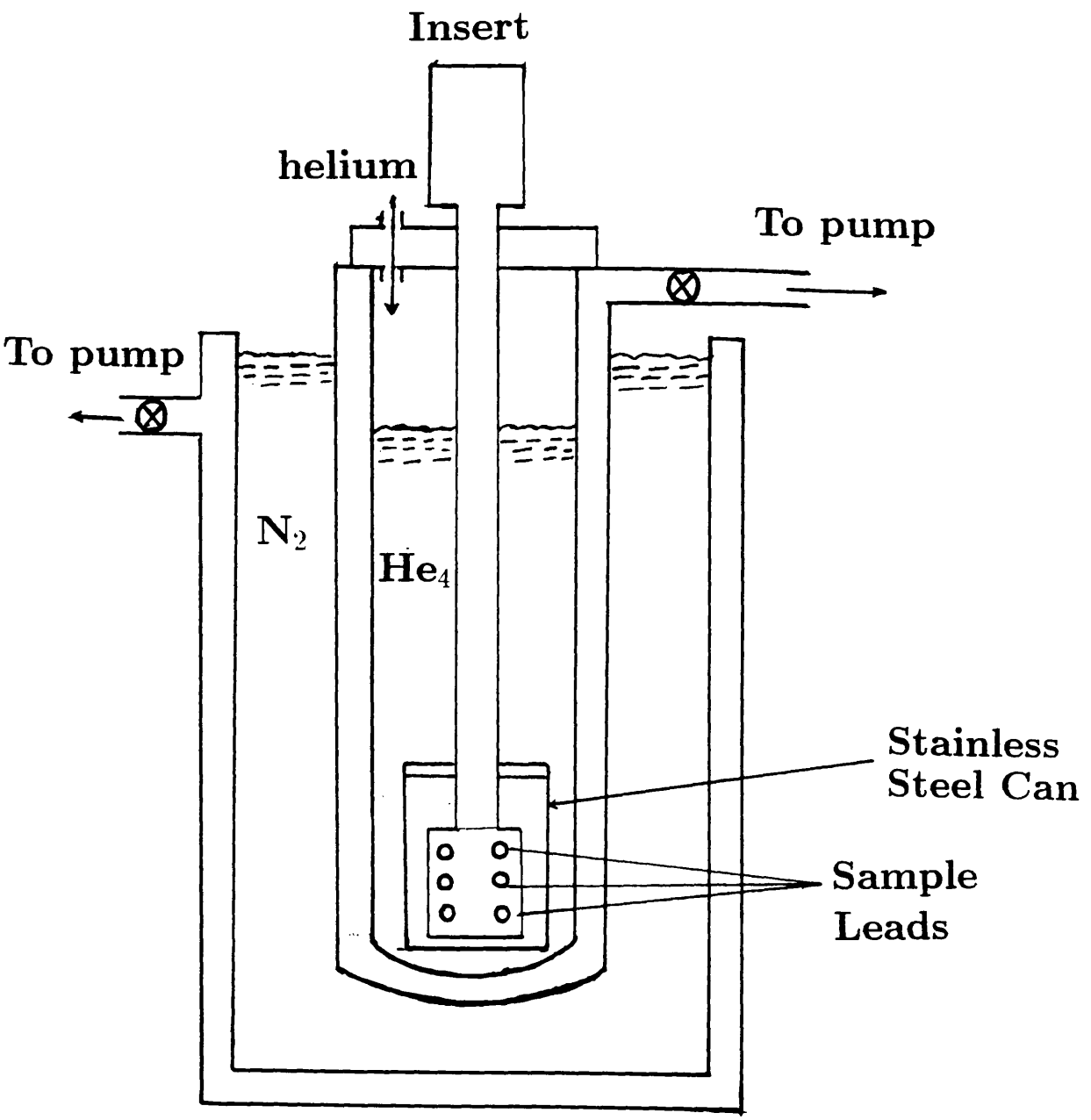

Figure 4.6: **Standard helium cryostat.**

Two major problems have to be considered when designing a low temperature insert. These are the heat input through the dewar walls and heat leak into the refrigerant bath. Fig.(4.7) shows the type of low temperature insert used during the course of this work. The first problem has already been discussed above. To tackle the second problem, two metallic discs (shields) are attached around the tubes. They reflect radiation from the top of the cryostat and minimize the heat leakage between the environment and the insert, so that the boil off of the refrigerant (helium) can be reduced. Also to minimize the heat leakage, several tubes of stainless steel were used to carry the wires through the helium bath to the sample. We used stainless steel tubing because of its high strength, small heat capacity, and poor thermal conductivity.

The sample should be isolated from the helium to let the temperature increases above the bath temperature if necessary. This was achieved by placing a vacuum can round the sample. Decreasing the temperature down to 1.2 K can be achieved by pumping the He_4. The sample was mounted on a copper tail-piece at the end of the insert. The substrate was glued to the tailpiece by a mixture of bostick (adhesive) and acetone in order to have a good thermal contact. Electrical connections were made to the sample through vinyl coated copper wires fed through the tubes. At the other end through the can, stycast compound is used to vacuum seal the wires. Another tube carries the thermometer wires and heater wires. The heater and copper and germanium thermometers were tightly screwed to the back of the copper tailpiece.

4.3.4 Temperature Controller.

The temperature measurement over the range 12 to 360K was monitored using two controllers. The first one, a Digital Temperature Controller (DTC-2), can be used for temperatures above liquid nitrogen. At low temperatures a Cryogenic Temperature Indicator (CTI model DT-500SP) was used with a silicon diode temperature sensing element. The second controller is more sophisticated than the first one, the

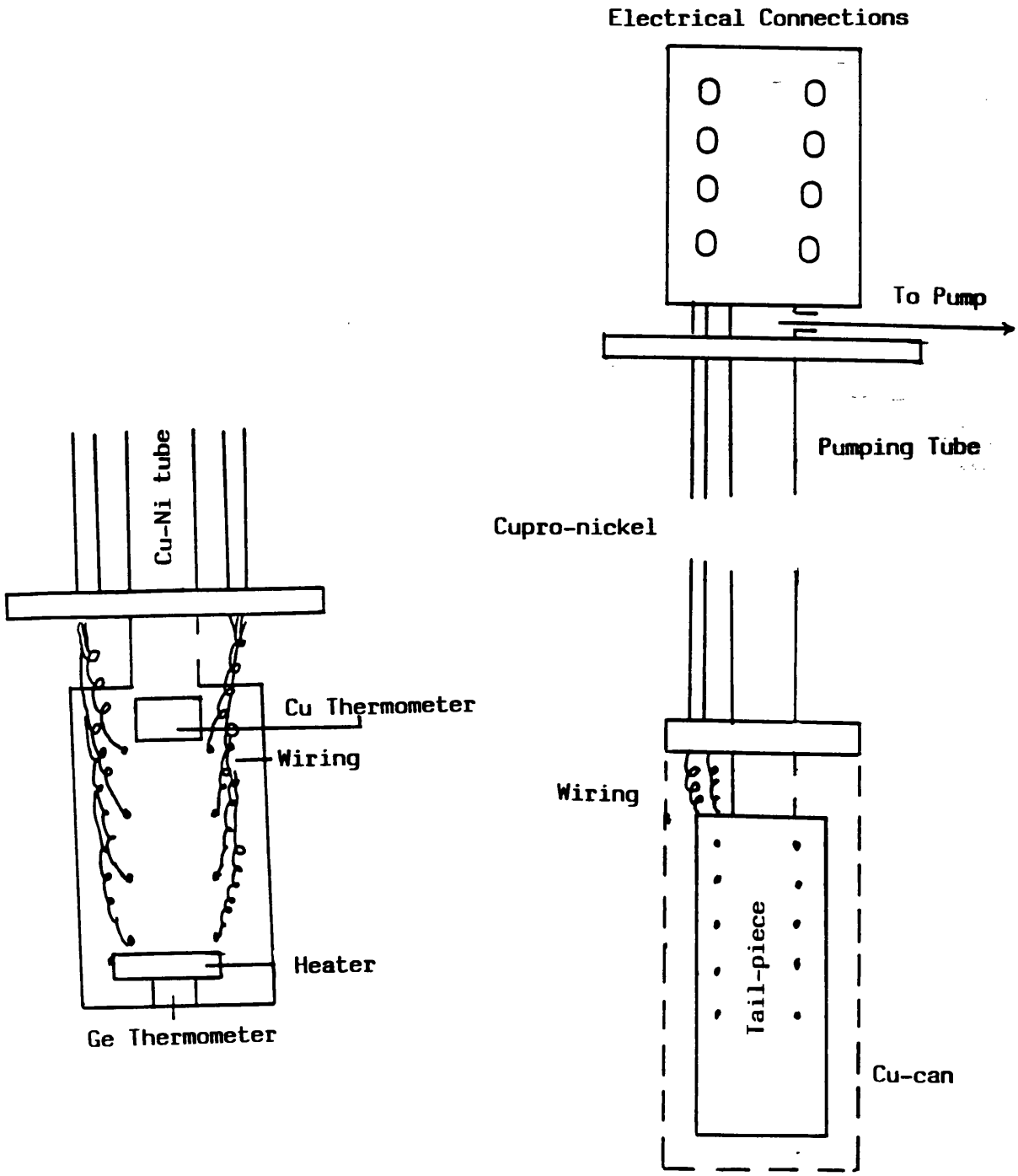

Figure 4.7: **(A) The Long-term low-temperature insert. (B) The interlead capacitance can be reduced by using the above wiring.**

operation principle of each was the same.

The main purpose of a controller is to maintain the temperature of a system as close as possible to the set point i.e the desired temperature, and also to decrease as much as possible the effect of change in the loss of heat from the system. To achieve this, here a description of the theory of operation of the CTI is given below.

We use the fig.(4.8) as a guide for describing the operating procedure of this instrument (see the operation manual).

- A constant current source generates 10 μA of d.c current to bias the diode. Then the voltage generated across is fed through an amplifier and creates a positive current through the 3MΩ resistor into the current summing amplifier.
- The digital set point is converted to an analog signal via a "Digital-to- analog convertor". This results in a negative voltage and to balance the sensor positive current an appropriate string of resistors is chosen.
- The error is displayed on a Null Meter. Its integral and differential are summed as current by an operational amplifier, which then drives the output power amplifier.

The fluctuations of temperature during the data acquisition could be monitored using a Solartron digital voltmeter and a computer. The drift at T $<$ 50K was less than 0.01K over the whole time of the experiment. Such fluctuation has an insignificant effect on the results.

4.4 Sample Illumination.

The sample was illuminated using a helium-neon laser of 5mW using the optical bench shown in fig.(4.9). It consists of a laser source, a neutral density filters holder, a 3m fibre and a Photodyne Model 88XLA optical power meter. To illuminate the sample, the power meter was used to set the relative magnitude of the light entering

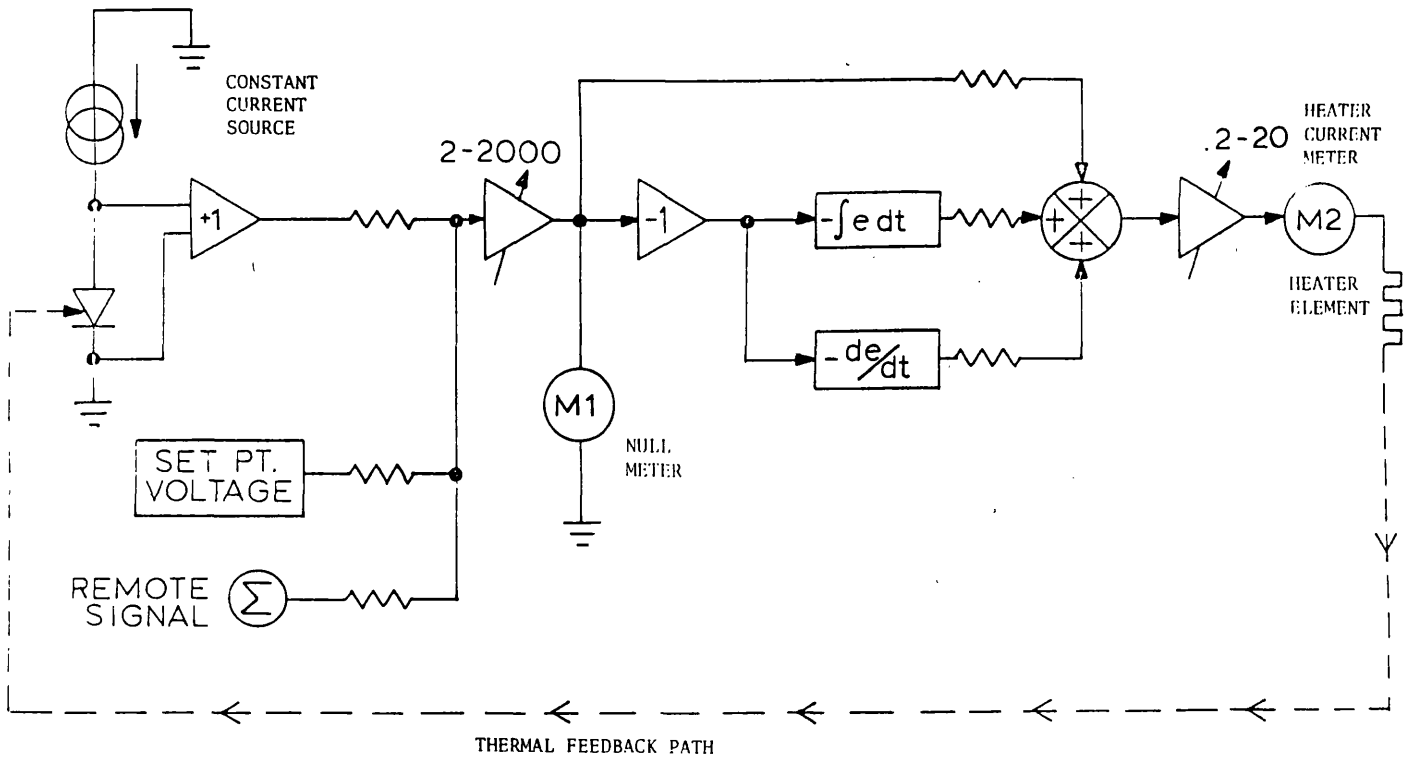

Figure 4.8: **Circuit used by the Lake-Shore TCU.**

the fibre. The fibre was connected to a fibre fitted in the cryocooler. The intensity falling on the sample could be varied from outside by introducing neutral density filters between the laser and the fibre. In order to eliminate the effect of the ambient light, the optical bench was covered with a black cloth during the measurement and at all intensities. The glow discharge samples were illuminated through the bottom ITO electrode. This was a semi-transparent material with low series resistance and resistive to oxidation. After each measurement, the intensity falling on the sample was calibrated using the procedure described in the next section.

4.4.1 Intensity Calibration

A number of factors play major roles in the loss of light coming from the source and falling on the sample. For this reason, the system must be calibrated after every measurement.

Firstly, using a Photodyne 88XLA light meter, the light was measured at the end of a 3m fibre before it was connected to the cryocooler as descibed above. Secondly, to estimate the real intensity absorbed by the sample a number of factors must be taken into account when the calibration is made:

- In the case when the junction-fibre distance differs from photodyne-fibre distance, the intensity is corrected by a factor using the inverse square law. Assuming that the intensity varies as the inverse of the square of the distance. This factor is calculated:

$$\frac{(insert\ fibre - photodyne\ distance)^2}{(insert\ fibre - junction\ distance)^2}$$

- The centre of the cone of light from the fibre is not necessarily normal to the junction see fig.(4.10). The dependence of the intensity on the distance from the centre is measured for a $\lambda = 633$ nm. Measuring the horizontal junction-centre of the cone and the vertical centre of the cone-fibre, the angle θ between

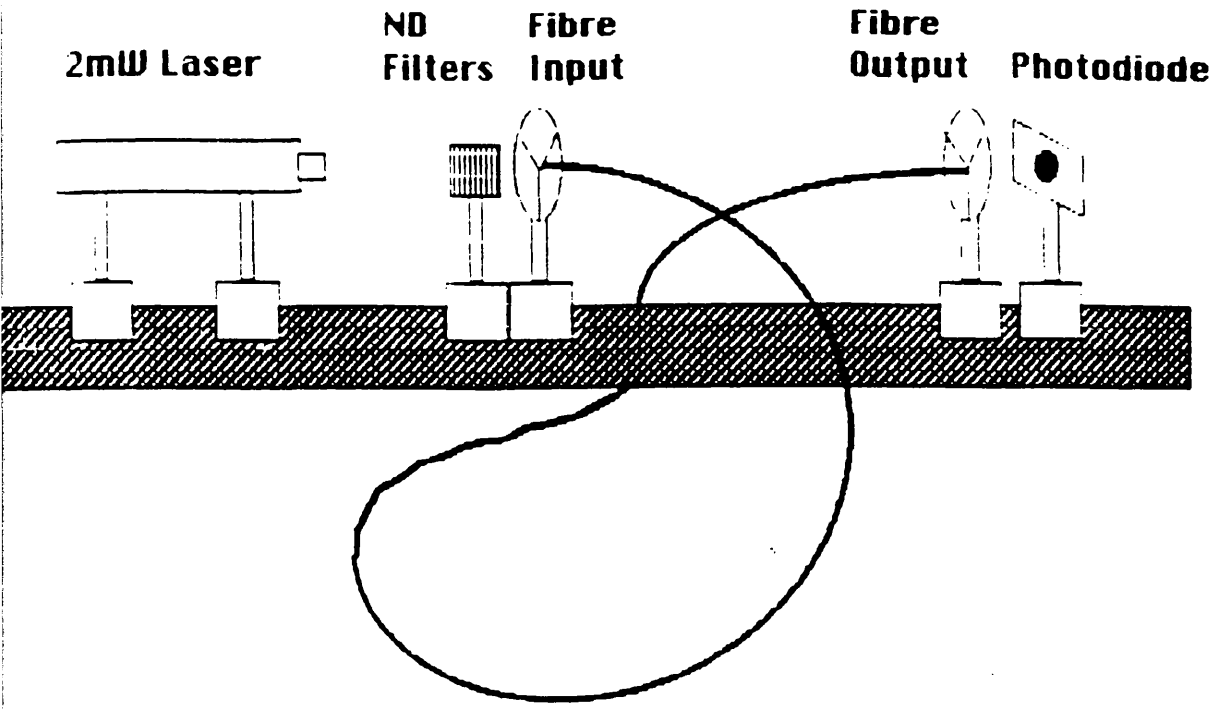

Figure 4.9: Optical bench arrangement used for sample illumination.

the light of the cone centre and the line from the junction to the fibre output can be calculated. A correction factor is found ranging from 0 to 1 for angle ranging from 90 to 0°.

- The active area of the diode sensing element in the light meter is 0.42cm^2 which is significant. This means that the displayed intensity is an average reading corresponding to the centre and to the less intense outer of the cone. A factor of $\frac{1}{.84}$ must be used to correct for this.

- The intensity is reduced by transmittance glass-ITO($T_{g/ITO}$) and reflectance from ITO/Si boundary, so a quantity $T_{g/ITO}R_{Si}$ is subtracted from the intensity incident on silicon. The light intensity is corrected by a factor of $T_{g/ITO} \times (1 - R_{Si})$. Hence we neglect multiple reflection within the films as R_g and R_{ITO} are very small and also the secondary reflections from the top Al are neglected due to the low transmittance of the Si.

- The loss from the fibre increases at low temperature, so this must be taken into account. Over the temperature range 13-50K, a reduction factor of 0.86 at λ= 633nm was measured.

The major errors contributing to the intensity calibration are mainly due to the measurements of the distances of the centre of the light cone to the junction in question and the distance fibre-junction. The latter is estimated to $\pm.2mm$

Another possible contribution to the error is due to the calibration of the neutral density filters. To minimize this error one set of filters was calibrated and used during this work.

Because of these many factors, the error in the absolute intensity falling on the sample was estimated accurate to around $\pm$50%. However relative intensities used during each run are believed to be accurate to $\pm$10%.

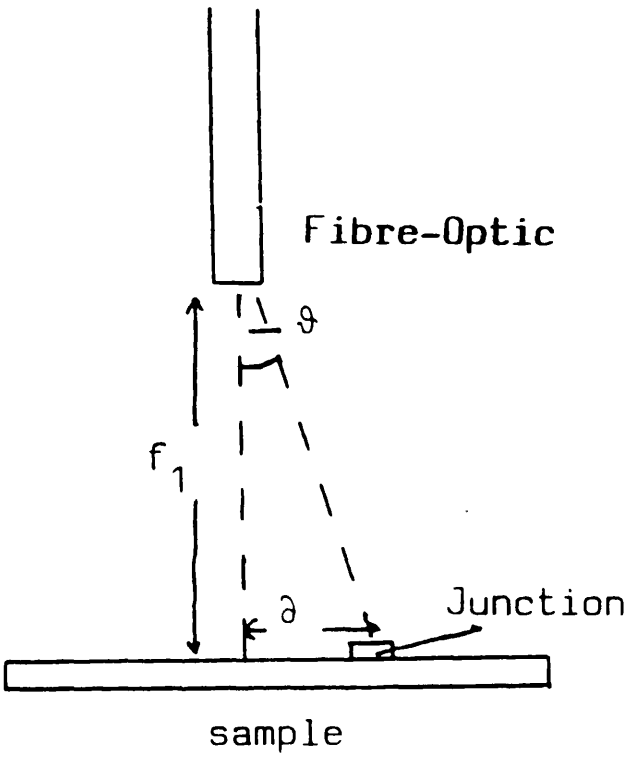

Figure 4.10: Definition of different angles and distances for intensity calibration.

4.4.2 Transmittance and Reflectance Measurements.

The measurements were performed on all the materials involved, the top electrode (Al), bottom electrode (ITO) and the semiconductor. This was done using a monochromater which allowed a desired wavelength to be selected and a photomultiplier to measure the reflected and transmitted intensities. In the case of the transmittance measurement, the photomultiplier was placed directly behind the sample and the readings were taken when the intensity passing through the sample(I_t) and when the latter is removed (I_0). The transmittance T is given by the ratio $\frac{I_t}{I_0}$. In the reflectance R measurements, the photomultiplier was set in position where the reflected intensities from the sample I_R and from a region on which an aluminium layer was deposited I_{Al} are collected and compared. The reflectance of the semiconductor is obtained by multiplying the ratio $\frac{I_R}{I_{Al}}$ by the relative reflectance of the aluminium R_{Al}. The transmittance of the Pt electrode was measured using a Unicom SP8000 Spectrophotometer. The transmittance is read directly from a chart using the same principle as for the photomultiplier. The absorbance of the material also can be defined as $A = \log_{10} \frac{I}{I_0} = \log_{10} T$. Another advantage of the instrument is that we can determine the thickness d of a thin film material (a-Si:H) to a very good approximation. The technique relies on the interference of light caused by multiple reflections in the film. At the high transmittance region at long wavelength we observe fringes. Since the refractive index of the silicon n_{Si} is greater than that of the glass, the maximum reflected intensity is given by $2d = (m + \frac{1}{2})\frac{\lambda}{n_{Si}}$, with m = 1,2,3,.... and λ the wavelength. This enables us to check the value of the film thickness derived from the deposition time.

4.5 Electrical Measurements.

4.5.1 D.C. Measurements

The circuit used to measure the d.c. characteristics is shown in fig.(4.11). To enable voltage sweeps to be taken a computer controlled system consisting of a Keithley 485 autoranging picoammeter used in fast feedback to minimize voltage drop and a Keithley 230 programmable voltage source in series with a QL computer were used. The Keithly 230 is programmed to produce a voltage sweep between -1 V to +1V in logarithmic steps. Ten current readings are taken for each voltage and the average value is then displayed. The I-V characteristic can be plotted as shown in fig.(5.1) see section.5.1. Either the d.c conductance, or photoconductance,or both were measured over the entire temperature range 12-360K. They were calculated in the low voltage linear region generally found for ($V \leq .1V$) because of the carrier injection which occurs at high electric fields ($E > 5 \times 10^4 Vcm^{-1}$) and this causes injection of space charge and hence a superohmic relation. In the case of the photoconductivity, this behaviour suggests that it is not due to the free carrier generation mechanism but to the transport dependence of the electric field.

4.5.2 A.C. Measurements

The a.c. loss or photo-induced loss in this context is the response to an alternating applied voltage either in the dark or under a steady illumination, not the response to a chopped illumination (which is associated with the recombination lifetime). The a.c. and induced a.c. losses of the sample were measured using two different instruments.

4.5.2.1 The Manual A.C. Bridge

The first bridge was a manual General Radio Capacitance Bridge (Type 1615A). It was used to measure the capacitance and the conductance over a frequency range

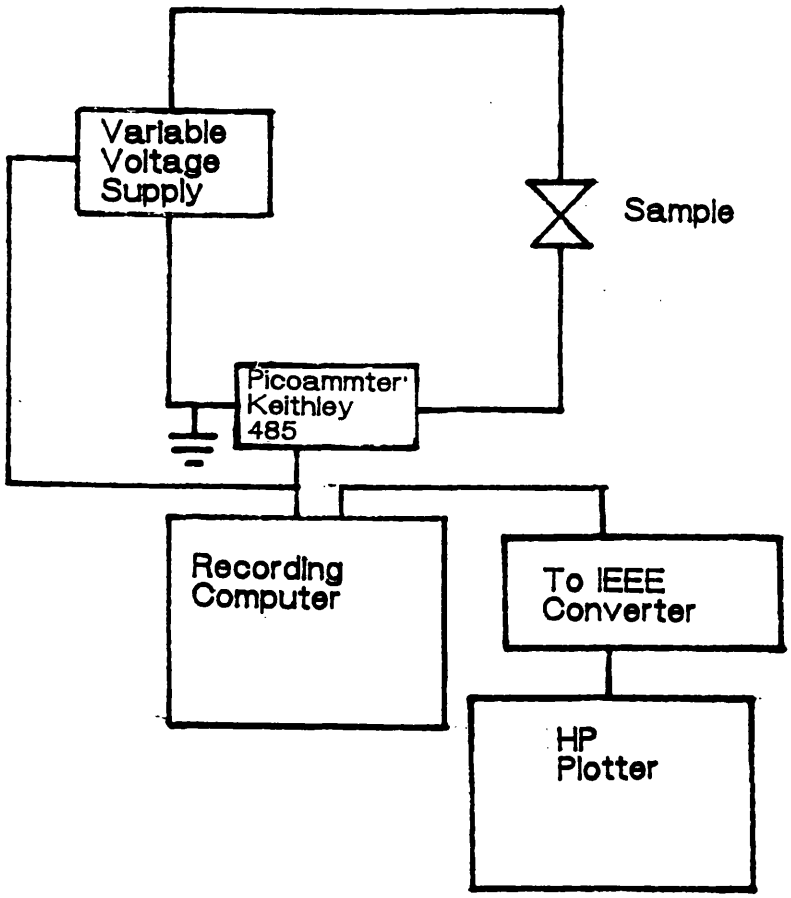

Figure 4.11: Circuit for the D.C. measurement.

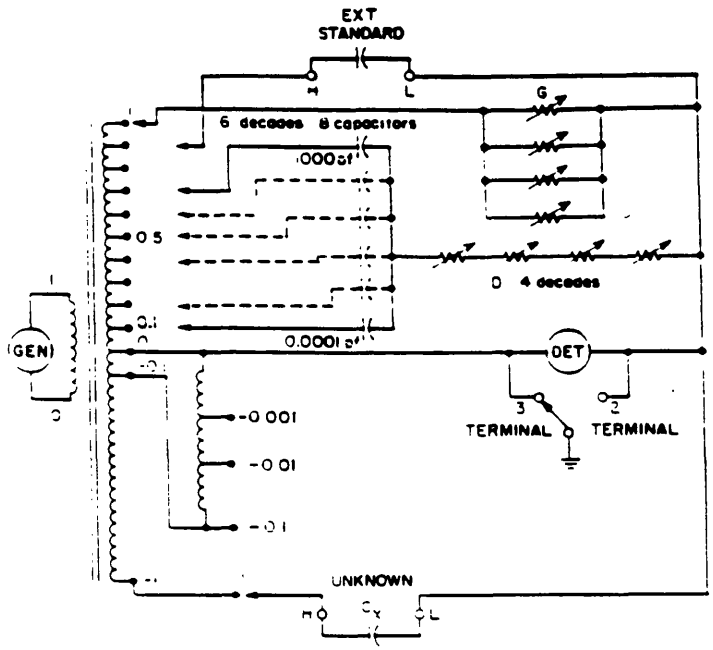

Figure 4.12: Schematic diagram of the General Radio A.C. bridge.

of 11Hz to 100kHz, it was supplied from a Levell Oscillator type TG200DMP. The excitation voltage from the oscillator was set so that the value of the voltage across the sample should be within the linear region of the d.c. characteristic of the sample. The instrument was very useful for measurements at low temperatures. A null method is used in this a.c. bridge in which the unknown capacitance (a-Si:H) is balanced against six calibrated variable capacitors see fig.(4.12). The conductance is compared to the variable impedances in the transformer arms. When the detector, which in this case is a phase sensitive detector (EG&G type 9503C), is reading zero voltage, the bridge is balanced and the specimen parameter can be read from the front panel.

The design of the bridge ensures high accuracy in the measurements. For instance in the frequency range 11Hz up to 20KHz, the capacitance data was accurate to about .01%, and the conductance can be detectecd down to 10^{-11} S sensitivity within 1% error.

Due to the wide range of frequencies available in the system and the high degree of accuracy, the instrument was very useful in the study of the glow discharge a-Si:H for the study of the inhomogeneity in the sample (transition from the dispersive to non-dispersive regime see section. (5.1.2).

4.5.2.2 Computer Controlled Measurement System

The measurements of large conductance values (up to 10^{-3}S) and the study of the decay of the capacitance necessitated the use of a Hewlett Packard 4274 LCR meter. This was an automatic test machine with 12 built-in frequencies of measurement in the range 100Hz to 100KHz. The a.c voltage could be varied between .001 and 5V, though generally a signal of 100mV was used. The meter has an offset compensation to account for the leads capacitance. Using high resolution mode the meter displays data after averaging 10 points at the same frequency. The LCR meter was connected

to a QL computer. This allows a.c. loss to be measured automatically. Using the programs developed in this department, it enables us to take a number of different measurements, such as frequency sweep in the dark and under illumination, the time dependence of the rise and the slow decay of the capacitance over periods as long as 24 hours. The data for this measurement could be taken every 1, 20, 60, 180, 600s at a desired frequency. When the frequency sweeps were recorded, each point was in fact the average of 20 high resolution measured points. At high temperatures, the data recorded on the Hewlett Packard Instrument was consistent with those taken using the General Radio Bridge, if we allow for the experimental error. As the temperature decreases towards the base temperature the loss angle decreases, which makes measurements less accurate. The error on the conductance becomes around (10%). At this stage it was necessary to switch to the manual Bridge.

When comparing results obtained from the two instruments, one can say that the General Radio bridge gives more accurate results than the LCR meter in the low temperature regime. Also the a.c loss can be investigated over a wider range of frequencies using the first bridge. However, the second bridge was very useful in recording the fast build up of the population of carriers when the sample is illuminated and the decay when the light is switched off. We were able to take up to one point/second using this system. At low temperatures when the light was removed, the two parameters of the dielectric constant of the sample were found to take days to return to their dark values. Therefore, it was preferrable to take an automatic recording overnight using the second system.

A plotting program developed in the department enabled us to output the different characteristics (i.e frequency sweep, time dependence of either capacitance or conductance, I-V characteristic etc..) to a Hewlett Packard (*hp*) plotter from which the data sets presented in subsequent sections are derived.

CHAPTER 5

Dark Loss

In this chapter we present some of the data taken on samples in the dark. This includes the study of the d.c. and a.c. conductivities over a limited range of temperatures and frequencies. Two different types of sample were measured during the course of this work (intrinsic and compensated) glow discharge a-Si:H and magnetron sputtered a-Si. The latter is supposed to have higher density of states than the former, and thus a greater value of a.c. loss at low temperatures is expected. The application of the inhomogeneous model (see Long 1989a,b) on the compensated material shows the existence of long-range potential fluctuations which contribute to the loss at high temperature. A comparison of our results with some recent results reported on the same material prepared similarly is made.

5.1 Glow Discharge Samples

5.1.1 D.C. Conductivity

The I-V characteristics of the sample at various temperatures were studied in parallel with the a.c. loss. The d.c conductivity was measured at around ± 100 mV, since the I-V characteristic in this region was generally linear (see fig.(5.1)), indicating that over this range injection effects can be ignored. At high electric field $> 5 \times 10^4$ Vcm^{-1} the I-V characteristic becomes strongly superohmic. The d.c. conductivity data for an intrinsic sample in the temperature range 210 to 360K is plotted in fig.(5.2) in the form of $\log \sigma_{dc}$ vs $10^3 T^{-1}$. The relation in fig.(5.2) is linear over the

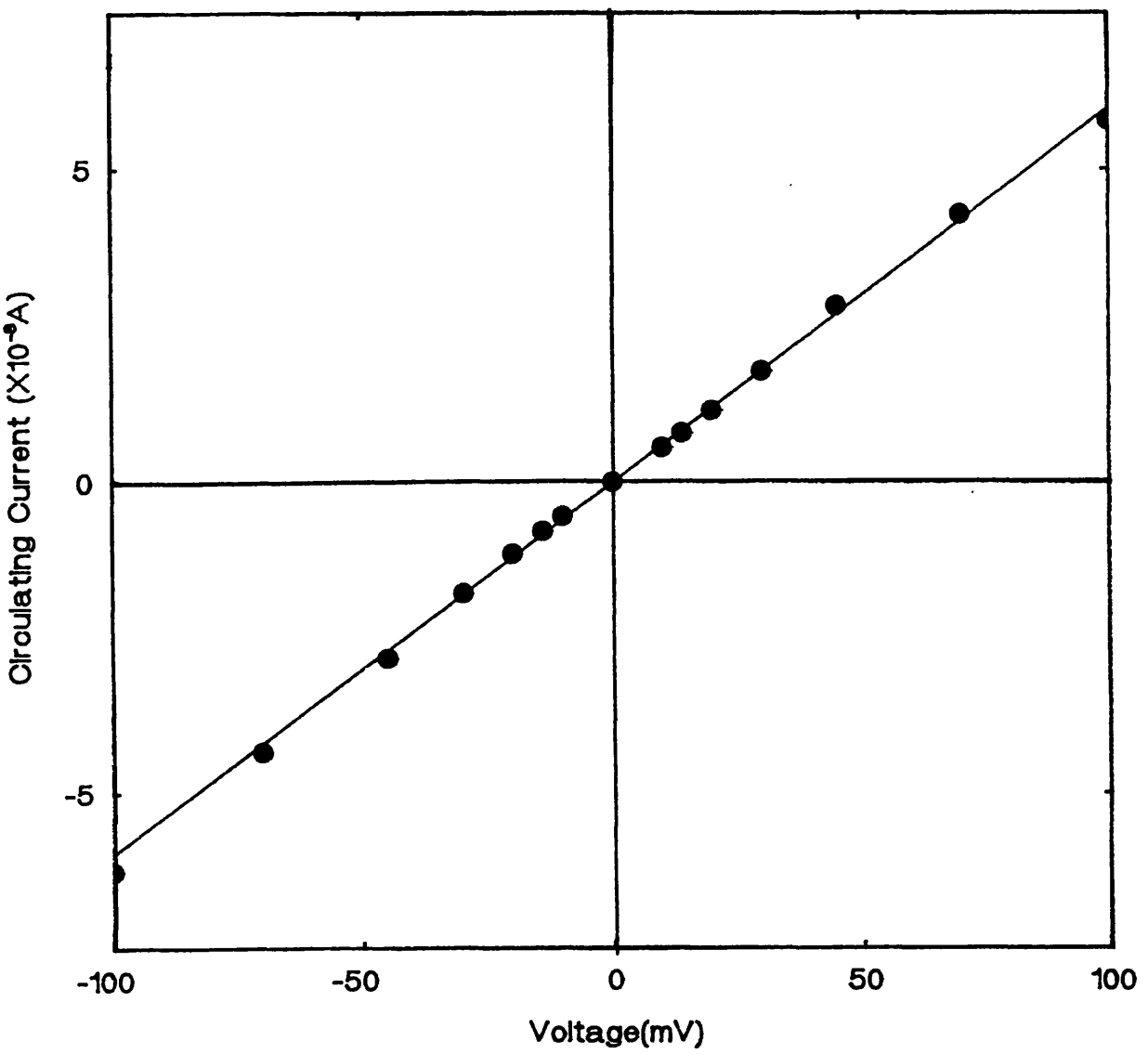

Figure 5.1: The current voltage characteristic at room temperature for an intrinsic sample (MS2). The solid line shows the best linear fit to the data.

whole range of data giving an activation energy of $\epsilon_c - \epsilon_f \approx 0.66 \pm .01$ eV. The d.c. conductivity for all samples measured was simply activated implying conduction in the extended states, and any other contribution such as from hopping in band tails can be counted out. Fig.(5.3) shows the same plot for two compensated samples with different doping ratios. The activation energies were found to be $0.707 \pm .003$eV and $.80 \pm .01$eV, for the 2.5vppm and 5vppm samples respectively see also the table. These values are in good agreement with recent results reported by Goldie, Spear and Liu (1990) for samples prepared similarly. The values are also consistent with a Fermi energy ϵ_F located near the midgap and this is strong evidence for the achievement of a complete compensation in these samples.

5.1.2 A.C. Conductivity Measurements.

The total a.c. conductivity $\sigma_{tot}(\omega, T)$ of the sample is affected by the d.c conductivity and the series resistance of the coaxial leads and the electrode material. To characterise the sample properly, these two factors must be removed from the total loss. The d.c. conductivity generally increases more strongly with temperature than the a.c. component. In the high temperature regime the a.c. loss is dominated by the d.c. conductivity. Therefore, the real a.c. conductivity must be separated from the d.c. The traditional way to do this, is to express the total conductivity as the sum of a dispersive and a non-dispersive term; thus:

$$\sigma_{tot} = \sigma_{dc} + \sigma_{a.c}(\omega, T) \tag{5.1}$$

This assumes that the d.c. and a.c. losses are governed by different mechanisms.

At low temperature below 200K, the d.c. conductivity was not detectable with the equipment used in the experiment. Therefore, the loss is dominated by the a.c. conductivity. Evidence for the assumption in equation (5.1) can be obtained by studying the capacitance with the frequency. In an inhomogeneous system, the capacitance increases with decreasing the frequency. Long (1989a) suggested that this behaviour is due to inhomogeneous regions within the system. As the frequency

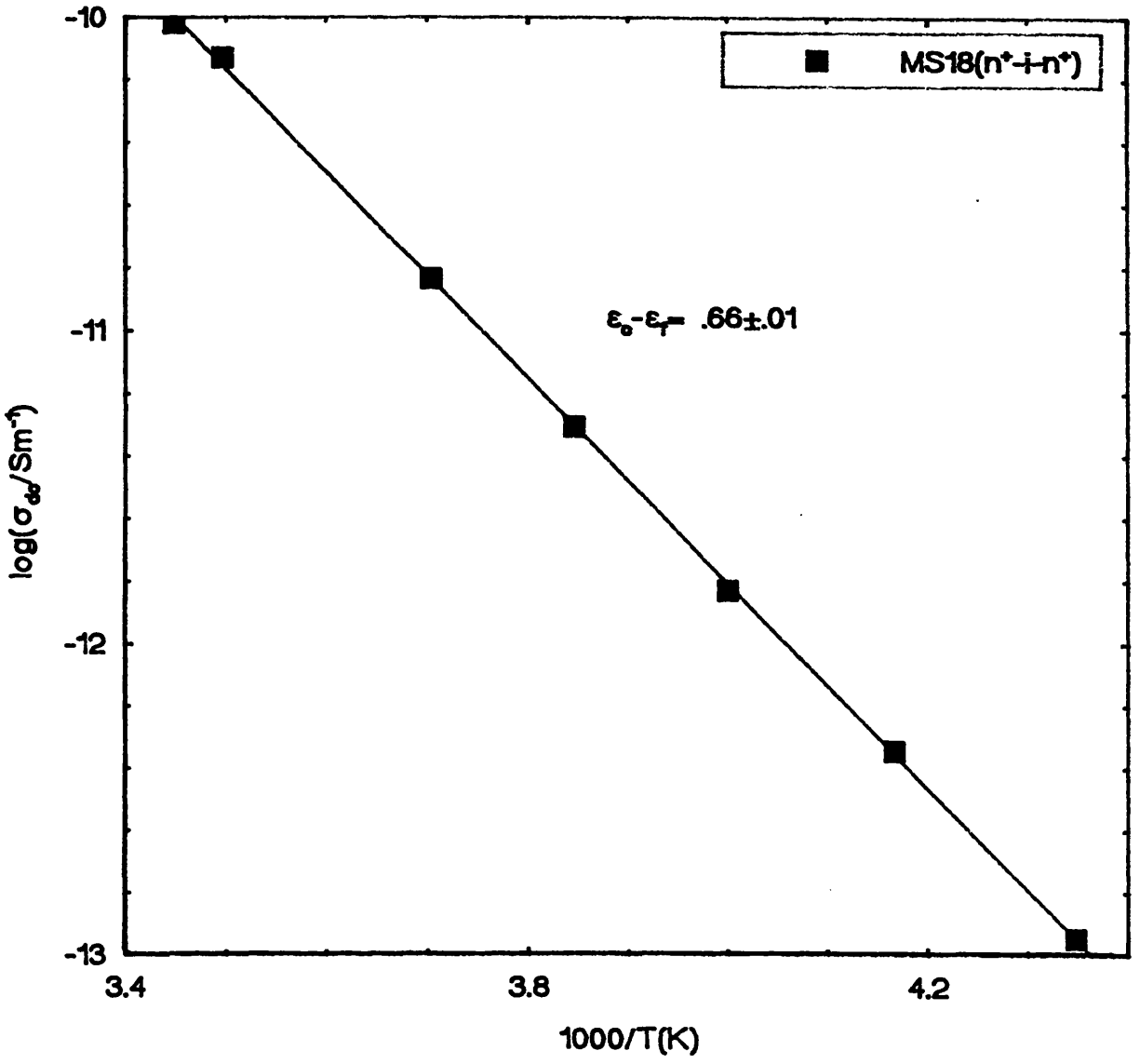

Figure 5.2: Temperature dependence of the d.c. conductivity for an intrinsic (MS18) .

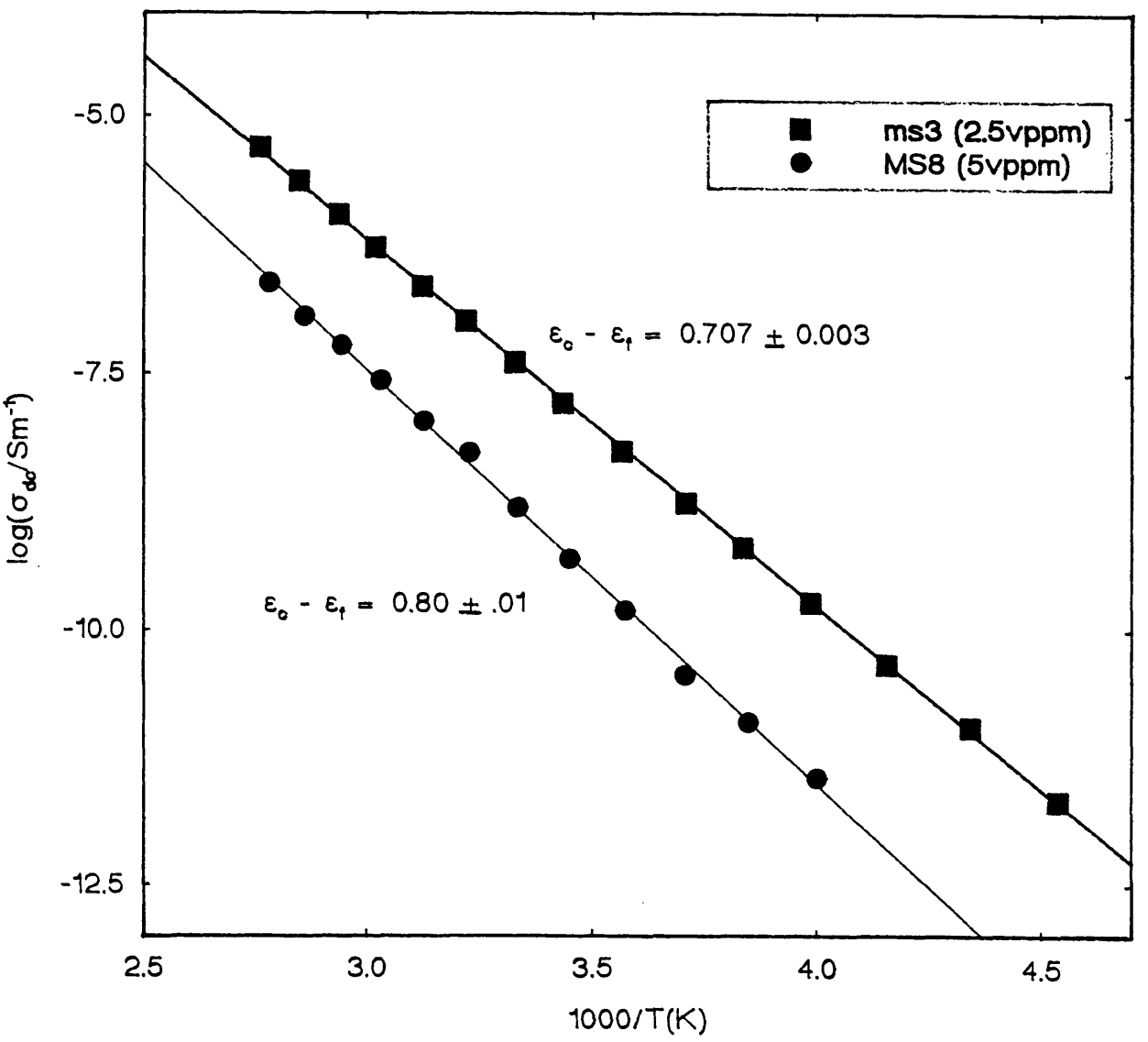

Figure 5.3: Temperature dependence of the d.c. conductivity for two compensated sample MS3 and MS8, the compensated doping level is given between brackets. The solid lines show the best linear fits.

is decreased more of these regions can respond to the applied field until a saturation is reached and the capacitance is almost constant. If this is the case, the plot of $\log(-\frac{dC}{d\ln\nu})$ against $\log\nu$ shows a peak. This is known as a loss peak and it is the characteristic of the systems where both a.c. and d.c. conduction processes are linked. This peak is observed for sputtered a-Si and a-Ge (Long et *al.* 1983, 1985). However, in the case of the glow discharge a-Si:H, this behaviour does not occur and we believe that a.c. and d.c. conduction mechanisms are independent of one another. In chapter 6, we study this behaviour in detail as we will see that the d.c. and a.c. photoconductances at low temperature are governed by the same hopping process.

The second effect arises from the series resistance in the electrode material and the leads. This has a great effect on the loss at high frequencies ($\nu > 14$kHz). The problem can be tackled by analysing the circuit in fig.(5.4). The series resistance is denoted as R_0. The effective conductance and capacitance are given by:

$$G_{eff} = \frac{(R_0 + R) + (\omega CR)^2 R_0}{(R_0 + R)^2 + (\omega CR)^2 R_0^2} \tag{5.2}$$

and

$$C_{eff} = \frac{R^2 C}{(R_0 + R)^2 + (\omega CR)^2 R_0^2} \tag{5.3}$$

At low frequencies $G_{eff} = R^{-1}$ and $C_{eff} = C$ with the assumption that $R_0 \ll R$. As the frequency increases, the effect of R_0 cannot be ignored and the effective conductance is expressed by approximating the equation (5.2) to first order, thus:

$$G_{eff} = G + \omega^2 C^2 R_0 \tag{5.4}$$

Such contribution is clear in fig.(5.7) where both the total and the real conductivity (after correction) are plotted against the measuring frequency. The effect of R_0 can be removed by calculating its value with the following procedure. Since R_0 is weakly temperature dependent, we considered the curve at the lowest temperature and assume that the plot of $\log(G_{eff})$ against $\log(\nu)$ is ideally linear. At high

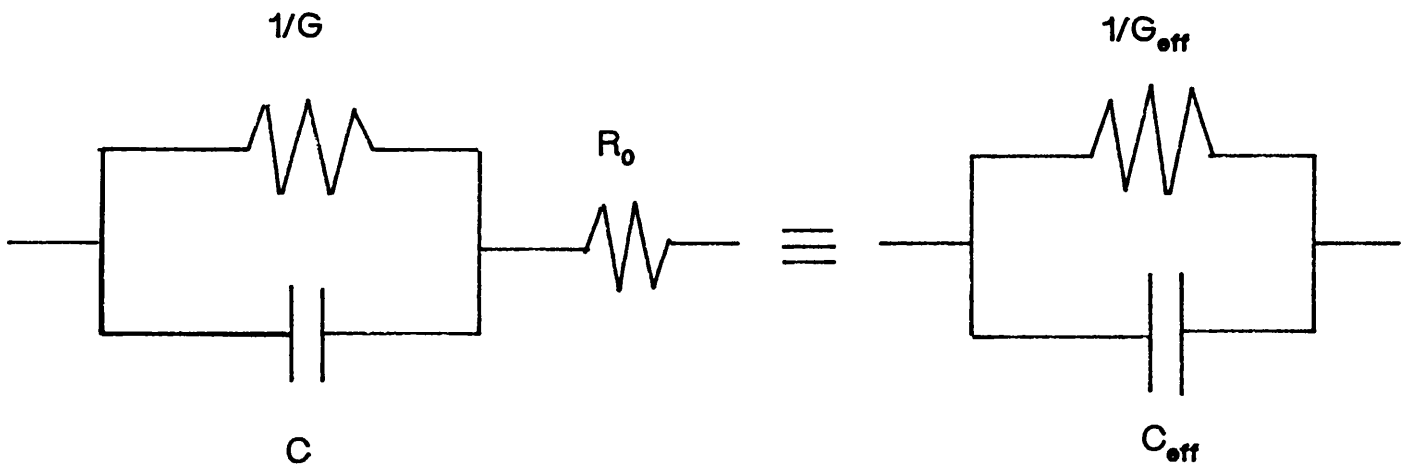

Figure 5.4: Configuration of the series resistance effect in the a.c. measurement.

frequencies the linear region is extended and subtracted from G_{eff}. The value of R_0 to use in equation (5.4) can then be deduced. The samples investigated have an ITO as the bottom electrode, a typical series resistance of the order of 3 - 14 Ω was obtained for such material

5.1.2.1 Frequency Dependence.

The total conductivity σ_{tot} as a function of the frequency for both intrinsic and compensated samples is shown in fig.(5.5) to (5.7) in the form of $\log(\sigma_{tot})$ vs $\log(\nu)$. The different curves were taken at various temperatures in the range 12.5 to 300K. The power law $\sigma \propto \omega^s$ is obeyed in all plots. It can be seen that in the low frequency regime ν <7kHz, the frequency exponent s which is the gradient of $\frac{d\ln\sigma}{d\ln\omega}$ increases with decreasing temperature and reaches a constant value below 200K see fig.(5.8). At temperatures below 100K a charge transfer by tunnelling is probably responsible for the conduction, since s is independent of temperature in accordance with equation(2.16).

In the high temperature region where the d.c. limit is reached (T≥ 240K) the rapid transition from dispersive to non-dispersive d.c behaviour is very pronounced without the existence of any loss peak. The frequency dependent term can therefore be attributed to a strong hopping process occuring in deep defect states close to the Fermi level.

The contribution to the total conductivity at high frequency ($\nu \geq$ 14kHz) is due to the electrode material (series resistance) see section. (5.1.2). After the substraction of the series resistance term the exponent s becomes weakly dependent on frequency (see fig.(5.7)).

5.1.2.2 Temperature Dependence.

The temperature dependence of the total conductivity for an intrinsic sample (n^+-i-n^+) is presented in fig.(5.9). Data are plotted for two frequencies of measurements

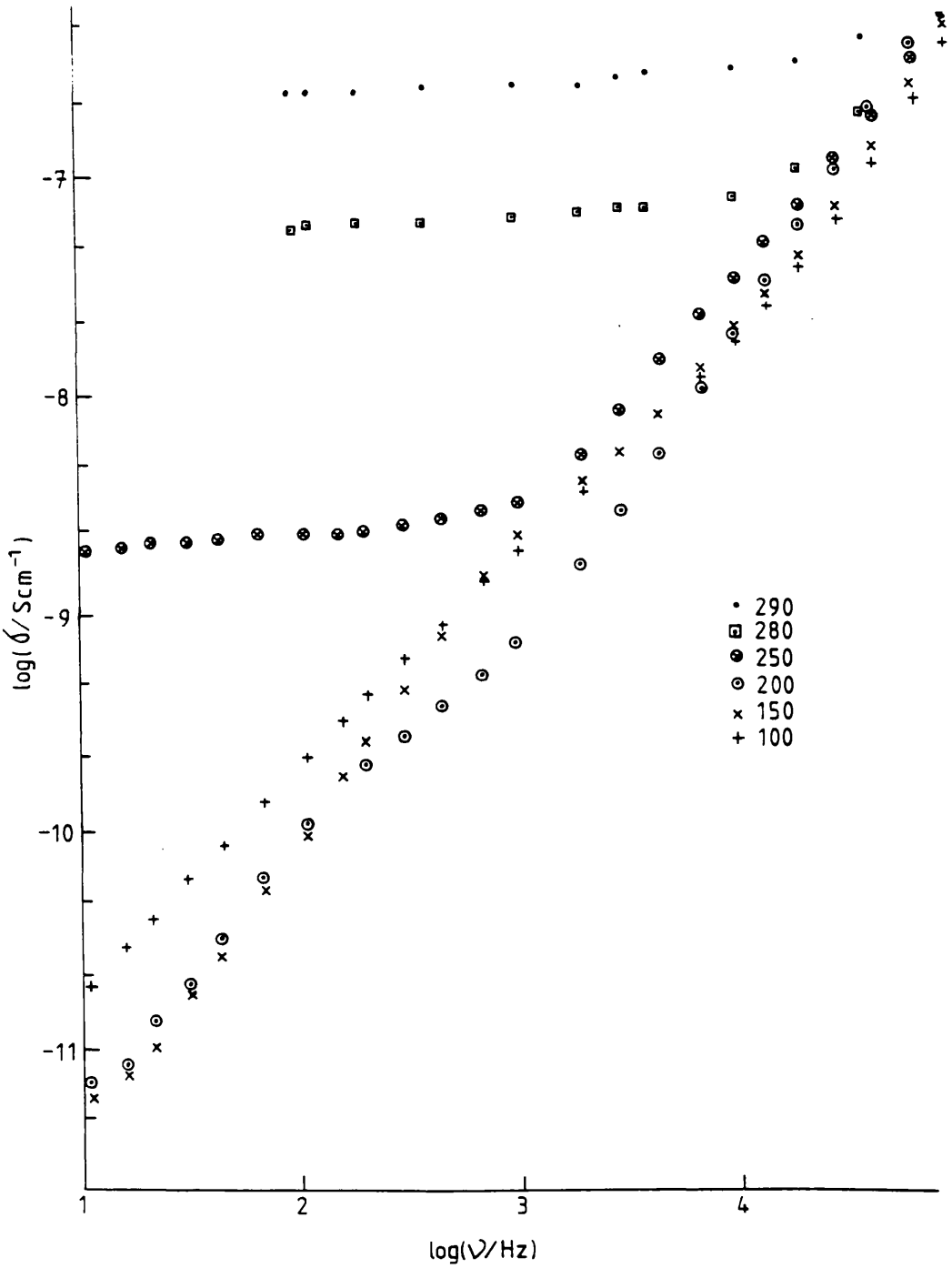

Figure 5.5: Frequency dependent conductivity for an n^+-i-n^+ (MS2). The measuring temperature is indicated in the graph.

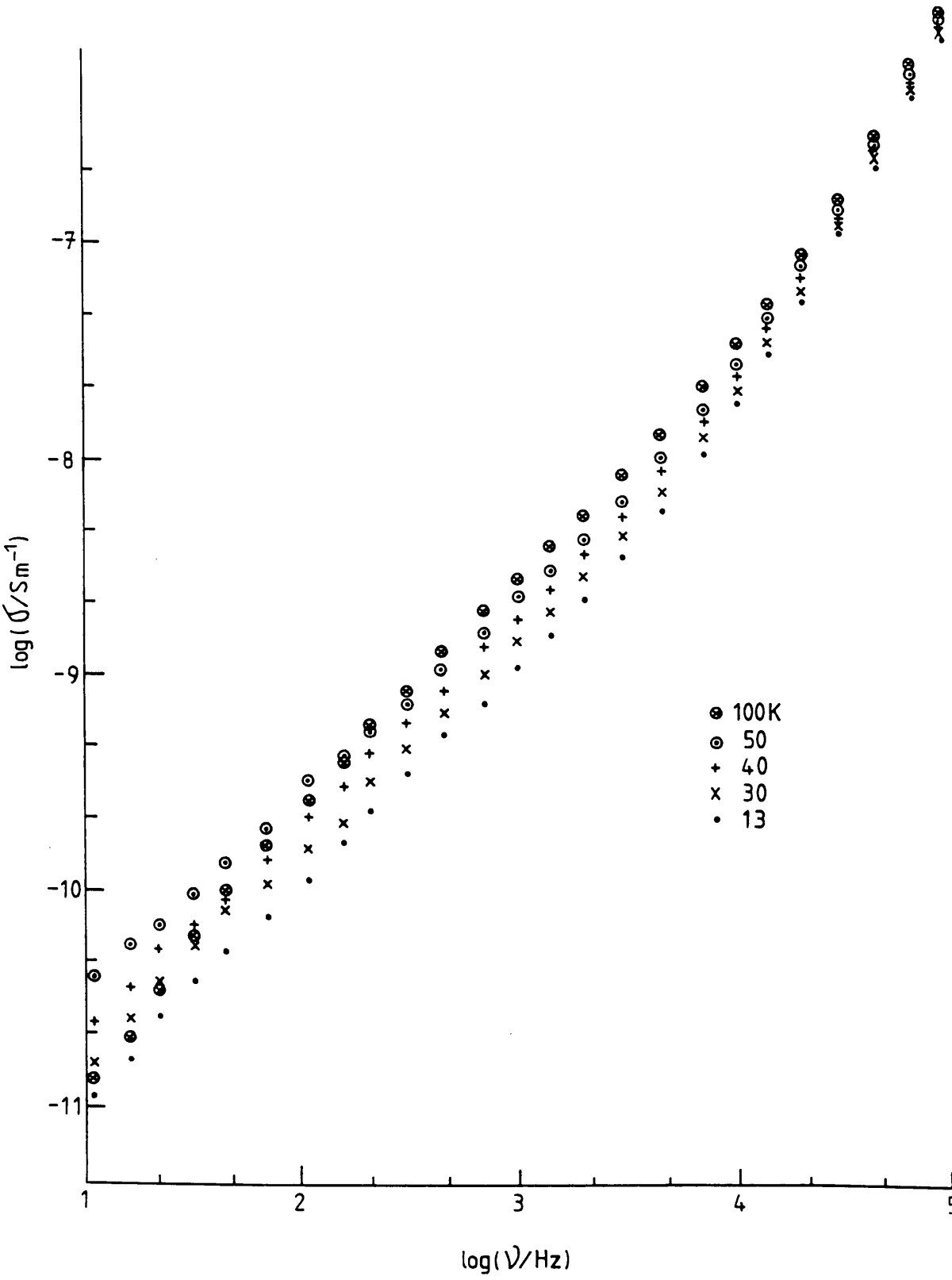

Figure 5.6: Frequency dependent conductivity for an n^+-BP-n^+ at low temperatures. The appropriate temperature is indicated in the graph.

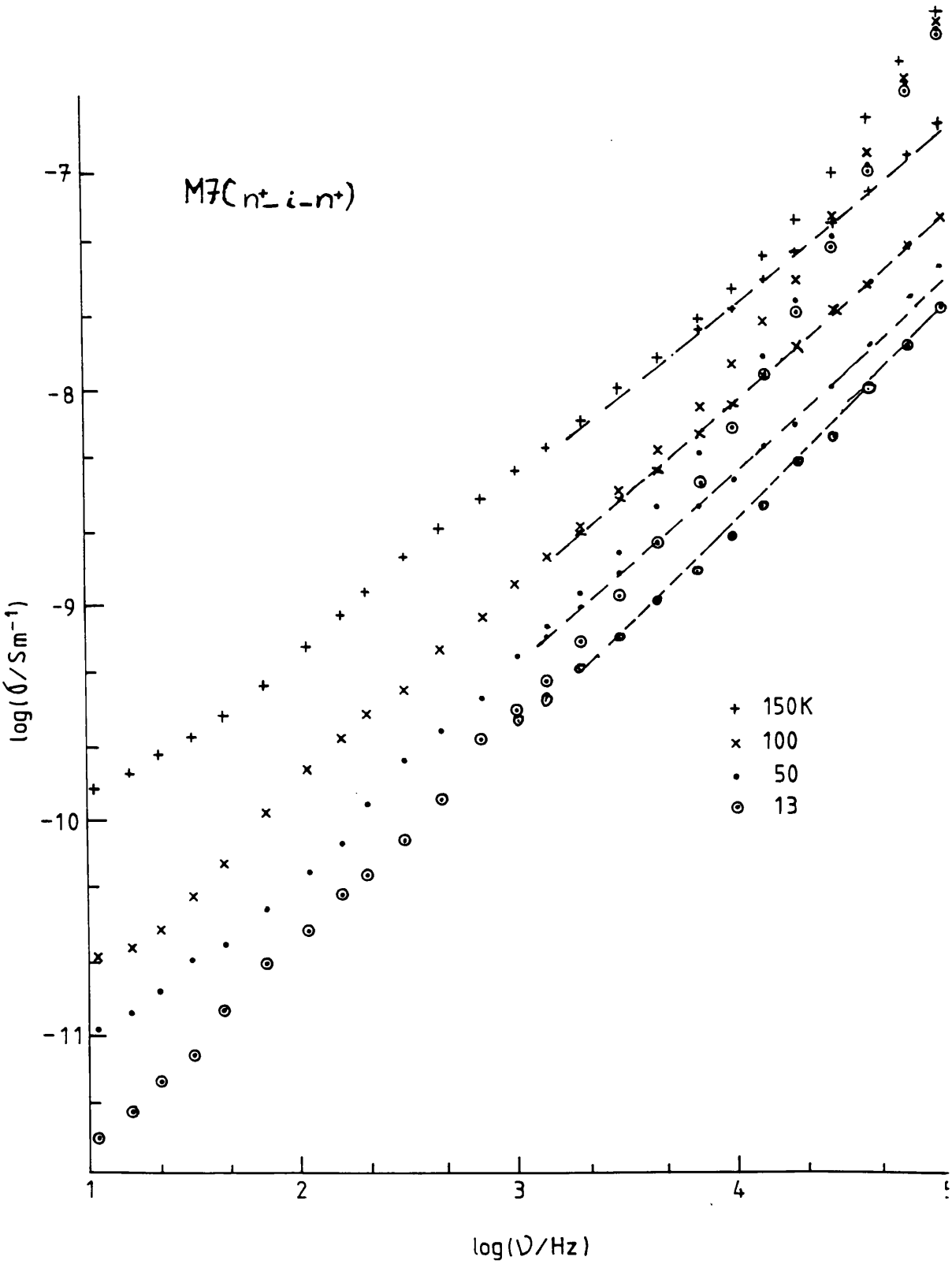

Figure 5.7: The frequency dependent conductivity, for an n^+-i-n^+ sample (MS7). The hatched lines correspond to the correction for the series resistance.

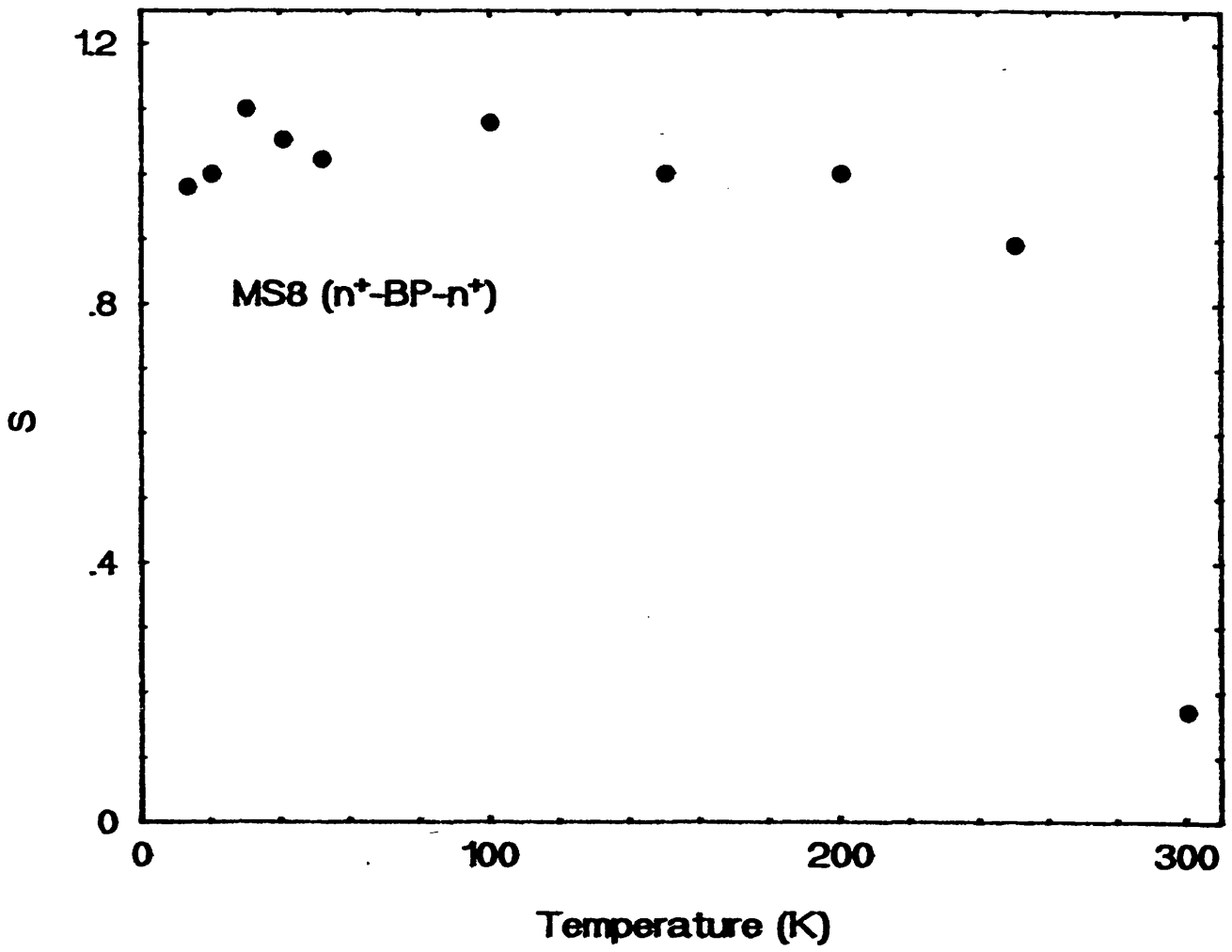

Figure 5.8: **The temperature dependence of the frequency exponent s for an n^+-BP-n^+ sample (MS8).**

210Hz and 2kHz in the form of log σ_{tot} vs T. This can be divided into two temperature regimes. In the low temperature regime where s is weakly temperature dependent a tunnelling process is responsible. The high temperature regime is attributed to carriers being activated in the extended states.

The peak is well established at around 120K at 210Hz and at 2kHz it shifts to 140K. This feature (peak) is not an intrinsic characteristic of the loss in the bulk material but it is attributed to the series n^+-layers (Shimakawa et *al.* 1987a). To confirm this we followed the method used by Shimakawa et *al.*. The n^+-layers are considered as a combination of parallel conductance G_s and capacitance C_s in series with the bulk (i-layer) which has G_b and C_b as conductance and capacitance respectively see fig.(5.10). This figure is similar to fig.(5.4) with an extra capacitance due to the n^+-layers. Therefore, we anticipate similar expressions for the conductance and capacitance. The total conductance and capacitance in this case are given as:

$$G_m = \frac{G_b G_s (G_b + G_s) + \omega^2 (G_s C_b^2 + G_b C_s^2)}{(G_b + G_s)^2 + \omega^2 (C_b + C_s)^2} \tag{5.5}$$

and;

$$C_m = \frac{(C_b G_s^2 + C_s G_b^2) + \omega^2 C_b C_s (C_b + C_s)}{(G_b + G_s)^2 + \omega^2 (C_b + C_s)^2} \tag{5.6}$$

At high temperatures G_s is large and therefore G_m and C_m are governed by the bulk parameters G_b and C_b i.e $G_m = G_b$ and $C_m = C_b$. With decreasing temperature G_s decreases and contributes to total loss.

$$G_m = G_b + \frac{\omega^2 C_b^2}{G_s} \tag{5.7}$$

We can see that equation (5.7) is similar to equation (5.2) when both effects are taken into account. Considering the data in fig.(5.9), the loss at high temperatures was extrapolated to obtain the bulk conductivity G_b(T), under the peak. Using equation (5.7), the conductivity of the n^+-layer was then deduced. The data for an intrinsic sample is shown in fig.(5.11). The conductivity is activated with an activation energy of 160 meV. The results are consistent for the 2 measuring frequencies

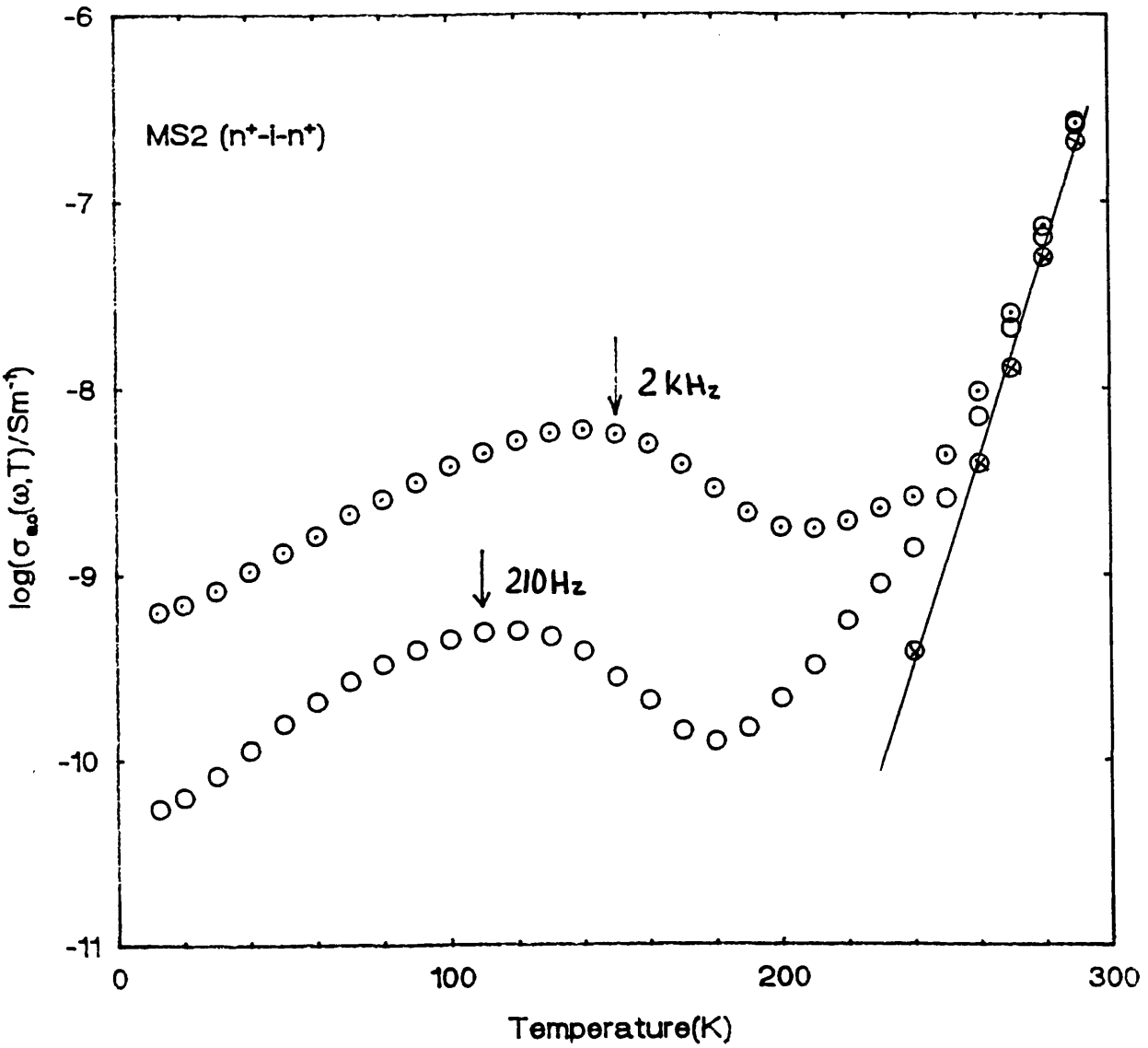

Figure 5.9: The temperature dependence of the conductivity for an n^+-i-n^+ sample MS2. ⊙: 2kHz, o: 210Hz, ⊗: d.c. conductivity and the solid line shows the best linear fit to the d.c. data.

Figure 5.10: The equivalent circuit used to analyse the effect of the n^+ layer. G_b and C_b represent the bulk sample and G_s and C_s represent the n^+ layer.

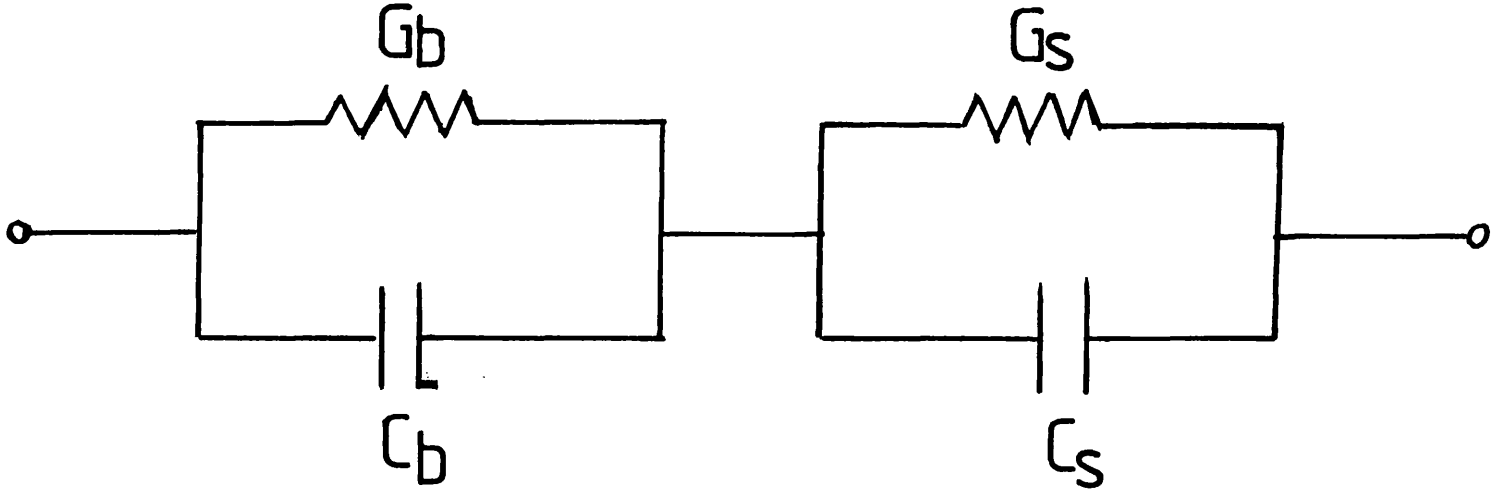

which we take it as an evidence of the correctness of this approach. Similar data was obtained for a compensated sample (MS3) (see Lemmon 1990). However, with another compensated sample which has a higher compensated doping level (5vppm), the results did not match for the 2 measuring frequencies, which may suggest the failure of the equation (5.7) and that in addition to the loss due to the injecting contacts, there is a significant contribution from other regions (inhomogeneous regions) which will be discussed in the next section.

The vertical lines above the curves in fig.(5.9) indicate where the loss angle is $\frac{\pi}{4}$ i.e $\omega C_s G_s = 1$, these are close to the peaks for frequencies as expected. As the temperature decreases this quantity becomes less than unity and hence the equation (5.7) fails. At temperatures below 80K the loss is still temperature dependent and larger than the bulk loss at higher temperatures (e.g. at 230K), subtracted from the extrapolation of G_b(T). This may suggest that even at this low temperature there is still some contribution to the measured loss from the n^+-layers and may be this is one reason why the conductivity does not reach a constant value as was observed by Shimakawa et *al.*

In fig.(5.12), we present the temperature dependence of the a.c. conductivity for an intrinsic sample (MS7). The data is plotted for three frequencies, 210Hz, 2 and 20kHz. The curve (3) is obtained from the curve (4) after we subtracted the term due to the series resistance. It can be seen from the first three curves that after this correction, the a.c. loss is proportional to the measuring frequency. Though, the data in fig.(5.9) and fig.(5.12) are for intrinsic samples, the n^+-peak is more pronounced in the first figure than in the second and it shifts to higher temperatures in the second figure. This is probably due to variation in the doping level of the n^+-layer in the samples.

In fig.(5.13) the data from one of our intrinsic sample (Dundee) is compared to that of Shimakawa et *al.*(1987a). We can see that the loss is much less in the Dundee sample. However, the d.c. conductivity is greater. This indicates a large

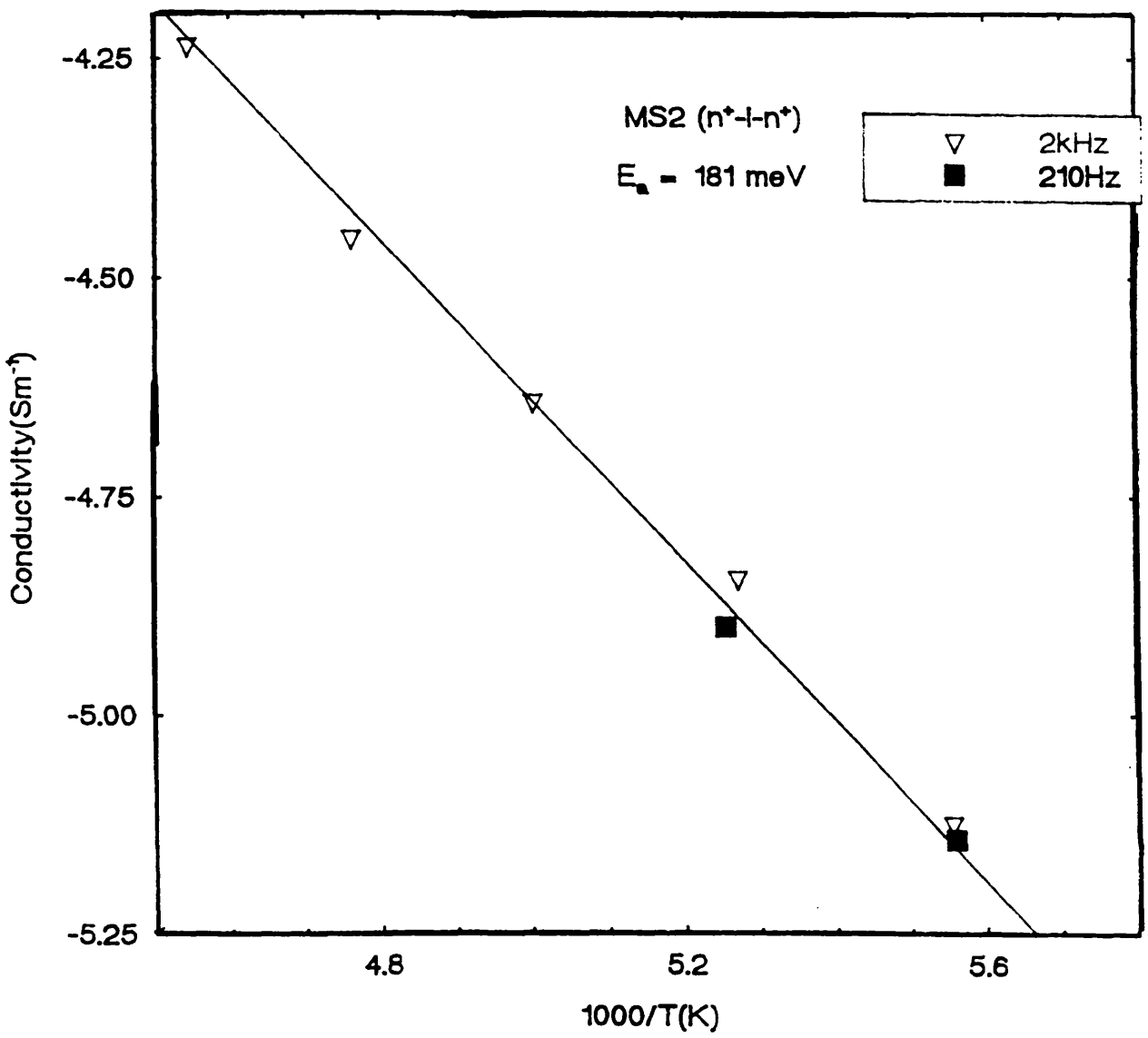

Figure 5.11: The temperature dependence of the conductivity of the n^+ layers for an n^+-i-n^+ sample (MS2). The solid line is the best linear fit.

activation energy in Dundee samples. These observations lead us to conclude that the Dundee samples are of higher quality. The low temperature regime (T< 100K) pointed out by Shimakawa et *al.* differs from ours, in that in the data of fig.(5.9) the a.c. conductivity is proportional to the temperature ($\sigma_{ac} \propto \omega^s T^n$) (see Long 1982). The temperature exponent n is approximately equal to unity at 210Hz and decreases with the frequency. This suggests that an uncorrelated hopping process is responsible for the behaviour in the low temperature regime.

In the high temperature regime, however with T > 190K the loss is almost one order of magnitude or more higher in Shimakawa sample. For example: at T= 220K and for 2kHz, the loss in Dundee sample is $\sigma_1 = 2.2 \times 10^{-11}$ Scm^{-1} whereas the Shimakawa sample gave a value of about $3.2 \times 10^{-10} Scm^{-1}$. The loss in the compensated sample (5vppm) was found around $1.55 \times 10^{-11} Scm^{-1}$. The loss at 210Hz at the same temperature is shown in the table. From these results (see table 5.1), it can be concluded that the additional loss due to inhomogeneous regions in the material, observed in the Shimakawa sample is not present in the intrinsic Dundee sample.

The temperature dependence of the conductivity in the compensated samples is shown in fig.(5.14) and (5.15) for the two samples with different doping ratios. Fig.(5.15) has been measured in conjunction with R. Lemmon (1990). In contrast to the intrinsic sample, there is an additional loss in the high temperature regime between 190K and 240K. The loss is more pronounced in the highly compensated sample (5vppm) than in the lighter one (2.5vppm). This indicates that compensated materials are considerably more affected by long-range fluctuations than the intrinsic materials, even at these small compensated doping levels.

5.1.2.3 Effect of Potential Flutuations on the Loss in Compensated a-Si.

In this section we try to apply the inhomogeneous model discussed in section (2.) to the data from compensated samples. Before that, we compare the a.c. loss in both

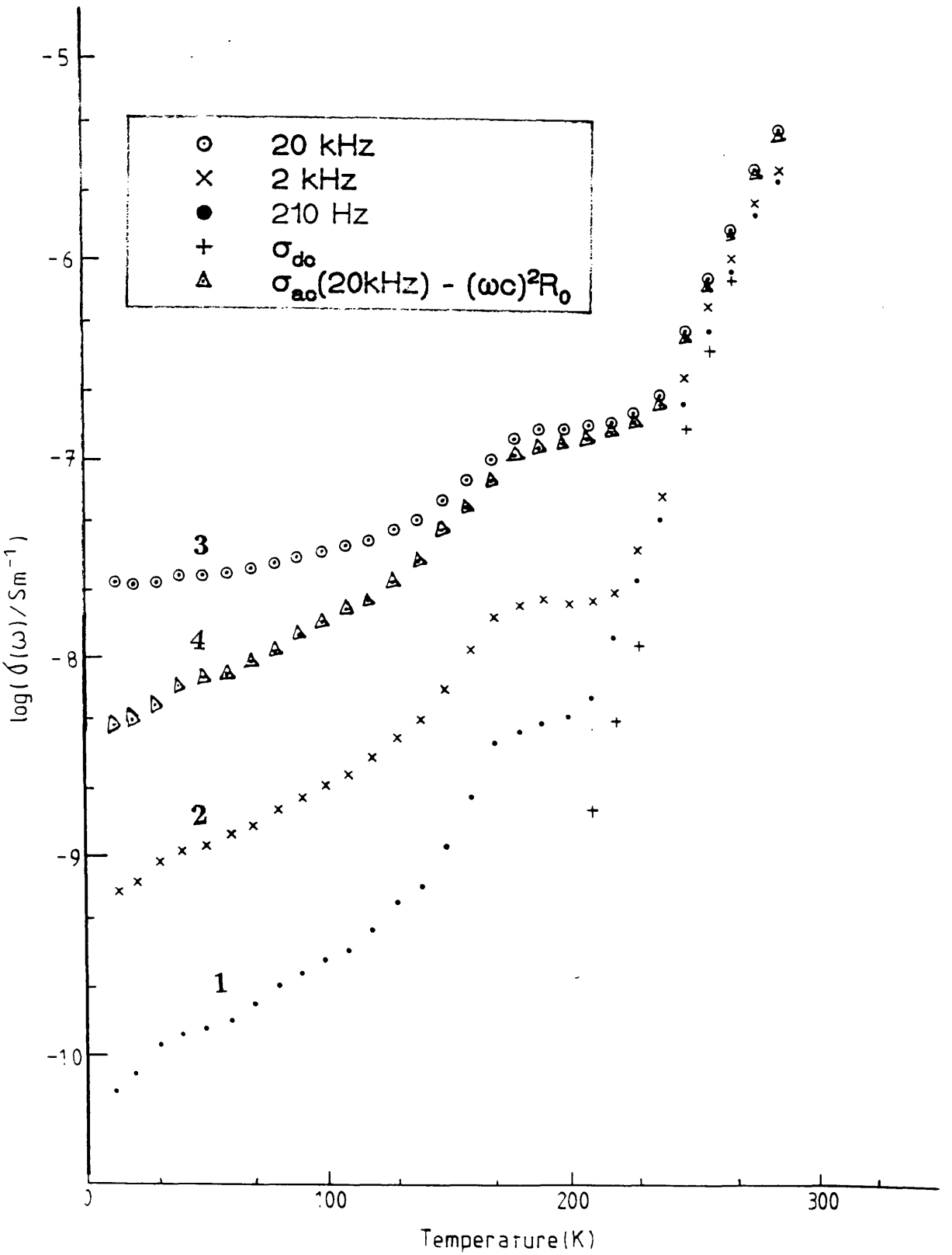

Figure 5.12: **The temperature dependence of the a.c. conductivity for an intrinsic sample (MS7) measured at three frequencies. Curve (4) corresponds to the data of curve (3) after correction for the series resistance.**

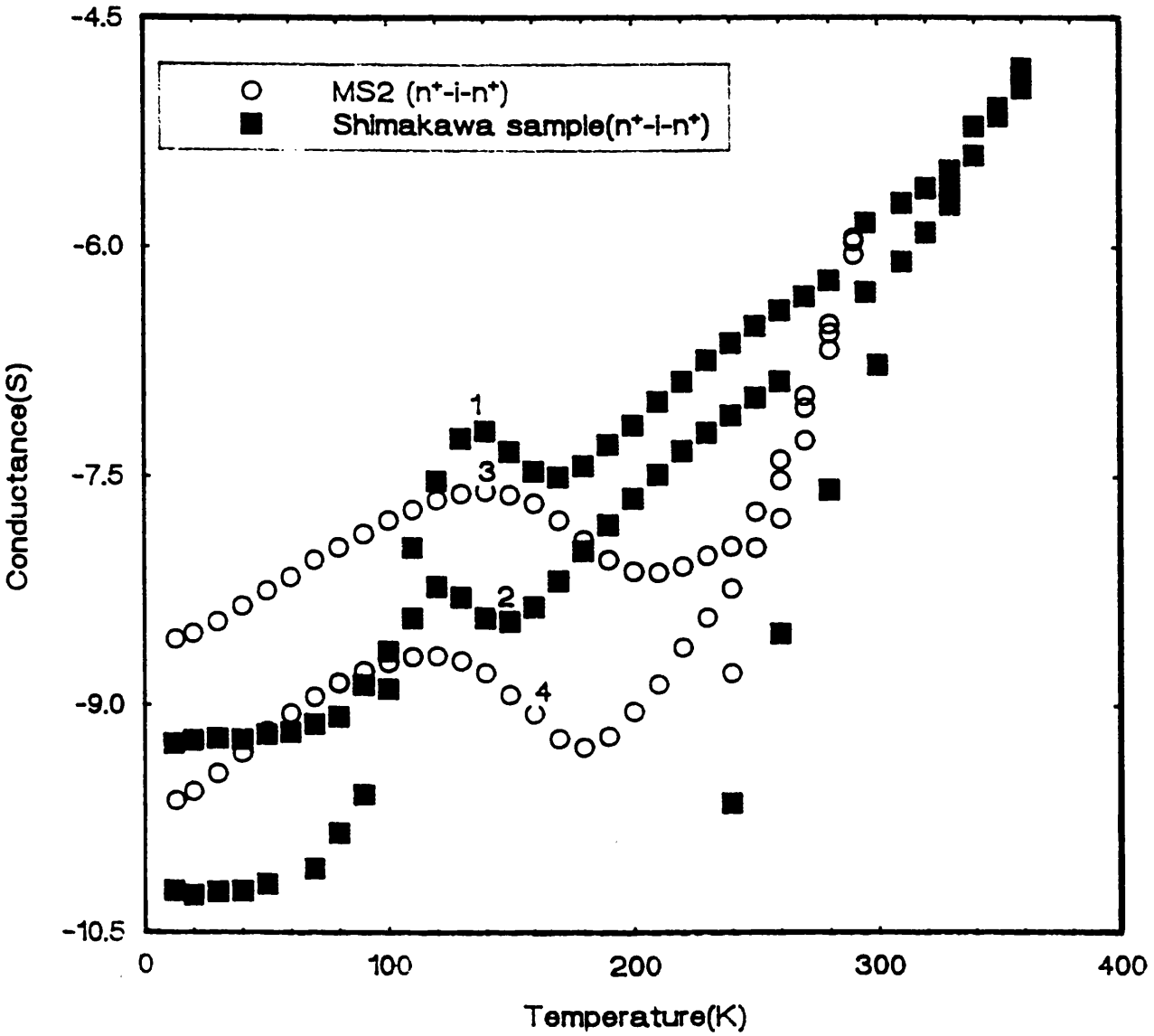

Figure 5.13: Comparison of the temperature dependence of the conductivity of the Dundee intrinsic sample MS2 with that of the intrinsic sample of Shimakawa et al 1987. Curves 1 and 3 : 2kHz, curves 2 and 4 : 210Hz, the corresponding d.c. conductivity is fitted with a linear relation.

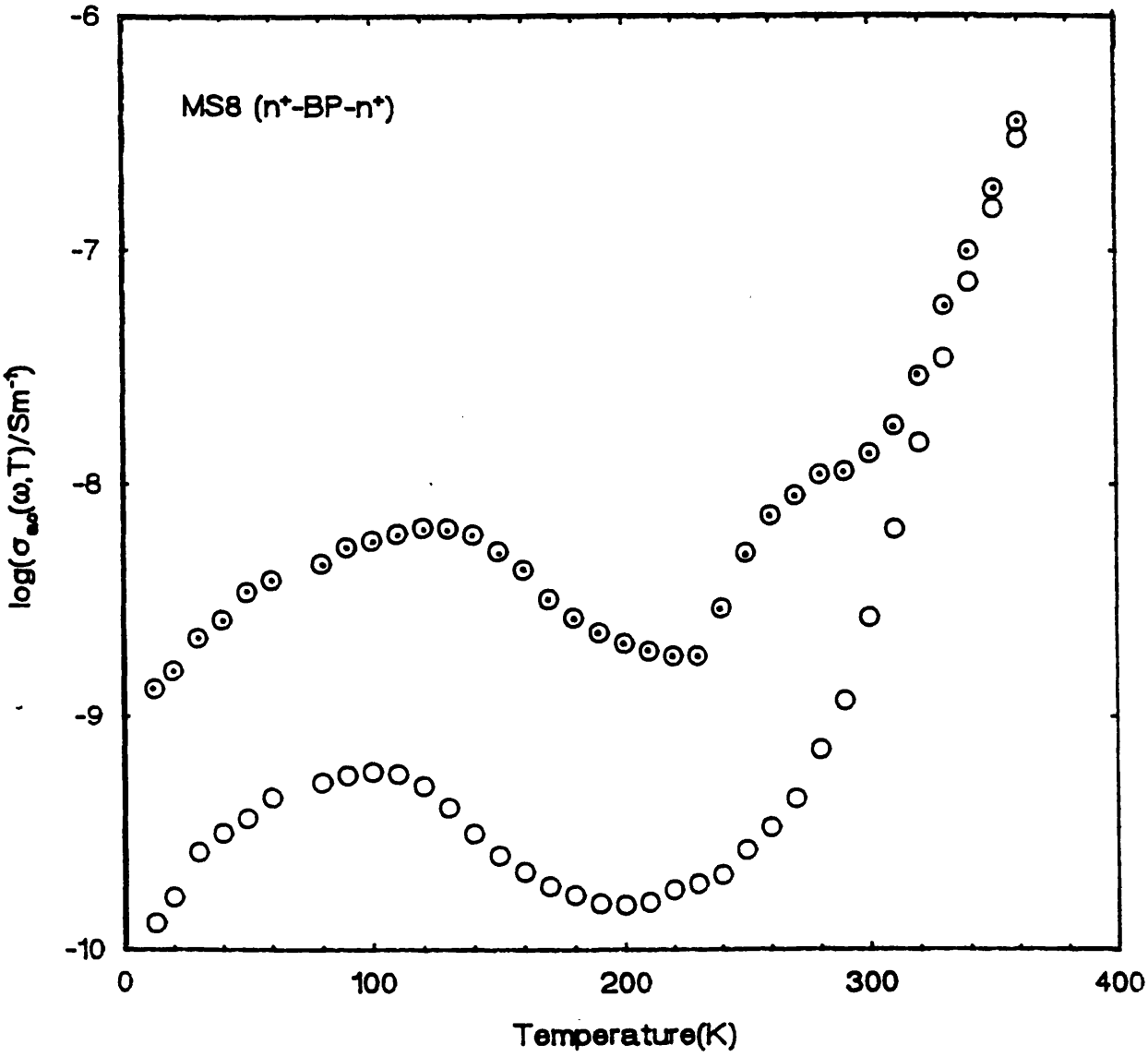

Figure 5.14: The temperature dependence of the conductivity for a compensated sample (MS8) D_c= 5vppm. ⊙: 2kHz and o: 210Hz.

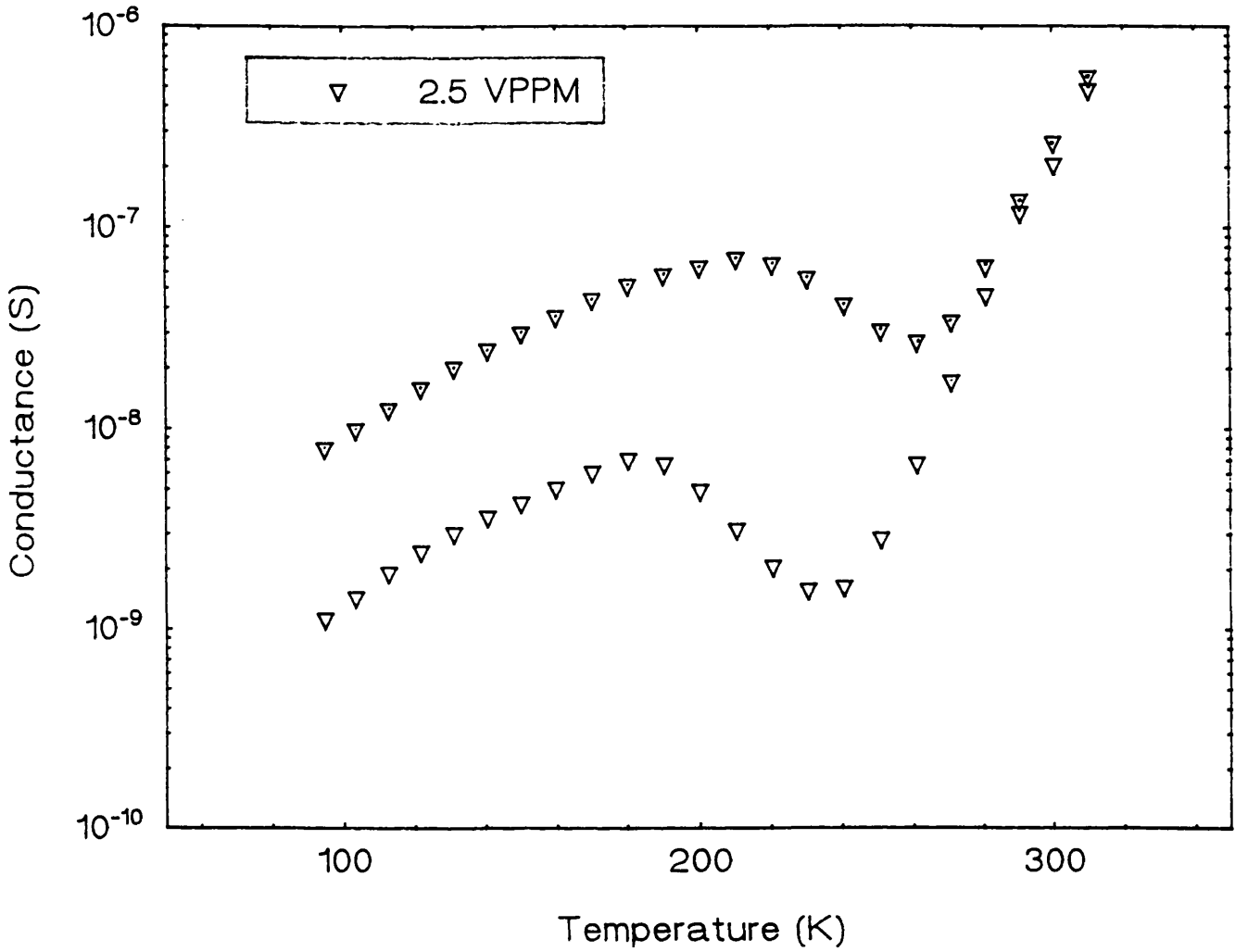

Figure 5.15: The temperature dependence of the conductivity for a compensated sample (MS3) D_c= 2.5vppm. ▲: 2kHz and △: 210Hz.

intrinsic and compensated samples and in two compensated samples with different doping ratios. In fig.(5.16), we plot the temperature dependence of the conductivity for two samples one intrinsic and the other compensated. It can be seen that they have the same features, except the contribution to the loss at high temperatures which is absent in the intrinsic sample as would be expected. In fig.(5.17) we present the same plot for two compensated samples with different doping ratios. It can be seen that the contribution at high temperatures is more significant in the sample with high doping ratio (5 vppm) than in the other one. Following the Long (1989a) model, the d.c. conductivity is assumed to be simply activated, thus:

$$\sigma_b = \sigma_0 exp\left(\frac{-E_0}{k_B T}\right) \tag{5.8}$$

From the plot of $\log \sigma_{tot}$ vs T, the absolute a.c. conductivity is proportional to T in the high temperature regime (T > 200K). This can be deduced from the empirical law describing the effect of fluctuations on the total conductivity:

$$\frac{\sigma_m}{\sigma_b} \propto C_0 (\omega \tau_b)^s \tag{5.9}$$

where s follows the empirical law s = 1- $\frac{T}{T_0}$.

Here C_0 is the concentration of high conductivity regions and $\omega\tau_b$ is the reduced angular frequency.

Substituting equation (5.8) in equation (5.9), gives:

$$\sigma_m = C_0 \sigma_0 exp\left(\frac{-E_0}{k_B T_0}\right)\left(\frac{\omega \epsilon_b \epsilon_0}{\sigma_0}\right)^{1-\frac{T}{T_0}} \tag{5.10}$$

This gives;

$$\log \sigma_m = A + \log B\omega - \frac{T}{T_0}\log B\omega \tag{5.11}$$

where A = $\log(C_0\sigma_0) - \frac{E_0}{k_B T_0}$ and B = $\frac{\epsilon_b \epsilon_0}{\sigma_0}$

Equation (5.11) shows that at constant frequency $\log \sigma_m$ is proportional to T. After fitting the equation to the data the values of T_0 and the other parameters can be deduced. T_0 is considered here to be the point at which the conductivity is

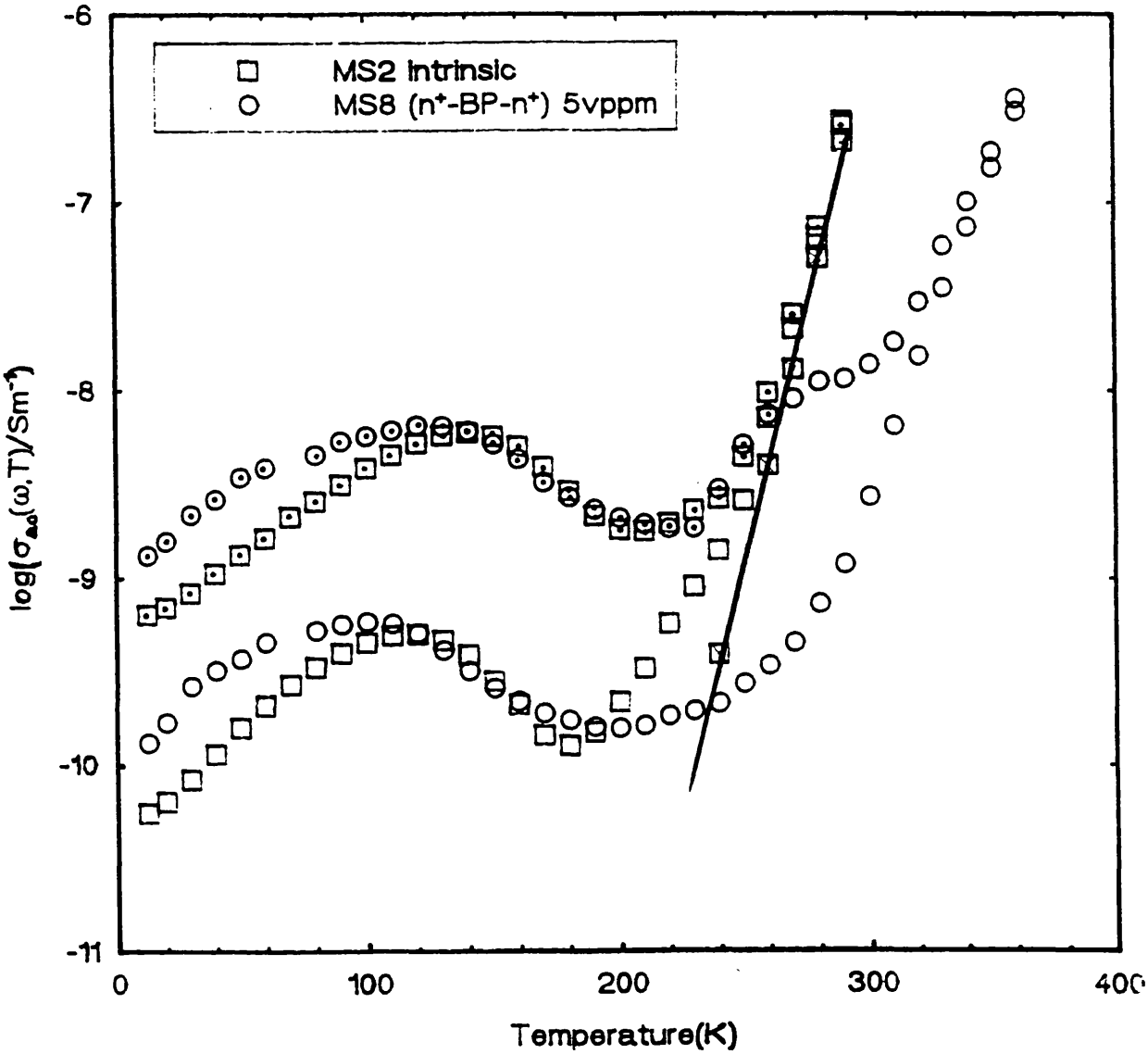

Figure 5.16: Comparison of the temperature dependence of the conductivity of an intrinsic (MS2) and a compensated (MS8) D_c= 5vppm samples. ⊙ and ⊡: 2kHz, o and □: 210Hz, the corresponding d.c. conductivitty is fitted with a linear relation.

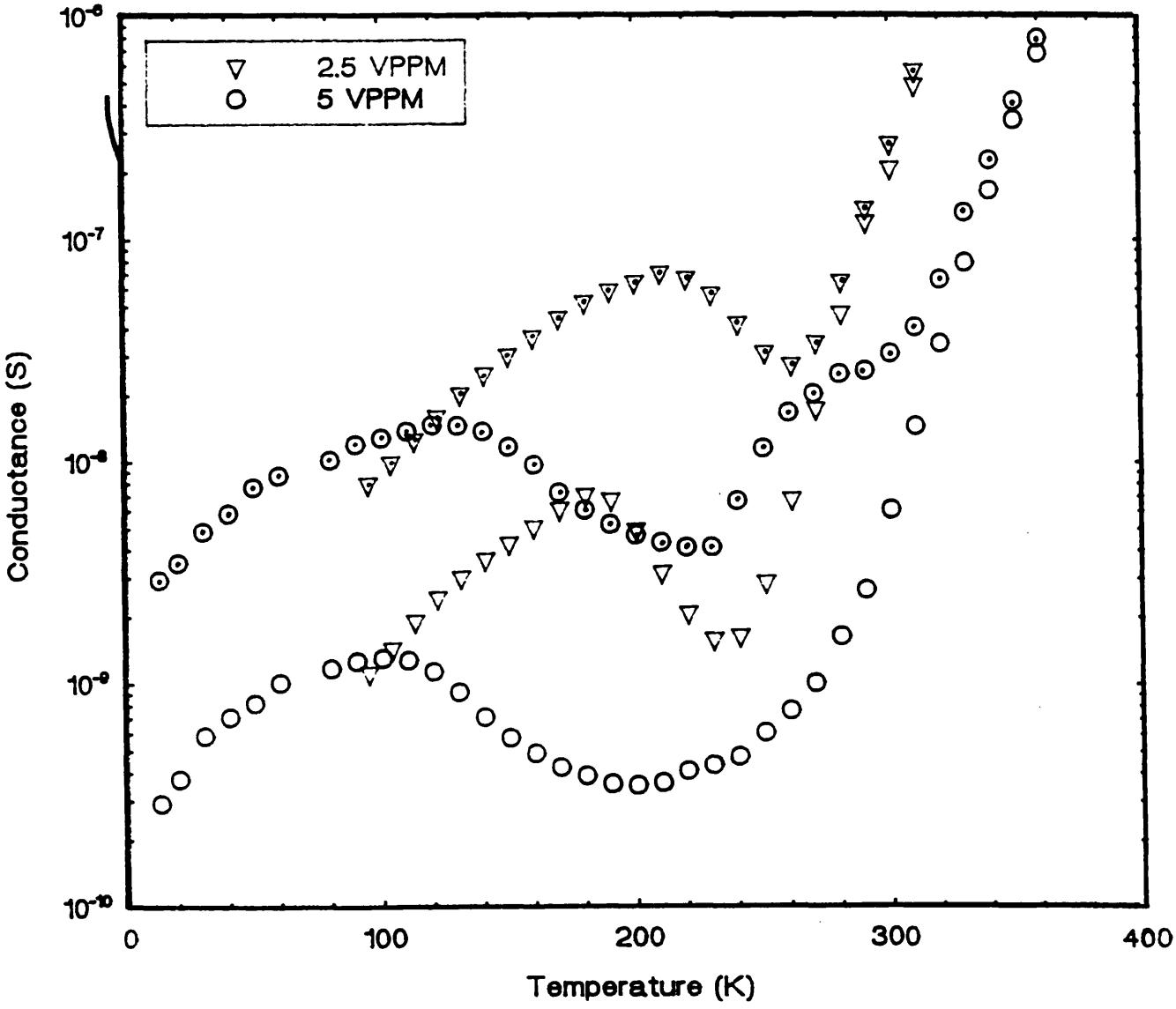

Figure 5.17: Comparison of the temperature dependence of the conductivity of two compensated samples (MS3) D_c= 2.5Vppm and (MS8) D_c= 5vppm. ⊙ and △: 2kHz; o and △: 210Hz.

independent of the frequency. At this point when
T = T_0 the equation (5.10) can be written as:

$$\log \sigma_m = \log C_0\sigma_0 - \frac{E_0}{k_B T} \tag{5.12}$$

Knowing the values of E_0 and σ_0 from the graph of $\log \sigma_b$ vs $\frac{1}{T}$, then the product $C_0\sigma_0$ can be found.

In our analysis, we eliminated the effect of the n^+-layers by extrapolating the loss at high temperatures (T>190K) below the peak, as we can see there is still a significant contribution to the total loss which we believe is not due to the injecting contacts but it is due to the inhomogeneous regions present in the compensated sample. Because of the presence of the secondary peak in the 2kHz curve, the data cannot be fitted with the equation (5.11). The reason for the differences observed is probably due to the distribution of the inhomogeneous regions in these samples being not exponential as assumed theoretically. There is no reason in principle why one should not use a different distribution. This secondary peak is difficult to explain on any physical grounds and we believe it is unphysical. The overall conclusion, is that we can confirm the existence of such inhomogeneities in the compensated samples and that they contribute significantly to the loss at high temperatures. The drift mobility measurements on these samples showed a fluctuation amplitude of the order of 0.1eV. From fig.(5.9), we believe that the undoped material is less effected by these long-range potential fluctuations than the compensated a-S:H.

5.2 Sputtered a-Si

5.2.1 D.C. Conductivity.

The temperature dependence of the dark d.c. conductivity at temperature below 77K for a magnetron sputtered a-Si is illustrated in fig.(5.18). It is apparent from the data that it follows the $T^{-1/4}$ relation as it would be expected from a variable range hopping system. The value of T_0 was calculated following the method described in

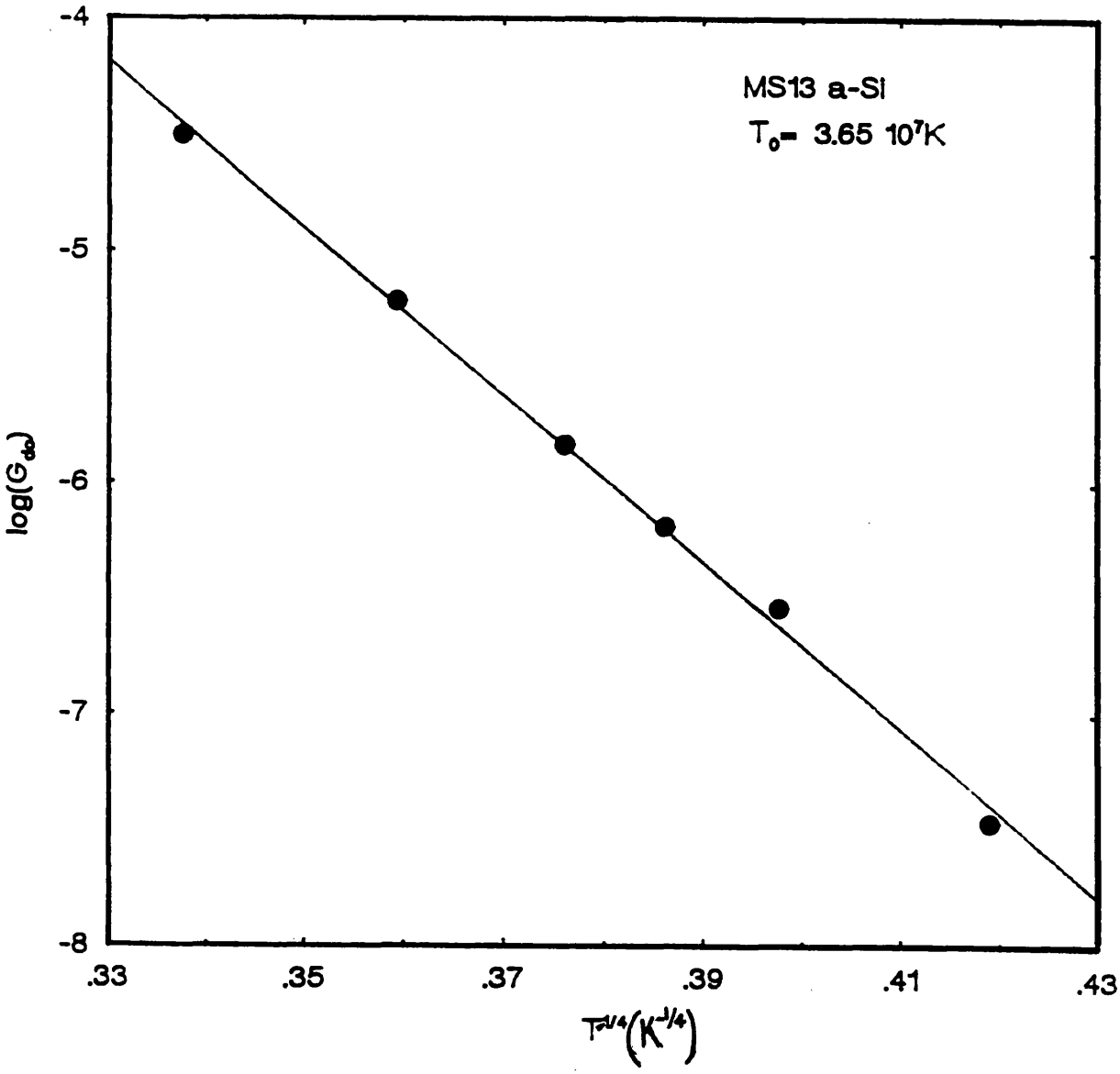

Figure 5.18: Temperature dependence of the d.c. conductivity of a magnetron sputtered a-Si (MS13). The solid lines shows the best linear fit to the low-temperature data.

Long et *al.*(1985) and it was found around $T_0 = 4 \times 10^7$K, which is comparable to previously reported data for the same material (see Long et *al.* 1988a).

5.2.2 A.C. Conductivity.

The a.c. conductivity in these sample was found to be so high that it was not measurable with the manual bridge. Therefore we had to use the HP4274 meter and this restricts the frequency range of measurement (100Hz< ν <100kHz). The data for the frequency dependence of the dark a.c. conductivity at liquid nitrogen temperature is shown in fig.(5.19). The behaviour is qualitatively similar to the glow discharge samples, with the frequency exponent s increasing with decreasing temperature. However, the loss in this type of film is higher (at T >77K, G $\geq 10^{-4}$S) than in the glow discharge material. It can be seen that the d.c. limit is reached at high temperatures as the frequency decreases. Two main processes are believed to be responsible for the conduction in this material. At low temperature, where s is independent of temperature, the conduction is attributed to an electronic tunnelling process which occurs within defect clusters (Long 1982). Whereas in the high temperature region where the d.c. and the a.c. merge together, the transport process is described by a hopping process between defects. These models are well established in the literature (see Long 1982 and Long et *al.* 1988a).

5.2.3 Scaling of the dark A.C. Conductivity.

We have seen in section (2.2.2.3), the Summerfield model predicts that the reduced conductivities $\frac{\sigma_1(\omega)}{\sigma_1(0)}$ should scale to a common reduced frequency $\tilde{\omega}$. The data presented in fig.(5.19) is plotted in fig.(5.20) in reduced form with $\tilde{\omega} = \frac{\omega e^2 \alpha}{k_B T \sigma_1(0,T)}$. (The different parameters are defined in chapter 2). The scaling relationship is satisfactorily obeyed. We should emphisize that only one parameter, the inverse decay length α^{-1} of the wavefunction, needs to be chosen arbitrarily in order to plot the data in this reduced form. Also in this graph we plot the prediction of the EPA theory. The

Fig.5.19

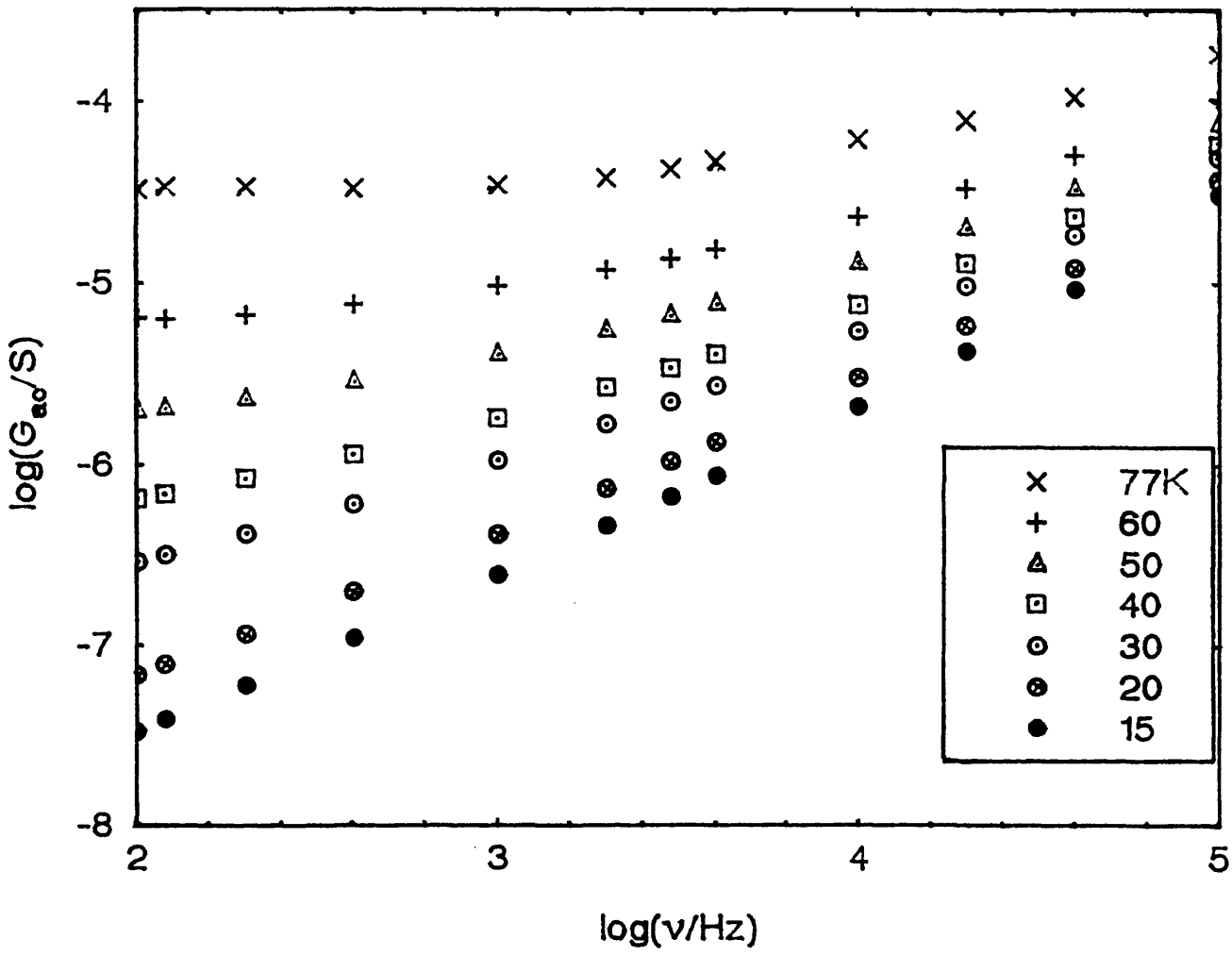

Figure 5.19: The frequency dependent conductivity of a magnetron sputtered a-Si. The appropriate temperature for each set of data is indicated in the graph.

scale on the abscissa was set by making a suitable value of α^{-1}. It can then be seen that the theoretical curve (EPA) passes through the data. The value of α^{-1} used was $\approx$1.2nm. This value is in good agreement with previous results reported by Balkan et *al.*(1985) and (1988a) for similar material prepared by the same technique.

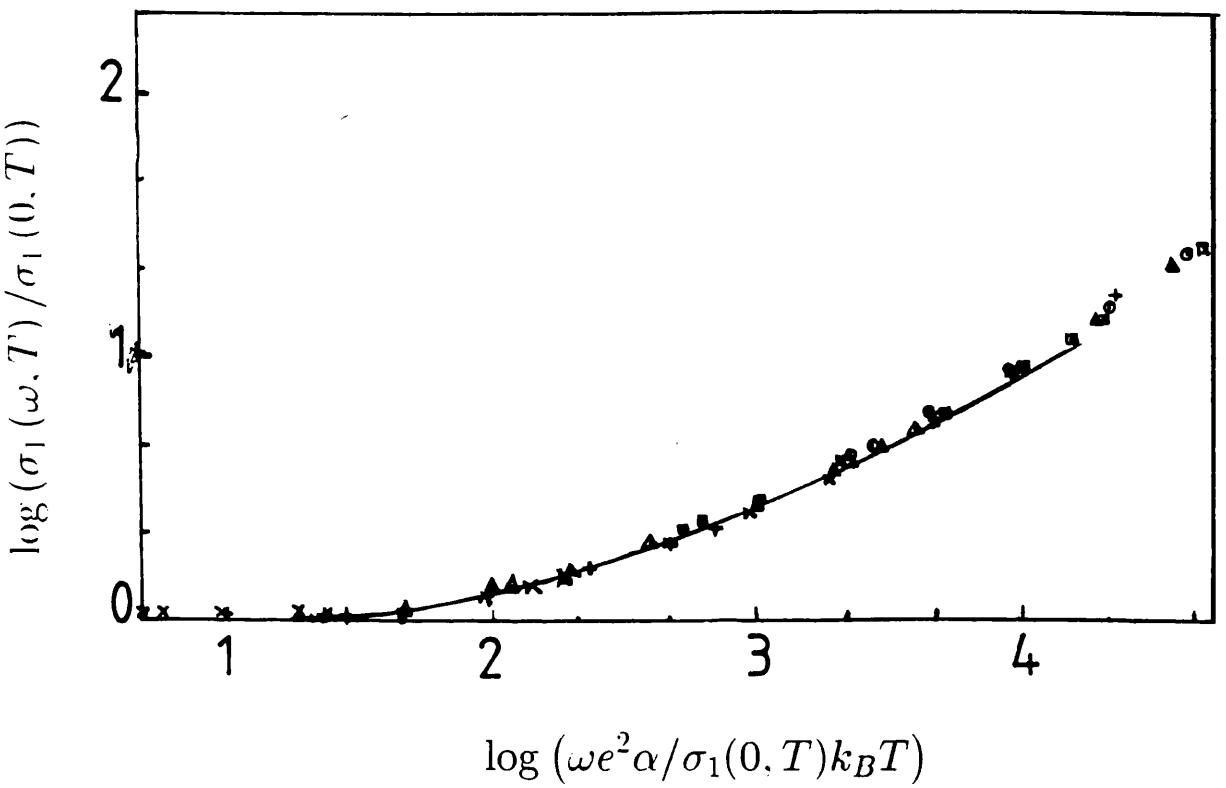

Figure 5.20: Data of fig.(6.19) in scaled form using the same symbols. The solid line is the prediction of the extended pair approximation.

Sample	Compensated D_c(vppm)	$\epsilon_c - \epsilon_f$ (eV)	$\sigma_{ac}(\omega, T)$/nSm $^{-1}$ at 240K, 2kHz	$\sigma_{ac}(\omega, T)$/nSm^{-1} at 240K, 210Hz	σ_0 Scm^{-1}
MS2	0	0.68 ± .01	2.6	1.38	208
MS3	2.5	0.71 ± .02	9.85	.386	970
MS7	0	0.58 ± .01	6.93	5.22	205
MS8	5	0.80 ± .03	2.95	.21	1631
MS18	0	0.66 ± .01	-	-	-
Shimakawa et *al.*	0	-	98	32.4	-

Table 5.1: The Fermi level energy, the a.c. conductivity at two frequencies and the prefactor σ_0.

CHAPTER 6

Scaling of the Low-Temperature Photoconductivity

Introduction

In the following a description of the d.c. and a.c. photoinduced losses for both glow discharge a-Si:H and R.F. sputtered a-Si is given, together with their intensity and temperature dependences. The scaling of the low temperature photoconductivity for different intensities of illumination is introduced and then a discussion of the observed results in the light of the existing models is given.

The sample was illuminated in the way described in section (4.4). The measurements were performed between 4.2 and 50K. Both parameters of the sample (capacitance and conductance) showed an increase when the light was applied.

At low intensities (below few μWcm^{-2}) the capacitance and conductance increase very slowly. It takes the sample several thousands of seconds to reach saturation depending on the intensity and the temperature. At high intensities however, the steady state value is reached within seconds. After the removal of light, the loss decreases. It showed a fast decay then slows down towards the dark value. At low temperature (T< 12.5K) the dark value is never reached unless the majority of the traps are emptied by raising the temperature.

6.1 Glow Discharge Samples.

6.1.1 D.C. Photoconductivity.

As we have seen in the previous chapter, the dark d.c conductivity at low temperatures was indetectable below 190K. However, when the sample is excited with a continuous illumination from a He-Ne laser, the d.c. photoconductivity increases by orders of magnitude depending on the intensity of illumination and temperature and becomes measurable. The results for an intrinsic and a compensated samples measured at 13K are shown in fig.(6.1) and in fig.(6.2) respectively. Here we plot the d.c. photoconductivity ($\sigma_1(0,I)$) against the intensity falling on the sample (I) in the log-log form. It can be seen that the relation is linear ($\sigma_1 \propto I^\gamma$ with $\gamma \approx 1$). This result is in agreement with previous measurements (see Long et *al.* 1988b and Hoheisel et *al.* 1983). As the temperature increases, γ decreases. This is illustrated in fig.(6.3) for an intrinsic sample measured at various temperatures. In fig.(6.2) the two compensated samples have different thicknesses, but the d.c. photoconductivities are the same. This suggests that the induced loss is due to the bulk material and any contribution from the surface edge or the formation of a barrier at the surface is almost negligible. It is worth mentioning here that the magnitude of our d.c. photoconductivity at various temperatures is much higher than that reported by Johanson et *al.*(1989), (see table 6.1). This indicates higher mobility in our samples.

6.1.2 A.C. Photoconductivity.

The frequency dependent photoconductivity was measured after the sample was illuminated with light from a He-Ne laser ($h\nu \approx$1.96 eV) and allowed to reach equilibrium. The experiment was done at either constant temperature and varying the intensity falling on the sample or vice-versa. We shall consider the different measurements in the next sections.

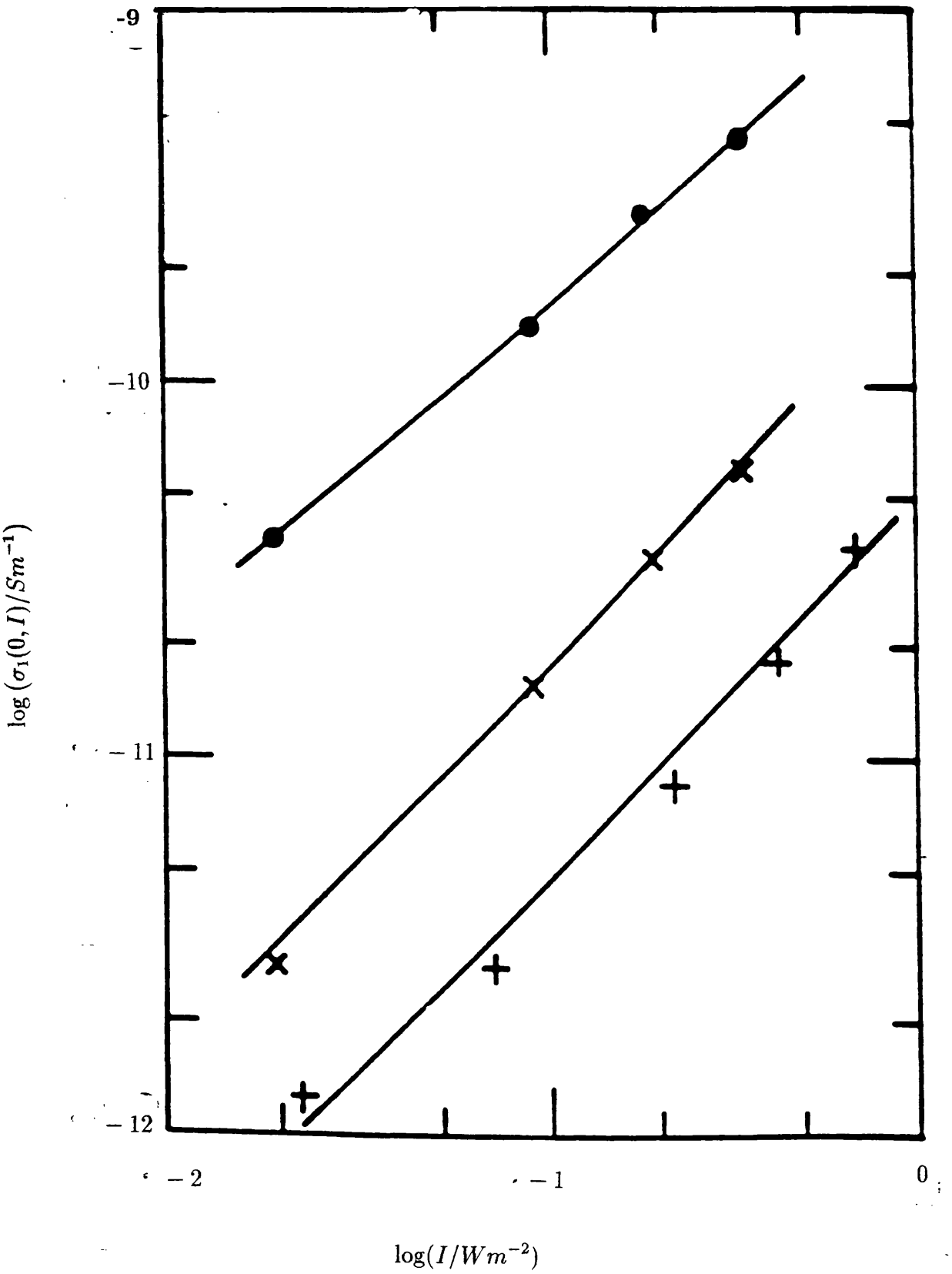

Figure 6.1: The intensity dependence of the d.c. photoconductivity for two samples. ×: intrinsic (MS2) at 12.5K, •: intrinsic at 50K and +: compensated (2.5vppm) (MS3) at 12.5K.

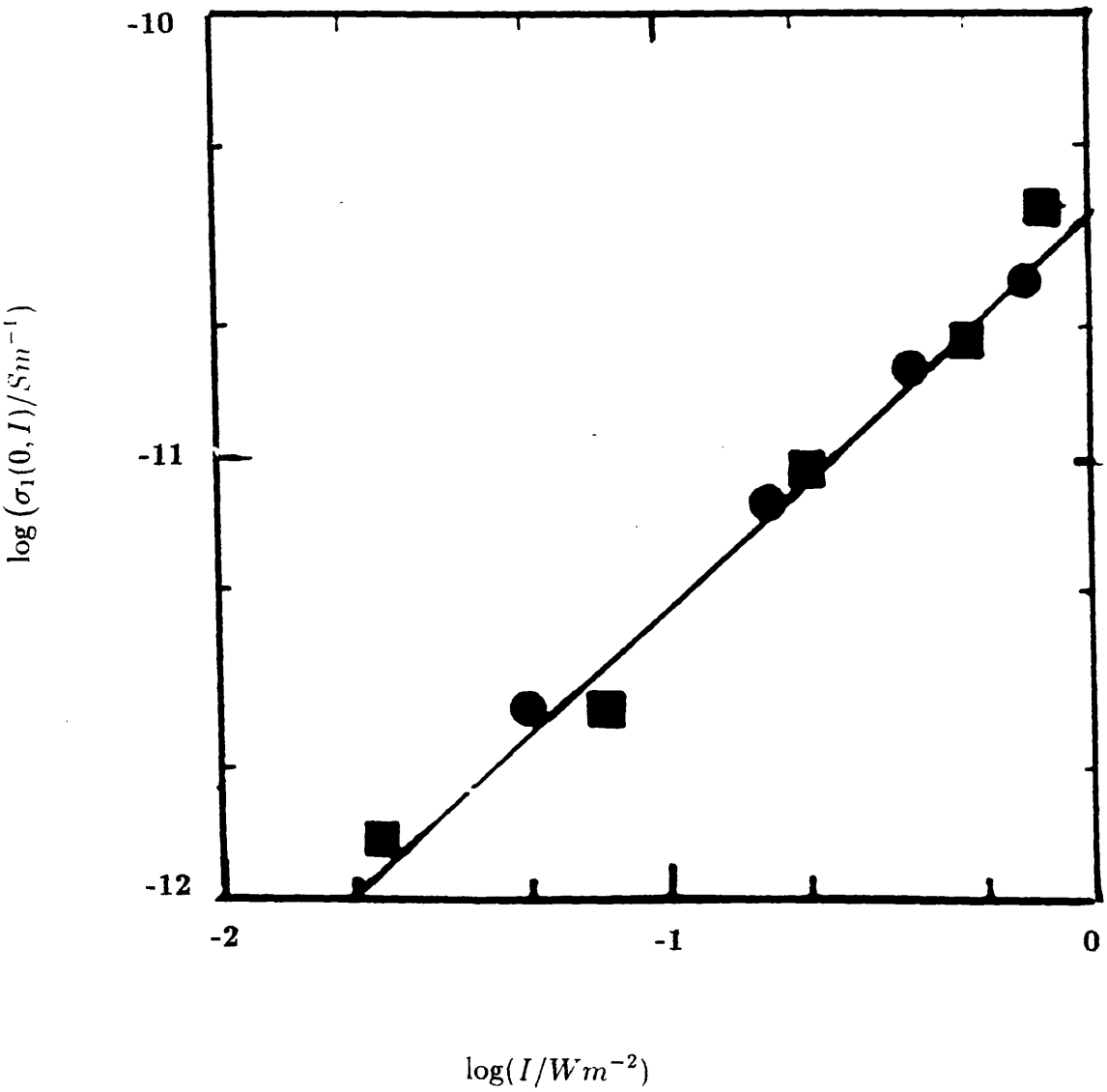

Figure 6.2: The intensity dependence of the d.c. photoconductivity for two compensated samples: ■: 2.5vppm and •: 5vppm, measured at 12.5K.

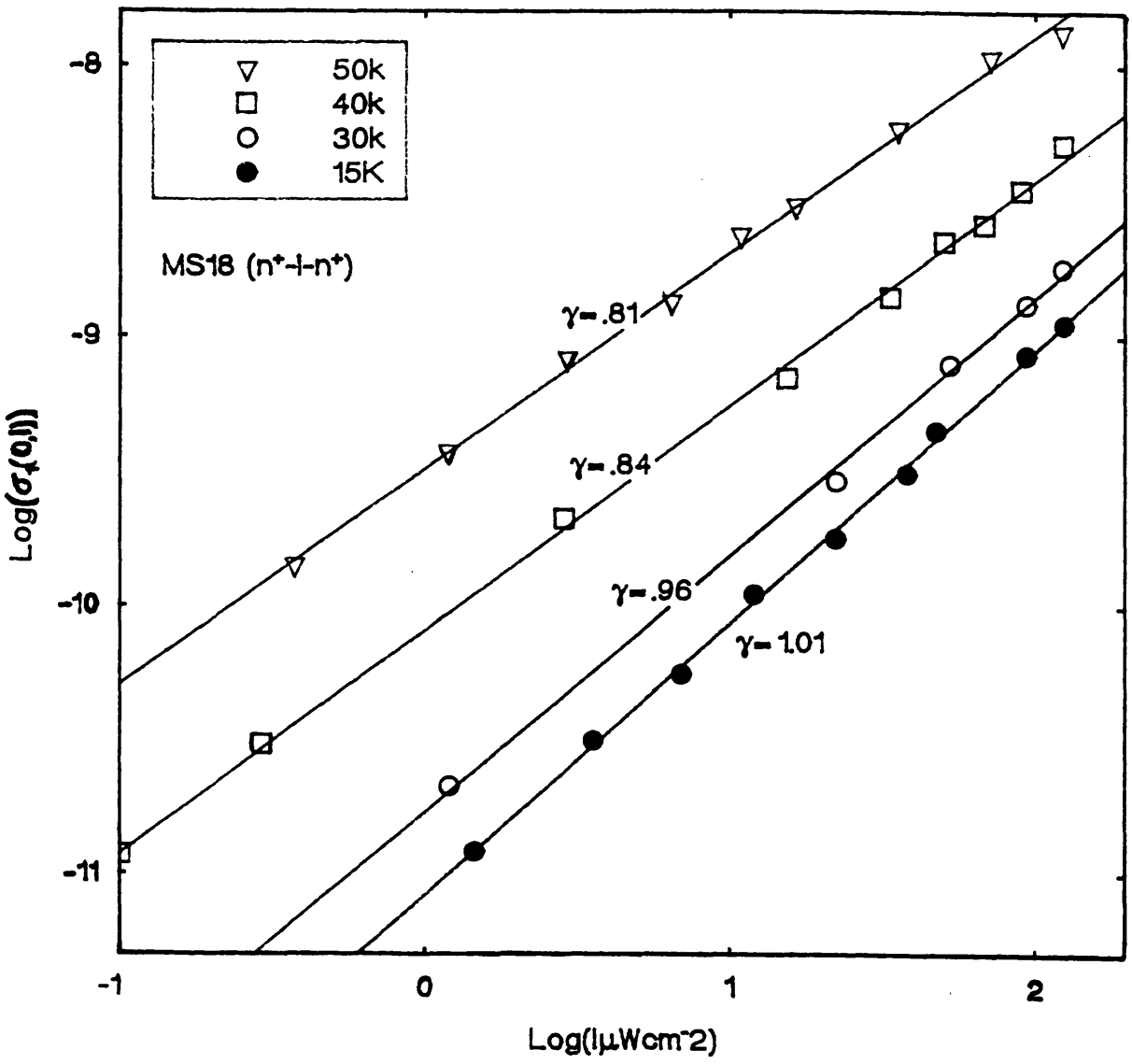

Figure 6.3: The intensity dependence of the d.c. photoconductivity for an intrinsic sample (MS18) at various temperatures. The appropriate temperature is given in the graph.

6.1.2.1 Frequency Dependent Photoconductivity.

The frequency dependences of the photoconductivity $\sigma_1(\omega, I)$ for an intrinsic and a compensated sample with a compensated doping level of 2.5vppm are shown in fig.(6.4) to (6.6) respectively. Here we kept the temperature constant and varied the intensity falling on the sample. The behaviour is similar for all the samples, with a slightly higher loss in the compensated samples in the low frequency regime. The general behaviour is well established i.e $\sigma_1(\omega, I) \propto \omega^s$ in all the graphs with s increasing slowly with ω. The horizontal lines in all graphs correspond to the equivalent d.c. photoconductivities at the appropriate intensity and temperature. Even at the highest value of excitation intensity the d.c. limit is not reached at 13K. Some of the loss at high frequencies ($\nu \geq 14$kHz) is attributed to the series resistance. This term has an effect on the data and has to be substracted (see section 6.1.3.1).

The photocapacitance behaves in a similar way to the photoconductance. It rises with the excitation intensity, as fig.(6.7) shows. The frequency exponent s was found to decrease with increasing intensity of illumination. As an example, the exponent s under illumination decreases from 0.8 to 0.57 when I changes from 0.018 to 0.34 Wm^{-2} at 12.5K in the case of an intrinsic sample. Similar values were obtained with the compensated specimens. This decrease in s is strong evidence that the a.c. photoinduced loss is different from and independent of the background loss. The increase cannot be ascribed to a thermal effect, but rather to the free carriers being generated by the incident light. The carriers are then trapped in the tail states and start responding to the applied a.c field.

Fig.(6.8) to (6.11) show similar data to fig.(6.4) but at different temperatures. The loss under constant illumination increases with temperature as expected. As the temperature increases, the non-dispersive d.c. limit is nearly reached in the case of 50K. For more clarity, in fig.(6.12) we plot the frequency dependent photoconductivity under constant illumination and varying temperature. This shows that there is a dependence of the real a.c. photoinduced loss on the intensity (in section. (6.1.3.1)

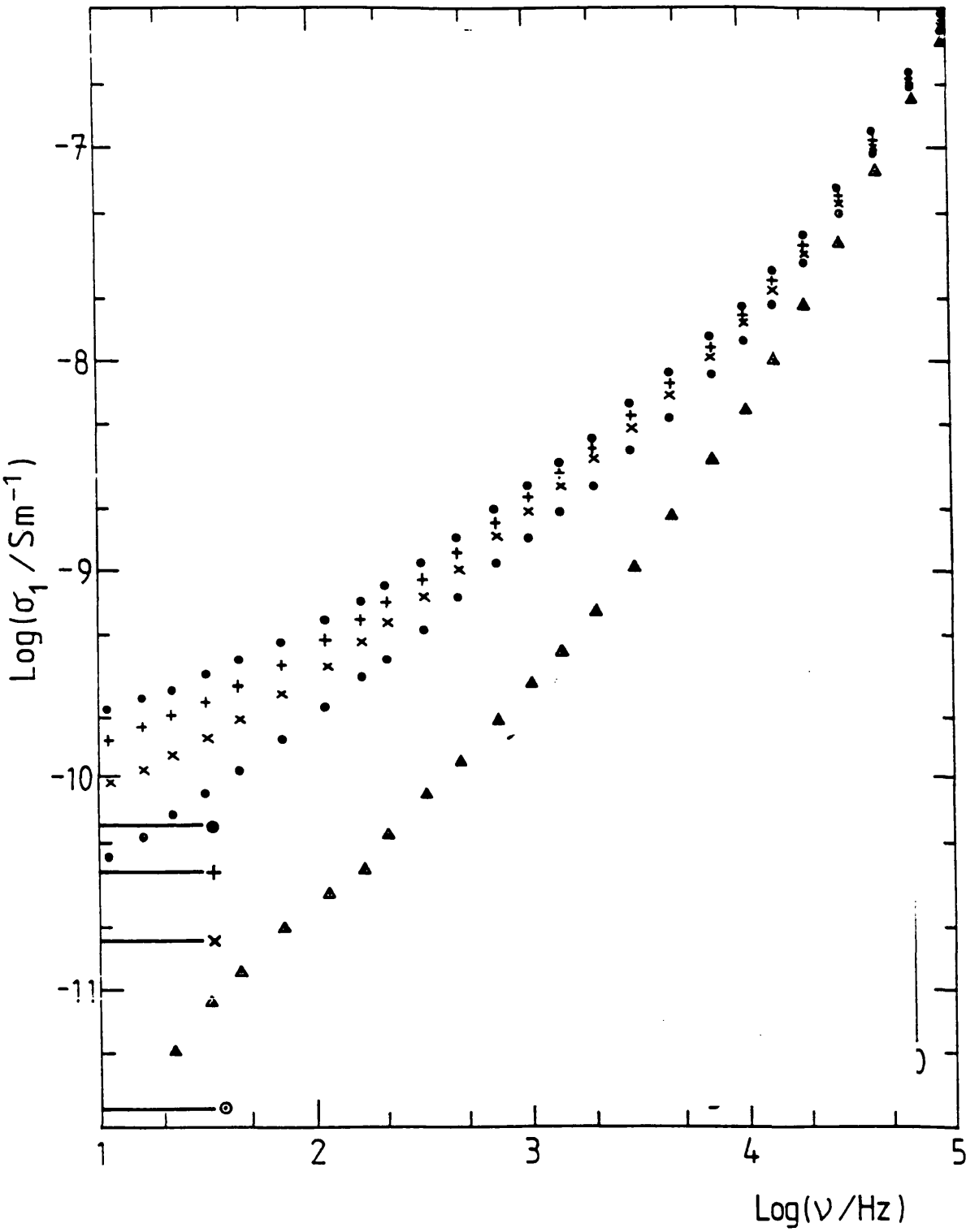

Figure 6.4: Frequency dependent photoconductivity for an n^+-i-n^+ (MS2) at 12.5K. $\triangle$:dark, $\odot$:18mWm^{-2}, $\times$:89mWm^{-2}, $+$:180mWm^{-2}, $\bullet$:340mWm^{-2}. The horizontal lines correspond to the appropriate d.c. photoconductivity. The superlinearity behaviour above 14kHz is due to series resistance.

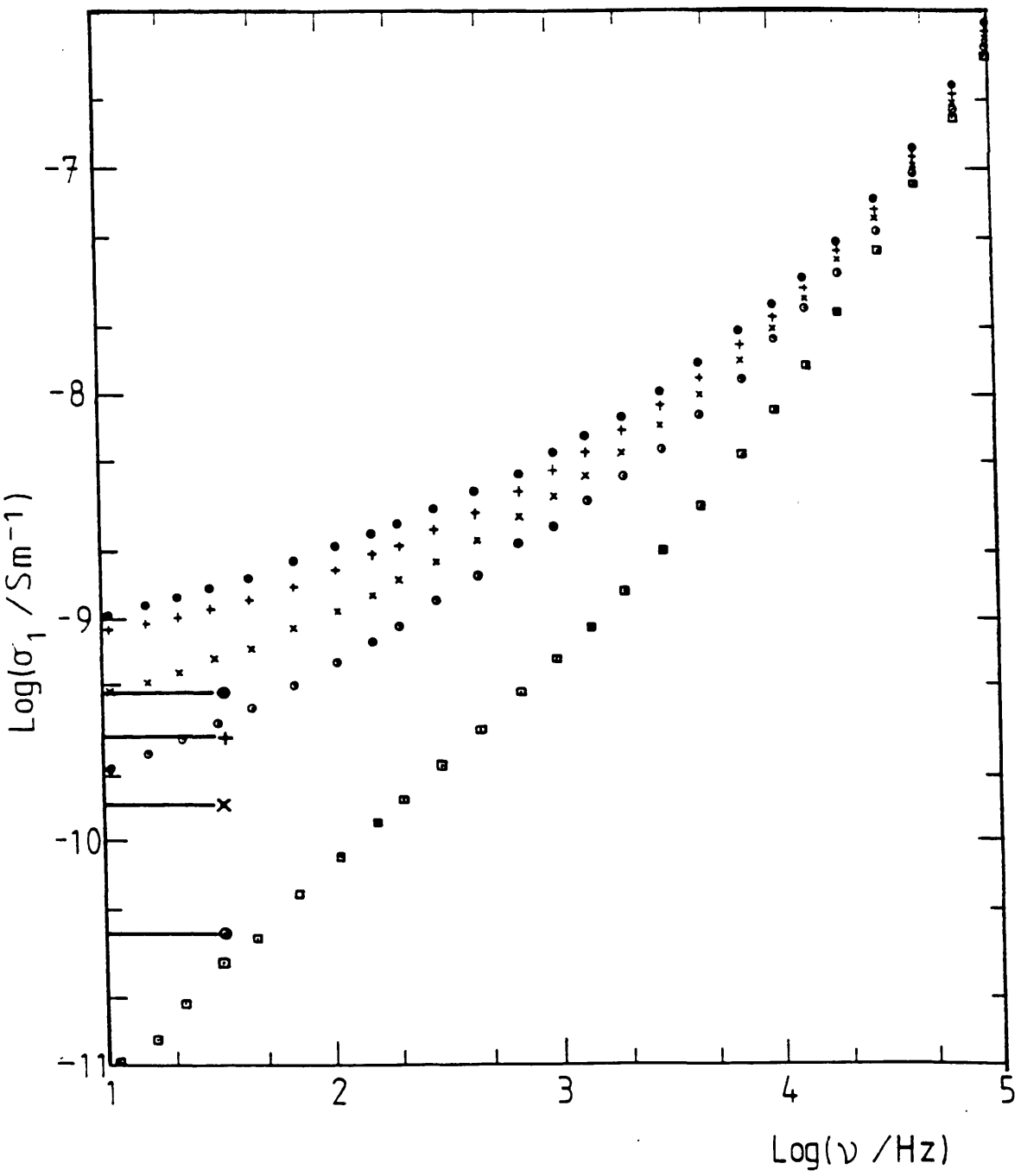

Figure 6.5: Frequency dependent photoconductivity for an n^+-i-n^+ (MS2) at 50K and various intensities. The same symbols as the previous graph. The horizontal lines correspond to the d.c. photoconductivity.

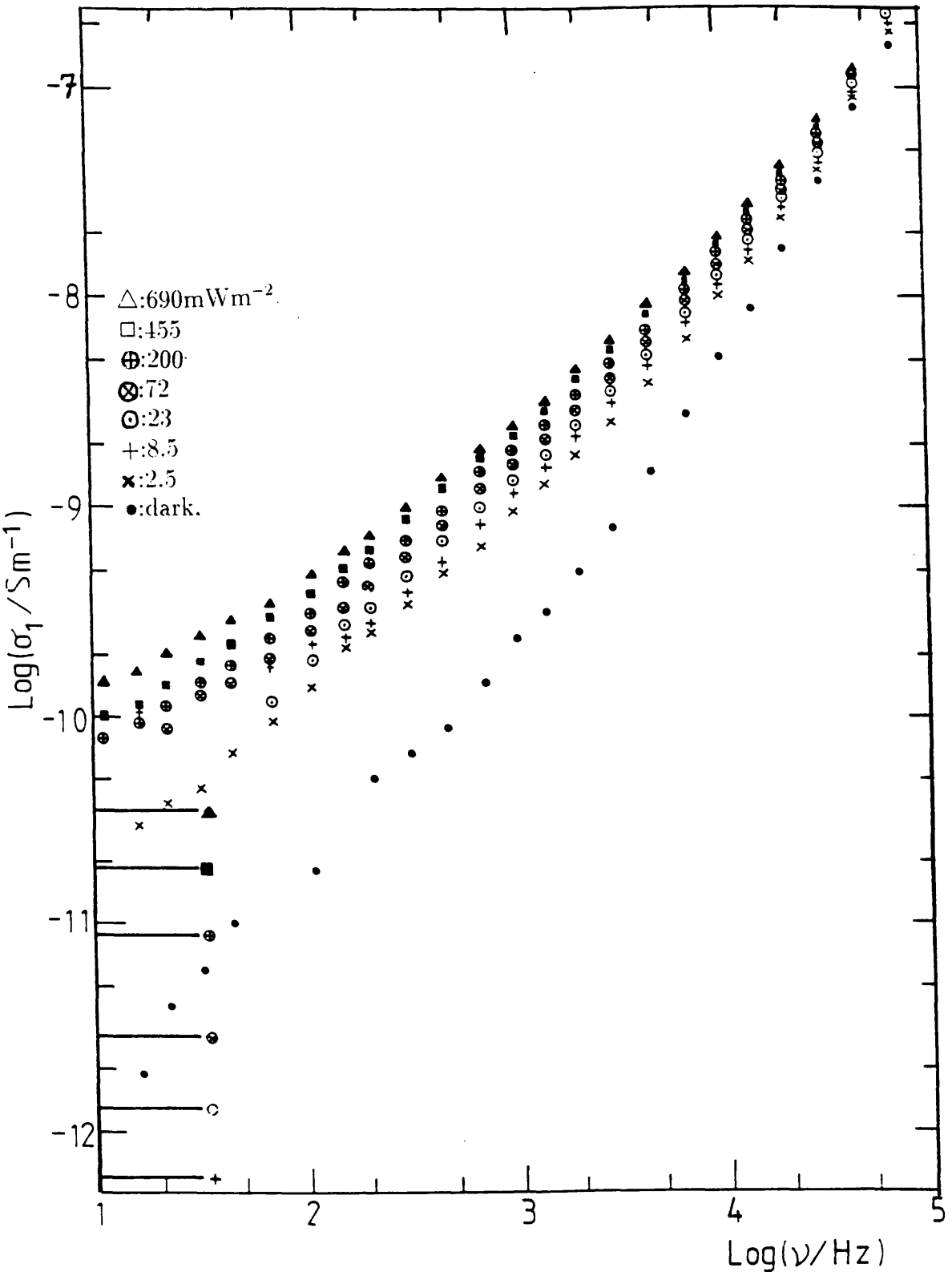

Figure 6.6: Frequency dependent photoconductivity for an n^+-BP-n^+ (MS3) at 12.5K and various intensities. The applied intensity is indicated in the graph. the horizontal lines correspond to the appropriate d.c. photoconductivity.

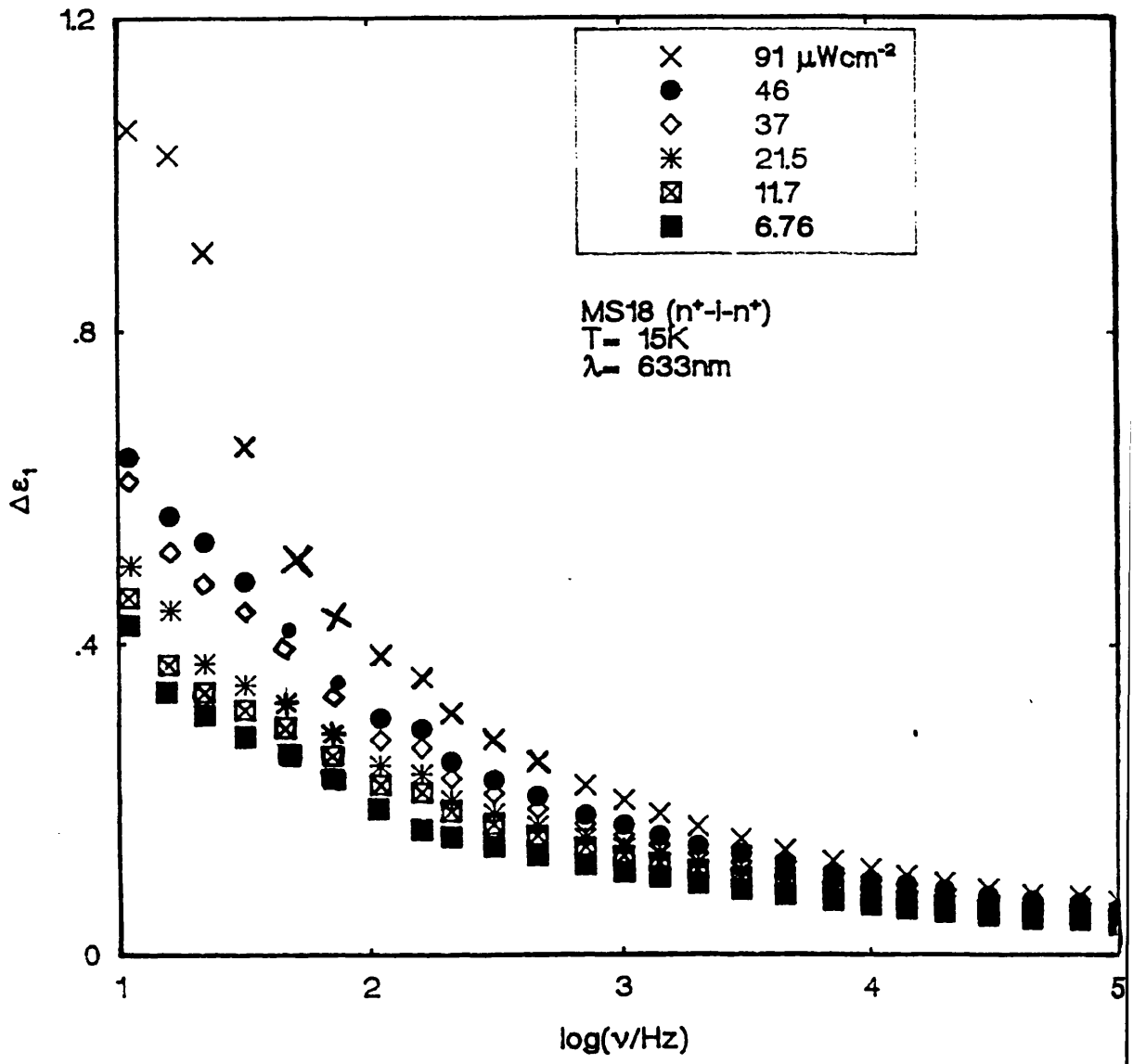

Figure 6.7: Frequency dependent photocapacitance for an n^+-i-n^+ (MS18) at 15K and various intensities. The applied intensity is indicated in the graph.

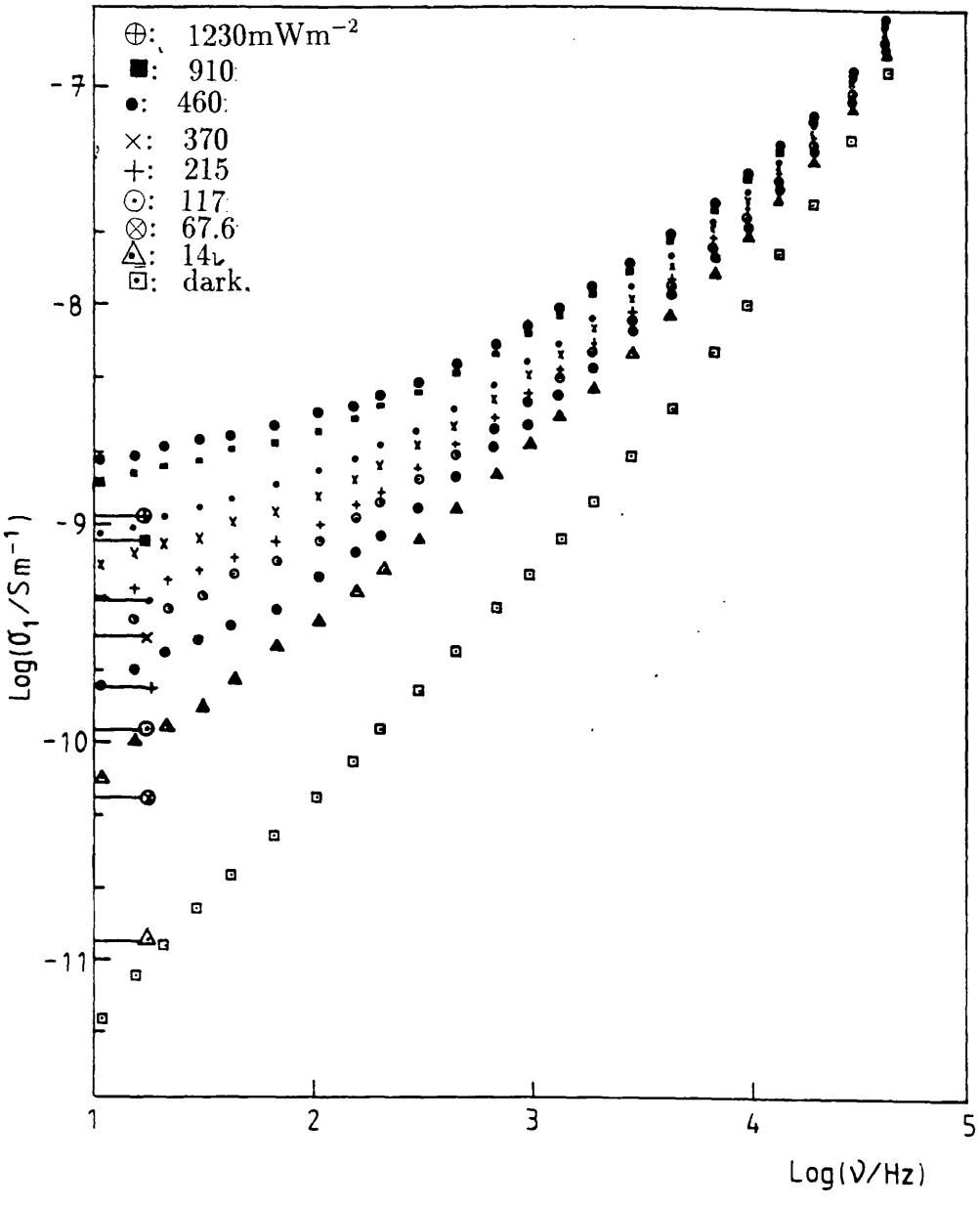

Figure 6.8: Frequency dependent photoconductivity for an n^+-i-n^+ (MS18) at 15K and various intensities. The applied intensity is indicated in the graph. the horizontal lines correspond to the appropriate d.c. photoconductivity.

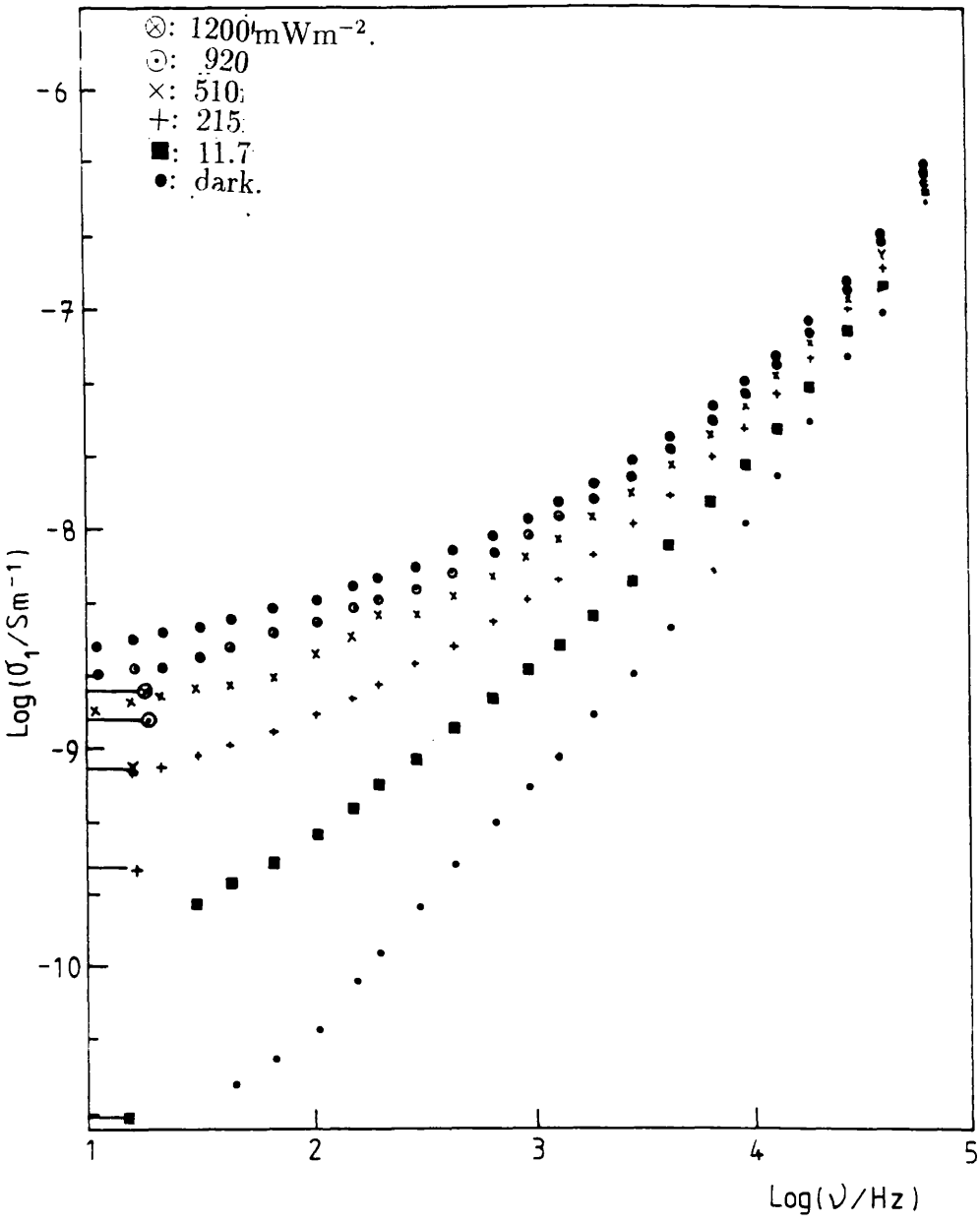

Figure 6.9: Frequency dependent photoconductivity for an n^+-i-n^+ (MS18) at 30K and various intensities. The applied intensity is indicated in the graph. the horizontal lines correspond to the appropriate d.c. photoconductivity.

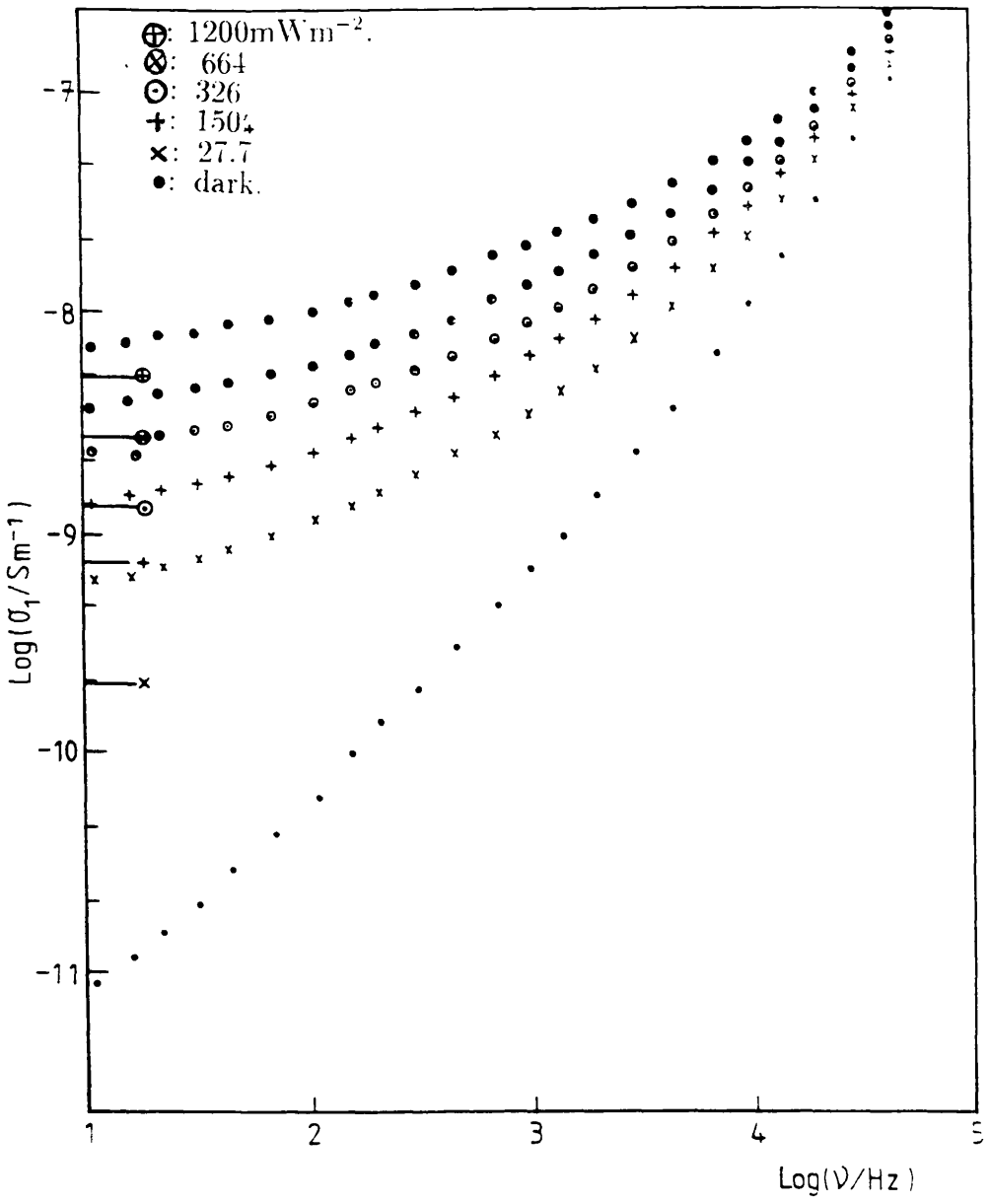

Figure 6.10: Frequency dependent photoconductivity for an n^+-i-n^+ (MS18) at 40K and various intensities. The applied intensity is indicated in the graph. the horizontal lines correspond to the appropriate d.c. photoconductivity.

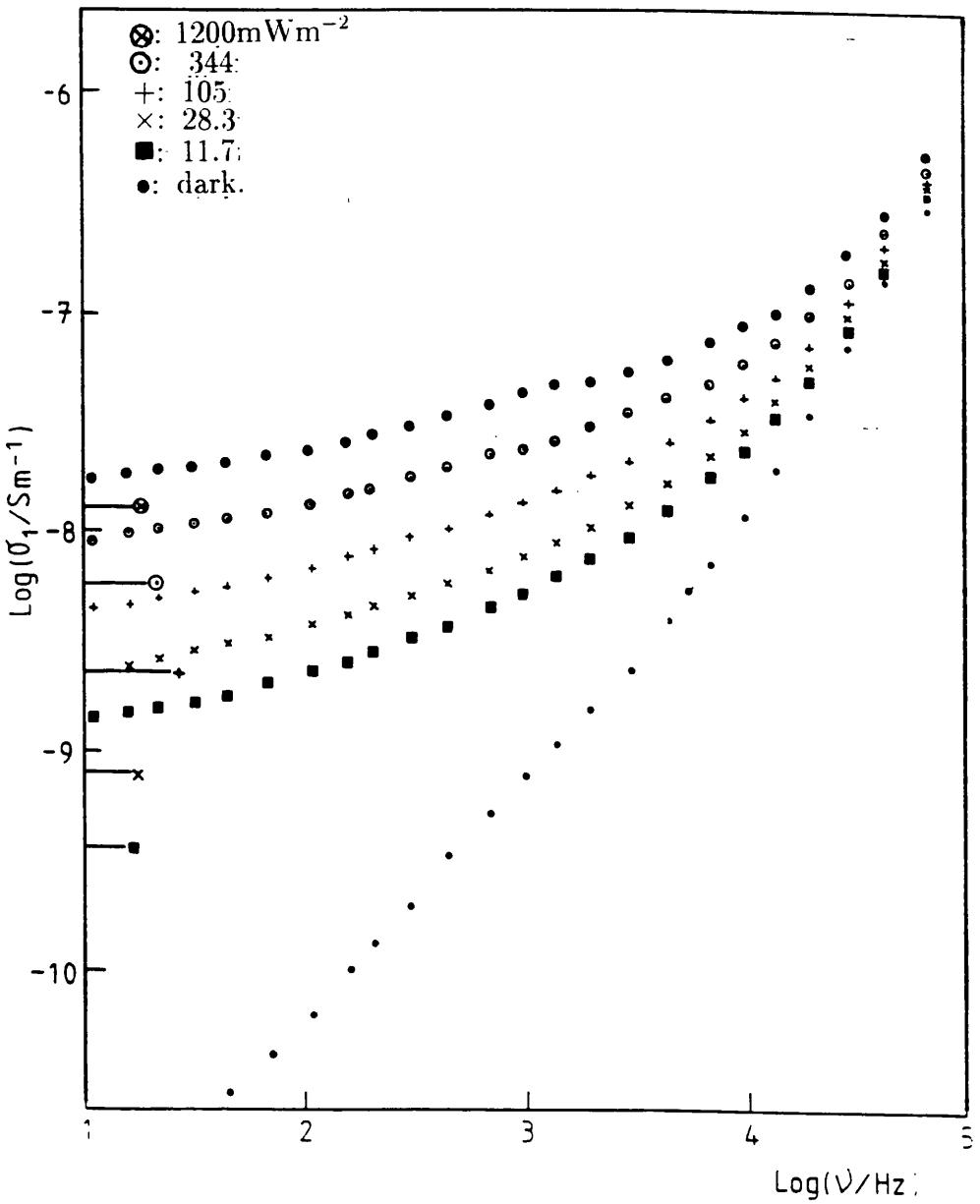

Figure 6.11: Frequency dependent photoconductivity for an n^+-i-n^+ (MS18) at 50K and various intensities. The applied intensity is indicated in the graph. the horizontal lines correspond to the appropriate d.c. photoconductivity.

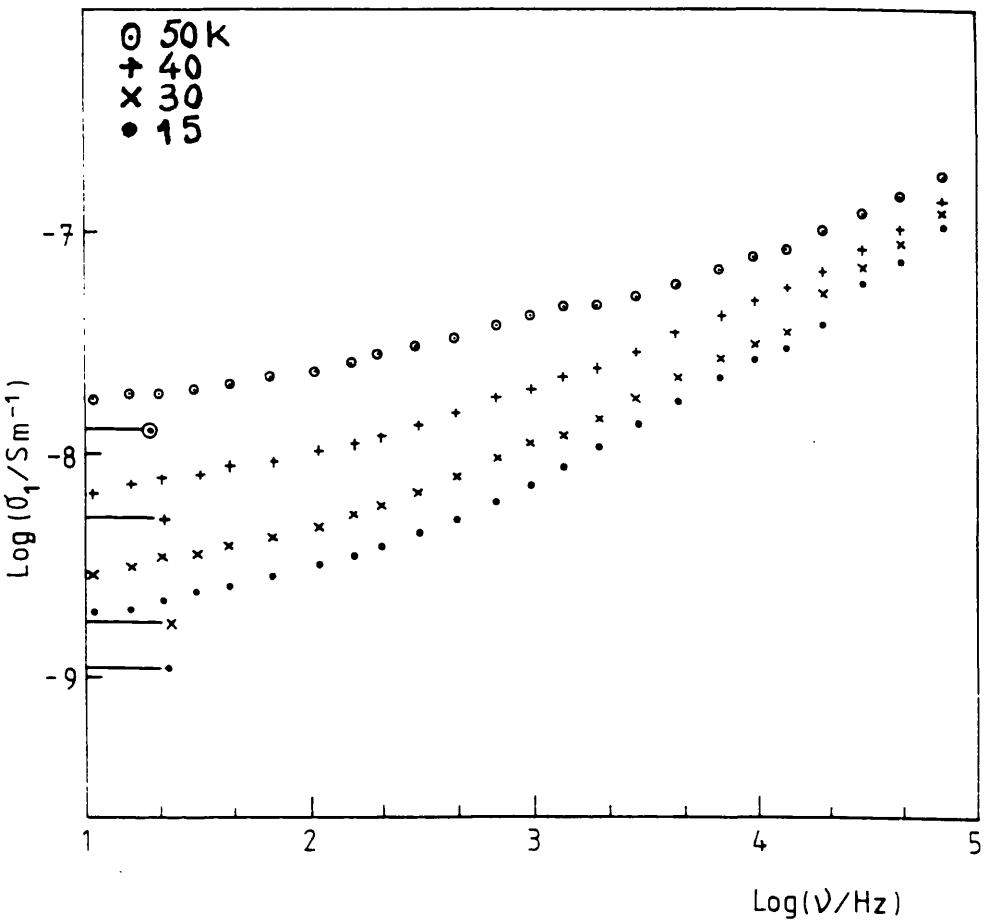

Figure 6.12: Frequency dependent photoconductivity for an n^+-i-n^+ (MS18) at various tempratures and under a constant excitation intensity $120\mu Wcm^{-2}$. The horizontal lines correspond to the appropriate d.c. photoconductivity.

we will explain what is meant by this term) since we have seen in chapter 5 that the dark a.c. conductivity is almost independent of temperature below 100K. However, this dependence is not as strong as for the d.c. photoconductivity (see next section).

6.1.2.2 Intensity Dependence of the Dielectric Constant (ϵ_1).

The change in the relative permittivity as a function of the intensity at 3kHz is plotted in fig.(6.13) to (6.15) for three different samples. The behaviour is similar regardless of the sample characteristics. A power law of the form $\Delta\epsilon_1 \propto I^{\beta}$ is followed, with β around 0.2 at the base temperature (12.5K) independent of the sample when measured under the same conditions. On the same graphs we plotted the equivalent of the imaginary part (a.c. photoconductivity ($\Delta\sigma_1$)). It shows similar behaviour to $\Delta\epsilon_1$. The real and imaginary parts of the dielectric constant are related by Kramer-Kronig transform and hence expected to show similar behaviour. If one takes into account the systematic error associated with the subtraction of the dark a.c. conductivity (which is less well known than the equivalent dark capacitance), then we believe that the data for real and imaginary parts are consistent with a single β value. As the temperature increases α increase slowly, at 50K α increases to around 0.30±.03. On the other hand $\Delta\sigma_1$ rises more strongly with temperature. Fig.(6.16) illustrates the same plots as fig.(6.13) and at various temperatures. The figure shows that the photoinduced loss increases with temperature at all intensities. This behaviour is common with all our samples. This observation is in contrast to what has been observed by Anderson (1989). We attribute this difference in measurements to the sample quality and conditions of preparation. It should be mentioned here that Anderson samples were the same ones measured by Shimakawa et *al.*(1987a). In their intrinsic material, inhomogeneities were very pronounced and as a result, the inhomogeneous model of Long (1989a) fits the data quite well. With our samples however, even the 2.5 vppm compensated sample which is expected to contain such inhomogeneities, only a small contribution has been observed (see Lemmon 1990 and

Fig.6.13

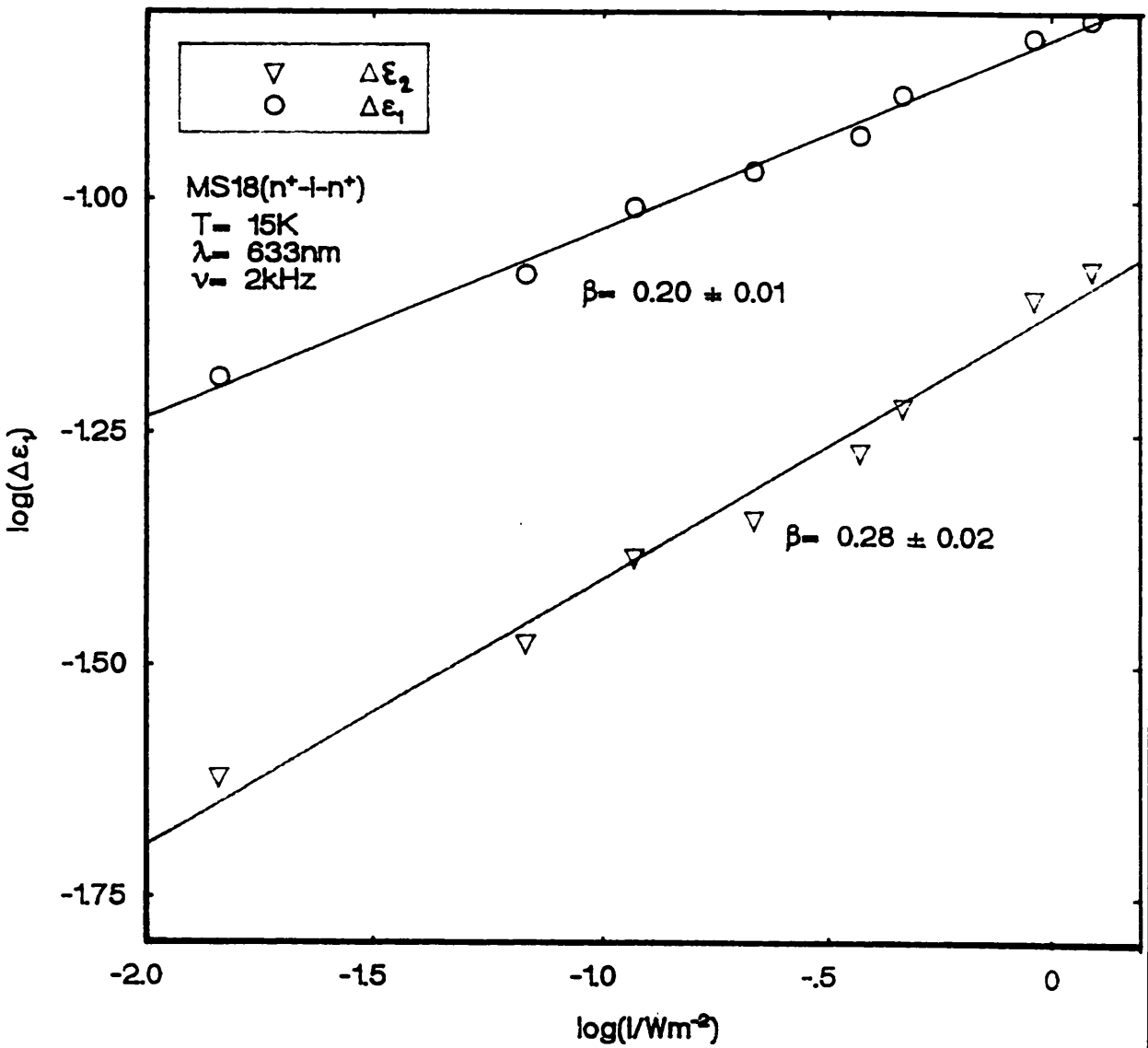

Figure 6.13: The intensity dependence of the real (photocapacitance) and the imaginary (photoconductance) parts of the dielectric constant for an intrinsic sample (MS18). The quoted error values are derived from random errors in data points and ignore systematic error associated with subtraction of dark values.

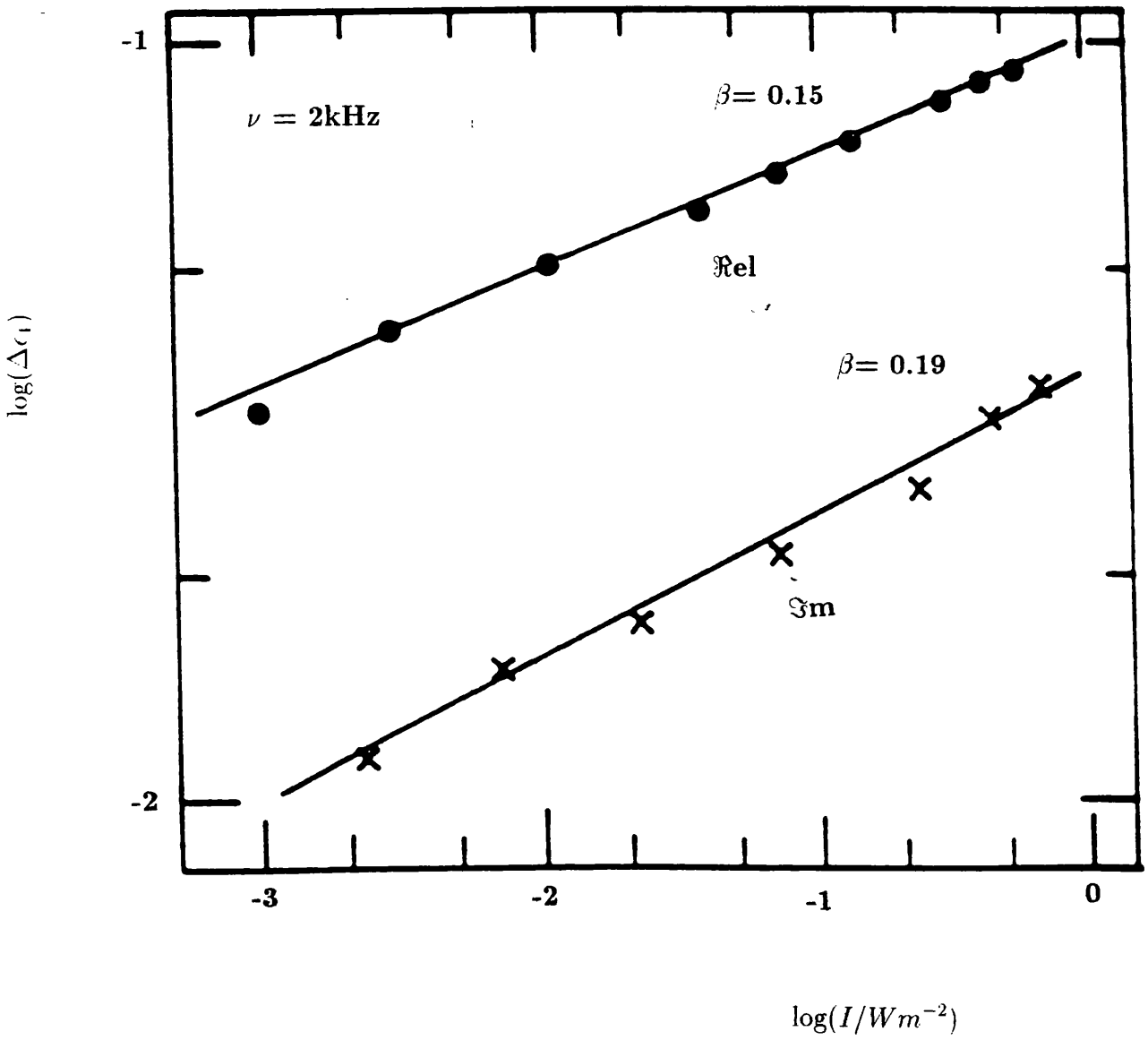

Figure 6.14: The intensity dependence of the real and the imaginary parts of the dielectric constant for an intrinsic sample (MS3).

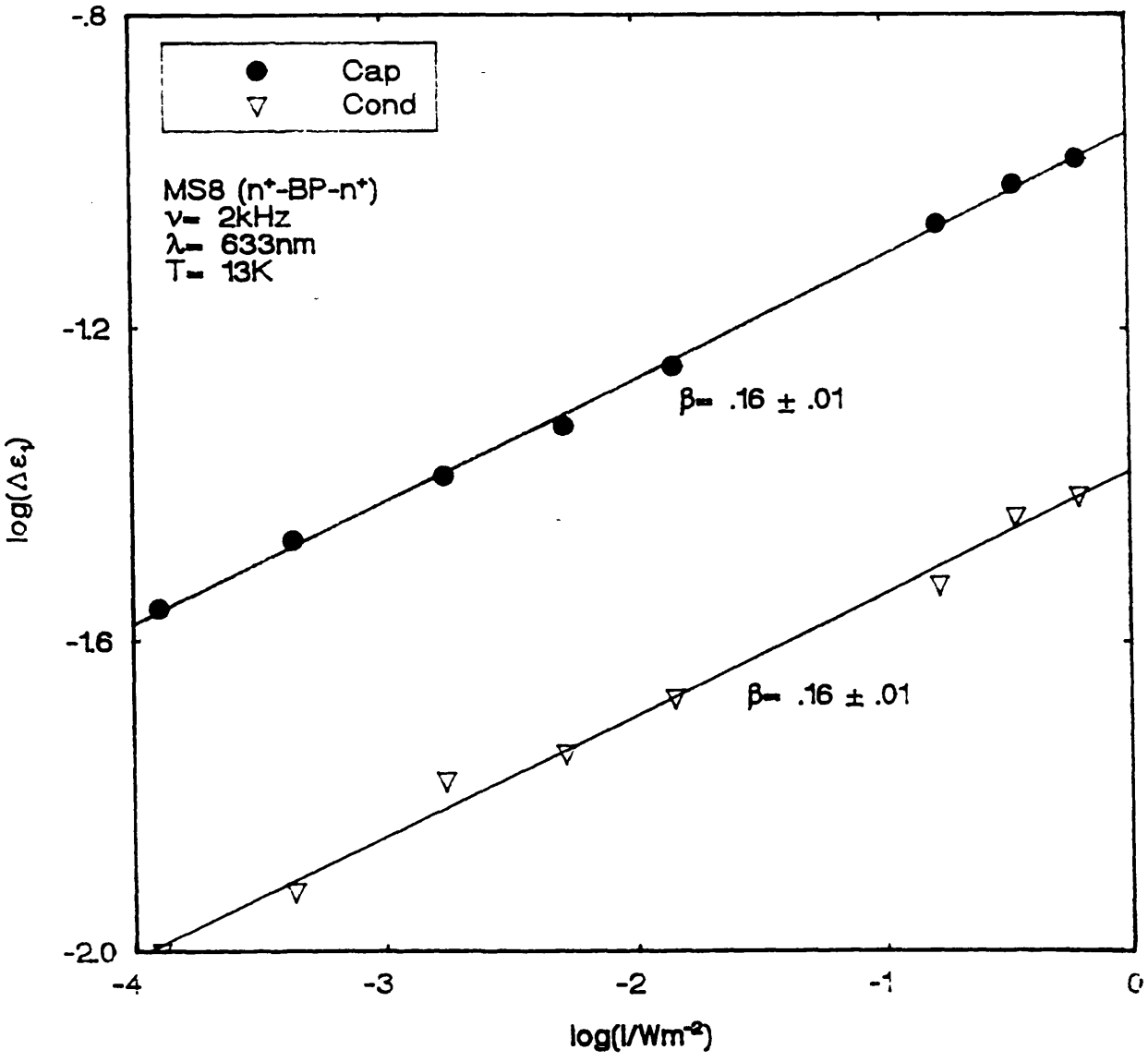

Figure 6.15: The intensity dependence of the real and the imaginary parts of the dielectric constant for an intrinsic sample (MS8).

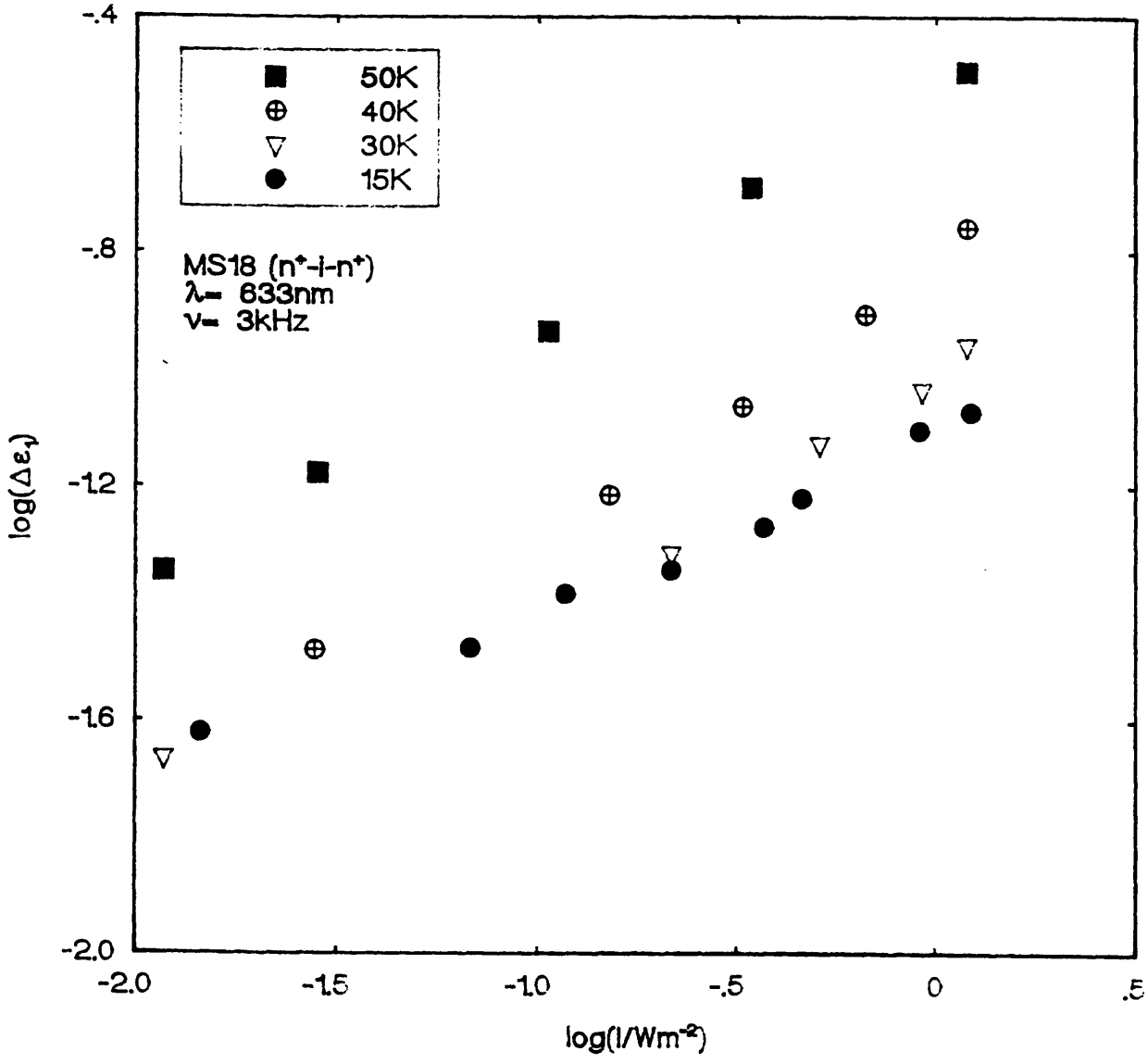

Figure 6.16: The intensity dependence of the relative photoconductivity for an intrinsic sample (MS18) at various temperatures.

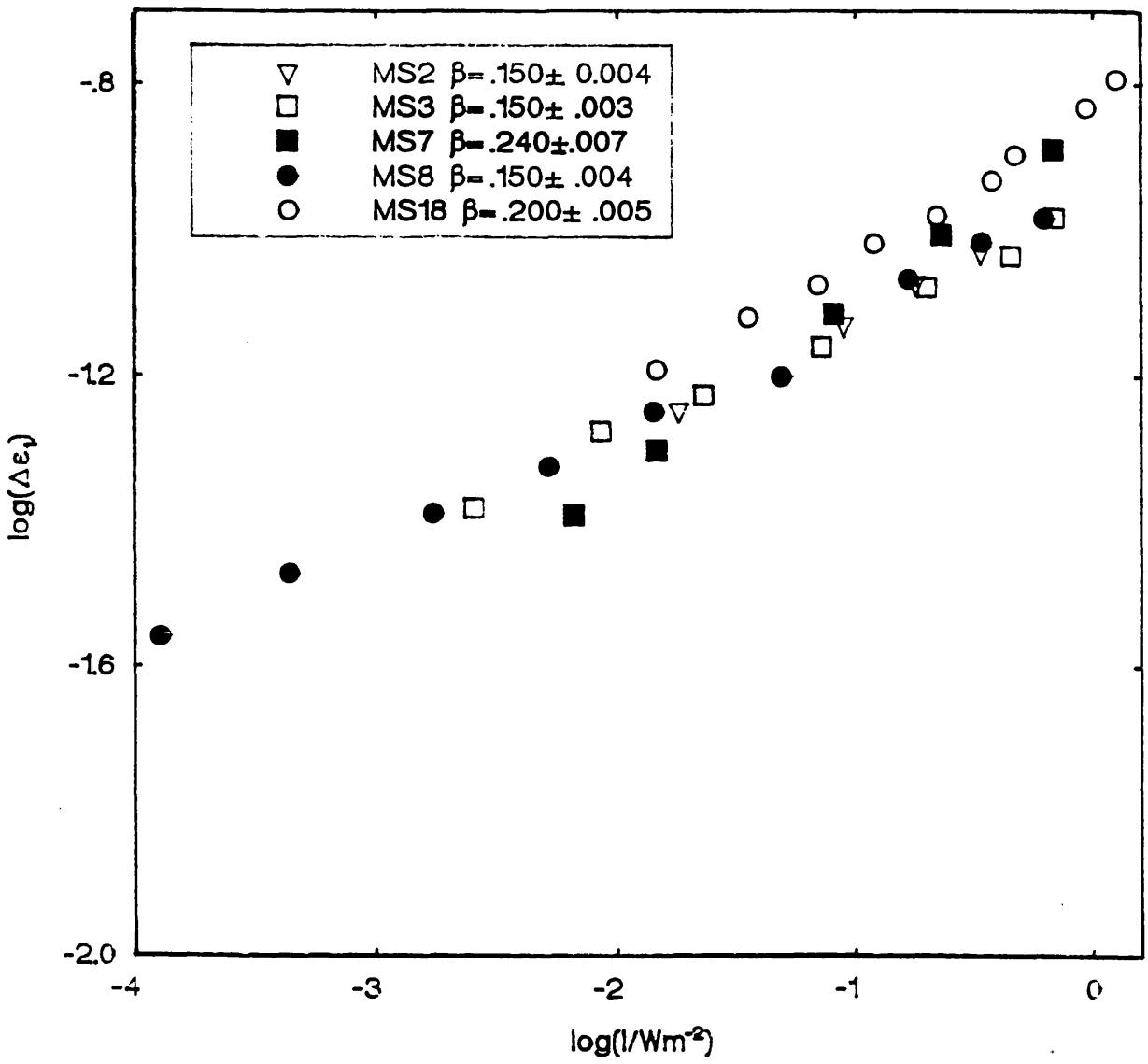

Figure 6.17: The intensity dependence of the dielectric constant of various samples. The intensity exponent for each sample is indicated in the graph.

chapter 5). Another possible reason for this difference in results, is that Anderson samples have low loss (see table 5.1). In fig.(6.17) $\log(\Delta\epsilon_1)$against$\log(I)$ at 13K is plotted for all samples studied during this work. The curves are remarkably similar for all the samples.

6.1.3 Scaling of the Low-Temperature Photoconductivity.

As we have already seen in section. (2.2.2.3), scaling behaviour is well established in the hopping systems. The EPA theory predicts that if the a.c. conductivity at a particular temperature is normalised to the d.c. conductivity, the loss follows a quasi-universal law of the frequency ω normalised to a characteristic frequency ω_c; i.e $\tilde{\omega} = \frac{\omega}{\omega_c}$, where ω_c is given by:

$$\tilde{\omega} = \frac{\omega}{\omega_c} = \frac{\omega e^2 \alpha}{\sigma_1(0,T) k_B T} \tag{6.1}$$

where ω is the angular frequency, α is the decay constant of the localised state wavefunction, e the electron charge, k_B Boltzmann constant and $\sigma_1(0,T)$ the d.c. conductivity. The reason for this scaling behaviour is that in a hopping system, for the infinite DC percolation network there is a critical longest hop with characteristic frequency ω_c; the d.c. hopping conductivity is proportional to this frequency. At frequencies above ω_c only finite clusters will be able to respond to the a.c. field and the conductivity will start increasing with frequency. Generally ω_c is a strong function of temperature, however when frequencies are expressed in terms of ω_c, the aspects of the hopping problem become to a good approximation independent of temperature. Therefore, the hopping curves can generally be plotted as a universal function of $\frac{\omega}{\omega_c}$. This type of scaling has been predicted by a number of theories including the effective medium theory (see Bryskin 1980, Movaghar et *al.* 1980, Butcher and Summerfield 1981 and Summerfield and Butcher 1982), the cluster theories (see Böttger et *al.* 1979 and Fishchuk and Rudko 1980) and macroscopic effective-medium theories (see Springett 1973 and Long 1989). A review of these

different theories is given by Long (1991). The scaling has been observed experimentally in the unhydrogenated and hydrogenated a-Si grown by R.F sputtering by Balkan et *al.*(1985), Long et *al.*(1988a) and for a-Si:H:Au by Long and Hansmann (1990) and in this work for a-Si:H prepared by RF magnetron sputtering technique (see section 5.2.3). The characteristics of the frequency dependence of the dark conductivity were varied by changing the temperature. In this work however, we present a new observation that the photoinduced conductivity of the glow discharge a-Si:H at low temperatures also exhibits a scaling behaviour, with the characteristics being varied by varying the excitation intensity.

6.1.3.1 Correction to the total photoconductivity.

Before presenting the scaling data two corrections were made to the measured photoconductivity $\sigma_1(\omega, I)$. Firstly, the additional contribution to the photoconductivity at high frequencies due to series resistance effect (as we have seen in chapter 5) is removed. The subtraction of this term is done in the same way to the one described in section. (5.1.2). Secondly, the dark a.c. loss has to be removed as well, for this loss occurs in deep states near the Fermi level, as pointed out by Shimakawa et *al.*(1987). After the subtraction of these two terms, we end up with what we call the real photoconductivity $\Delta\sigma_1(\omega, I)$ which is believed to occur in localised band tail states and is given by:

$$\Delta\sigma_1(\omega, I) = \sigma_1(\omega, I) - (\omega C)^2 R_0^2 - \sigma_1(\omega, 0) \tag{6.2}$$

The data we present here is in the form of $\log\left(\frac{\Delta\sigma_1(\omega,I)}{\sigma_1(0,I)}\right)$ against $\log\left(\frac{\omega\epsilon_0}{\sigma_1(0,I)}\right)$, where ϵ_0 is the permittivity of free space and is introduced here in order to give a dimensionless scaled frequency.

6.1.3.2 Scaling of $\Delta\sigma_1(\omega, I)$ at constant temperature.

The data for the intrinsic and compensated samples measured at 13K (see fig.(6.4) to (6.6)) are plotted in fig.(6.18) to (6.20) respectively. The data is reduced in this

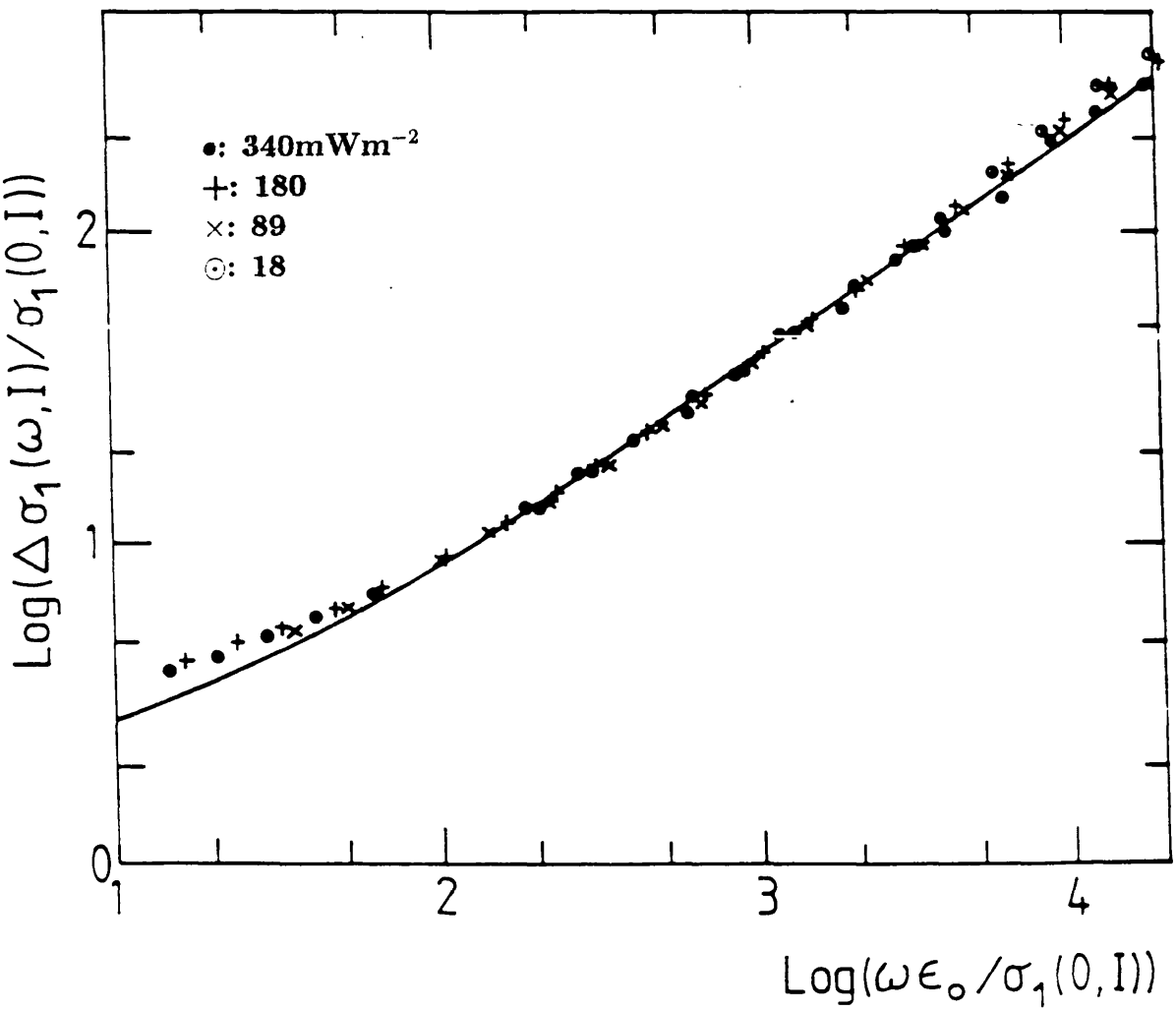

Figure 6.18: The data of fig.(6.4) in scaled form, with the same symbols. Solid line is the prediction of the extended pair approximation with an arbitrary scaled frequency axis.

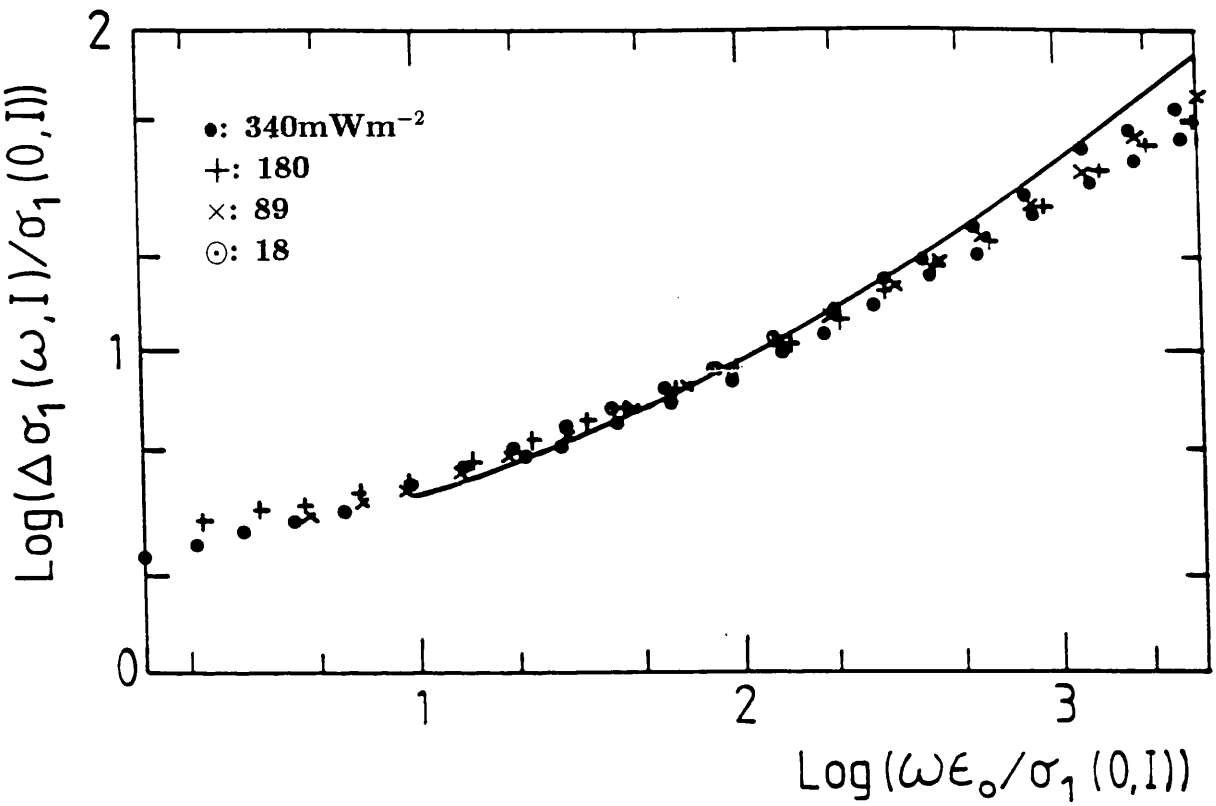

Figure 6.19: The data of fig.(6.5) in scaled form, with the same symbols. Solid line is a fit to the data of fig.(6.18), transferred at the same scale values.

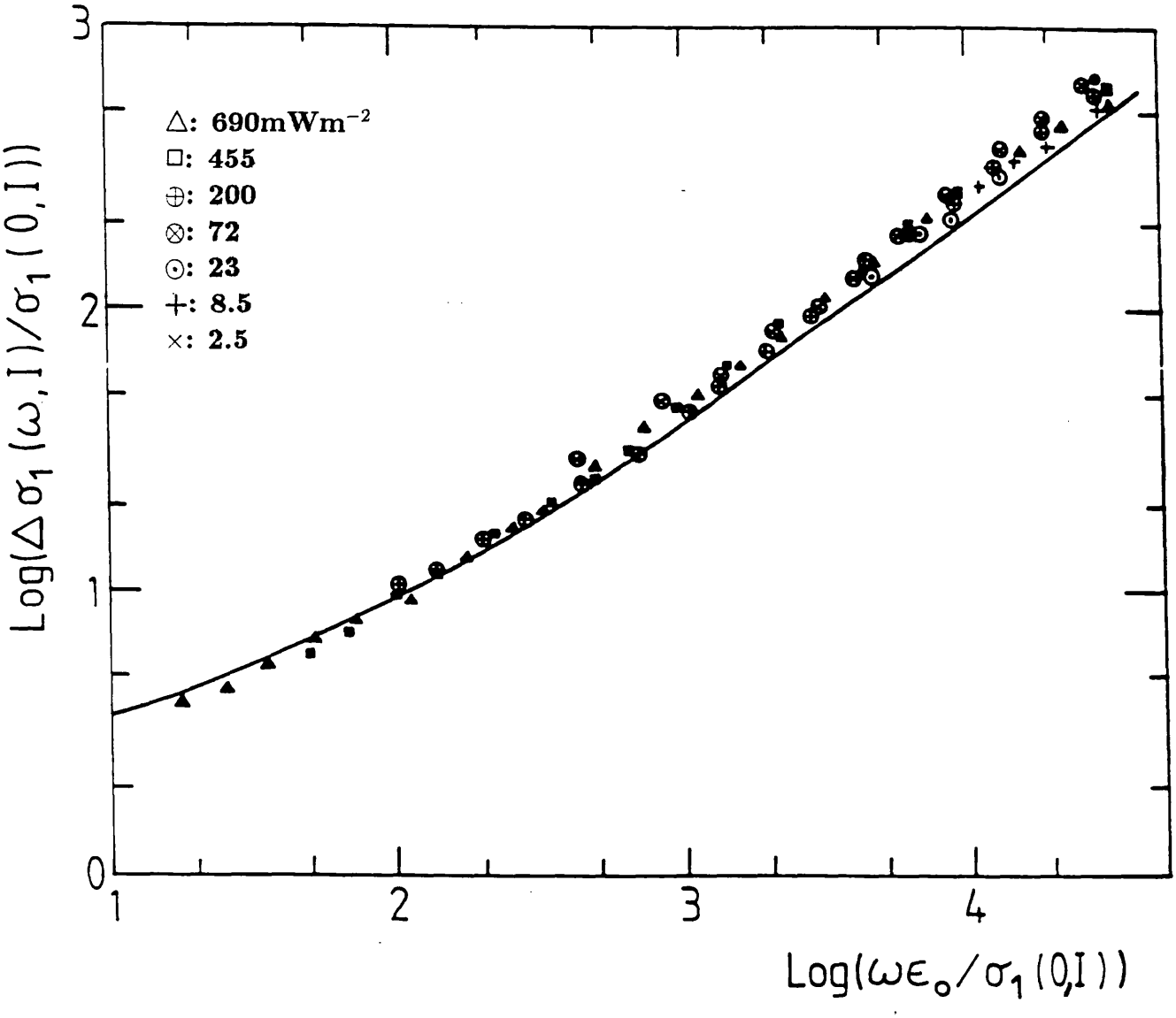

Figure 6.20: The data of fig.(6.6) in scaled form, with the same symbols. Solid line is a fit to the data of fig.(6.18), transferred at the same scale values.

scaling plot to a common curve. The curves are very similar for all the samples. This indicates that the scaling relationship is an intrinsic feature of the a-Si:H and is not affected by any potential fluctuations in the case of the compensated samples. These potential fluctuations due to inhomogeneous regions in the sample as we have seen in chapter 5 act as traps for carriers and contribute significantly to the dark a.c. loss at high temperatures. However, in the photoinduced data, they have a minor effect on the overall loss if any at all.

The theoretical prediction of the scaling relationship could in principle be calculated in a unified theory of both the a.c. and d.c. photoconductivities. Currently no such theory exists. The only theory which might be used to compare with the observed results is the SFB model (see Shklovskii et *al.* 1989a), but for the a.c. loss this model is based on the pair approximation and hence does not consider the effect of clusters, including the non-dispersive conduction from the infinite cluster. Now the existing theories generally fit the observed temperature-dependent hopping data quite closely (see Long 1991), and the form of our scaling data is similar to those observed before. Hence, we plot in fig.(6.18) the scaling curve computed by Summerfield and Butcher (1983) for variable range hopping using the EPA at the same scale. As far as the shape is concerned, the agreement between theory and experiment is excellent. This strongly suggests that a hopping process in band tails governs both d.c. and a.c. photoconductivities and that the network aspects of this hopping process are similar to those of the standard temperature dependent variable range hopping. This result has also another significant meaning in that it casts doubt on the model proposed by Hoheisel et *al.* (1983 and 1984) that the contribution of generated carriers to the d.c. transport occurs during their thermalization in the extended states, since if it was the latter which dominates, the scaling behaviour would not be observed.

The scaling of the real part of the dielectric constant (capacitance) was also observed. The data for an intrinsic sample presented in fig.(6.7) is plotted in fig.(6.21)

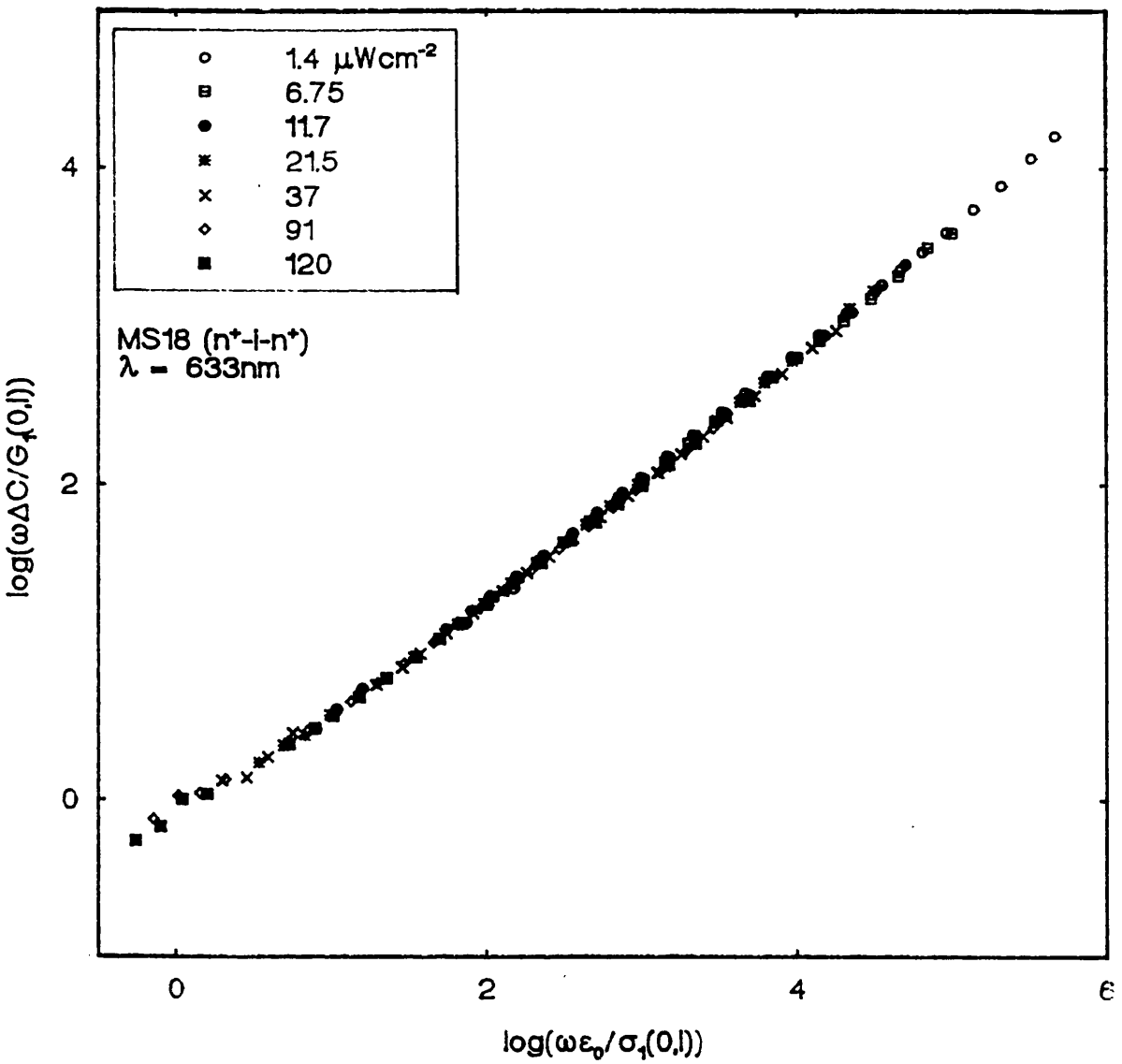

Figure 6.21: The data of fig.(6.7) in scaled form, with the same symbols.

in the form of $\log(\omega\Delta C/G_1(0,I))$ against $\log(\omega\epsilon_0/\sigma_1(0,I))$. The term ΔC represents the photocapacitance after subtracting the capacitance in the dark from the measured capacitance, since the dark and the photoinduced losses are due to different effects as we have already seen with the imaginary part (conductance). The scaling data in fig.(6.21) is more accurate than the data in previous figures, which is a clear indication that the capacitance was measured more accurately than the conductance. Other samples showed the same behaviour, irrespective of the film type.

6.1.3.3 Effect of Temperature on the Scaling.

In fig.(6.22) to (6.25) the data corresponding to fig.(6.8) to (6.11) respectively are plotted in the scaled form. It can be seen that the scaling is excellent up to 40K where it starts deteriorating, particularly at low frequency. This effect is attributed to the thermalization of the carriers which is more pronounced at temperature above 40K than at 13K. Also at around this temperature $\sigma_1(0,I)$ increases with temperature. This observation is in good agreement with the prediction of the SFB model, e.g. for an intensity I=120 μ Wcm^{-2}, $\sigma_1(0,I) = 1.15\times10^{-9}$ Sm^{-1} at 15K and $\sigma_1(0,I) = 5.2\times10^{-9}$ Sm^{-1} at 40K for an intrinsic sample. In fig.(6.26) we represent the data of fig.(6.22) to (6.25) each one by a single symbol and plot the four graphs on a single master curve. All the curves regardless of the temperature of measurement lie on the same curve except in the low frequency regime where the curve corresponding to 50K deviates from the rest of the data. This is also another confirmation that the photoconductivity at temperature below 50K is almost constant and this is in a good agreement with the observation of Hoheisel et *al.*(1983) and (1984), Cloude et *al.*(1986), Spear (1988) and Johanson et *al.*(1989).

Although the problem here is somewhat different from the temperature dependent hopping system, since the carriers are photogenerated rather than thermally created, the reason for the scaling behaviour is we believe similar. We start with a

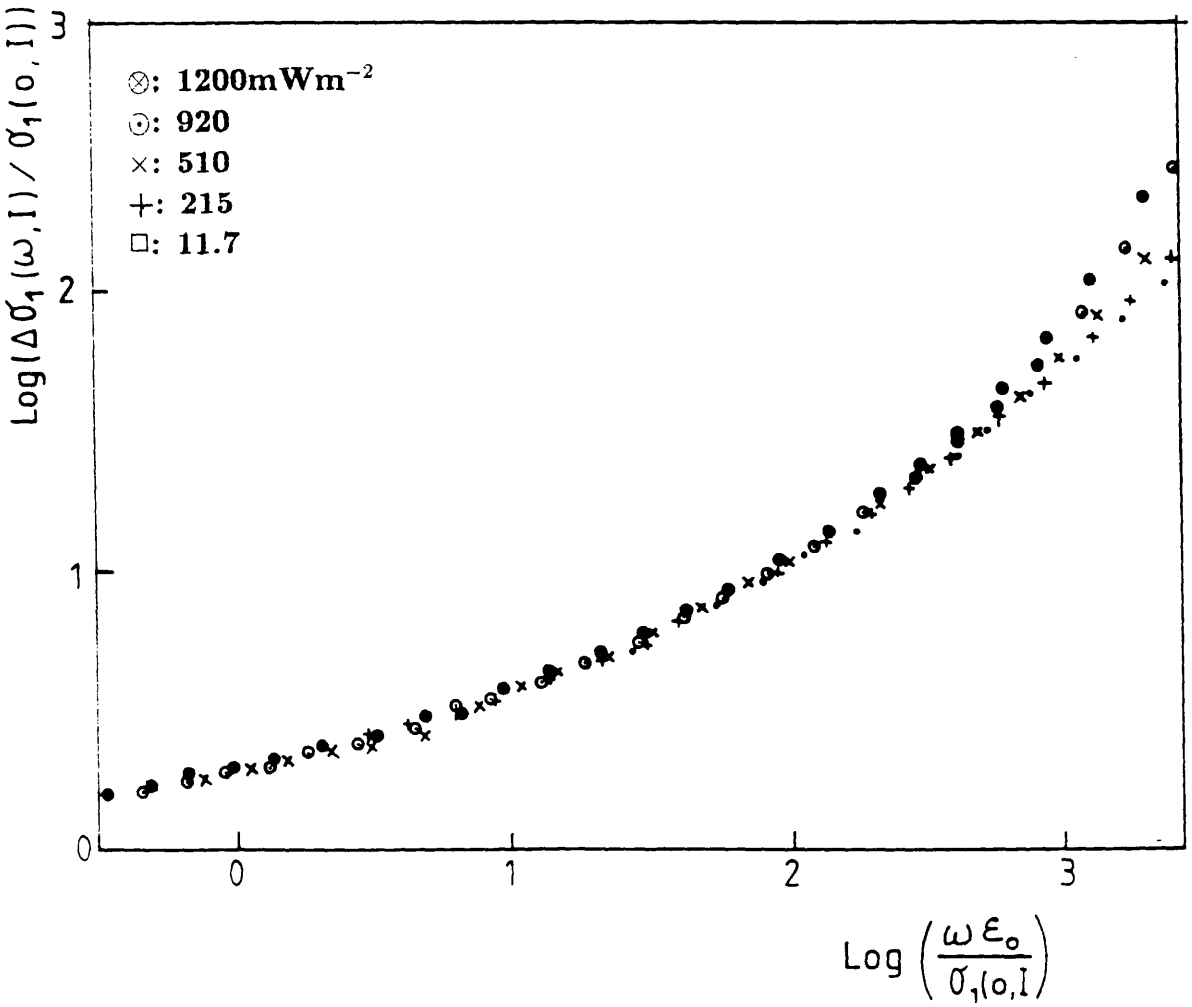

Figure 6.23: The data of fig.(6.9) in scaled form, with the same symbols.

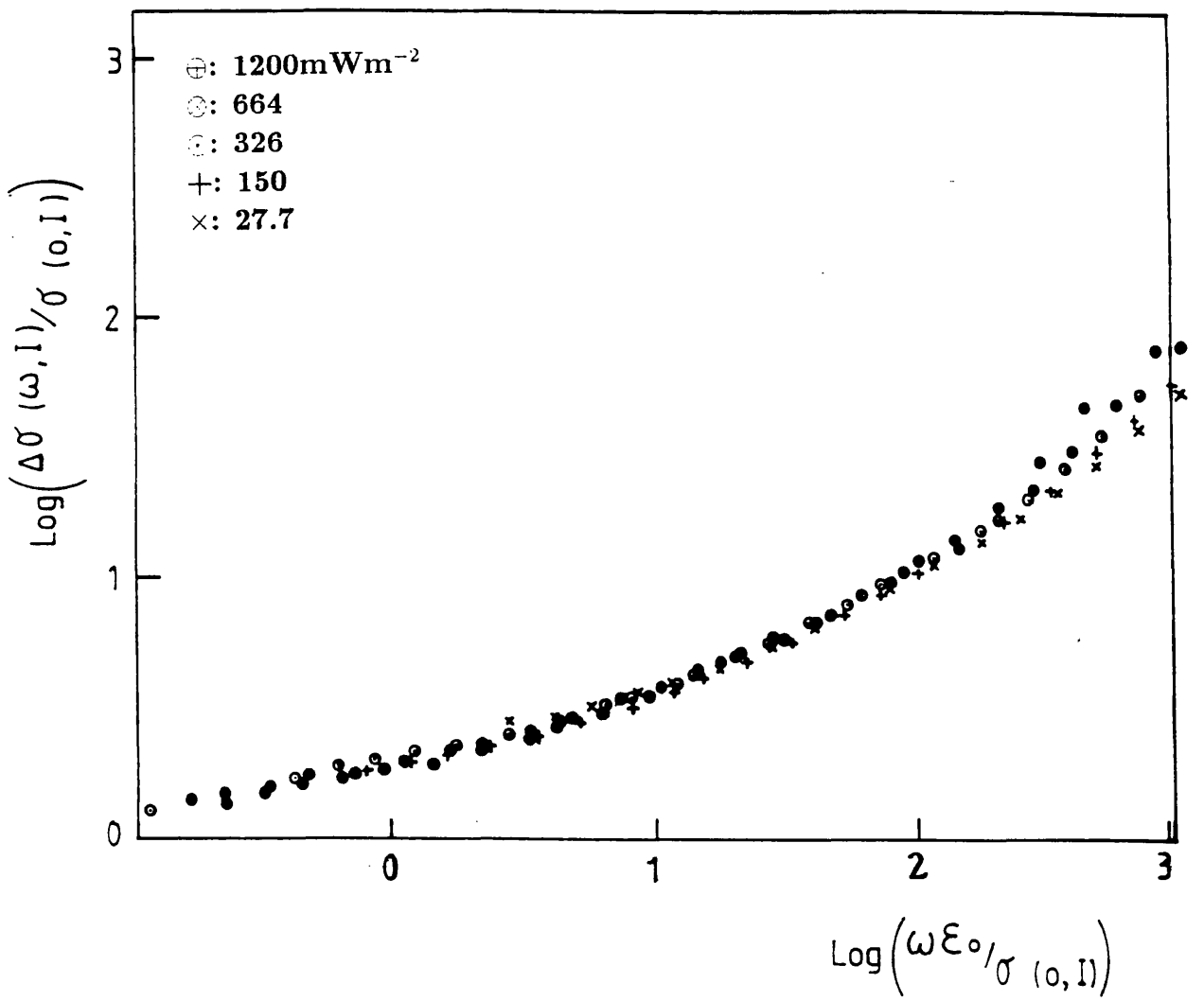

Figure 6.24: The data of fig.(6.10) in scaled form, with the same symbols.

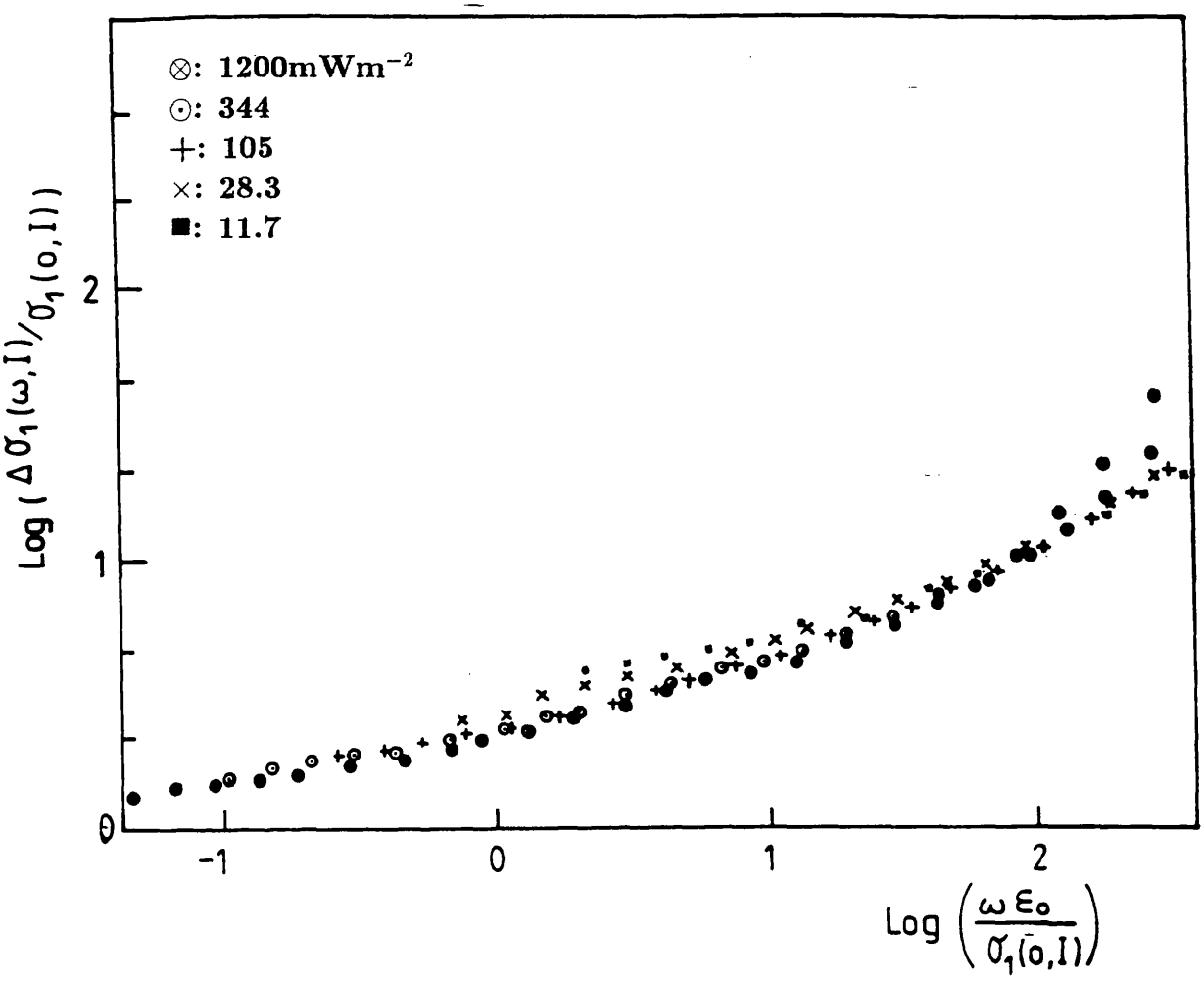

Figure 6.25: The data of fig.(6.11) in scaled form, with the same symbols.

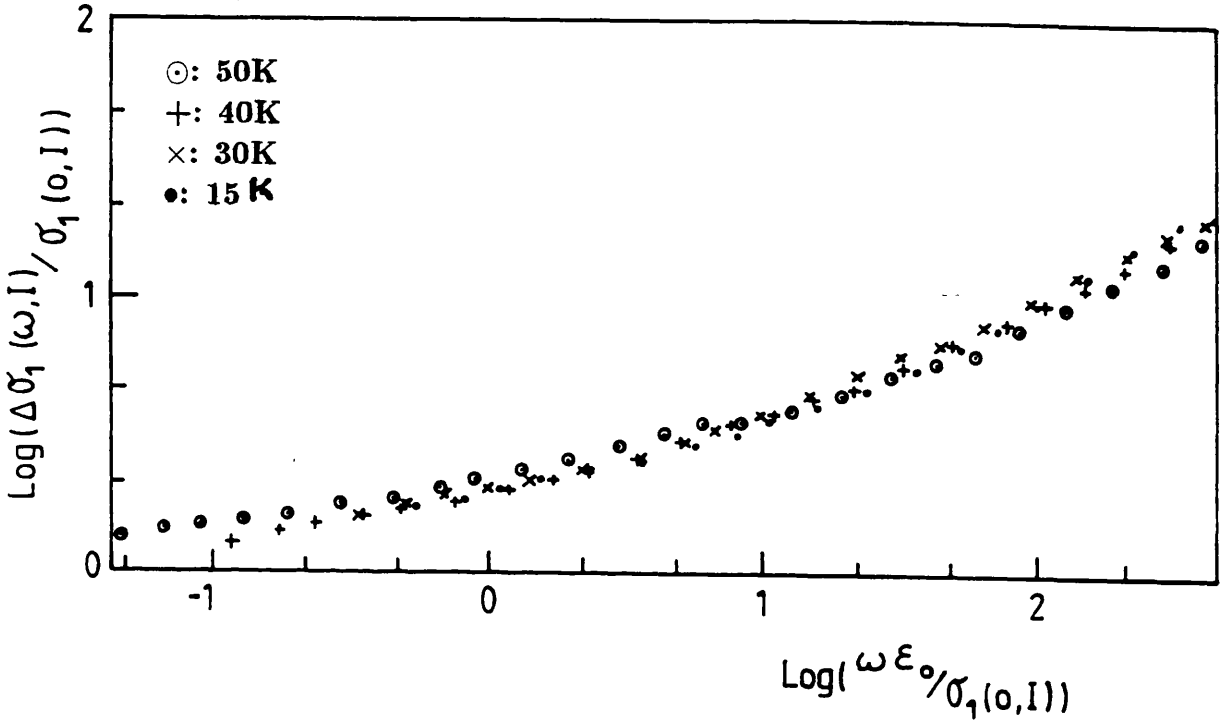

Figure 6.26: The data of fig.(6.12) in scaled form, with the same symbols.

hypothetical statement. Following other authors (see Spear et *al.* 1986, Shklovskii et *al.* 1989a,b and Searle 1990), we assume that the photogenerated carriers at low temperature diffuse rapidly into the band tails and thereafter they continue relaxing from site to site losing energy through the process before the recombination occurs by tunnelling. Because of the random distribution of the tail states, the hopping process is expected to be of a percolative nature and therefore we anticipate the existence of a critical frequency ω_c to which the d.c. photoconducitivity will be proportional. Then, scaling in the form we observed follows. Now, let us reverse the argument, the fact that we observe the scaling behaviour is a strong evidence that both d.c. and a.c. photoinduced loss are related and that d.c. transport occurs by a percolative hopping mechanism and that when the percolation network splits up into clusters at finite frequencies, the a.c. photoinduced loss increases.

Another important feature of these results is the similarity between the intrinsic and the compensated samples. In the inhomogeneous model Long (1989) has shown that long range potential fluctuations can lead to an a.c response suggestive of that observed in tunnelling systems, with a critical frequency related to the bulk conductivity relaxation frequency. But from the data reported above we do not think that such fluctuations have a significant effect on the scaling as the graphs for all the samples are identical, despite of the fact that the intrinsic sample was almost free from any fluctuations. Another way to show that d.c. and a.c. are linked was discussed in chapter 5 section (5.1.2). We have seen that if the two conduction mechanisms are related then the plot of $\log\left(-\frac{dC}{d\ln(\nu)}\right)$ against $\log(\nu)$ shows a peak near the critical frequency. Some relevant data is plotted in fig.(6.27) for various temperatures and constant excitation intensity. There is little evidence for a peak in these curves. We ascribe to the fact that the d.c. limit was not reached at this intensity. We believe that if the sample was measured under higher intensities and over an extended low frequency range (ν <10Hz), the peak would be observed.

Finally we compare the latest theory of Shklovskii et *al.*(1989a,b) with the ex-

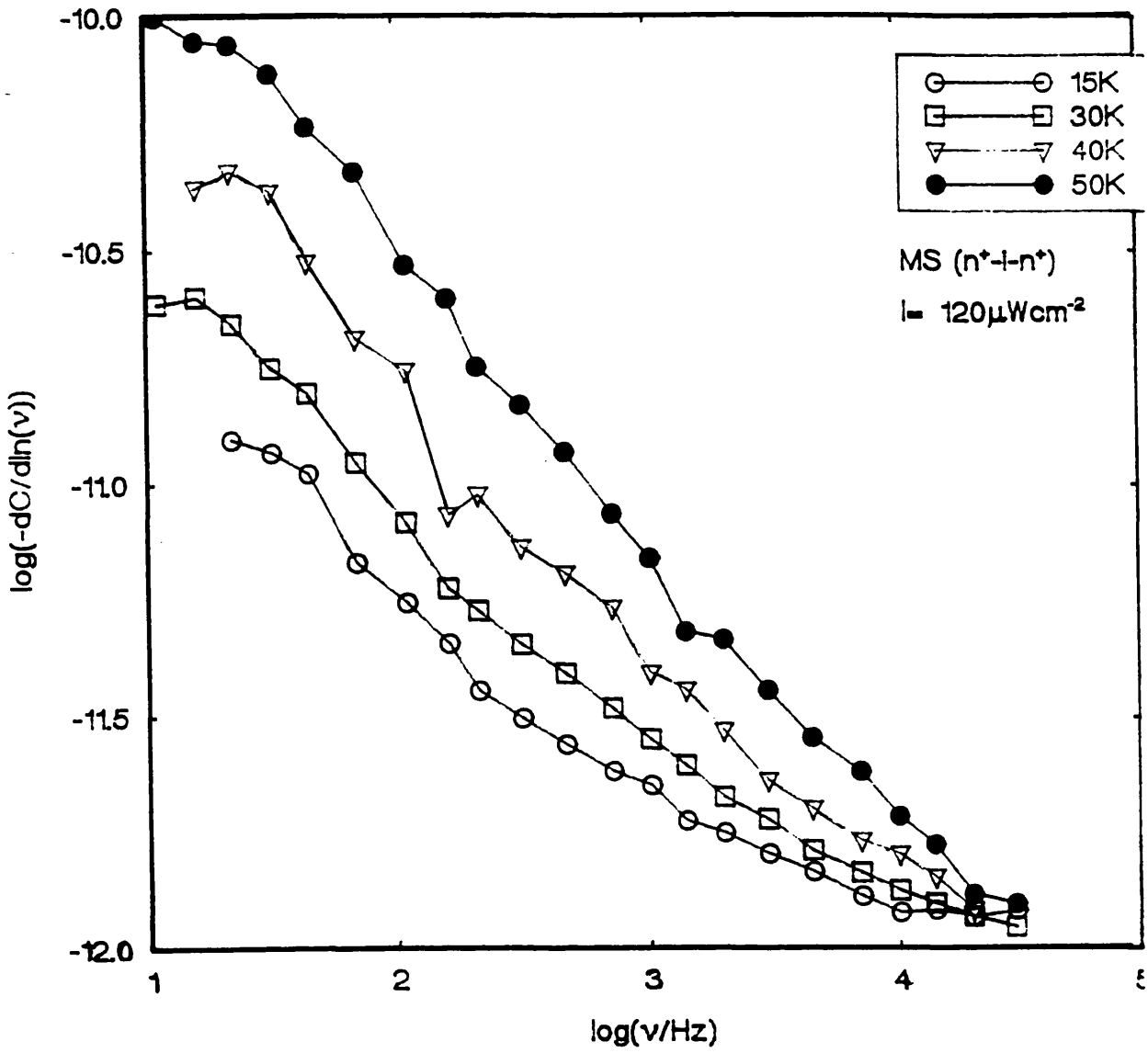

Figure 6.27: The frequency dependence of $\log(-\frac{dC}{d\ln(\nu)})$ for an intrinsic sample.

perimental data. The theory as already discussed in chapter 3 predicts that d.c. photoconductivity should vary as I^{γ} with $\gamma \approx 1$. The a.c photoinuced loss based on the pair approximation model should vary as $\omega^{0.8}$. If we approximate the empirical scaling relation in fig.(6.18) for instance over a given limited region of characteristic in the high frequency regime by a power law:

$$\frac{\sigma_1(\omega, I)}{\sigma_1(0, I)} \propto \left(\frac{\omega}{\sigma_1(0, I)}\right)^{\beta} \tag{6.3}$$

then this implies a relation of the form

$$\sigma_1(\omega, I) \propto \omega^{\beta} I^{\gamma(1-\beta)} \tag{6.4}$$

The SFB model predicts a frequency dependence of around $\omega^{0.8}$ which is closer to the experimental data and an intensity dependence of the a.c. photoconductivity of the order of $I^{0.3}$ at low temperature, which is rather higher than the experiment.

There is however an inconsistency between this theory and the scaling data. The theory attributes the frequency dependence to a loss based on the pair approximation model, which involves the distribution of relaxation times within a random population of sites. Whereas, the intensity dependence is ascribed to the distribution of the photogenerated carrier concentration. The two powers are therefore decoupled theoretically. But the success of the scaling relation in explaining the data suggests otherwise. The decoupling is not appropriate and there is a strong necessity for a theory which incorporates both effects and takes into account the effects of cluster.

The photoconductivity normalized by the charge and the bulk generation rate G of photocarriers: $\frac{\sigma_p}{eG}$ had a value of $6.51 \times 10^{-12} \pm 0.04$ cm^{-2}V^{-1}: for the intrinsic sample (MS2) and $1.43 \times 10^{-12} \pm 0.05$ cm^{-2}V^{-1} for the compensated sample (MS8). These values are comparable with the theoretical predictions.

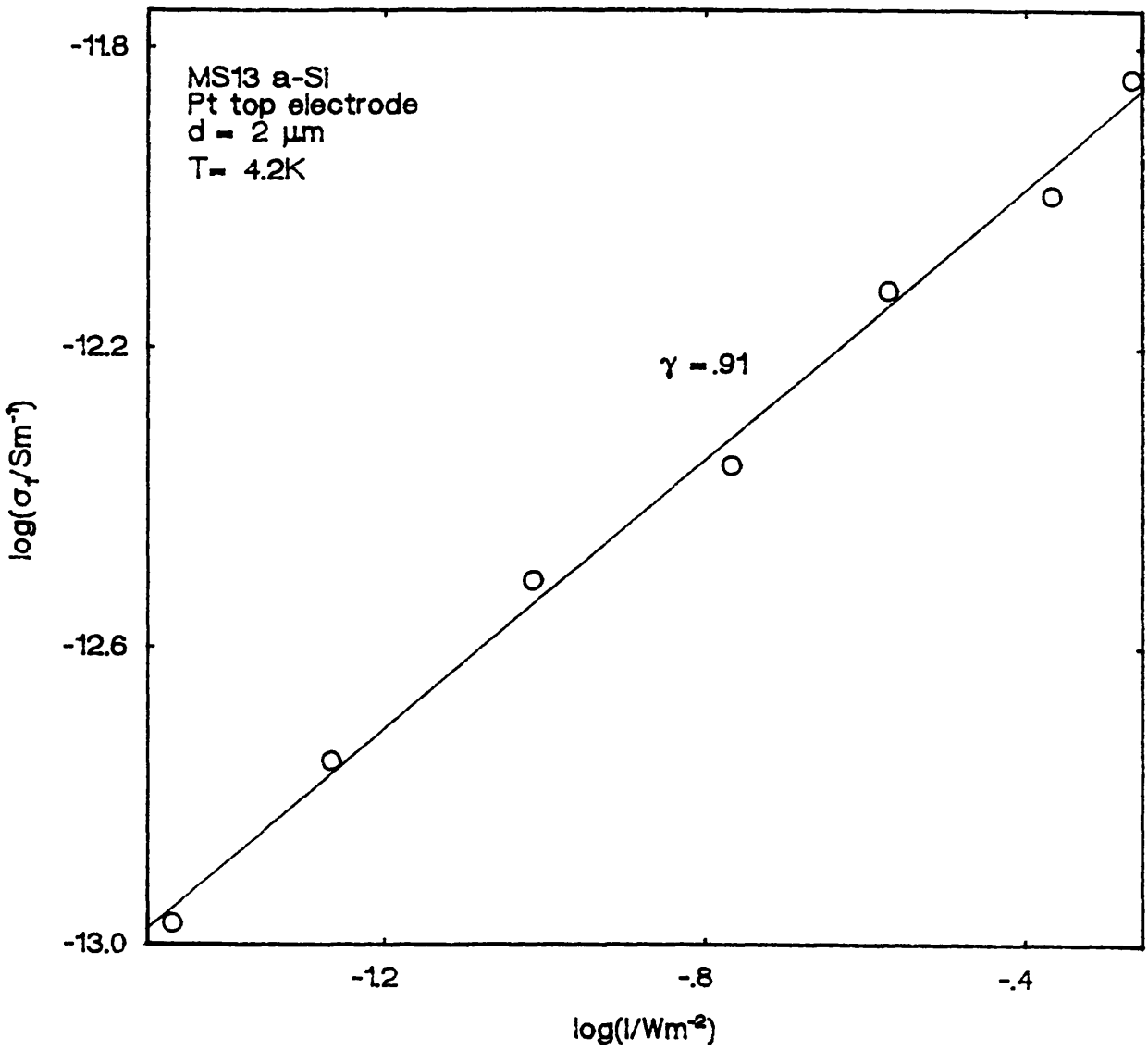

Figure 6.28: The intensity dependence of the d.c. photoconductivity for a magnetron sputtered a-Si at 4.2K.

6.2 R.F. Sputtered Sample.

6.2.1 D.C. Photoconductivity.

Only one sample of a-Si (MS13) was investigated in order to compare with the low density sample (a-Si:H). The d.c. conductivity as a function of the intensity of illumination behaves similarly to the glow discharge samples. However the magnitude is smaller, a typical characteristic of $\sigma_1(0, I)$ against the excitation intensity at 4.2K is shown in fig.(6.28). The characteristic is linear with the intensity exponent $\gamma \approx 0.91 \pm 0.03$. This value is similar to that previously reported by Holland (1987) and Anderson (1989). Because of the low magnitude of the d.c. term, its effect on the total conductivity was very small.

6.2.2 A.C. Photoconductivity.

The frequency dependent photoconductivity of MS13 is shown in fig.(6.29). The data is plotted in the log-log form after the subtraction of the series resistance and the dark conductivity terms. It can be seen that s hardly changes with the frequency. As in the glow discharge material, the photoinduced loss is distinct from the background loss and cannot be explained by temperature changes. Anderson (1989) has shown that the energy provided by the a.c. measuring equipment and the laser light source to the sample, if converted to a thermal energy, would lead to an increase of only 1mK in temperature. Such a rise in temperature is obviously insufficient to account for the observed change in ΔC and ΔG under illumination.

6.2.2.1 Intensity Dependence of $\Delta\epsilon_1$

The intensity dependence of the relative permittivity in the sample MS13 is shown in fig.(6.30) measured at helium temperature and at 2kHz. the relation is linear and the permittivity increases with the intensity at a power of $I^{0.32}$ without any abrupt transition in the behaviour. The power value is rather different from the one

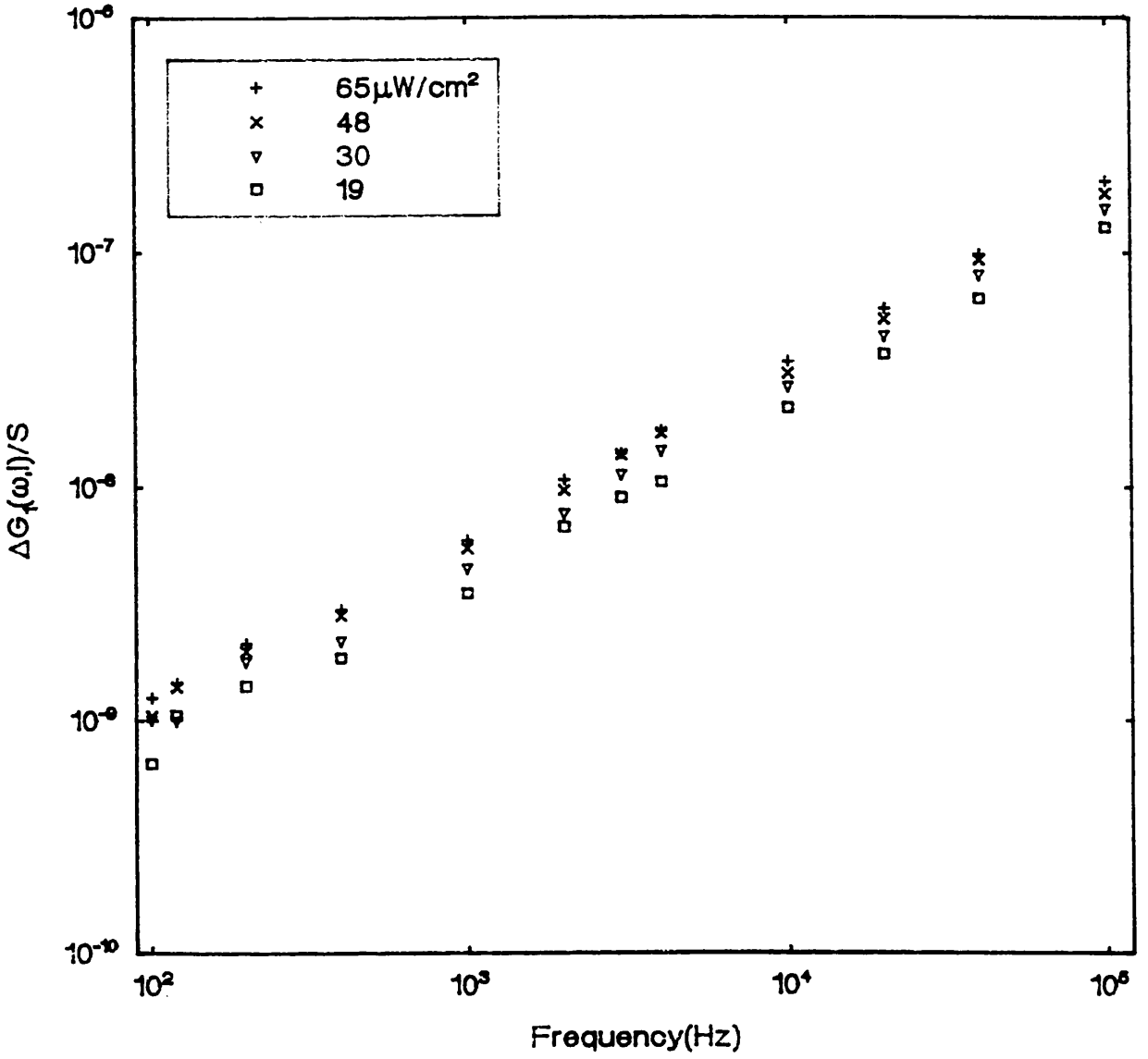

Figure 6.29: The frequency dependent photoconductivity at various intensities of illumination for the same sample as in fig.(6.28) at 4.2K . The appropriate intensity is given in the graph.

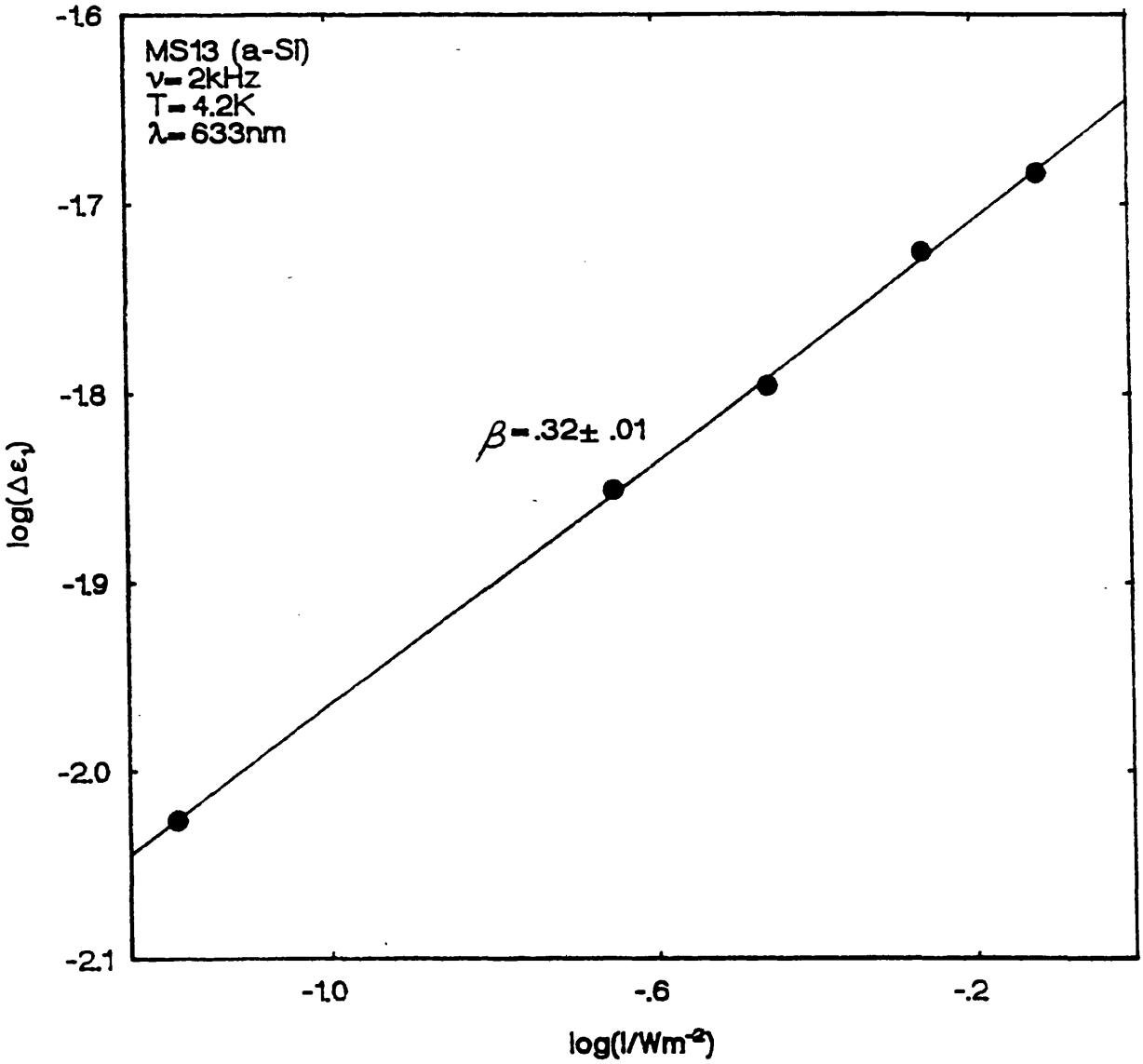

Figure 6.30: The intensity dependence of the dielectric constant for the same sample as in fig.(6.28) at 4.2K.

reported by Holland (1987). The latter observed that the relation changes from $I^{1/2}$ to $I^{1/4}$ with increasing the excitation intensity. We believe that the difference may be due to the fact that the range of intensities used during this work was not as low as the range used by Holland. The purpose of this work was to excite the sample with high excitation intensities in order to study the behaviour in the d.c. limit.

6.2.2.2 Scaling of the A.C. photoconductivity ($\Delta\sigma_1(\omega, I)$)

The data discussed in section (6.2.2) is plotted in scaled form, the same as for the glow discharge material. The shape is not as good as the latter, though it shows that the d.c. and the a.c. photoconductivities are related. The curve is rather linear which means that we are in the high frequency regime and we need to measure the sample at lower frequency range and at higher excitation intensities to reach the d.c. limit. However, we were faced by the problem of finding a suitable electrode for this kind of measurement and we were not able to find a suitable solution in the time available.

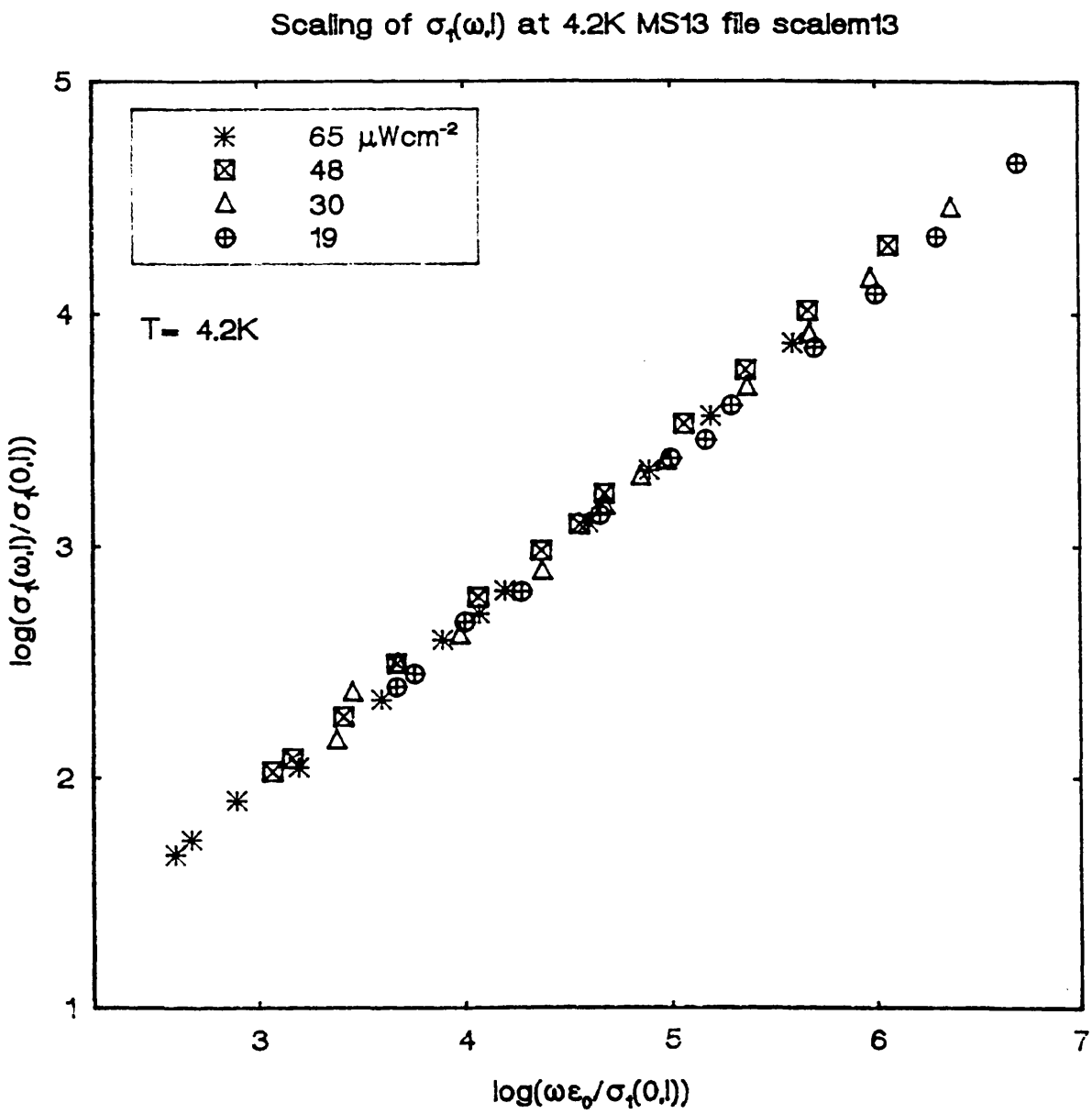

Figure 6.31: The data of fig.(6.29) in scaled form, using the same symbols.

Sample	T°K	G $\times 10^{18}$ ($cm^{-3}s^{-1}$)	$\frac{\sigma}{eG}$ (cm^2/V)	Gamma ($\sigma_1 \propto I^{\gamma}$)
MS2	12.5	3	6.51×10^{-12}	1
	50	3	5×10^{-11}	0.87
MS3	12.5	6	1.93×10^{-12}	1
MS7	13	6	2.8×10^{-12}	0.93
MS8	13	5.7	1.43×10^{-12}	1
MS18	15	8.3	3.4×10^{-11}	0.97
Johanson et *al.* 1989	4.2	200	3×10^{-12}	0.93

Table 6.1: The normalized photoconductivity and the intensity exponent γ for various samples.

CHAPTER 7

Time Dependence of the D.C. and the A.C. Response

7.1 Introduction.

The time dependence of the optically induced loss in amorphous semiconductors prepared by either sputtering or glow discharge techniques has been studied in this department for the last 5 years (see Holland 1987, Long et *al.* 1988b and Anderson 1989). A model was proposed by Long and Holland (1985) to explain the behaviour of the build up of the carriers with time in sputtered a-Si and a-Si:H. They suggested that free carriers are created by the incident light. Because of the high density of defect states in these materials, these carriers are rapidly trapped in the defect clusters near the mid gap. The trapped carriers can then respond to the applied a.c. field and thus enhance the a.c. loss see section (7.8) for more details. However, Anderson reported an inconsistency between the model and some of the observed data for the same material (see Anderson 1989). Anderson observed that the intensity dependence changes from $I^{1/2}$ to $I^{1/4}$ as the intensity increases. Also the decay of $\Delta\epsilon_1$ with time could not be fitted by a 1/t relation and when fitted with ln(t) relation, it gave a straight line. This inadequacy of the model was attributed to the fact that the random distribution of the trapped carriers was not preserved as the time progressed. It is believed that the more closely spaced trappped electron and hole recombine before more distantly separated pairs. As a result, the recombination time increases. The dark decay in the glow discharge a-Si:H has also been investigated by Anderson (1989) and a model was proposed. This was based on the

assumption that equal number of electrons and holes are trapped. It was also assumed that holes are fixed and only electrons diffuse to allow for the recombination to occur. The diffusion before recombination occurs by tunnelling through the band tail states. The rate of recombination was calculated from the rate of diffusion using Movaghar et *al.*(1986, 1987) theory, this gives:

$$\frac{dn}{dt} = -D_0 n^{5/3} \left(\frac{t_0}{t}\right)^{1-\xi} \tag{7.1}$$

where $\frac{dn}{dt}$ is the rate of recombination, D_0 the diffusion coefficient, n the number of diffusing electrons, t the time , t_0 is a scaling time and ξ is a parameter. The fitting procedure was found to give a good account of the experimental data, with some discrepencies at short times less than 10 seconds after the removal of the light.

In this work we are mainly concerned with the rate of increase of carrier population in glow discharge a-Si:H under illumination and how the photoinduced loss varies with the number of carriers trapped in the band tails. We study this as a function of the excitation intensity and temperature. This will help us to come to a conclusion on which recombination mechanism dominates in the range of intensities covered by the measurements.

7.2 Preparation of the Dark State

One of the major problems in measuring the photoinduced loss in the a-Si:H material is defining the dark state. It has been observed that even at the base temperature in the dark, the sample parameters continue to decrease with time. However, this change is very small e.g. a change of 0.05% over several days. In order to minimize problems in defining the starting configuration, the following standard procedure was adopted throughout the optically induced measurements. After the measurement of the sample characteristics in the dark as a function of temperature (chapter 5), the sample was annealed at 150K for around 30 minutes to empty the majority of the traps. It was then cooled to the base temperature and left to relax for

several hours. The base values, (i.e. capacitance and conductance) of the sample were recorded immediately before the light was applied. The relevant intensity of light was then applied. Either the a.c. or the d.c. photoresponse were monitored until equilibrium was reached. A d.c. characteristic and a frequency dependent photoconductivity sweep were measured. After the removal of light, the response was allowed to decay for a further period of time. The sample was then annealed again at 150K for 30 minutes and the cycle repeated. This preparation procedure resulted in a reproducible starting configuration for the measurements.

7.3 Intensity Dependence.

The time dependence of the relative permittivity for a compensated sample is shown in fig.(7.1a). The data was taken at 13K and measured at 2kHz and under $23\mu\text{Wcm}^{-2}$. After the light is switched on, this rises approximately linearly with time to a plateau (see fig.(7.1b)). Similar characteristics to that of fig.(7.1a) are shown in fig.(7.2) for two different intensities of illumination 0.17 and 34.4 μWcm^{-2} respectively. It can be seen that at low intensity, the equilibrium is only reached after many thousands of seconds have elapsed. This is due to the fact that the build up of the trapped carriers population does not accumulate sufficiently fast so that the generation rate could be balanced by the recombination rate. However, high intensity results in the increase of the generation rate, and therefore the population of the trapped carriers rises more quickly until it is balanced by the recombination rate and the equilibrium is reached more rapidly. The permittivity will then have a constant value and the relation between $\Delta\epsilon_1$ and the excitation intensity can be calculated. This was found to be linear of the form $\Delta\epsilon_1 \propto I^{\alpha}$ (with $\alpha \approx 0.16$) (see chapter 6). The rise time of course depends strongly on the excitation intensity and temperature. It decreases with increasing the intensity or temperature (see next section). This observation is in agreement with previous measurements (see Long et *al.* 1988b and Bort et *al.* 1991). This behaviour is common to all our

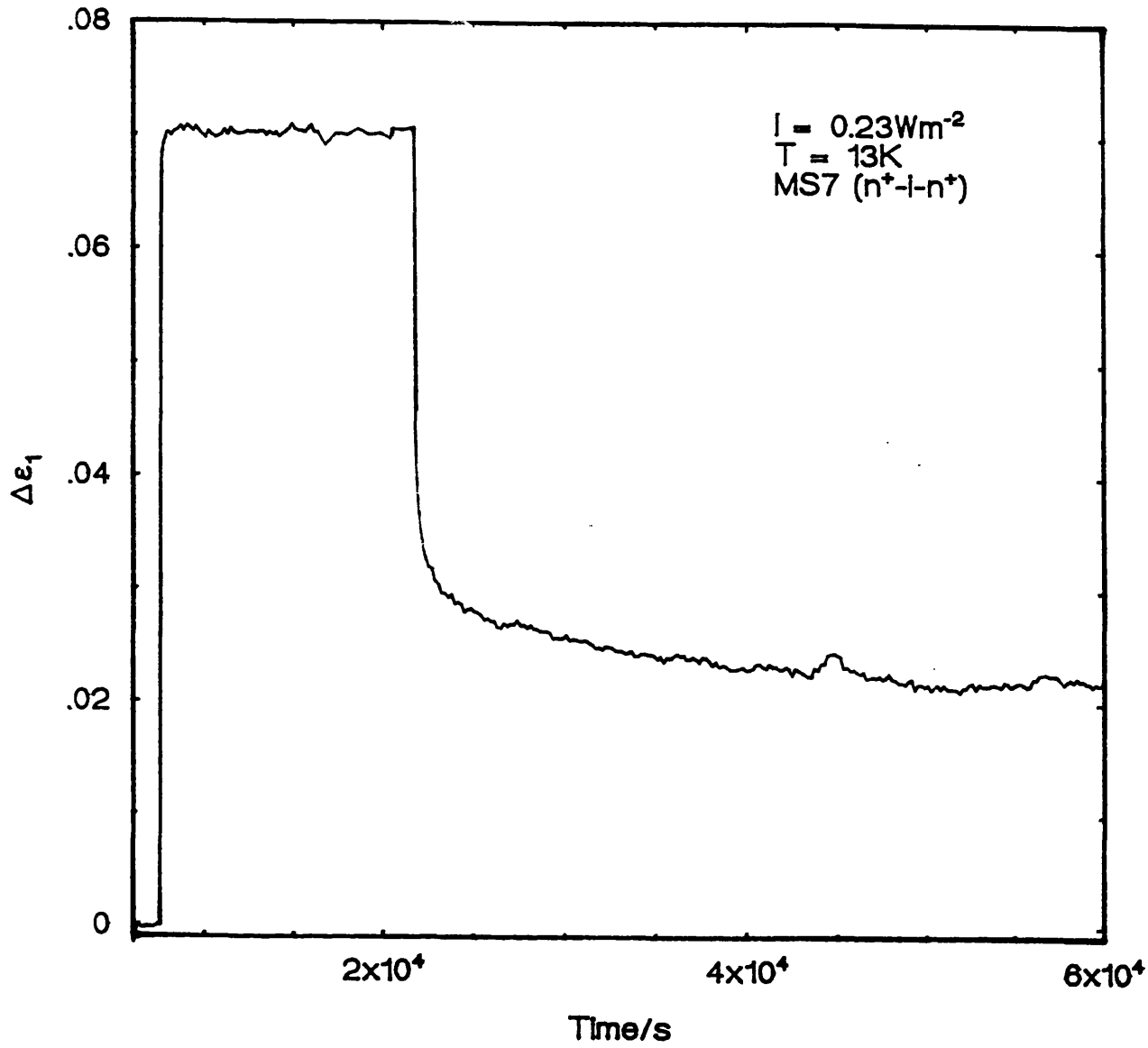

Figure 7.1a:Dielectric constant against time for an n^+-i-n^+ sample (MS7) at 23μWcm^{-2} at 13K measured at 2kHz.

Fig.7.1b

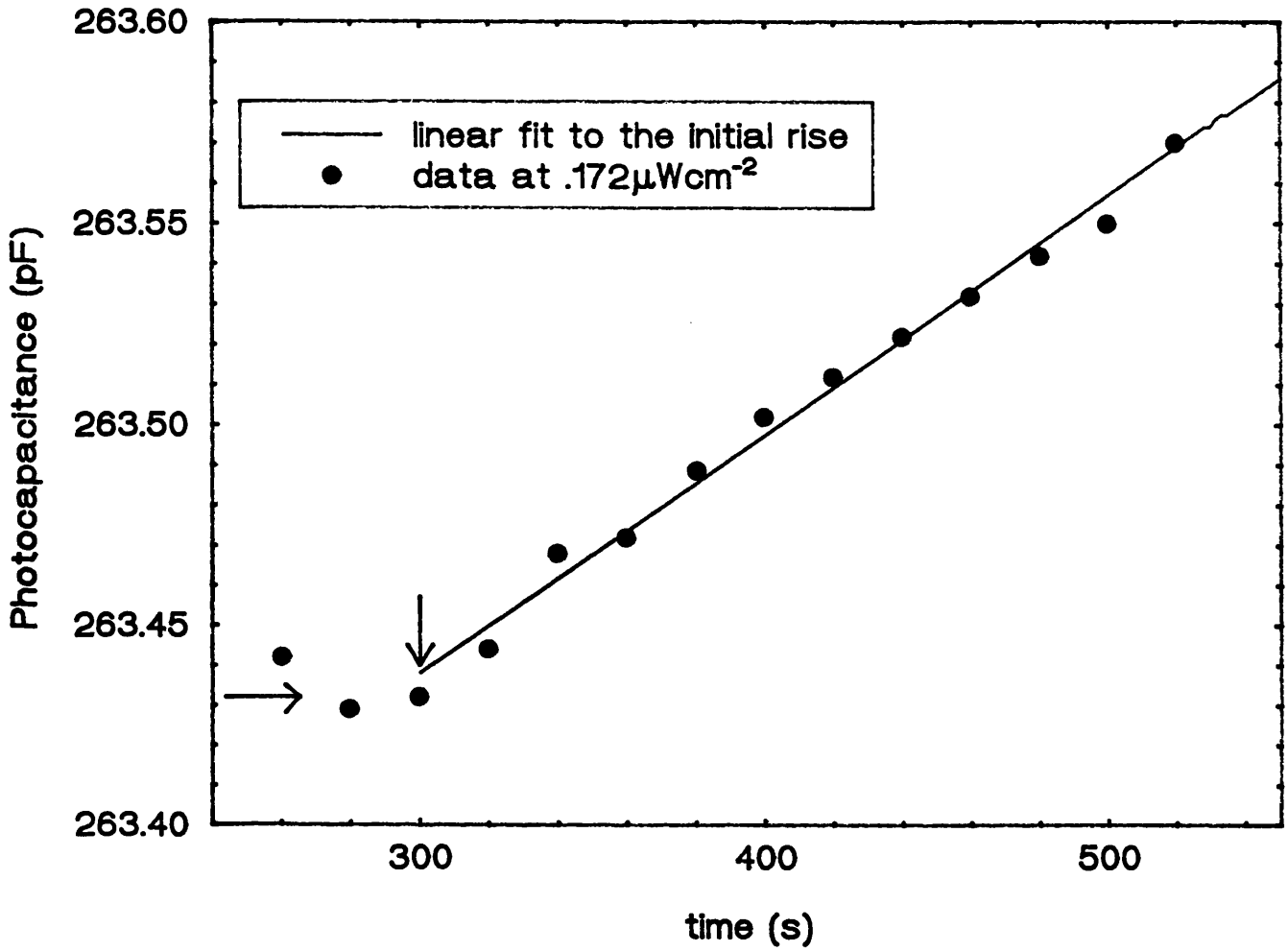

Figure 7.1b:The capacitance against time at short time scale to show the linearity of the rise. The horizontal and vertical arrows correspond to the capacitance and time respectively, when the light was applied.

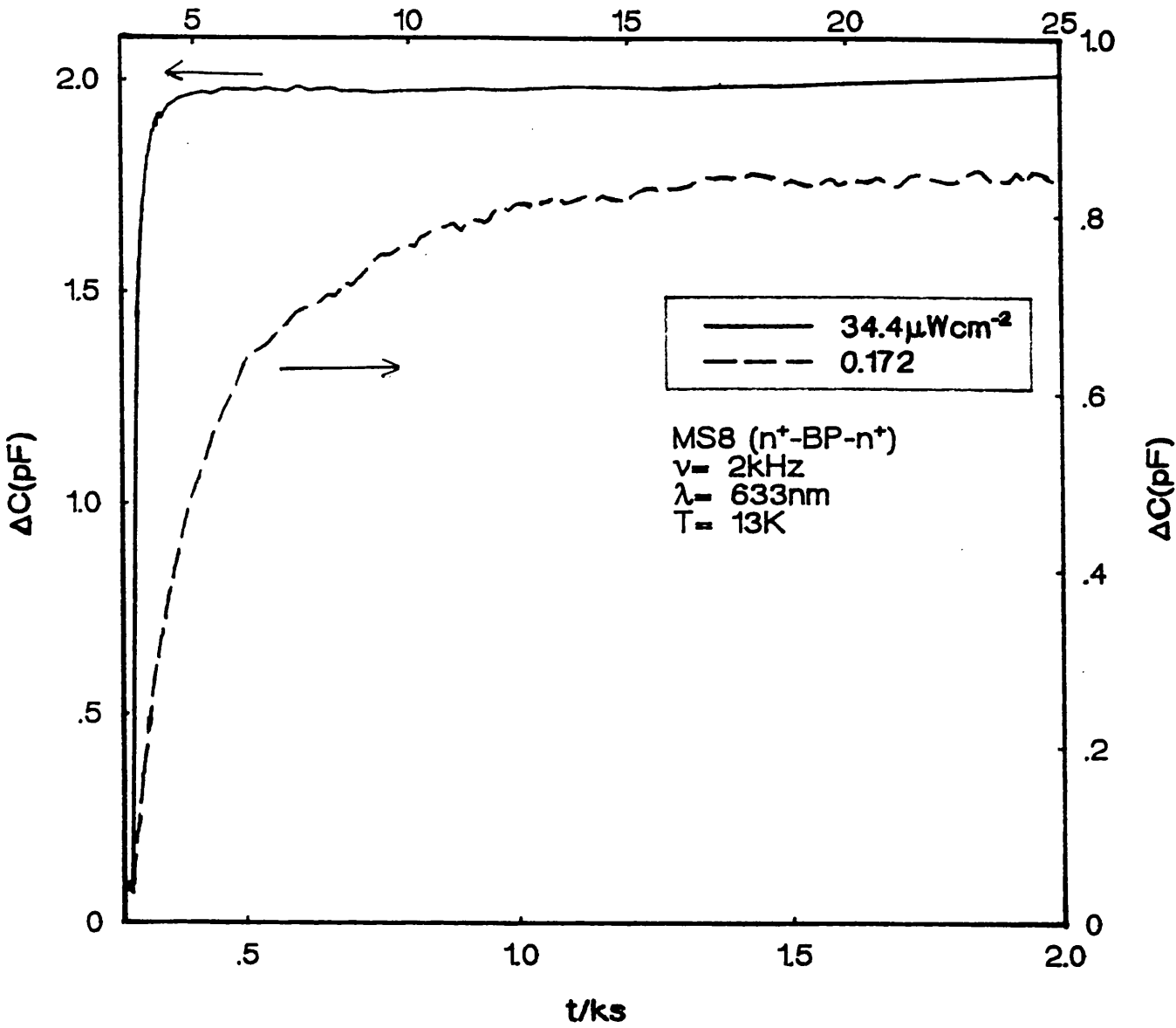

Figure 7.2: The capacitance against time for a n^+-BP-n^+ sample (MS8) for 2 intensities at 13K measured at 2kHz. The appropriate intensity of illumination is indicated in the graph.

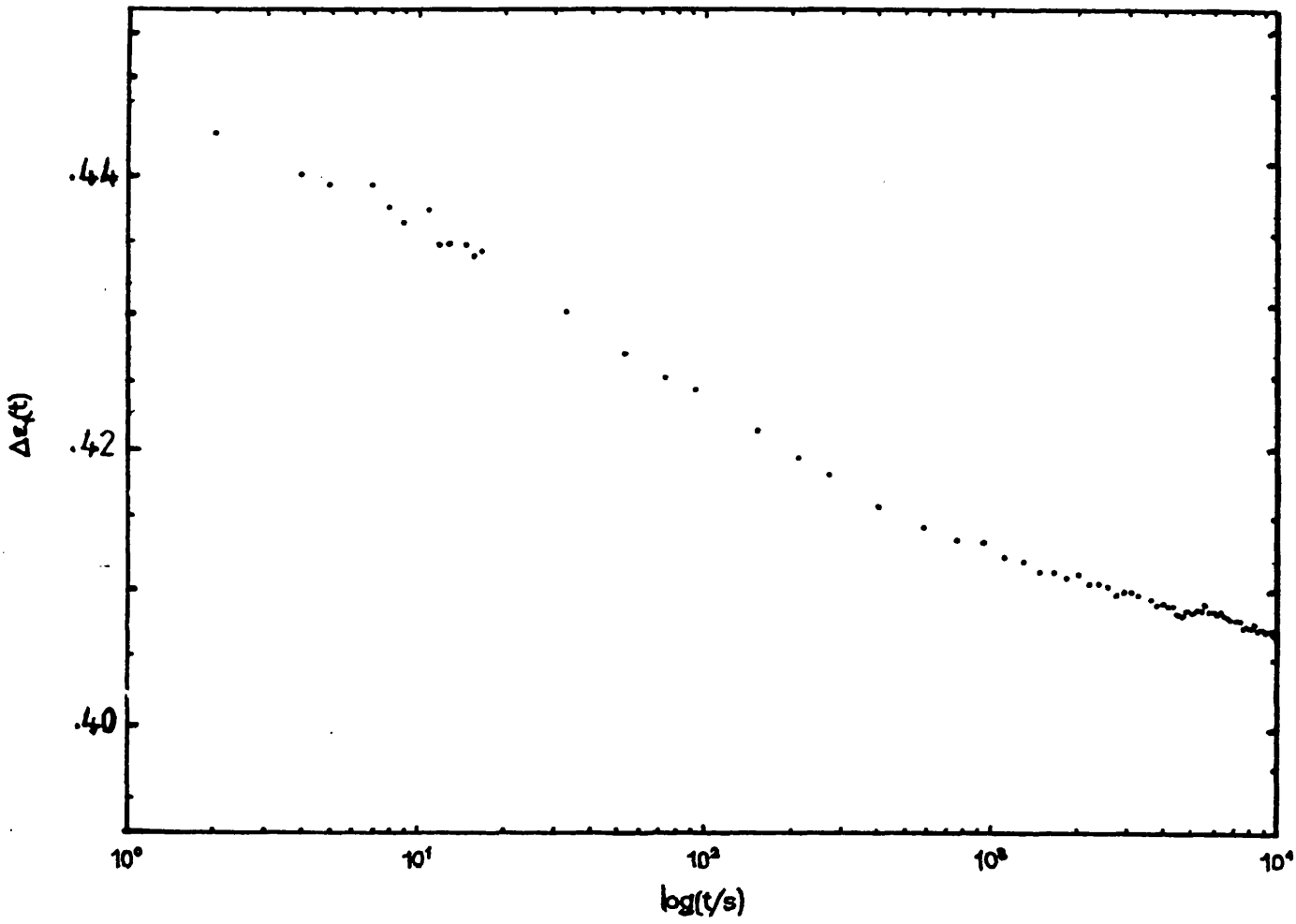

Figure 7.3: The dark decay for the same sample as in fig.(7.1) at 13K.

samples (intrinsic and compensated). There is one other point worth mentioning. It was found that the rise time is shorter for intrinsic than for compensated samples measured under the same excitation intensity and temperature, e.g. at an intensity of $1.4\mu Wcm^{-2}$ the time to reach equilibrium increases from 14s in the intrinsic sample to 134s for the compensated sample. A possible reason for this is that potential fluctuations in the compensated sample act as traps for carriers (see chapter 5) and therefore increase their lifetime before the recombination occurs

After the removal of the light, the long tail observed in earlier a.c. loss measurements (Long et *al.* 1988b) is seen (see fig.(7.3)). This can be easily fitted by a lnt relation. The a.c. photoconductivity corresponding to the permittivity of fig.(7.1) is plotted in fig.(7.4). As already explained in chapter 6 these two quantities behave similarly, and hence the curves have a similar shape.

7.4 Temperature Dependence.

The time dependence of the rise of photoinduced loss measured at various temperatures is illustrated in fig.(7.5). Here we plotted the characteristics at a constant intensity and varied the measuring temperature. Between every two successive runs the annealing procedure described in section (7.2) was performed. It can be seen that the rise time decreases with increasing temperature. In other words the gradient of the curve gets steeper as we increase the temperature. As the temperature is increased, more thermal energy is provided for the generated electron and hole. Therefore, they diffuse apart and escape the geminate recombination and contribute to the loss and this is seen by the increase of the permittivity at high temperatures. This behaviour is in agreement with the observation of Street (1981). The removal of the light results in the decay of the response towards the dark value. The rate of the decay is temperature dependent. At 12.5 K the decay was still continuing after maximum periods of measurement approximately 24 hours and extrapolation suggests it would continue for weeks or ever longer for the dark value to be reached,

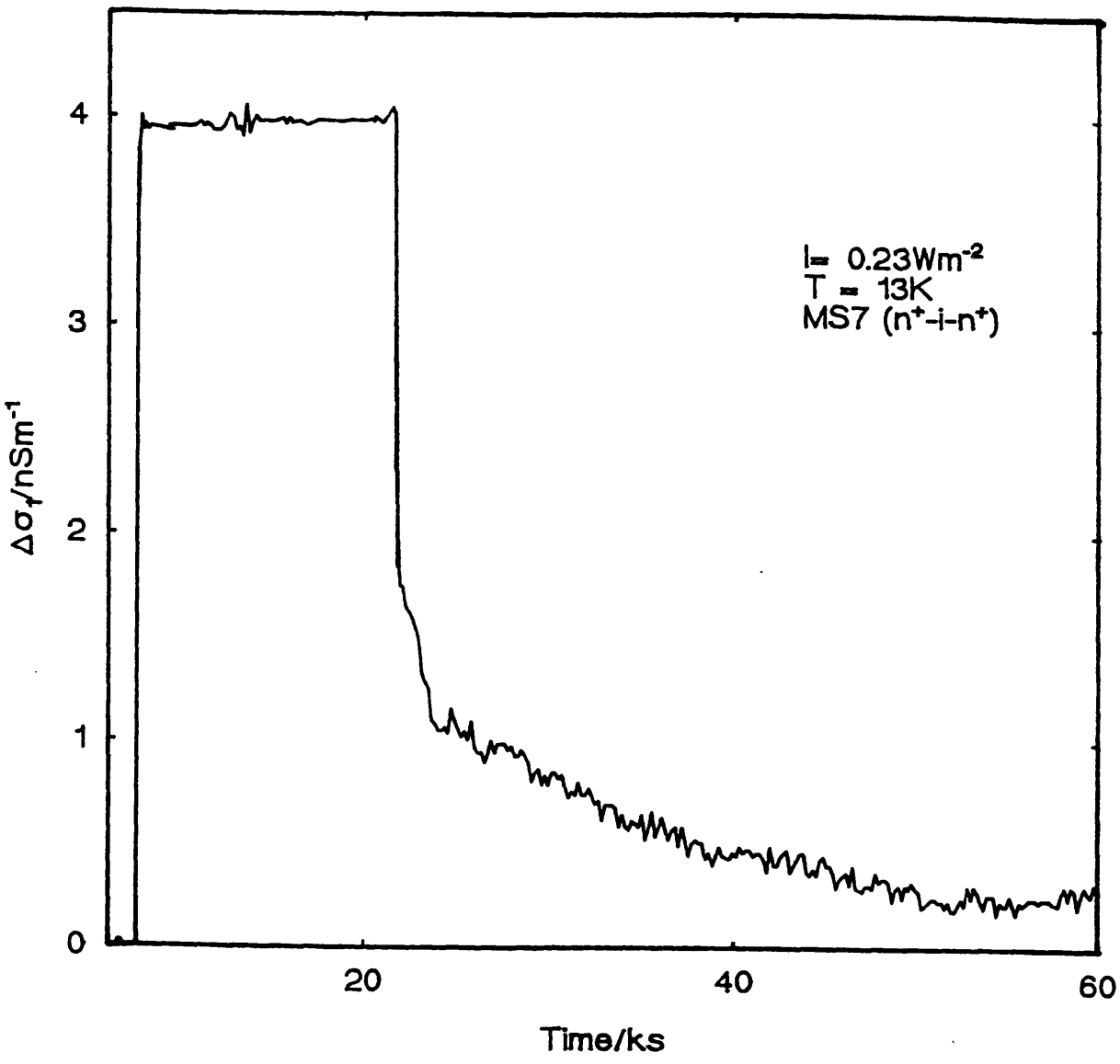

Figure 7.4: The equivalent conductivity to fig.(7.1) plotted against time at the same intensity and temperature.

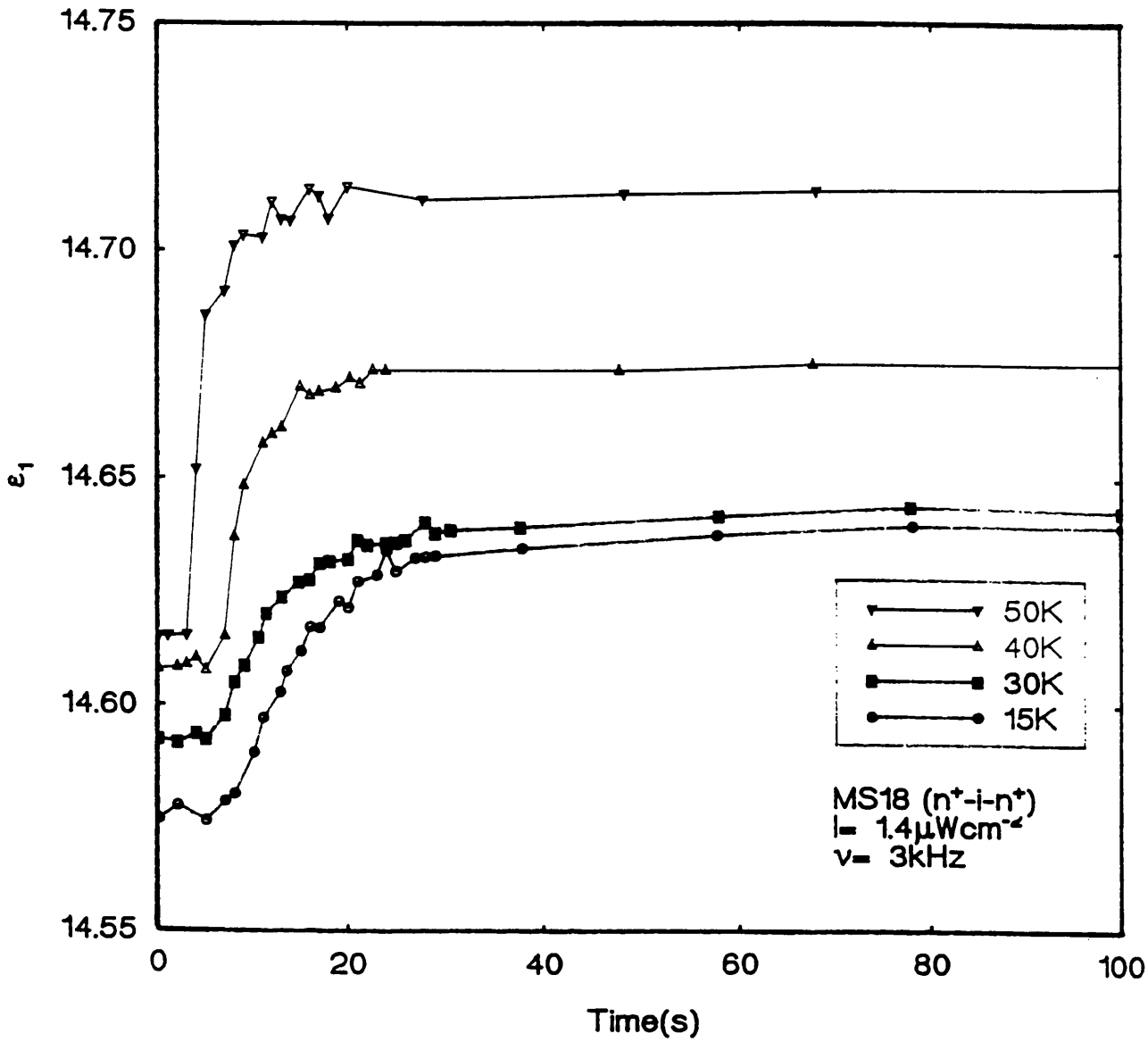

Figure 7.5: The dielecrtic constant against time for an n^+-i-n^+ sample (MS18) at various temperature , measured under a constant intensity of illumination $1.4\mu\mathrm{Wcm}^{-2}$ and at 3kHz.

whereas at higher temperatures (e.g. 50K) the response returns to the intial state after a few hours.

7.5 Time Dependence of D.C. Response.

The evolution of the d.c. photoconductivity with time is shown in fig.(7.6) under $0.17 Wm^{-2}$ at 13K. The behaviour in curve (a) is rather different from that of curve (b). It reveals that the rise time of the d.c signal is much more rapid than that of the a.c.. After the removal of the illumination at 500s, the conductivity drops to its dark value within 10s. This is in agreement with the data of Hoheisel et *al.*(1984) who observed very rapid changes in quasi-d.c. photoconductance response at higher illumination intensities.

Perhaps the most interesting results then is that after the d.c. current has reached its equilibrium value, it does not change as the background population builds up to its steady state value. This suggests that the states which respond to the high frequency a.c. signal have no effect on the d.c. current. This behaviour is reminiscent of that reported by Bort et *al.*(1991). They observed that the risetime of the photoluminescence was much faster than that of the LESR signal and that during the rise of the LESR signal, the luminescence intensity did not change.

7.6 Analysis of the Rise Time.

In order to study the rise time signal quantitatively and in more detail, we plot in fig.(7.7) the rate of increase of relative permittivity and conductivity with time in the initial parts of the characteristic after the start of illumination. It can be seen from the diagrams, these rates of increase are adequately fitted by I^{δ} relation with $0.97 < \delta < 1.0$ at low temperatures. The data is from a compensated sample and was measured at 2kHz. Similar data for an intrinsic sample is shown in fig.(7.8). Throughout the range of intensities covered by the measurements we have not seen any variation in the behaviour as might be expected if there were a transition from

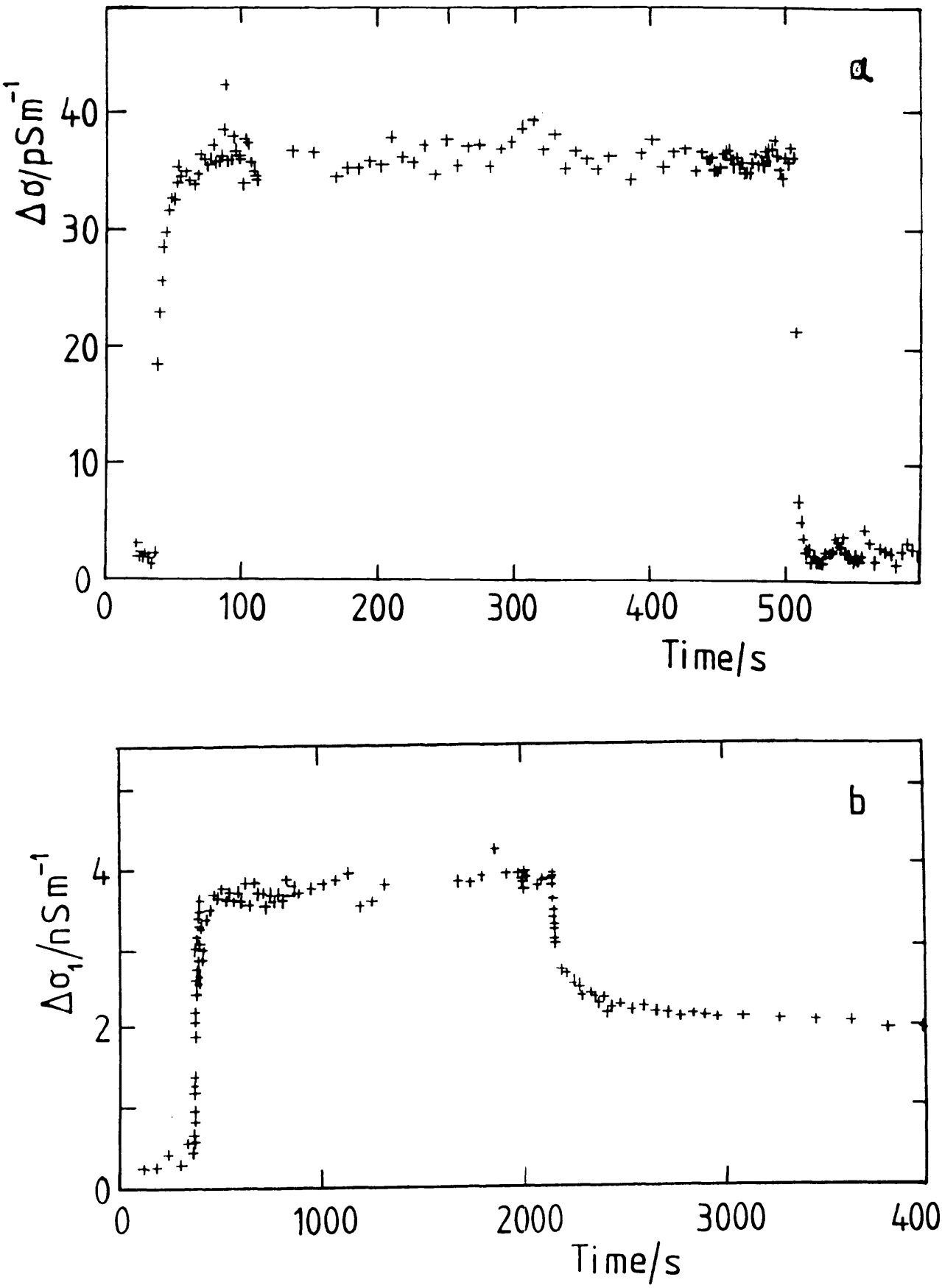

Figure 7.6: Time evolution of response to 17μWcm^{-2} at 13k for a n$^+$-BP-n$^+$ sample (MS8). (a) D.C. conductivity changes for a short excitation pulse. (b) The a.c. conductivity changes measured at 2kHz.

geminate to non-geminate behaviour. As the temperature increases the intensity exponent decreases slowly as it is shown in fig.(7.9), where δ decreases from .97±.03 at 15K to 0.86± 0.02 at 50K. This figure also reveals that the rate of increase of $\frac{d\Delta\epsilon_1}{dt}$ at a given intensity increases monotonically with temperature. This behaviour is similar to that described in fig.(6.16) where the equilibrium permittivity change increases with temperature at a given excitation intensity. Fig.(7.10) represents the rate of increase for three samples at 13K. All samples have essentially similar behaviour at low temperature.

The rate at which photogenerated carriers are trapped can be used to calculate the quantum efficiency η. Assuming for simplicity that the build up to equilibrium is governed by one lifetime to be exponential up to the equilibrium and if $\Delta\epsilon_1(t)$ is the change of the relative permittivity with time t, then:

$$\Delta\epsilon_1(t) = \Delta\epsilon_{eq}\left(1 - e^{-t/\tau}\right) \tag{7.2}$$

this gives;

$$\frac{d\Delta\epsilon_1(t)}{dt} = \frac{\Delta\epsilon_{eq}}{\tau}e^{-t/\tau} \tag{7.3}$$

where $\Delta\epsilon_{eq}$ is the steady state value of the permittivity change and τ is the lifetime of the trapped carriers and is determined by recombination:

$$\tau = \frac{\Delta\epsilon_{eq}}{\frac{d(\Delta\epsilon)}{dt}}\,|_{t=0} \tag{7.4}$$

$\frac{d\Delta\epsilon}{dt}$ is the gradient at a point on the experimental curve. The efficiency η is the ratio of the number of excess carriers by the factor $G\tau$, where G is the bulk generation rate. The calculation is done for the curve (2) of fig.(7.2), where the intensity of illumination is 0.172 μWcm^{-2}. The absorption coefficient is determined by the transmittance and the reflectance measurements, this gives a value $\approx 0.342\mu$m. the thickness of the sample (MS8) is 1.7μm, this indicates that most of the absorption occurs in the region near to the surface. A value of around 1.57^{16}photon cm^{-3}s^{-1} for G is obtained. In order to calculate n we need to know the constant of proportionality

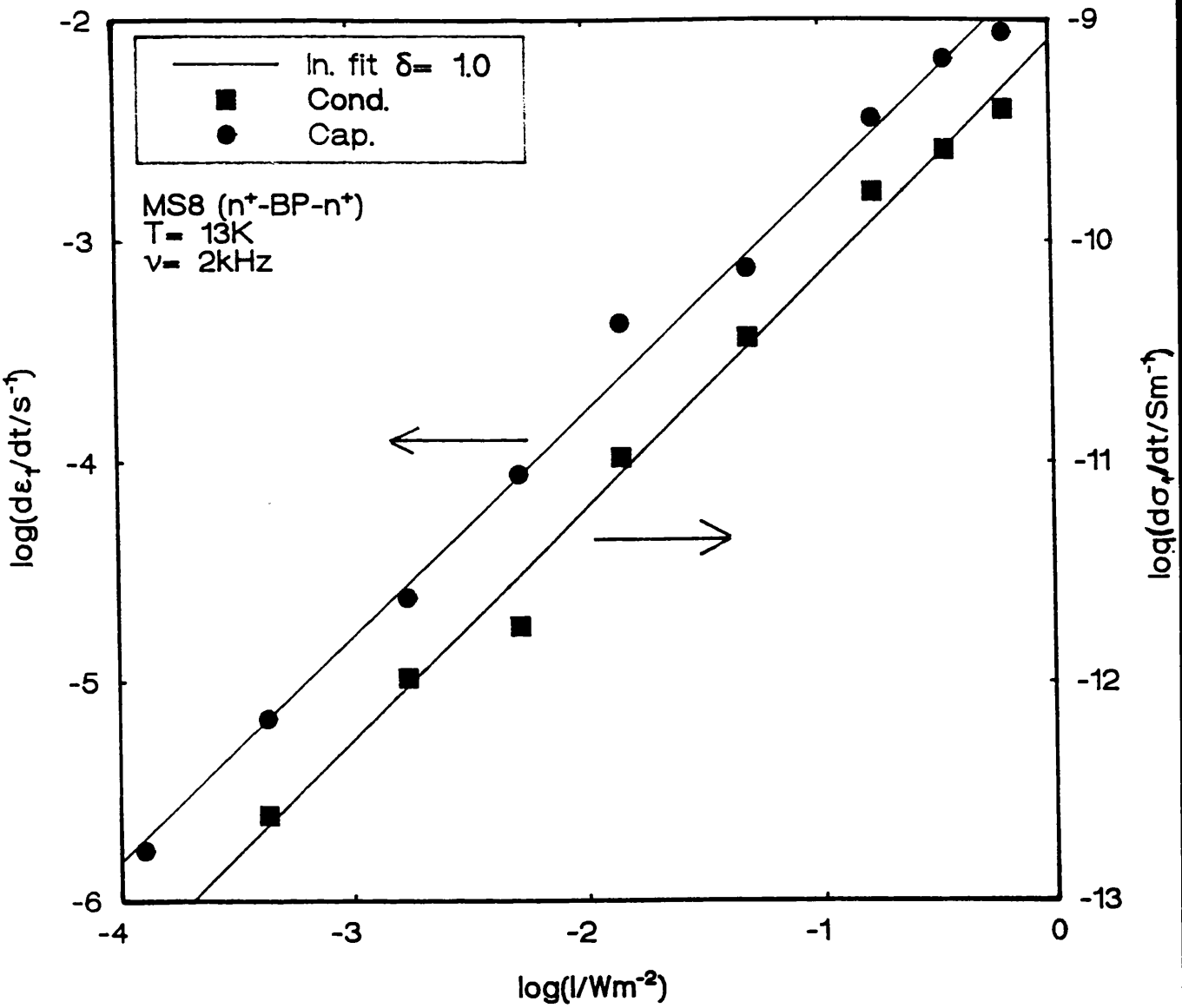

Figure 7.7: The initial rates of rise in the linear region after the start of illumination for a n^+-BP-n^+ sample (MS8). The solid lines have gradients 1.0.

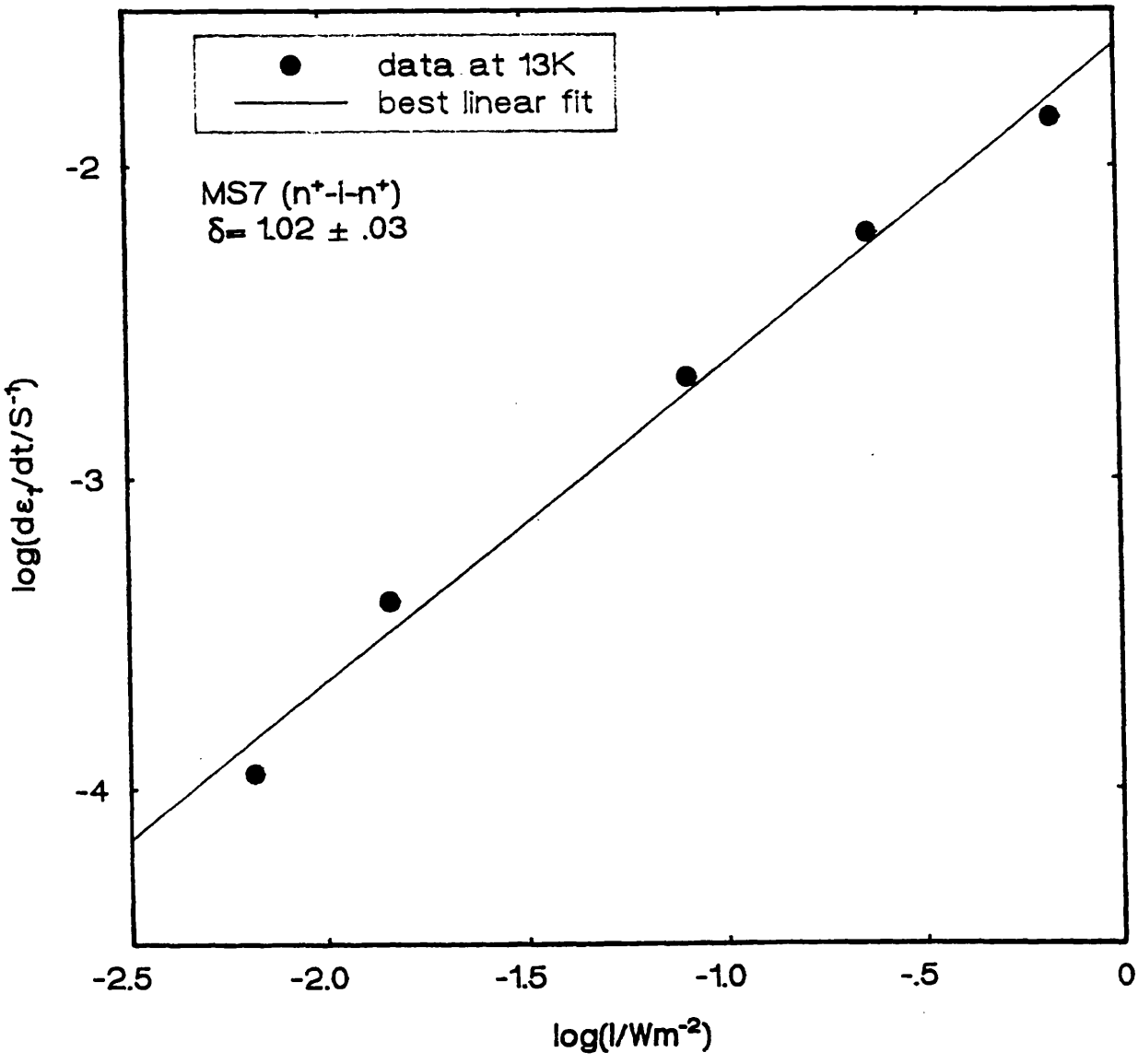

Figure 7.8: The initial rate of rise of the dielectric constant in the linear region for an n^+-i-n^+ sample (MS7) measured at 2kHz. the solid line has gradient 1.0.

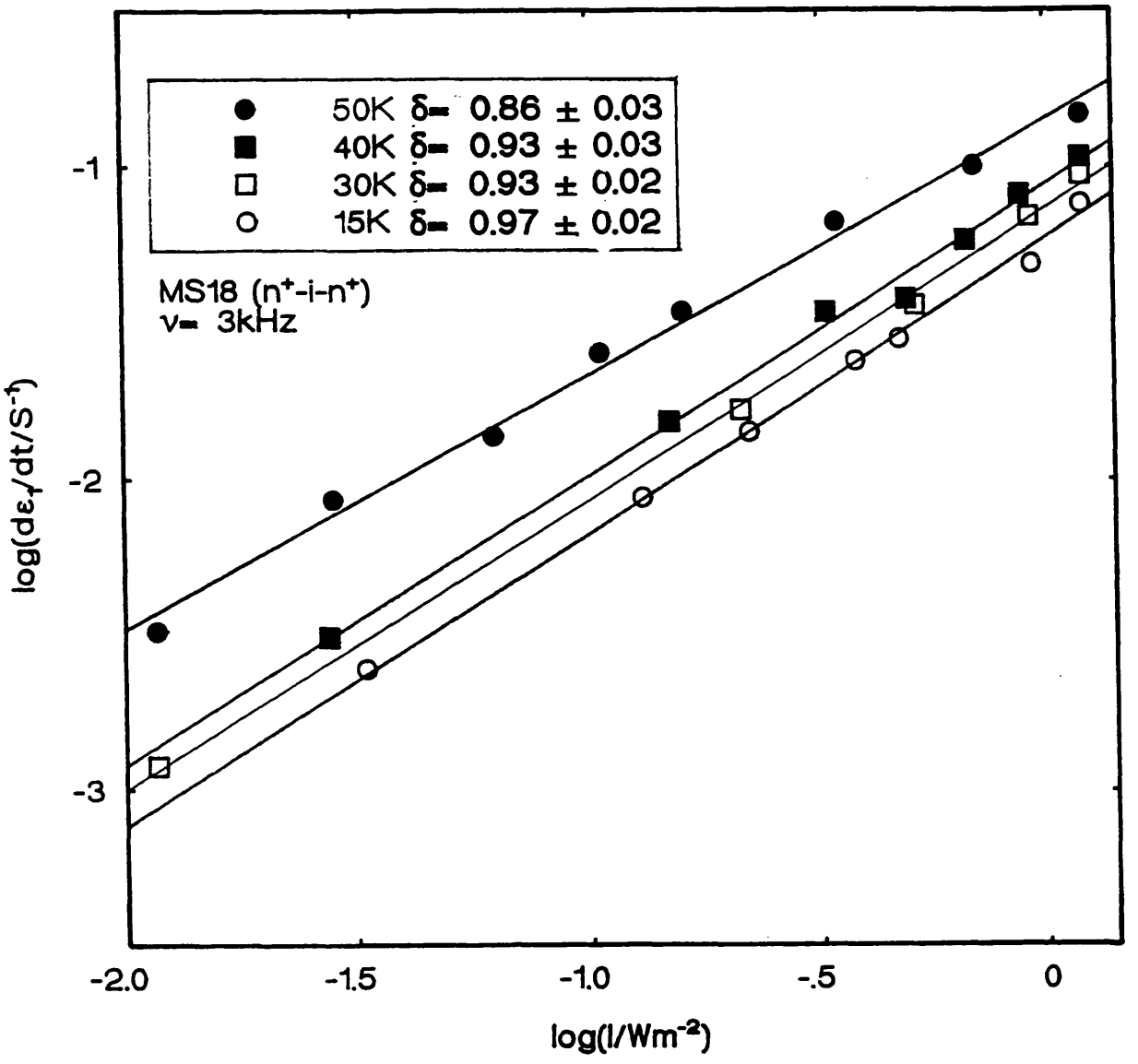

Figure 7.9: The initial rate of increase of the dielectric constant for an n^+-i-n^+ at various temperatures. The appropriate temperature is given in the graph.

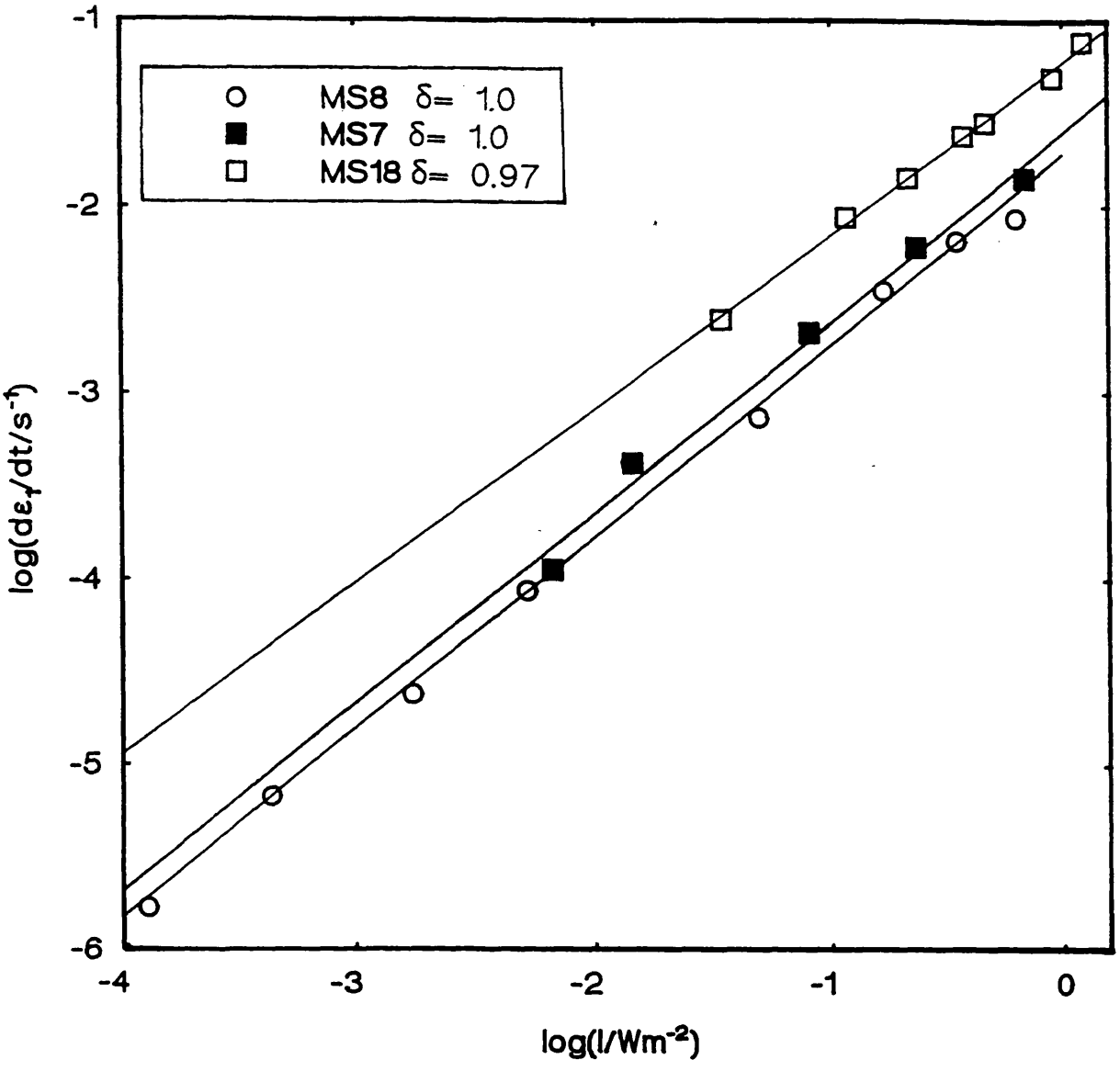

Figure 7.10: The initial rate of increase of the dielectric constant for three samples at 13K. The appropriate sample and gradient are given in the graph.

between $\Delta\epsilon_1$ and n, K. Given the uncertainty in the model describing the loss, there is no reliable direct way of calculating it, but we use a method based on the LESR measurements of Boulitrop and Dunstan (1982). We use their value for the number of spins generated at a given generation rate G to give us the value of n which together with the value $\Delta\epsilon_{eq}$ at the intensity I give the constant K. We obtain a value for n $\approx 1.43 \times 10^{17}$ cm^{-3} and equation (7.4) gives a value of τ = 1700s. Therefore the value for the efficiency η at 0.172μWcm^{-2} is found to be $\eta \approx 5.35 \times 10^{-3}$. This is similar to the value found by Lemmon (1990) of $\eta \approx 5.8 \times 10^{-3}$ on similar material. The efficiency was calculated for the curve (1) in fig.(7.2) where the intensity is 34.4μWcm^{-2} and found to be $\eta \approx 5 \times 10^{-3}$. Calculating the efficiency for other samples give similar values (see table 7.1). These low quantum efficiencies confirm that the majority of the incoming light generates carriers which recombine directly and do not contribute to the population determining the long lived a.c. loss.

In order to proceed further we need to know how the photoinduced relative permittivity ($\Delta\epsilon_1$) varies with the number of carriers n. Now $\Delta\epsilon_1$ rises approximately linearly with time after the commencement of generation and in the absence of effective recombination at short times, one would expect quite generally that n would rise linearly with time. It is therefore natural to assume that $\Delta\epsilon_1 \propto n$. There is however no theoretical ground for this assumption. The only existing model is that of SFB (model explained in chapter 3). According to equation (3.28), it suggests that the loss varies as the square of the number of carriers ($\Delta\epsilon_1 \propto n^2$). Our initial transient behaviour can then be represented by the empirical relation.

$$n \sim (It)^{1/2} \tag{7.5}$$

this yields:

$$\frac{d(\Delta\epsilon_1)}{dt} \propto \frac{d}{dt}(It) \propto I \tag{7.6}$$

Such a square root rise of n(t) at short times is also apparent in the LESR data of Bort et *al.*(1991) which suggests that this analysis is on the right lines.

Unfortunately, none of the simple models predict a square root rise of carrier density with time. This is most easily seen from the distant pair recombination model of Searle (1990):

$$\frac{dn}{dt} = G - \frac{n}{\tau(n^{-1/3})} with \tau = \tau_0 \exp(-n^{-1/3}/a) \tag{7.7}$$

At short times n/τ is negligible because τ is so long. Hence one predicts $n \propto Gt$ which is not what is observed. The SFB model concerns steady state and is not easy to adapt to discuss transient behaviour. However there is no reason to believe that the number of carriers will not increase linearly.

There is one model however which predicts a behaviour approximately of this type, that of Baranovskii, Ivchenko and Shklovskii (1987). The model assumes that electrons and holes are created randomly in the band tails and they only recombine if their separation R is less than a critical distance $\mathcal{R}$. Using a computer simulation, the authors could calculate the steady state concentration N. They injected particles and by fixing the distance $\mathcal{R}$, they found that N is reached more rapidly as $\mathcal{R}$ increases. The number N was averaged over the states in the system with the number of injected particles around 8000 and they ended up with a relation of the form $N = \frac{\mu}{\mathcal{R}^3}$ with $\mu \approx 0.25$.

Baranovskii, Ivchenko and Shklovskii also solved a simpler model valid at short times with a single carrier species undergoing self-recombination when they were injected into the system close to another. The concentration of these particles was found to satisfy the relation $N = \frac{\nu}{\mathcal{R}^3}$ with $\nu \approx 0.165$. This number was calculated by considering a Poisson distribution since the particles are randomly distributed. In the equilibrium state, the probability that an injected carrier recombines immediately is equal to 1/2, this probability is the same as the probability of finding no particle at distance less than $\mathcal{R}$, thus:

$exp(-\frac{4\pi}{3}N\mathcal{R}^3) = 1/2$, this implies that N = $\frac{3ln2}{4\pi\mathcal{R}^3} \approx \frac{.165}{\mathcal{R}^3}$.

The computer simulations showed that the time dependence of the rise in carrier number at short times was sub-linear (square-root like) for both models.

7.7 A Model for the Rise time

We now introduce a new analytic approach which is based on the Baranovskii et *al.*(1987) model and is close to the observed experimental data. We also apply the theory to the latest results on the LESR measurements (see Bort et *al.* 1991). Analytically, it is assumed that equal number of electrons and holes are generated by the incident light (n=p). It is also assumed that these free carriers become randomly distributed in space. Then it is possible to use a Poisson distribution to calculate the probability P(R) of finding the nearest neighbour hole to a given electron in the distance dR at R, where R is the electron hole separation. This probability is given by the probability of finding a state multiplied by the probability of finding no nearer neighbour at a distance less than R, thus.

$$P(R) = 4\pi n R^2 \left(1 - \int_0^R P(r)dr\right) \tag{7.8}$$

If we assume a solution to the equation as:

$$P(R) = 4\pi \mathrm{nR}^2 \exp(-\frac{4}{3}\pi \mathrm{nR}^3)$$

Then the integral gives:

$$\int_0^R P(r)dr = 1 - \exp(-\frac{4}{3}\pi n R^3)$$

Substituting these in the equation (7.8), yields the well-known self consistent result:

$$P(R) = 4\pi \mathrm{nR}^2 \exp(-\frac{4}{3}\pi \mathrm{nR}^3) \tag{7.9}$$

Only carriers which escape the geminate recombination can take part in the build up of the long-lived population with time. We model this by specifying the electron-hole separation for such carriers must be greater than $\mathcal{R}$. Therefore the time dependence of the steady state concentration of the photoelectrons on the excitation intensity $\frac{dn}{dt}$ is given by: The probability for an electron to be trapped at a

distance greater than $\mathcal{R}$ from the hole, i.e.

$$\int_{\mathcal{R}}^{\infty} P(R)dR = exp(-\frac{4}{3}\pi p\mathcal{R}^3)$$

less the probability of finding a hole at a distance less than R, i.e.

$$\int_{0}^{\mathcal{R}} P(R)dR = 1 - exp(-\frac{4}{3}\pi n\mathcal{R}^3)$$

Hence, $\frac{dn}{dt}$ is given by:

$$\frac{dn}{dt} = g\left[\left(exp(-\frac{4}{3}\pi p\mathcal{R}^3) - (1 - exp(-\frac{4}{3}\pi n\mathcal{R}^3)\right)\right] \tag{7.10}$$

where g is the generation rate of free carriers. From the first assumption n=p, we have:

$$\frac{dn}{dt} = g\left(2exp(-\frac{4\pi n}{3}\mathcal{R}^3) - 1\right) \tag{7.11}$$

To use a dimensionless scale, we write:

$$\nu = n\mathcal{R}^3$$

$$\tau = tg\mathcal{R}^3$$

The equation (7.11) can be expressed as :

$$\frac{d\nu}{d\tau} = 2exp(-\frac{4\pi}{3}\nu) - 1 \tag{7.12}$$

The above equation can be solved analytically. A solution is given by:

$$\frac{4\pi}{3}\nu = \ln\left(2 - e^{-\frac{4\pi}{3}\tau}\right) \tag{7.13}$$

At long times, $\nu \Longrightarrow \frac{3}{4\pi}\ln 2$, in agreement with the result of the Baranovskii et *al* simulation for a single randomly distributed carrier. The difference from the long time result of the electron-hole simulation is believed to reflect the fact that we have assumed random carrier distributions; in practice there will be signifficant non-randomness. However we ignore this difference, in particular we assume that the time dependence is correctly described by our analytic result equation (7.13).

Fig.(7.11) shows $\nu(\tau)$. The function is normalized to a suitable scale. Also on the same graph the experimental data taken by Bort et *al.* 1991 is compared with $\nu(\tau)$. The fit is reasonable especially in the region at short times in which we are most interested. Fig.(7.12) represents the square of $(\nu(\tau))^2$ together with one of our time dependence data taken under 43nWcm^{-2}. It can be seen that these two curves are in a quite good agreement although the fitting is not perfect.

Quantitatively we note that the maximum number of carriers from relation (7.13) is obtained by equating $\frac{d\nu}{d\tau} = 0$, this gives:

$$2\exp(-\frac{4\pi}{3}\nu) - 1 = 0, \text{ this implies that } \nu = \frac{3ln2}{4\pi} = 0.165$$

therefore $\nu = n\mathcal{R}^3 = 0.165 \Longrightarrow n = \frac{0.165}{\mathcal{R}^3}$. This number of carriers is the number obtained by Baranovskii et *al.* Although at very short times $\nu \propto \tau$, fig.7.12 shows that for a range of times ν^2 increases approximately linearly with τ. In this range $\frac{d(n^2)}{dt} \sim \frac{n^2_{max}}{t_1}$ where $t_1 \approx \frac{0.4}{g\mathcal{R}^3}$. Substituting for n^2_{max} gives:

$$\frac{d\epsilon}{dt} \propto \frac{dn^2}{dt} \sim \frac{n^2}{t_1} \sim 0.07g/\mathcal{R}^3 \tag{7.14}$$

This suggests that the rate of increase of ϵ_1 will be proportional to $g^{1.0}$, as is observed, provided that $\mathcal{R}$ is a constant.

Physically this model implies that, if electron-hole pairs are generated which end up more than a distance $\mathcal{R}$ apart, then they will last for a long time and contribute to the a.c. loss. If when trapping occurs, the pairs end up less than $\mathcal{R}$ apart they will recombine and will not contribute to the loss. However such an abrupt cut-off, cannot be the complete story. One can see this in two ways. Firstly, equation (7.13) implies that n will always rise to the same value $0.165/\mathcal{R}^3$ independent of g. This violates our observation that $\Delta\epsilon_1$ (when t $\rightarrow \infty$), and hence n, increases slowly with I. Secondly, there is no provision in equation (7.12) for the population to decay ($\frac{d\nu}{dt} for g = 0$). this analysis should therefore be regarded as only a first approximation to the time dependent behaviour of the long lived carriers.

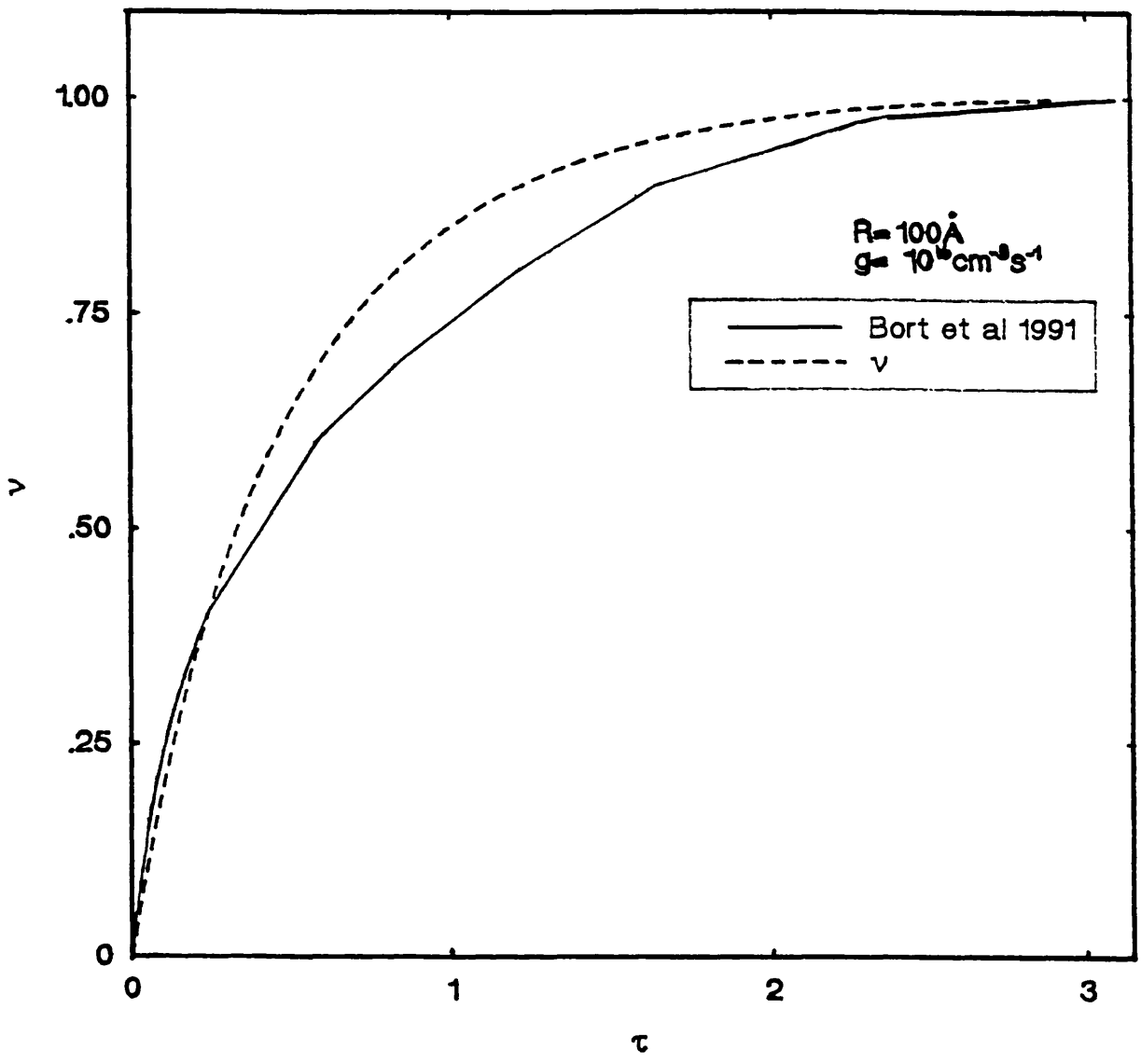

Figure 7.11: The function $\nu(\tau)$ as a function of τ. The solid curve corresponds to the LESR data of Bort et *al.* 1991. The fitting parameters are given in the graph.

7.8 Discussion

To summarize, we have seen that the equilibrium relative permittivity rises with the excitation intensity in a power law $\Delta\epsilon_1 \propto I^{0.16}$ over the accessible range of intensities. We have also observed that the rate of increase of the photoinduced loss increases as $I^{1.0}$ over the full intensity range, i.e. 10^{14} to $10^{18}cm^{-3}s_{-1}$ no transition is seen from predominantly geminate to predominantly non-geminate recombination as expected theoretically (see Shklovskii et *al.* 1989a), when the effective behaviour rise time for the loss changes with the intensity of illumination. When the light was removed, the long decay of $\Delta\epsilon_1$ with time was observed and the behaviour could be satisfactorily described by a $\ln t$ relation. The decay towards the dark value was also temperature dependent, it was faster at higher temperatures than at lower temperatures. The phenomenon is attributed to the excitation of the carriers trapped in the tail states. At high temperatures, the trapped carriers could be excited and recombine with the excess of holes. The process could be enhanced because of the presence of thermal energy whereas at low temperatures, the process is very slow and takes place by tunnelling.

Unlike the a.c. response, the evolution of the d.c. photocurrent was found to respond within the time resolution of our measuring system ($\sim$1 sec) when the light is applied, and likewise decays rapidly to zero when the light is removed. The d.c. photocurrent was not altered by the build up of the background population to the steady state value. This may suggest that the two responses behave differently and can be treated separately. However, we have seen in chapter 6 that under CW illumination, the steady state a.c. photoconductivity measured at different intensities, when normalised to the appropriate d.c. photoconductivity, $\frac{\sigma_1(\omega,I)}{\sigma_1(0,I)}$ scales to a reduced frequency $\frac{\omega}{\sigma_1(0,I)}$. With the scaling behaviour being similar to that of other hopping systems, at least in the shape of the behaviour, this indicates strongly that the d.c. and a.c. photoconductions are governed by the same hopping mechanism and occur within the same group of states. These two observations are not neces-

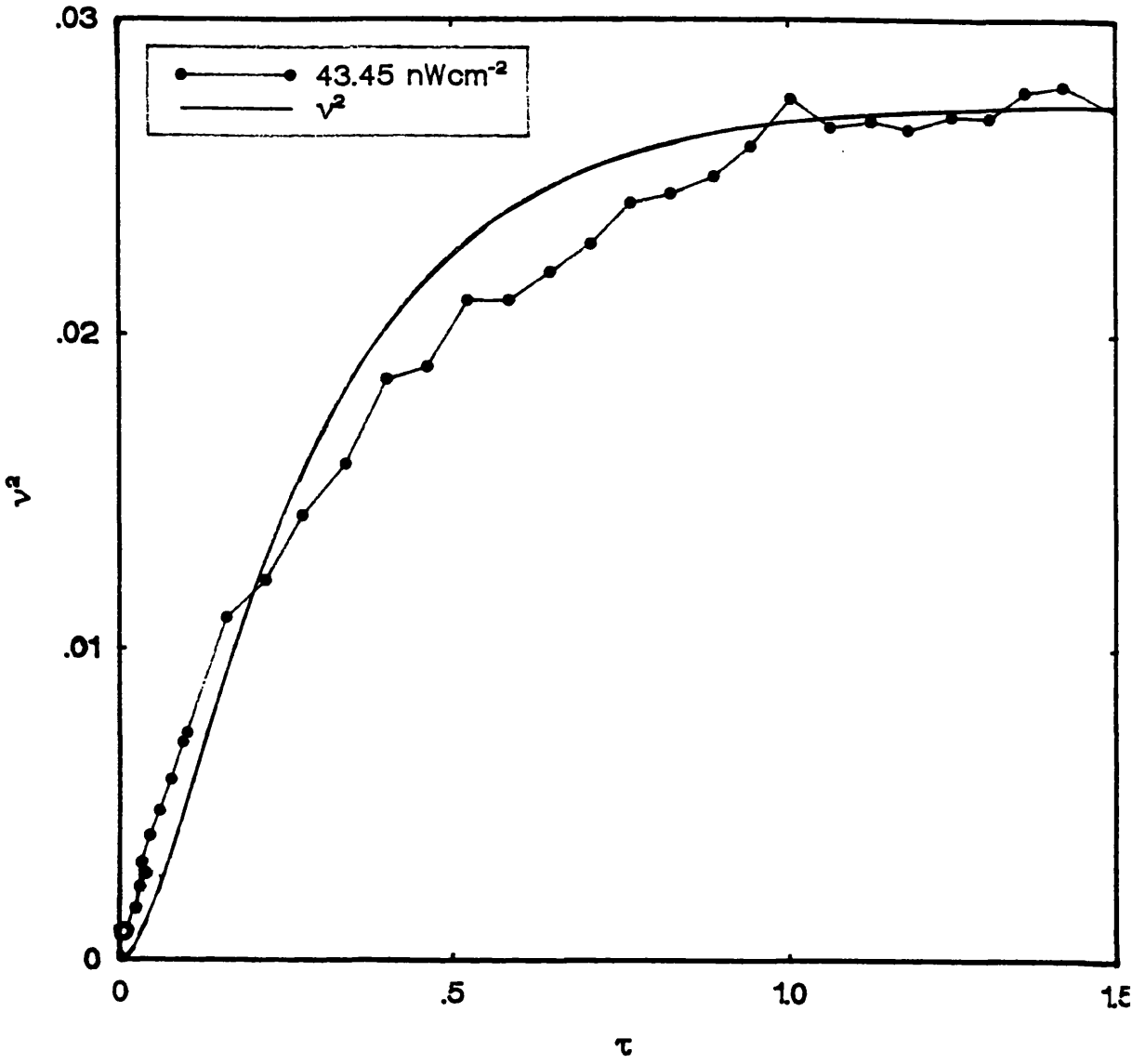

Figure 7.12: The function $\nu^2(\tau)$ against τ. the curve (2) corresponds to the dielectric changes with time measure under 43nWcm^{-2} plotted at the same scale. A value of $\mathcal{R} = 100\mathring{A}$ is used for the fitting.

sarily incompatible, because if we assume that the d.c. photoconduction takes place in states relatively high in the tail states, after the removal of the light, the first decaying carriers will carry d.c. photocurrent, which will die out quickly. When the response reaches the deep states, which are likely to lie further down in the tails, then the dominating steady state population will start responding.

The rise and the decay of the d.c. response behaves in an analogous way to the photoluminescence signal as reported by Bort et *al.*(1991). This indicates the existence of a geminate photoluminescence alike in our measurements which occurs immediately after the light is switched on or off.

When comparing the experimental observations with the existing theories, we think that at the present there is no single approach that describes the data adequately for the following reasons:

For example consider again the model proposed by Searle (1990), which analytically has much in common with the SFB theory except that it ignores any geminate recombination and does not consider any downwards hopping. The probability $\eta(R)$ (see equation 3.11) of escaping geminate recombination is set to be 1, whereas in the SFB model it is of the order of 10^{-2}. The model predicts an intensity dependence of the d.c. photoconductivity of the form $\sigma_{dc} \propto G^{0.93}$ which is similar to the SFB value and close to observations. The time dependence in this case is given as:

$$\frac{dn}{dt} = G - \frac{n}{\tau(n^{-1/3})} \tag{7.15}$$

All parameters have been defined before. The rise time of the response is predicted by equation (7.15) to be linear (see section 7.6); however, previous data by Hoheisel et *al.* and recent data by Bort et *al.*(1991) suggest experimentally a square root relationship which our own work confirms. One other thing about the model is that the decay of signal predicted from equation (7.15) when the light is removed is given by:

$$\frac{dn}{dt} = -\frac{n}{\tau(n^{-1/3})} \tag{7.16}$$

This predicts a behaviour rather slower than that observed and curved on a $\ln t$ plot; and it is not in any way close to the $\ln t$ behaviour described by Long et *al.*(1988b) and observed in the present work. The SFB model is difficult to adapt for the time dependence but qualitatively we do not expect it to be very different from that of Searle.

The Baranovskii et *al.* model on the other hand, gives the best estimate of the rise of the distant pairs without ignoring those carriers that undergo self-recombination (geminate) immediately after they were injected. Assuming that the loss varies as the square of the number of carriers, the shape of the curve of the rise is qualitatively described by the model provided we ignore the quadratic region just after the commencement of illumination. However the model fails to predict any decay of the signal. A priori, theoretically after the light is removed g=0, it predicts that:

$$\frac{dn}{dt} = 0$$

which is of course completely at variance with the observation. It must therefore be regarded as only a suggestive first approximation to the true behaviour.

As far as our experimental data is concerned, we believe that the rise of the photoinduced response can be reasonably explained by Baranovskii et *al.* model and the slow decay behaviour, however can be described by the model suggested by Long et *al.*(1988b) in which the holes are assumed trapped and immobile and electrons diffuse apart from the hole before a geminate recombination occurs. The diffusion process is assumed by electron tunnelling through the band tail states. This model gives a good description of the data and is better than any other model available in the literature.

Obviously we are aware of the simplicity of the model discussed in section (7.7). Nonethless it is still more adequate than the general theory. Practically, we believe that there is a strong need for a detailed model that combines the best features of the geminate model of Shklovskii et *al.* (1989a), the Baranovskii et *al.* (1987) theory and the statistical elements of the present discussion to improve the explanation

of the experimental results including in particular the rate of increase of the loss with the intensity and the decoupling of the intensity dependence and the frequency dependence of the photoinduced loss.

Sample	Compensated Doping level (vppm)	Temperature (K)	η
MS3	2.5	12.5	5.8×10^{-3}
MS7	0	13	8×10^{-3}
MS8	5	13	5.35×10^{-3}
MS18	0	15	0.022
Anderson(1989)	0	12.5	8.4×10^{-3}

Table 7.1: The quantum efficiency for various samples.

CHAPTER 8

Summary and Conclusion.

The aim of this work was to study some of the electrical properties of the hydrogenated amorphous silicon: These include the d.c. and a.c. conductivities in the dark and under illumination, the time dependence of both conductivities and the scaling of the low temeprature photoconductivity and the recombination mechanism within the range of excitation intensity used to illuminate the sample.

The characteristics in the dark revealed that the material prepared in Dundee University is of higher quality than the one measured by Shimakawa et *al.* in that no additional high temperature a.c. loss such as that due to inhomogeneities was observed in the intrinsic material. Also, the d.c. conductivity was found to be higher and the overall loss was lower in Dundee samples and this indicates higher mobility. The compensated samples on the other hand showed some contribution to the loss at high temperature as expected theoretically. The other part of the thesis was devoted to the optically induced loss. The D.C. photoconductivity as a function of the excitation intensity folows a power law of the form $\sigma_1(0,I) \propto I^{\gamma}$ with $\gamma \approx 1$ at low temperature over the accessible range of intensities. As the temperature increases, γ declines. The change in the dielectric constant obeys a similar power law but with a weaker exponent, i.e $\Delta\epsilon_1 \propto I^{\beta}$ with $\beta \approx 0.16$. The exponent is weakly temperature dependent. The observed $\frac{\sigma_\phi}{eG}$ and η and $\sigma_1(\omega,I) \propto \omega^s$ of the both intrinsic and compensated samples were of the form reported previously. The results also agree quite well with the latest theory proposed by Shklovskii et *al.*(1989a,b). We

observed a novel scaling relationship of the low temperature frequency dependent photoconductivity under varying intensites of illumination. The scaling behaviour was excellent at 12.5K but as the temperature increases above 50K the scaling starts deteriorating as a result of thermal effects on the carriers becoming more significant. This scaling relationship is a strong evidence that both D.C. and A.C photoconductions are governed by hopping process and that carriers percolate through the band tails before recombining. Both intrinsic and compensated samples showed a similar form of scaling. This suggests that the scaling relationship is an intrinsic feature of the amorphous material and it is not affected by the potential fluctuations which are supposed to exist in the compensated material as observed. Currently, there is no theoretical approach to calculate the shape of the observed data. However, as regards the shape, the results could be fitted with a theoretical curve originally proposed for variable range hopping systems. The time dependence data showed that the relative permittivity rises linearly with time and that the risetime decreases with increasing the generation rate. The risetime of the D.C. photoconductivity was found to be several orders of magnitude less than that of the A.C. photoresponse. Also, the build up of the number of carriers trapped in band tails to the steady state value does not affect the risetime of the D.C. photoconductance. The states which respond to the high frequency a.c. signal have no effect on the d.c. current. After the removal of illumination, the D.C. conductivity decays rapidly to the dark value within seconds, whereas, the A.C. showed an initial fast decay followed by a slow rate decrease. This suggests that the D.C. transport occurs in higher states in band tails. An important point about our results is that the behaviour we observed varies uniformly throughout the range of intensities covered by the measurement (corresponding to carrier generation rates between 10^{14} and 10^{18} $cm^{-3}s^{-1}$). There is no sign of any discontinuity which might be expected at a transition from geminate to non-geminate recombination.

REFERENCES

- Abkowitz, M., Le Comber, P. G. and Spear, W. E., *Commun. Phys.*, **1** (1976) 175.
- Ambegaoker, V., Halperin, B. I., and Langer, J. S., *Phys. Rev.* **B, 109** (1971) 2612.
- Anderson, M. J., *PhD Thesis*, University of Glasgow, (1989).
- Apsley, N. and Hughes, H. P., *Phil. Mag.*, **30** (1974)963; *Ibid.*, **31** (1975) 1327.
- Austin, I. G. and Mott, N. F., *Adv. Phys.*, **18**(1969) 41.
- Balkan, N., Butcher, P. N., Hogg, W. R., Long, A. R. and Summerfield, S., *Phil. Mag.*, **B 51** (1985)L7.
- Baranovskii, S. D., Ivchenko, E. L., and Shklovskii, B. I., *Sov. Phys.* JETP., **65** (1987)1260.
- Baranovskii, S. D., Fritzsche, H., Levin, E. I., Ruzin, I. M., and Shklovskii, B. I., *Sov. Phys.* JETP., **69** (1989) 773.
- Baranovskii, S. D., Saleh, R., Thomas,¶., Vaupel, H., *Proceedings of the 14th International Conference on Amorphous Semiconductors- Science and Technology, Garmisch-Partenkirchen 1991* edited by Bauer, G. H., Fuhs, W., and Ley, L. p. 567.
- Beyer, W., Fischer, R. and Overhof, H., *Phil. Mag.*, **B 39**(1979) 205.

- Beyer, W., and Mell, H., (*Proceedings of the 7th International Conference on Amorphous and Liquid Semiconductors,* ed. W. E. Spear, (CICL , University of Edinburgh 1977), p. 333.
- Beyer, W., Mell, H. and Overhof, H., (*Proceedings of the 7th International Conference on Amorphous and Liquid Semiconductors,* ed. W. E. Spear, (CICL , University of Edinburgh 1977), p. 328.
- Bort, M., Carius, R., and Fuhs, W., *J. Non-Cryst. Solids.,* **114** (1989)280.
- Bort, M., Fuhs, W., Liedtke, S., and Stackowitz, R., *Phil. Mag. Lett.,* **64** (1991)227.
- Böttger, H., Bryksin, V. V., and Yashin, G. Yu., *J. Phys. C: Solid State Phys.* **12** (1979)3951.
- Boulitrop, F., and Dunstan, D. J., *Solid. Stat. Comm.,* **44** (1982)841.
- Bryksin, V. V., *Sov. Phys. Solid State* **22** (1980) 1421.
- Butcher, P. N., and Summerfield, S., *J. Phys. C: Solid State Phys.* **14** (1981) L1099.
- Carius, R., and Fuhs, W., *J. Non-Cryst. Solids.,* **77&78** (1985) 659.
- Cloude, C., Spear, W. E., Le Comber, P. G., and Hourd, A. C., *Phil. Mag.* **B. 54** (1986)L113.
- Dersch, H., Schweitzer, L., and Stuke, J., *Phys. Rev.* **B 28** (1983)4678
- Dunstan, D. J., *Phil. Mag.* **B. 52** (1985)111.
- Elliott, S. R., *Adv. Phys.,* **36** (1987) 135.
- Emin, D. *Phys. Rev. Lett.,* **32** (1974)303
- Fishchuk, I. I., and Rudko, V. N., *J. Phys. C: Solid State Phys. 13* (1980)L493.

- Fritzsche, H., *J. Non-Cryst. Solids.,* **114** (1989)1.
- Fuhs, W., *J. Non-Cryst. Solids.,* **77&78** (1985)593.
- Hoheisel, M., Carius, R., and Fuhs, W., *J. Non-Cryst. Solids.,* **59&60** (1983) 453; *ibid* **63** (1984)313.
- Holland, M. C., *PhD Thesis*, University of Glasgow, (1987).
- Huang, C. Y., Guha, S., and Hudgens, S. J., *Phys. Rev.* **B 27** (1983)7460.
- Jahn, K., Carius, R., and Fuhs, W., *J. Non-Cryst. Solids.,* **97&98** (1987)575.
- Jahn, K., Fuhs, W., and Pierz, K., *J. Non-Cryst. Solids.,* **114** (1989)307.
- Johanson, R. E., Fritzsche, H., and Vomvas, A., *J. Non-Cryst. Solids.,* **114** (1989)274.
- Le Comber, P. G. and Spear, W. E., *Phys. Rev. Lett.,* **25** (1970) 509.
- Long, A. R., *Adv. Phys.,* **31** (1982) 553.
- Long, A. R., *Phil. Mag.,* **B, 59** (1989a) 377.
- Long, A. R., *J. Non-Cryst. Solids.,* **114** (1989b) 348.
- Long, A. R., in *Hopping Transport in Solids* ed. by M. Pollak and B. Shklovskii. (1991) p.208. Long, A. R., and Hansmann, L., 1990, in "*Hopping and related Phenomena*", eds. Fritzsche, H., and Pollak, M.,(World Scientific, Singapore)p.77.
- Long, A. R., Hogg, W. R., Balkan, N., *Phil. Mag.,* **B 48** (1983)L55.
- Long, A. R., Hogg, W. R. Holland, M. C., Balkan, N., and Ferrier, R. P., *Phil. Mag.,* **B, 51**(1985) 39.
- Long, A. R., McMillan, J., Balkan, N., and Summerfield, S., *Phil. Mag.,* **B, 58**(1988a) 153.

- Long, A. R., Anderson, M. J., Shimakaw, K., and Imagawa, O., *J. Phys. C: Solid. Stat. Phys.* **21** (1988b) L1199.
- Long, A. R., Mostefa, M., Lemon, R., *J. Phys. C: Condens. Matter.* **3** (1991a) 2589
- Long, A. R., Mostefa, M., Lemon, R., *J. Non-Cryst. Solids.*, **137&138** (1991b)419.
- Miller, A., and Abrahams, E., *Phys. Rev.,* **120** (1960) 745.
- Misra, D. S., Kumar, A., and Agarwal, S. C., *Phys. Stat. Solidi (a)* **85** (1984)297.
- Monroe, D., *Phys. Rev. Lett.,* **54** (1985)146.
- Mott, N. F., *Phil. Mag.,* **19** (1969) 835.
- Mott, N. F., and Davis, E. A., *Electronic Processes in Non-Crystalline Materials,* (Oxford: Clarendon Press 1979).
- Movaghar, B., Grünewald, M., Ries, B., and Bässler, B., *Phys. Rev.* **B 33**(1986)8.
- Movaghar, B., Pohlmann, B. and Sauer, G. W., *Phys. Status Solidi* **B 97** (1980)533.
- Nagels, P., *in Amorphous Semiconductors,* (ed. M. H. Brodsky., 1979) p. 113.
- Nashashibi, T. S., Austin, I. G., and Searle, T. M., *Phil. Mag.,* **35** (1977)831.
- Nitta, S., shimakawa, K., and Sakaguchi, K., *J. Non-Cryst. Solids.*, **24**(1977) 137.
- Overhof, H., and Beyer, W., *Phil. Mag.,* **B 43** (1981) 433.
- Overhof, H., and Beyer, W., *Phil. Mag.,* **B 47** (1983) 377.

- Overhof, H. and Thomas, P., *Electronic Transport in Hydrogenated Amorphous Semiconductors* (Springer-Verlag, Berlin, 1989).
- Pollak, M., *Phil. Mag.,* **23** (1971) 519.
- Pollak, M., *J. Non-Cryst. Solids.,* **11** (1972) 1.
- Pollak, M., and Geballe, T. H., *Phys. Rev.,* **122** (1961) 1742.
- Searle, T. M., *Phil. Mag. Lett.* **61** (1990) 153.
- Shimakawa, K., Long, A. R., and Imagawa, O., *Phil. Mag. Lett.,* **56** (1987) 79.
- Shimakawa, K., Long, A. R., Anderson, M. J., and Imagawa, O., *J. Non-Cryst. Solids.,* **97&98** (1987) 623.
- Shklovskii, B. I., Fritzsche, H., Baranovskii, S. D., *Phys. Rev. Lett.,* **62** (1989a) 2989.
- Shklovskii, B. I., Fritzsche, H., Baranovskii, S. D., *J. Non-Cryst. Solids.,* **114** (1989b) 325.
- Shklovskii, B. I., Levin, E. I., Fritzsche, H., Baranovskii, S. D., 1990, in *"Advances in Disordered Semiconductors."* Vol.III., *Transport, Correlation and Structural Defects,* edited by Fritzsche, H., (Singapore: World Scientific), p. 161.
- Spear, W. E., 1988 in "*Amorphous Silicon and Related Materials*" ed. Fritzsche, H., (World Scientific, Singapore) P.721.
- Spear, W. E., and Cloude, C., *Phil. Mag. Lett.,* **55** (1987)271.
- Springett, B. E., *Phys. Rev. Lett.,* **31** (1973) 1463.

- Stachowitz, R., Bort, M., Carius, R., Fuhs, W., and Liedtke, S., *Proceedings of the 14^{th} International Conference on Amorphous Semiconductors- Science and Technology, Garmisch-Partenkirchen 1991* edited by Bauer, G. H., Fuhs, W., and Ley, L. p. 551.
- Stachowitz, R., Fuhs, W., and Jahn, K., *Phil. Mag.,* **B 62** (1990)5.
- Staebler, D. L., Wronski, C. R., *Appl. Phys. Lett.,* **51** (1980)3262.
- Street, R. A., *Adv. Phys.* **30** (1981a) 593.
- Street, R. A., *Phys. Rev.,* **B 23** (1981b) 861.
- Street, R. A., *Phys. Rev.,* **B 18** (1978) 1880.
- Street, R. A., and Biegelsen, D. K., *Solid. Stat. Comm.,* **44** (1982) 501.
- Summerfield, S., and Butcher, P. N., *J. Phys.,* **C 15** (1982) 7003.
- Summerfield, S., *Phil. Mag.,* **B 48** (1985) 9.
- Vaněček, M., Kočka, J., Demo, P., Šípek, F., and Tříska, A., *J. Non-Cryst. Solids.,* **90** (1987)183
- Vanier, P. E., and Griffith, R. W., *J. Appl. Phys.* **53** (1982)3098.
- Varmis, C., Hirsch, M. D., and Vanier, P. E., AIP. Conf., **120** (1984)133.
- White, G. K., "*Experimental Techniques in Low Temperature Physics.*" (Oxford: Clevendon Press. 1979).
- Wronski, C. R., and Carlson, D. E., *proceedings of the seventh International Conference on Amorphous and Liquid Semiconductors, Edinburgh, 1977* edited by Spear, W. E.,(CICL University of Edinburgh 1977), p. 452.
- Yoon, G. G., and Fritzsche, H., *Phil. Mag. Lett.,* **63** (1991) 101.